UNIVERSITI TEKNOLOGI MARA

AN INTEGRATED HEAT RECOVERY SYSTEM FOR ENHANCED THERMOELECTRICAL PERFORMANCE OF A POLYMER ELECTROLYTE MEMBRANE FUEL CELL

MUHAMMAD HADRAMI BIN HAMDAN

PhD

August 2026

UNIVERSITI TEKNOLOGI MARA

AN INTEGRATED HEAT RECOVERY SYSTEM FOR ENHANCED THERMOELECTRICAL PERFORMANCE OF A POLYMER ELECTROLYTE MEMBRANE FUEL CELL

MUHAMMAD HADRAMI BIN HAMDAN

Thesis submitted in fulfilment
of the requirements for the degree of
Doctor of Philosophy
(Mechanical Engineering)

Faculty of Mechanical Engineering

August 2026

CONFIRMATION BY PANEL OF EXAMINERS

I certify that a Panel of Examiners has met on 14th May 2026 to conduct the final examination of Muhammad Hadrami bin Hamdan on his Doctor of Philosophy thesis entitled "An Integrated Heat Recovery System For Enhanced Thermoelectrical Performance Of A Polymer Electrolyte Membrane Fuel Cell" in accordance with Universiti Teknologi MARA Act 1976 (Akta 173). The Panel of Examiners recommends that the student be awarded the relevant degree. The Panel of Examiners was as follows:

Aidah Jumahat, PhD
Professor
Faculty of Mechanical Engineering
Universiti Teknologi MARA
(Chairman)

Aman Mohd Ihsan Mamat, PhD
Associate Professor
Faculty of Mechanical Engineering
Universiti Teknologi MARA
(Internal Examiner)

Rizalman Mamat, PhD
Professor
Faculty of Mechanical and Automotive
Engineering Technology
Universiti Malaysia Pahang
(External Examiner)

PROF DR HJH ZURAEDA IBRAHIM
Dean
Institute of Postgraduate Studies
Universiti Teknologi MARA

Date: 24 August 2026

AUTHOR'S DECLARATION

I declare that the work in this thesis was carried out in accordance with the regulations of Universiti Teknologi MARA. It is original and is the results of my own work, unless otherwise indicated or acknowledged as referenced work. This thesis has not been submitted to any other academic institution or non-academic institution for any degree or qualification.

I, hereby, acknowledge that I have been supplied with the Academic Rules and Regulations for Postgraduate, Universiti Teknologi MARA, regulating the conduct of my study and research.

Name of Student	:	Muhammad Hadrami bin Hamdan
Student ID. No.	:	2021354077
Programme	:	Doctor of Philosophy (Mechanical Engineering) – EM950
Faculty	:	Mechanical Engineering
Thesis Title	:	An Integrated Heat Recovery System For Enhanced Thermoelectrical Performance Of A Polymer Electrolyte Membrane Fuel Cell
Signature of Student	:	……..
Date	:	August 2026

ABSTRACT

Operational efficiency in polymer electrolyte membrane fuel cells remains fundamentally constrained by the inherent loss of chemical energy as low grade waste heat. Evaluating mathematical model of a waste heat recovery architectures for vehicular application requires advancing beyond idealised steady state environments to capture transient on road physical uncertainties. Consequently, this research developed and evaluated a passive integrated heat recovery architecture for simultaneous hydrogen preheating and solid state thermoelectric generation. The sequential methodology progressed through three dimensional computational fluid dynamics, controlled steady state laboratory testing, and dynamic on road evaluations utilising a lightweight fuel cell buggy. Initial numerical models predicted the internal temperature distributions with approximately 90% accuracy. During laboratory validations, hydrogen preheating mitigated the operational voltage drop, which yielded a primary electrical power increment of up to 11.1% and improved absolute efficiency by 4.6 percentage points. Concurrently, the integrated solid state modules generated 192.5 mW of auxiliary power. Subsequent dynamic on road driving cycles confirmed these passive gains, as the architecture reduced absolute hydrogen consumption from 5.2 g/km to 4.4 g/km and improved dynamic electrical efficiency by 5.3%. Despite these electrochemical improvements, experimental temperature measurements revealed that absolute waste heat utilisation remained strictly bounded below 3%. This low utilisation originated from a severe 50% upstream temperature degradation caused by continuous ambient thermal dissipation and chaotic environmental exposure. These findings confirm that dynamic on road physical testing remains an indispensable methodology to accurately quantify the true thermodynamic limits and experimental errors of vehicular thermal networks.

ACKNOWLEDGEMENT

First and foremost, Alhamdu lillahi Rabbil 'alamin. All praise is due to Allah, the Most Gracious and the Most Merciful. A Special dedication to my religious, spiritual and life Guru, Saiyidi Syeikh Mursyid Azizul Wahyu An-Naqsyabandi. I also dedicate this milestone to my father Ir. Dr. Hj. Hamdan Bin Hj. Ya and to the loving memory of my very dear late mother who initiated the spark for this PhD journey and whose belief in me has been a constant source of strength. Also to my beloved wife Syafiza Binti Sabre, also all my in laws and my dear friend Muhammad Hasif Aiman Bin Mohd Sarwar Kamal Helal. The greatest gratitude to all the mention above as my life line.

I would like to express my deepest gratitude to Professor Dr. Wan Ahmad Najmi bin Wan Mohamed, my main supervisor, for his invaluable guidance, continuous support, and insightful feedback. His expertise and encouragement have been foundational in exploring this research. Much appreciation also goes to my co-supervisors, Assoc. Prof. Ir. Dr. Irnie Azlin @ Nur Aqilah Zakaria, Assoc. Prof. Dr. Mohd Faizal bin Mohamad, and Assoc. Prof. Ir. Dr. Masli Irwan Rosli, for their endless support and guidance.

I extend my sincere appreciation to the Faculty of Mechanical Engineering at Universiti Teknologi MARA for providing the necessary resources, facilities, and a conducive research environment. Special thanks to the laboratory staff and technical assistants (Mr. Mohd Ezzuan bin Salleh, Mr. Mohd Fadhli bin Mohamed Basir, Mohd Helmi bin Omar, Ahmad Faiz Bin Nawawi, Mohamad Tolha bin Subhi, Fazly Zaimie bin Yaacob, Tc. Mohd Alif bin Jalaluddin, Ir. Ts. Mohamad Firhan bin Morni, Mr. Mohd Arzuan bin Kassim and Mohd Farid bin Mohd Saad) for their assistance in conducting the experimental work, troubleshooting technical challenges, and helping me navigate the inevitable errors and complexities present in experimental research.

My heartfelt thanks also go to my colleagues and fellow researchers for their collaboration, thought-provoking discussions, and unwavering support. I also deeply cherish the valuable experiences and knowledge shared during conferences and exhibitions with researchers across the globe.

I am profoundly grateful to my extended family and friends for their patience, motivation, and unconditional support. Your positive words and encouragement have provided the boost needed to face my challenges.

This work would not have been possible without the contributions and encouragement of all those mentioned above, and I sincerely appreciate their roles in the completion of this thesis.

TABLE OF CONTENTS

Page

CONFIRMATION BY PANEL OF EXAMINERS **ii**
AUTHOR'S DECLARATION **iii**
ABSTRACT **iv**
ACKNOWLEDGEMENT **v**
TABLE OF CONTENTS **vi**
LIST OF TABLES **x**
LIST OF FIGURES **xii**
LIST OF SYMBOLS **xx**
LIST OF ABBREVIATIONS **xxi**
LIST OF NOMENCLATURES **xxiii**

CHAPTER 1 INTRODUCTION **1**

1.1 Research Background 1
1.1.1 Thermal Management of PEM fuel cells 2
1.1.2 Waste heat recovery 3
1.1.3 Fuel cell vehicles (FCV) 9
1.2 Motivation for This Work 11
1.3 Problem Statement 13
1.4 Research Objectives 15
1.5 Research Question 15
1.6 Significance of Study 16
1.7 Limitation Scopes of Study 18
1.7.1 Scope for Objective 1: Mathematical and Numerical Design Investigation 18
1.7.2 Scope for Objective 2: Experimental Test Bench Validation 19
1.7.3 Scope for Objective 3: Dynamic On Road Evaluation 19
1.8 Limitations of Study 20
1.8.1 Limitations for Objective 1: mathematical and Numerical Methodologies 20
1.8.2 Limitations for Objective 2: Experimental Test Bench Validation 22
1.8.3 Limitations for Objective 3: Dynamic On Road Evaluation 23
1.9 Thesis Overview 24

CHAPTER 2 LITERATURE REVIEW 27

2.1 Introduction 27
2.2 PEM Fuel Cell Thermodynamics and Performance Limitations 28
2.2.1 Operating Principles and Energy Partitioning 28
2.2.2 Polarization Losses 29
2.2.3 Temperature Dependency of Cell Performance 31
2.3 Conventional Thermal Management Architectures and Operational Bottlenecks 32
2.3.1 Current Cooling Strategies: Overview of Passive and Active Architectures 32
2.3.2 Limitations of Conventional Thermal Management: Parasitic Power and the Boundaries of Heat Rejection 33
2.4 Waste Heat Recovery Strategies in Fuel Cell Systems 34
2.4.1 Overview of Heat Recovery Architectures: Organic Rankine Cycles, Cogeneration, and Solid-State Conversion 38
2.4.2 Challenges in Low Grade Heat Recovery: Thermodynamic Bottlenecks and Spatial Constraints 39
2.4.3 Heat Exchangers and Heat Pipes for Thermal Management 40
2.4.4 Reactant Thermal Conditioning and Hydrogen Preheating 44
2.4.5 Thermoelectric Generators for Solid State Energy Recovery 48
2.5 Computational Fluid Dynamics in Thermal System Design and Multi Physics Coupling 50
2.5.1 Mathematical Modelling of Heat Exchangers: Numerical Approaches for Compact Geometries 51
2.5.2 Validating Fuel Cell Thermal Models: CFD Capabilities and Inherent Numerical Uncertainties 52
2.6 Experimental and Dynamic Testing Protocols for Fuel Cells 53
2.6.1 Controlled Laboratory Bench Testing: Polarization Curve Extraction and Steady State Thermal Mapping 54
2.6.2 Dynamic Drive Cycles and Real World Environmental Effects: Transient Loads and Convective Variables 55
2.7 Summary and Research Gaps: Toward Integrated Dynamic Validation 56

CHAPTER 3 RESEARCH METHODOLOGY 59

3.1 Introduction 59

3.1.1 Methodological Novelty and Empirical Contributions 63
3.2 Mathematical Modelling and Numerical Methodology (Achieving TRL 2) 64
3.2.1 Design Criteria and Architectural Baseline 64
3.2.2 Geometric Specifications of the Evaluated Architectures 67
3.2.3 Mathematical Thermodynamic Modelling 69
3.2.4 Computational Fluid Dynamics Setup and Discretization 79
3.2.5 Mathematical Verification of Numerical Models 96
3.3 Experimental Test Bench Validation (Achieving TRL 4) 97
3.3.1 Physical Fabrication of the Integrated Architecture 98
3.3.2 Instrumentation and Data Acquisition Setup 102
3.3.3 System Pretesting and Calibration Protocols 107
3.3.4 Experimental Procedure and Testing Matrix 109
3.3.5 Experimental Repetition 111
3.3.6 Mathematical Formulation of Performance Metrics 111
3.3.7 Experimental Uncertainty and Error Propagation 116
3.3.8 Numerical Calibration Feedback Loop 120
3.4 On Road Dynamic Testing 122
3.4.1 Lightweight Vehicle Specifications and System Integration 122
3.4.2 Mobile Instrumentation and Data Acquisition 124
3.4.3 Environmental Boundary Conditions and Test Location 128
3.4.4 Constant Speed Evaluation Protocols 129
3.4.5 Scaled Dynamic Driving Cycle Protocols 132
3.4.6 Dynamic Data Processing and Transient Uncertainty 135

CHAPTER 4 RESULTS AND DISCUSSION 142

4.1 Introduction 142
4.2 IHR Design Evaluation for PEMFC Operation (results based on objective 1) 142
4.2.1 Full Domain Three Dimensional Computational Fluid Dynamics Visualisation 143
4.2.2 Verification of Hydrogen Preheated Temperature and TEG Temperatures Model 148
4.2.3 Hydrogen Preheating Performance 156
4.2.4 Fuel Cell Predicted Performance 161
4.2.5 TEG Thermal Behaviour and Electrical Power 163
4.2.6 Waste Heat Utilization (WHU) 166
4.2.7 Summary 168

4.3 Experimental Test Bench Results 169
4.3.1 Fuel Cell Electrical Performance 169
4.3.2 FC and IHR System Thermal Performance 174
4.3.3 Hydrogen Flow Rate Profile 181
4.3.4 Hydrogen Preheating Performance 183
4.3.5 TEG Thermal and Electrical Performance 185
4.3.6 Fuel Cell Efficiency 188
4.3.7 Waste Heat Utilization 190
4.3.8 CFD Validation against Test Bench Results 192
4.3.9 Summary of Experimental Test Bench Validation 195
4.4 On-Road Test Introduction 196
4.4.1 Constant Speed On-Road Test 196
4.4.2 Dynamic On-Road Testing 244

CHAPTER 5 CONCLUSION 276

5.1 Objective 1: Mathematical and Numerical Design Investigation 276
5.2 Objective 2: Experimental Test Bench Validation 276
5.3 Objective 3: Dynamic On Road Evaluation 277
5.4 Recommendations 278
REFERENCES 281
APPENDICES 297
AUTHOR'S PROFILE 312

LIST OF TABLES

Tables	Title	Page
Table 2.1	Comprehensive Comparison of Waste Heat Recovery Strategies and System Configurations in Fuel Cell Application	36
Table 2.2	Comparative Analysis of Thermal Management and WHR Architectures	39
Table 3.1	Specifications of the Selected PEM Fuel Cell	65
Table 3.2	Integrated Heat Recovery System Design Criteria	66
Table 3.3	Summary of Macroscopic Geometric Specifications for the Four Evaluated Architectures	68
Table 3.4	Input Parameters for the Integrated Heat Recovery System Based on PEMFC Operational Conditions	70
Table 3.5	Material Properties Assigned for the Computational Fluid Dynamics Domains	87
Table 3.6	Parameters for Computational Fluid Dynamics Setup	89
Table 3.7	Spatial Mapping of Temperature Sensor Distribution Across the Integrated Architecture	104
Table 3.8	Technical Specifications of Experimental Instruments and Sensors	106
Table 3.9	Specifications of the Experiment Parameters	110
Table 3.10	First Layer Independent Measured Parameters and Hardware Uncertainty	118
Table 3.11	Second Layer Propagated Uncertainty for Calculated Performance Metrics	119

Table 3.12	Specifications and Baseline Instrumented Mass of the Mobile Test Platform	124
Table 3.13	Spatial Mapping of Temperature Sensor Distribution Across the Mobile Architecture	127
Table 3.14	Experimental Test Matrix for the 1 Km Constant Speed Evaluations	131
Table 3.15	Scaled NEDC Dynamic Driving Profile Mapped to Buggy Physical Limits	133
Table 4.1	Full Model Temperature and Pressure Profile	147
Table 4.2	Predicted Temperature Profiles for the IHR System Domain from CFD	194
Table 4.3	Overall Statistics for the Fuel Cell Electrical Power (a) 3P (b) 2P (c) 1P	203
Table 4.4	Statistical Verification Metrics Between Mean Fuel Cell and Motor Power Values Compared to Dynamic Profiles	248

LIST OF FIGURES

Figures	Title	Page
Figure 1.1	Thesis Overview Flowchart	26
Figure 2.1	(a) Experimental Setup of an MH Canister Studying Hydrogen Discharge Rate Behavior With Heat Addition Mimicking the Heat Supplied by A Fuel Cell. (b) Schematic Diagram of the Experimental Setup Used to Study the Hydrogen Discharge Rate of the MH Canister Utilising Thermal Management [114]	46
Figure 3.1	Master Methodology (a) Fish Bone Diagram (b) Flowchart	62
Figure 3.2	Schematic Diagram of the IHR System Concept	65
Figure 3.3	Mathematical Modelling Flowchart	71
Figure 3.4	Example of Universal Thermal Resistance Network for IHR Architecture	74
Figure 3.5	Simplified Linear Thermal Resistance Circuit	75
Figure 3.6	PEM fuel cell power output increment per degree of fuel preheating (extracted from literature [17])	78
Figure 3.7	Workflow for Phase 2 Computational Numerical Modelling	83
Figure 3.8	IHR Design 1 Assembly and Systems Component	84
Figure 3.9	IHR Design 2 Assembly And Systems Component	84
Figure 3.10	IHR Design 3 Assembly and Systems Component	85
Figure 3.11	IHR Design 4 Assembly and Systems Component	85
Figure 3.12	Overall Mesh Quality for the 4 Evaluated Architectures	91
Figure 3.13	Grid Independence Test Computational Time	92

Figure 3.14	Grid Independence Test Evaluating (a) Hydrogen Pressure Drop (b) TEG Temperature Difference	93
Figure 3.15	Convergence Residuals Versus Iteration Sequence	95
Figure 3.16	Thermodynamic Stability Profile of the Cold Chamber Pressure Drop Versus Iteration Sequence	96
Figure 3.17	Sequential Physical Fabrication And Assembly Process Flowchart	99
Figure 3.18	Fabrication Process For IHR Heating Heat Exchanger (Tube-Heatsink)	100
Figure 3.19	IHR Cooling Heat Exchanger And IHR Preassembly Without the Channelling Hot and Cold Air Chambers	101
Figure 3.20	Fully Integrated And Insulated Physical Prototype With External Fluid Chambers	102
Figure 3.21	a) Schematic and b) Photographic Representation of the Fully Assembled Laboratory Test Bench and IHR Architecture	103
Figure 3.22	Three-Dimensional Spatial Mapping of Thermocouple Locations	104
Figure 3.23	Photographic Representation of The Fully Assembled Fuel Cell Buggy, Detailing The Physical Integration of The Primary Stack, IHR System, Protective Casing, and Instrumentation	123
Figure 3.24	Electrical Schematic Diagram of the Mobile Fuel Cell Buggy Illustrating the Isolated 12V Instrumentation Circuit and the Primary Motor Powertrain	125
Figure 3.25	Three Dimensional Spatial Mapping of the Ten Thermocouple Locations for the Mobile Architecture	127
Figure 3.26	Aerial Geographical Mapping of the Tun Abdullah Mohd Salleh Hall Parking Lot Driving Circuit at UKM	128

Figure 3.27 Experimental Test Matrix for the 1 Km Constant Speed Evaluations 131

Figure 3.28 Scaled NEDC Dynamic Driving Profile 134

Figure 4.1 Preheated Hydrogen Temperature Predictions From (a) Mathematical Model (b) CFD Model 150

Figure 4.2 TEG Hot Side Surface Temperatures for (a) Mathematical Model (b) Numerical Model 152

Figure 4.3 TEG Cold Side Surface Temperatures for (a) Mathematical Model (b) Numerical Model 153

Figure 4.4 Comparison of Results Between CFD and Mathematical Modelling: Preheated Hydrogen Temperature 155

Figure 4.5 Comparison of Results Between CFD and Mathematical Modelling: TEG Hot Side Temperature 155

Figure 4.6 Comparison of Results Between CFD and Mathematical Modelling: TEG Cold Side Temperature 156

Figure 4.7 Numerical Analysis of Hydrogen Temperature Distribution During Preheating for the IHR Designs at 1500 W Fuel Cell Power 158

Figure 4.8 Hydrogen Temperature Rise (ΔT) Across the Preheater for Four IHR Designs At 500–2000 W Fuel Cell Power 159

Figure 4.9 Hydrogen Heat Transfer Rate in the Preheating Section for Four IHR Designs at 500 to 2000 W Fuel Cell Power 160

Figure 4.10 Predictions From Mathematical Electrochemical Model Based on Simulated Relative Hydrogen Preheated Temperatures (a) Fuel Cell Power Enhancement, (b) Enhancement Percentage From Base Output Without IHR. 162

Figure 4.11 Simulated Temperature Contour of the TEG Hot and Cold Sides Under Variations of Fuel Cell Power 165

Figure 4.12 Simulated TEG Temperature Difference for the IHR Designs as a Function of Fuel Cell Power 166

Figure 4.13 Estimated TEG Electrical Power Output Based on CFD-Predicted Temperature Differences at 500 to 2000 W Fuel Cell Power 166

Figure 4.14 Waste Heat Utilisation of The IHR Designs as A Function of Fuel Cell Power at 500 to 2000 W 168

Figure 4.15 Fuel Cell Polarization Profiles of the Baseline System Compared With The Installation of IHR Under Simulated Vehicle Speeds 171

Figure 4.16 Fuel Cell Power Increment Compared to Baseline Case in (a) Unit Watts, and (b) Percentage Increment 173

Figure 4.17 Effect of Fuel Cell Stack Current Load Variations to its Temperature Profiles 175

Figure 4.18 Generated Thermal Power Profiles of the Fuel Cell Stack 176

Figure 4.19 Spatial Temperature Distribution Across the IHR System Under Variations of Simulated Vehicle Speeds (a) 0 m/s (b) 5 m/s and (c) 10 m/s 180

Figure 4.20 Measured Hydrogen Flow Rates Under Variations in Stack Current 182

Figure 4.21 Hydrogen Temperature Profiles (a) at the Inlet and Exit of the IHR, and (b) Resulting Temperature Differences 184

Figure 4.22 Heat Absorbed By Hydrogen Flow During Preheating at the IHR 185

Figure 4.23 TEG Temperature Difference Trend Relative To Fuel Cell Stack Current Variation 186

Figure 4.24 Heat Transfer Rate Across the TEG 187

Figure 4.25 Electrical Power Generated by the TEG 188

Figure 4.26	Fuel Cell Conversion Efficiency Profiles Across Load Current Polarization	189
Figure 4.27	Absolute Difference of Fuel Cell Efficiency Under Stack Current Variation	189
Figure 4.28	Absolute Difference of Fuel Cell Efficiency Across Hydrogen Temperature Difference Variations	190
Figure 4.29	Waste heat utilization for the IHR cases	191
Figure 4.30	Temperature Distribution Profiles for the Hydrogen Stream And TEG Surface Temperatures Based on Experimental Boundary Conditions At 60 A	194
Figure 4.31	Validation of CFD Results Against Test Bench Experiment Results	195
Figure 4.32	Fuel Cell Electrical Power Profile for 3P Cases (a) Day (b) Night	198
Figure 4.33	Electrical Motor Power Profile for 3P cases (a) Day (b) Night	199
Figure 4.34	Electrical Motor Demand Energy For All Cases	201
Figure 4.35	Electrical Motor Demand Difference (Between IHR Against Baseline) For All Cases	201
Figure 4.36	Fuel cell electrical mean power for all cases	202
Figure 4.37	Fuel Cell Electrical Relative Power For All Cases	203
Figure 4.38	Fuel Cell Electrical Power Against Current With the Normalize Trendline for Day Time Cases (a) 3P (b) 2P (c) 1P	207
Figure 4.39	Fuel Cell Electrical Power Against Current With the Normalize Trendline for Night Time Cases (a) 3P (b) 2P (c) 1P	209
Figure 4.40	Fuel Cell Electrical Power Increments as Compared to Baseline Respective to the Load Conditions (a) 3P (b) 2P (c) 1P	211

Figure 4.41	Fuel Cell Thermal Power Produced for Cases of 3P During the Day Time (a) Raw Data (b) Average	213
Figure 4.42	Total Fuel Cell Thermal Energy Produced for All Cases	214
Figure 4.43	Baseline (FC Without IHR) Dimensionless Temperature Profile (a) Day (b) Night Conditions	215
Figure 4.44	Fuel Cell with IHR Dimensionless Temperature Profile (a) Day (b) Night Time Conditions	217
Figure 4.45	Hydrogen Preheated Temperature from IHR system for Cases (a) 3P (b) 2P (c) 1P	221
Figure 4.46	**3s** Cases for Hydrogen (a) Final Temperature Difference (b) Calculated Energy Absorb Energy	223
Figure 4.47	**2s** Cases for Hydrogen (a) Final Temperature Difference (b) Calculated Energy Absorb Energy	225
Figure 4.48	**1s** Cases for Hydrogen (a) Final Temperature Difference (b) Calculated Energy Absorb Energy	227
Figure 4.49	Hydrogen Flow Rate Through the Cases	230
Figure 4.50	Hydrogen Tank Pressure Dropped Through the Cases	230
Figure 4.51	Hydrogen Consumption Measured in Grams for All Cases	232
Figure 4.52	Fuel Cell Efficiency for (a) Day (b) Night for All Cases	233
Figure 4.53	Instantaneous TEG Temperature Difference Throughout The Whole Testing for Cases (a) 3P (b) 2P (c) 1P	237
Figure 4.54	The Final TEG Surface Temperatures and Temperature Difference for All Conditions	237
Figure 4.55	The Total TEG Heat Transfer for All Conditions	238
Figure 4.56	Maximum TEG Electrical Power Produced Through Out the Testing for All Conditions	239

Figure 4.57	Total TEG Electrical Production for All Conditions	240
Figure 4.58	Total WHU for All Conditions	242
Figure 4.59	Power Profiles for the Fuel Cell Stack and the Traction Motor Corresponding to Scaled-Down NEDC – Daytime Operation Without IHR	246
Figure 4.60	Power Profiles for the Fuel Cell Stack and the Traction Motor Corresponding to Scaled-Down NEDC – Daytime Operation Using IHR	246
Figure 4.61	Power Profiles for the Fuel Cell Stack and the Traction Motor Corresponding to Scaled-Down NEDC – Nighttime Operation Without IHR	247
Figure 4.62	Power Profiles for the Fuel Cell Stack and the Traction Motor Corresponding to Scaled-Down NEDC – Nighttime Operation Using IHR	247
Figure 4.63	Total Fuel Cell Power Generation and Motor Power Consumption Across All Driving Conditions	248
Figure 4.64	Average Fuel Cell Electrical Power for a) Day Driving Condition, b) Night Driving Condition	251
Figure 4.65	Fuel Cell Electrical Power Mapping Against Load Current for a) Day Driving Condition, b) Night Driving Condition	253
Figure 4.66	The Polarization Curves of the Fuel Cell Stack With and Without IHR During Daytime Operation	254
Figure 4.67	The Polarization Curves of the Fuel Cell Stack With and Without IHR During Nighttime Operation	254
Figure 4.68	Electrical Power Improvement Percentage From the Application of IHR	255
Figure 4.69	Fuel Cell and IHR System Dimensionless Temperature Profile for All Cases	257

Figure 4.70	Fuel Cell Thermal Power for Night Cases	258
Figure 4.71	Fuel Cell Thermal Power for Day Cases	259
Figure 4.72	Total Thermal Energy Generated by the Fuel Cell for All Cases	260
Figure 4.73	Hydrogen Temperature Profiles at the IHR Inlet and Outlet Across All Cases	261
Figure 4.74	Hydrogen Temperature Difference For All Cases	262
Figure 4.75	Hydrogen Preheating Power Responses Corresponding to Dynamic Drive Cycles	263
Figure 4.76	Total Thermal Energy Absorbed by the Hydrogen During Preheating	264
Figure 4.77	Transient Hydrogen Fuel Flow Rate for Daytime	265
Figure 4.78	Transient Hydrogen Fuel Flow Rate for Nighttime	265
Figure 4.79	Hydrogen Tank Pressure Dropped Under Different Test Configurations	266
Figure 4.80	Fuel Cell Fuel Consumption, (a) Total Hydrogen Consumption, and (b) Fuel Economy Per km Distance	267
Figure 4.81	Transient TEG Surface Temperature and Difference	268
Figure 4.82	Transient TEG Heat Transfer	269
Figure 4.83	Transient TEG Electrical Power	269
Figure 4.84	Total TEG Heat Transferred	270
Figure 4.85	Total TEG Power Produced	271
Figure 4.86	Fuel Cell Efficiency for All Cases	272
Figure 4.87	Fuel Cell With IHR Waste Heat Utilization	273

LIST OF SYMBOLS

Symbols

Bi_2Te_3	Bismuth Telluride
C	Condenser Section
C1	Configuration 1
C2	Configuration 2
C3	Configuration 3
C4	Configuration 4
CB,C	Cold Section Copper Block
CB,H	Hot Section Copper Block
e	Electron
E	Evaporator Section
HE,C	Cold Section Heat Exchanger
HE,H	Hot Section Heat Exchanger
HP,C	Cold Section Heat Pipe
HP,H	Hot Section Heat Pipe
IF	Interface
N_{FIN}	Number of Fins
s-CO_2	Supercritical CO_2 Brayton Cycle
S_n	Swirling Number
TEG,C	Cold Section Thermoelectric Generator
TEG,H	Hot Section Thermoelectric Generator

LIST OF ABBREVIATIONS

Abbreviations

CFD	Computational Fluid Dynamics
CHP	Combined Heat and Power
CPV	Concentrator Photovoltaic
CS	Cooling Supply
CTEG	Cable Thermoelectric Generator
DL	Double Layered
FC	Forced Cooling
FCV	Fuel Cell Vehicle
GHC	Gas Hydrate Heat Cycle
HE	Heat Exchanger
HRSG	Heat Recovery Steam Generators
HVAC	Heating, Ventilation and Air Conditioning
IHR	Integrated Heat Recovery
MCHP	Micro-Channel Heat Pipe
MPP	Maximum Power Output
NC	Natural Cooling
ORC	Organic Rankine Cycle
PEM	Polymer Electrolyte Membrane
SDG	Sustainable Development Goals

SL	Single Layered
STEG	Solar Thermoelectric Generator
TE	Thermoelectric
TEG	Thermoelectric Generator
TEM	Thermoelectric Generator Module
TLC	Trilateral Cycle
WH	Waste Heat
WHR	Waste Heat Recovery

LIST OF NOMENCLATURES

Nomenclatures

A	Surface Area (m^2)
A_E	Heat Pipe Heat Transfer Area (m^2)
A_{FF}	Free Flow Area (m^2)
A_{FIN}	Area of Fins (m^2)
A_{GAP}	Area Between Fins of Heat Exchanger (m^2)
A_T	Total Surface Area (m^2)
C_{MIN}	Minimum Heat Capacity Rate of Fluid (J/K)
D_H	Hydraulic Diameter (m)
D_{HP}	Outer Diameter of Heat Pipe (m)
d_{HP}	Inner Diameter of Heat Pipe (m)
D_{WICK}	Diameter of Wick (m)
h	Heat Transfer Coefficient ($W.m^2K$)
H	Operating Hour (hr)
I	Current (A)
I_{SC}	Short Circuit Current (A)
k	Thermal Conductivity (W/m.K)
k_{EFF}	Effective Thermal Conductivity of Heat Pipe Wick Structure (W/m.K)
k_{FIN}	Thermal Conductivity of Fin (W/m.K)
k_{WALL}	Thermal Conductivity of Heat Pipe Wall (W/m.K)

k_{WATER}	Thermal Conductivity of Water (W/m.K)
k_{WICK}	Thermal Conductivity of Wick Structure (W/m.K)
$L_{HP,C}$	Heat Pipe Condenser Length (m)
$L_{HP,E}$	Heat Pipe Evaporator Length (m)
$\dot{m}_{AIR}$	Mass Flow Rate of Air (kg/s)
N_{HP}	Number of Heat Pipe
Nu	Nusselt Number
N_{WICK}	Number of Wick
P	Electrical power (W)
Pr	Prandtl Number
Q_{ACTUAl}	Actual Heat Transfer (W)
Q_{MAX}	Maximum Heat Transfer (W)
Q_{TEG}	Thermoelectric Generator Heat Transfer (W)
R	Thermal Resistance (Ω)
Re	Reynolds Number
R_{INT}	Internal Resistance (Ω)
R_L	External Load Resistance (Ω)
S_{RTE}	Regenerated Thermal Energy Saving (RM/year)
S_T	Transvers Pitch (m)
S_{TEG}	Thermoelectric Generator Power Saving (RM/year)
S_{TOTAL}	Total Annual Saving (RM/year)
t	Thickness (m)
T_{AMB}	Ambient Temperature (^oC)

T_E	Electricity Tariff (RM/kWh)
t_{FIN}	Thickness of Fin (m)
T_G	Natural Gas Price (RM/MMBtu)
V	Voltage (V)
V_A	Average Velocity of Fluid (m/s)
V_F	Volumetric Flow Rate of Fluid (m^3/s)
v_{MAX}	Maximum Velocity of Fluid (m/s)
V_{OC}	Open Circuit Voltage (V)
v_{SHP}	Heat Pipe Vapour Spacing (m)
ZT	Figure of Merit
ε_{HE}	Heat Exchanger Efficiency (%)
ε_P	Wick Porosity
μ_{AIR}	Dynamic Viscosity of Air ($N.s/m^2$)
μ_{FIN}	Fin Efficiency (%)
μ_o	Overall Surface Efficiency (%)
μ_{TEG}	Thermoelectric Generator Efficiency (%)
ρ_{AIR}	Air Density (kg/m^3)

CHAPTER 1
INTRODUCTION

1.1 Research Background

The transition toward net-zero energy systems is accelerating worldwide, driven by mounting concerns over climate stability, long-term energy security, and the escalating cost of carbon-intensive development. Global decarbonisation pathways increasingly highlight hydrogen as an enabling vector for energy system flexibility as well as security. The International Energy Agency (IEA) assessments identify clean hydrogen as a critical component in achieving deep emissions reductions across transport, industry and power balancing. The global hydrogen economy is characterized by a projected shift from industrial feedstock use toward energy-centric applications, supported by maturing technologies and rapid cost improvements in emerging hydrogen value chains [1].

Malaysia recognises hydrogen as a potential future energy vector within a broader national transition plan. The National Energy Policy (NEP) 2022–2040 [2, Ch. 2] and the National Energy Transition Roadmap (NETR) [3], open the pathway for an exploratory stage of the hydrogen economy in Malaysia. National roadmaps such as the 2023 Hydrogen Economy and Technology Roadmap (HETR) outline strategic aspirations with practical considerations relating to infrastructure readiness, system integration, safety standards, and ESG compliance [4]. To achieve the goals of HETR, innovative research in the diverse areas of hydrogen economy is necessary, particularly focusing on novel technologies that attempt to optimise hydrogen yield from specific applications.

The global hydrogen movement toward sustainable energy systems necessitates efficient and clean power conversion technologies. The PEM fuel cell functions as one of the core technologies in the hydrogen economy plan. This specific electrochemical device converts hydrogen gas and oxygen directly into electrical power, emitting only water and heat. The PEM fuel cell plays an important role in the partial decarbonisation of the transportation sector and helps mitigate the effects of greenhouse gases on the climate. While PEM fuel cells offer high theoretical energy conversion rates, the

practical operational efficiency of these cells remains heavily constrained by internal thermodynamic losses and complex system level energy management challenges [5].

1.1.1 Thermal Management of PEM fuel cells

The theoretical thermodynamic limit for PEM fuel cell efficiency reaches 80%, yet the practical efficiency range remains bounded between 45% and 60% [6]. The system generates thermal energy due to continuous process irreversibilities and exothermic reactions [7]. For low temperature stacks, active cooling mechanisms remove approximately 80% of the generated heat from the physical stack [8]. Active cooling mechanisms achieve this heat removal utilising induced air streams for open cathode architectures, whereas closed cathode systems utilise deionised water. Open cathode PEM fuel cell stacks operate at low temperatures of approximately 60 °C, and the resulting exit air stream temperature typically measures slightly lower than the internal stack temperature [9].

During standard power generation, the PEM fuel cell loses approximately half of the input chemical energy as waste heat. This continuous thermal generation originates from internal irreversibilities categorised into three main domains including activation polarisation, ohmic resistance, and mass transport limitations [10]. Although mathematical models provide general baseline percentages, acknowledging that exact energy loss distributions inevitably fluctuate due to inherent manufacturing flaws and experimental uncertainties during dynamic physical operation remains vital. According to mathematical heuristics, activation polarisation dominates at low current demands, consuming approximately 40% of the potential energy strictly to overcome the physical energy barrier required to initiate the chemical reaction at the catalyst layer [11]. As the electrical demand increases, ohmic resistance within the polymer membrane and the bipolar plates contributes further to the absolute thermal load, accounting for roughly 20% to 30% of the total voltage degradation [12]. At peak operational currents, mass transport limitations restrict reactant flow, causing additional steep voltage drops and corresponding heat surges that represent up to 30% of the total energy loss [12]. Furthermore, minor fuel crossover and internal electron leakage typically contribute a negligible degradation of less than 1% [13]. Managing this continuous and varying heat generation remains critical because the polymer membrane must operate within a strict

and narrow temperature boundary, typically between 60 °C and 80 °C, to maintain optimal hydration and structural integrity [14].

Consequently, fuel cell systems rely on active thermal management system to prevent overheating and subsequent material degradation. Furthermore, the electrical power output of a PEM fuel cell depends heavily on reactant inlet temperatures and humidity levels [15]. Conventional thermal management architectures, utilising liquid coolant loops or forced air convection, treat the generated heat purely as a parasitic byproduct. These conventional systems actively pull thermal energy away from the stack through conductive heat transfer and reject the heat directly into the ambient environment via convective radiators. This conventional approach presents two distinct disadvantages. First, discarding the thermal energy represents a fundamental thermodynamic loss, which reduces the overall energy utilisation of the system. Second, the auxiliary components required for active cooling, such as liquid water pumps and radiator fans, consume a portion of the electrical power generated by the fuel cell. This continuous parasitic power draw inherently reduces the net electrical output and suppresses the overall system efficiency, particularly in lightweight vehicles where spatial constraints and strict weight limitations restrict the use of large cooling assemblies [16].

1.1.2 Waste heat recovery

Advanced thermal management utilises waste heat recovery strategies. Waste heat recovery of PEM fuel cells represents a newly developing area and presents significant challenges because the thermal output typically fluctuates between 50 to 70 °C and falls under the classification of low grade waste heat advanced thermal management applies waste heat recovery strategies. Waste heat recovery of PEM fuel cells is a new developing area and is highly challenging because the thermal output, typically between 50 to 70oC, is classified as low grade waste heat [17]. Research on waste heat recovery from fuel cells gains momentum in recent years. Researchers recycle the generated fuel cell heat by integrating the stack with a thermodynamic system that utilises the waste heat. Heat from PEM fuel cells provides a viable source for low temperature purposes such as space heating and supplying domestic hot water [18]. Implementing these systems enables the energy efficiency of the entire fuel cell network to increase between 50 to 90% [19] . The thermal energy produced by a fuel

cell also initiates sorption cooling cycles for combined cooling and power (CCP) or combined cooling heating and power supply (CCHP) applications [20]. Furthermore the thermal energy drives organic Rankine cycles (ORC) [21], thermoelectric generators (TEG), and thermally regenerative electrochemical cycles for power cogeneration purposes [22].

Most technical articles focus on high temperature Solid Oxide Fuel Cells (SOFC) while reporting limited work on PEM fuel cells which generate much lower thermal outputs. Current research on PEM fuel cells focuses predominantly on heating coupled with cooling for domestic applications rather than industrial purposes [23]. In brief, reported fuel cell hybrid systems focus on the coupling of PEM fuel cells with a heat pump [24], a refrigeration cycle [25], organic Rankine cycle [26] and absorption chiller [27]. These hybrid couplings present a high potential as the integration increases the power density by as much as 20% from a thermally regenerative fuel cell electrochemical cycle [28].

Additional research explores waste heat utilisation from fuel cells for internal fuel cell process needs. A popular research area redirects the waste heat to increase the hydrogen release rate of metal hydride (MH) canisters. The internal temperature of the MH requires strict maintenance between 20 to 30 °C to provide sufficient hydrogen flow. Tetuko et al. [29] evaluate a heat pipe assisted model of a 500 W PEM fuel cell and report that the magnesium hydride canister requires less than 20% of the waste heat produced by the PEM fuel cell to achieve the necessary hydrogen discharge rate. Nasri et al. [30] study a waste recovery concept of a PEM fuel cell vehicle (FCV) system utilising thermal storage in a magnesium hydride canister for cabin heating and cooling during hydrogen desorption. Most importantly the study reports the potential to extend the driving range of the FCV by approximately 17%. Furthermore, Dawahdeh et al. [31] numerically evaluate the thermal integration of a fuel cell with a Lanthanum Nickel metal hydride storage system. The analysis indicates that while the architecture remains thermally self sufficient during moderate driving speeds, prolonged low speed operation restricts waste heat generation and creates a critical thermal deficit. Resolving this transient limitation requires a 200 W auxiliary electric heater to sustain hydrogen desorption, demonstrating that actual dynamic driving conditions impose severe physical constraints on continuous waste heat recovery.

Energy recovery for the FCV utilising low grade waste heat to enhance vehicle performance outputs represents a developing area where the main criteria demand

device compactness and passive mechanics [11]. These strict criteria are necessary to minimise the power to weight impact and to improve the techno economic viability by minimising the maintenance cost of the auxiliary heat recovery components. Two potential passive energy approaches offer a fitting solution which includes hydrogen preheating and thermoelectric generation.

1.1.2.1 Waste Heat Recovery of Fuel Cells: Hydrogen Preheating

Heat recovery from fuel cells primarily focuses on stack heating for cold start applications using uniquely designed heat exchangers and electrical heating elements. Preheating the cold winter air helps increase the activation potential of the reactant mixture and allows the electrochemical reactions to occur and sustain. This preheating process also prevents localised cold spots that typically cause water condensation and subsequent gas channel flooding thereby maintaining a uniform temperature distribution across the cell. For fuel cell cold start applications the operational approach preheats the air supply line using electrical heaters supported by the stack waste heat. A PEM fuel cell frequently suffers freeze thaw cycle operations under sub zero temperatures that lead to ice formation, membrane dehydration, start up problems, and efficiency loss [6]. Simulation findings by Nguyen et al. [32] show that external electrical heaters assisted by heat generated by the PEM fuel cell stack successfully conserve 30% of the PEM fuel cell electrical output for internal heating.

For direct stack power enhancement reactant thermal conditioning represents a recently studied energy recovery method involving the specific preheating of hydrogen gas before the reactant enters the fuel cell stack [33]. Mohamed and Kamil develop a setup on this novel idea in 2016 and obtain 8 to 10% positive power enhancements for a 1 kW open cathode fuel cell under laboratory conditions [17]. Analyses indicate that elevating the reactant temperature prior to the electrochemical reaction modifies the internal thermodynamics by increasing the process enthalpy and lowering the activation energy barriers. This physical mechanism mitigates internal voltage drop under high current loads and yields a higher primary electrical power output for the exact same fuel consumption rate. Additionally, Haghighi et al. [34] demonstrate that increasing stack temperatures by 60 °C boosts efficiency by 0.8% per degree. Furthermore experiment evaluations by Alper Uzun et al. [35] indicate that applying an 11 °C thermal elevation to the reactant yields a corresponding 9% increase in primary electrical power output.

An important performance metric from fuel cell system evaluation relies on the fuel utilisation of fuel cell stacks. Hydrogen acts as the primary fuel and the consumption of hydrogen requires strict maximisation to obtain a more positive techno economic outlook. Improving hydrogen utilisation remains important to achieve technological competitiveness and broader market acceptance. The United States (US) Department of Energy targets the cost of hydrogen production to drop below United States Dollar (USD) 2.30 per kg of hydrogen in order to allow the hydrogen economy to become a viable competitor for the oil and gas economy [36].

The PEM fuel cell architecture relies on open cathode and closed cathode configurations. The open cathode provides a simpler design for 2 kW or less demonstration projects or small scale applications. The primary characteristic of this design involves the function of ambient air as both a reactant and a coolant as the air flows within the stack. The closed cathode stack design uses a separate fluid for cooling purposes typically deionised water and nanofluids [14]. Consequently the mass balance of oxygen for the electrochemical reactions remains undisrupted by the rapid inlet outlet movement required for effective thermal dissipation. This stability results in higher achievable power densities.

Regardless of the selected cooling configuration, the continuous heat generation within the fuel cell stems from several inherent factors, including exothermic water formation, internal ohmic resistance, and overall reaction irreversibility [37] The absolute magnitude of this generated heat correlates directly with the internal polarisation behaviour, which depends heavily on the external current density drawn during active operation. At a typical 50% stack efficiency, the generated waste heat theoretically equals the magnitude of the electrical power produced [33]. In open cathode stacks, the ambient cooling air stream absorbs this thermal energy, and the resulting exhaust temperature normally equilibrates with the internal stack operating temperature due to continuous thermal balance effects.

Under steady state conditions the temperature of each component in the stack theoretically equals the stack temperature. At the Gas Diffusion Layer (GDL) and Catalyst Layer (CL) of the membrane assembly the diffusion and electrochemical reactions remain highly temperature sensitive [37]. Low local temperatures at the GDL and CL lower the reaction equilibrium between the anode and cathode electrodes consequently leading to potential energy losses. If one electrode operates with slower reaction kinetics this imbalance reduces the cell potential to produce electrical current

as indicated by the Nernst reaction [17]. Thus if the hydrogen reactant flows into the stack at a low temperature and the reactant is not adequately heated along the reactant pathway before reaching the GDL and CL the local reaction temperature drops lower than optimal leading to limited power output as well as a higher hydrogen requirement [6].

1.1.2.2 Waste Heat Recovery of Fuel Cells: Thermoelectric Generators (TEG)

A parallel recovery strategy utilises solid state TEG modules. These semiconductor modules employ the Seebeck effect to convert a spatial temperature difference directly into secondary electrical power without utilising moving parts. Integrating TEG modules into the fuel cell exhaust stream provides a reliable method to harvest low grade waste heat. However, the electrical output of the TEG modules depends entirely on maintaining the thermal gradient between the internal hot and cold surfaces. Therefore, successful implementation requires a physical architecture that absorbs heat effectively from the exhaust source while simultaneously providing robust cold side heat rejection.

Research regarding the design of unique TEG system configurations for PEM fuel cell stacks gains continuous interest. An exergoeconomic model for a hybrid PEM fuel cell and TEG system developed by Cai et al. [38] indicates a strong potential in coupling fuel cells with thermoelectric conversion to optimise hydrogen consumption. Sulaiman et al. [39] design a heat pipe assisted TEG system focusing on ultra low waste heat temperatures below 40 °C typically produced by open cathode PEM fuel cell stacks. The researchers state the importance of analysing the relative characteristics of each individual component to achieve better power outputs for low grade waste heat sources. Sun et al. [40] offer similar conclusions when modelling the application of TEG arrays on a large 60 kW fuel cell system.

The challenging aspect of utilising TEG modules for waste heat recovery from low temperature PEM fuel cells involves the low electrical performance per module. This low performance occurs because the fuel cell temperature typically fluctuates between 50 °C and 80 °C depending on the electrical load produced. The typical TEG efficiency in low temperature PEM fuel cell applications remains less than 1%. In contrast, applying TEG modules to high temperature PEM fuel cells operating between 120 °C and 200 °C achieves a significantly higher efficiency approaching 3.5% [41].

Research regarding TEG and fuel cell integration grows to include diverse designs and operating approaches. Ebrahimi and Derakhshan [42] apply a combined heat and power concept utilising a TEG cell system for a PEM fuel cell with an 80 °C waste heat stream, obtaining an overall system efficiency of nearly 55%. Parise and Jones [43] investigate the application of thermoelectric modules for internal cooling as part of an innovative fuel cell thermal management strategy. Behzadi et al. [44] design an integrated TEG module with a biomass fired PEM fuel cell system for the cogeneration of power, heat, and domestic hot water.

Regarding component design for thermoelectric subsystems, Zamri et al. [45], Hasani and Rabani [46] and Gao et al. [41] apply computational parametric analysis and agree that the power output of a TEG module depends heavily on the efficiency of the cooling boundary. Forced convection acting over an efficient heat sink design operates as an essential parameter to optimise TEG power output. These researchers explore various models of compact plate fin heat exchanger designs to accommodate thermoelectric generators for fuel cells and industrial heat recovery. Gao et al. [47] also discover the impact of different electrical connection methods when utilising multiple TEG cells within the heat recovery subsystem. Due to the diverse range of power outputs relative to the heating source and the specific heat exchanger design, the authors suggest that configuring TEG cells as branching modules potentially leads to an optimised power output.

In lightweight vehicle applications, securing adequate cooling presents a highly difficult task. The vehicular system must rely entirely on ambient air as the ultimate heat sink. If the external convective cooling remains insufficient, the cold side of the TEG module absorbs latent heat and the thermal gradient collapses, which consequently halts all secondary electrical generation. Overcoming this thermal bottleneck requires advanced heat exchanger designs utilising extended cooling fins and highly conductive heat pipes to pull thermal energy away from the semiconductor surface [48]. Utilising an open cathode air cooled 1 kW FCV platform as a case study, Sulaiman et al. validate a thermal circuit model for a hybrid TEG and heat pipe architecture [17]. The ultra low waste heat of 40 °C allows only a very low power output from a single TEG cell, generating roughly 250 μW under a 37 °C waste heat boundary and a 7 m/s nominal cooling air velocity. Mapping the power densities indicates an optimal region of operation relative to the stack current density and overall efficiency.

Based on the preceding literatures, waste heat recovery for fuel cells operates as a developing technology demonstrating further potential for expansion due to the need for improved fuel cell techno economics. While previous computational and experimental studies explore hydrogen preheating and TEG electrical generation independently, integrating both mechanisms into a single passive recovery unit presents a complex thermal balancing challenge. When both mechanisms share the identical waste heat source, designing the internal geometry strictly to maximise reactant heating inadvertently elevates the overall component temperature. This thermal elevation subsequently reduces the cold side thermal gradient required by the TEG modules. Investigating and resolving this thermal distribution requires precise geometric sizing to balance internal heat absorption with external heat rejection prior to physical manufacturing.

Furthermore, current literature indicates that most existing research relies heavily on idealised steady state laboratory testing. In highly controlled test bench environments, fuel cells operate at fixed current loads with constant ambient temperatures and steady cooling fan speeds. While steady state testing successfully isolates specific variables, static testing fails to capture the fluctuating thermal dynamics inherent to actual vehicle operation. Real world driving involves continuous transient cycles of acceleration, steady cruising, and sudden deceleration. These dynamic electrical loads cause rapid spikes and drops in waste heat generation. Additionally, moving vehicles experience variable external convection rates dictated by the specific cruising speed, alongside fluctuating ambient temperatures occurring between day and night operations.

1.1.3 Fuel cell vehicles (FCV)

The transportation sector plays a key role in the success of the hydrogen economy, with hydrogen powered FCVs serving as a critical component of this transition. The FCV represents a new generation of automotive powertrain technology developed specifically for the planned hydrogen economy. The vehicle runs on hydrogen fuel, where a fuel cell stack converts the chemical hydrogen energy directly into electrical power for the drivetrain. FCV technology offers a practical pathway toward a sustainable, electrified, and low carbon future in the transportation sector. By

significantly reducing greenhouse gas emissions, FCVs actively support global climate action efforts [49].

The market size for FCVs projects to gain at an annual compound growth rate of 66.9% [50]. However, achieving widespread adoption remains a major challenge due to strict infrastructure limitations, varying hydrogen production efficiency, and broad economic feasibility concerns. To accelerate market adoption, stakeholders including policymakers, industry leaders, and technology innovators must collaborate to develop a robust hydrogen ecosystem [51].

Commercialisation of the FCV and increasing the corresponding market share within the transportation industry remains desirable due to three primary reasons:

i) The FCV provides a green transport solution emitting zero atmospheric pollution and discharging only water from the vehicle exhaust.
ii) Operators refuel the FCV at stations similar to traditional petrol cars, and the subsequent travelling range remains highly comparable.
iii) The advantages of high fuel cell conversion efficiency coupled with a motor drive possessing dynamic and rapid load response ensure the FCV powertrain operates as a high performance system.

Popular FCV platforms developed by major manufacturers include the 128 kW Toyota Mirai [52] boasting a current fuel cell power density of 5.4 kW per litre, and the Honda Clarity featuring a power density of 3.1 kW per litre. Approximately 5000 FCVs currently operate on the road primarily in California, Germany, and Japan, spearheading the charge on hydrogen transportation logistic studies [53]. In Los Angeles, infrastructure includes approximately 30 hydrogen refuelling stations, while Germany supports 64 hydrogen refuelling stations. However, the most significant infrastructure expansion occurs in Japan, where strategic roadmaps plan to deploy 800,000 FCVs across the nation by 2030, requiring a substantial amount of hydrogen refuelling stations to serve the FCV logistics [54].

FCV commercialisation for public use generally remains limited by compounding issues of durability and cost [55]. Durability coupled with high manufacturing cost currently represent the two most significant obstacles requiring resolution. In modern fuel cells, operational durability declines as engineers reduce platinum loading in new designs. For example, empirical testing shows the performance of the Toyota Mirai declines after reaching 5000 operating hours [56]. The United States

Department of Energy establishes 8000 operating hours as the current target for FCVs, which serves as one of the great technical challenges facing the industry. Regarding manufacturing cost, market analyses demonstrate a significant FCV price decrease of 60% over the past ten years. In 2020, the United States Department of Energy goals for fuel cells in lightweight vehicles target USD 40 per kW and USD 30 per kW, alongside a lumped USD 600,000 target for a hydrogen powered bus [57]. In the United States, 30 fuel cell buses remain in continuous operation, providing transport for more than 17 million passengers as of 2017 [58].

Since the conceptualisation of the hydrogen economy as a core agenda to mitigate global climate change, the FCV progresses into a mature and safe technology. To improve the overall acceptance rate of the public, engineers must introduce new technologies to achieve higher vehicle performance alongside better ownership costs. Technologies that directly conserve hydrogen fuel while simultaneously enhancing the fuel cell power density provide exactly the type of innovation that assists the FCV toward a higher level of market acceptance. To achieve this future market acceptance, a major engineering criterion focuses directly on the FCV performance. Utilising hydrogen energy efficiently in FCV systems is absolutely necessary due to the high financial cost of hydrogen production. Engineering literature acknowledges that a vehicle possessing high fuel utilisation, translating into more generated useful power per litre alongside extra driving mileage, inherently commands greater market value [59]. Thus, integrating waste heat recovery mechanisms into the FCV powertrain architecture provides an important technological pathway toward contributing to broader commercial market acceptance.

1.2 Motivation for This Work

PEM fuel cells lose a significant amount of energy as heat. To prevent the fuel cell from overheating, vehicles utilise active cooling systems such as water pumps and fans. However, these cooling components consume electrical power directly from the vehicle. This creates a dual energy loss where the system wastes electrical power simply to cool down wasted. The primary motivation of this project is to address this specific inefficiency. By capturing the exhaust heat passively, without requiring any additional moving parts or electrical power, this research aims to repurpose that thermal energy to directly improve the overall performance of the vehicle. Existing literature consistently

indicates that recovering waste heat from a primary energy system yields measurable improvements in systemic energy conservation and secondary power generation [60], [61], [62], [63], [64], [65].

Isolated investigations into waste heat recovery indicate that reactant preheating and solid state thermoelectric generation provide measurable performance gains when evaluated independently. Furthermore, contemporary empirical evaluations suggest that reactant thermal conditioning yields a comparatively more substantial enhancement in primary electrical power output [17], [32], [35], [66], [67]. However, physically integrating these distinct mechanisms into a single passive unit introduces a complex thermal balancing challenge. The engineering motivation here is to design a unified architecture that successfully balances internal heat absorption with external cold side heat rejection. Utilising internal heat sinks to elevate incoming hydrogen temperatures theoretically reduces internal electrochemical polarisation losses, yet trapping too much heat inadvertently elevates the overall component temperature, which collapses the cold side thermal gradient required by the solid state modules. Therefore, investigating the specific geometric sizing of internal copper tube passes and external heat pipes to passively balance this thermal distribution serves as a major technical driver for this work.

Transitioning from mathematical designs to physical vehicular application introduces complex environmental variables. Controlled steady state laboratory conditions provide a necessary foundational baseline. However, static environments inherently isolate the system from the continuous transient electrical loads and fluctuating convective cooling conditions experienced during actual vehicle operation. Evaluating the recovery architecture under dynamic constraints is essential because physical momentum and varying atmospheric parameters continuously alter the thermal rejection boundary. Furthermore, practical implementation introduces fundamental hardware constraints, such as the inherently low hydrogen mass flow rate mandated by a 2 kW fuel cell, which acts as a permanent physical bottleneck for absolute thermal absorption.

Consequently, a strong technical motivation exists to conduct extended dynamic on road testing. Evaluating the integrated heat recovery system over prolonged continuous driving cycles is necessary to observe how the physical thermal mass of the passive components absorbs and retains latent heat over time [30], [40], [68], [31], [64]. Extended dynamic operation exposes the system to thermal saturation, revealing the

actual physical viability and thermodynamic limits of the architecture when subjected to the chaotic environmental noise outside of a simulated test bench. Transitioning from mathematical models to physical reality requires acknowledging the limitations of empirical data. Physical on road evaluations inherently introduce unavoidable experimental uncertainties, such as severe upstream conductive heat losses, transient thermal lag, varying ambient wind resistance, and minor sensor measurement noise. The motivation of this work is not to present a flawless idealized performance model, but rather to rigorously quantify the actual recoverable energy within these practical, noisy physical boundaries. By progressing from computational fluid dynamics to controlled test bench validation, and ultimately to extended dynamic on road evaluation, this research aims to provide a reliable, empirically grounded framework for enhancing fuel cell efficiency through integrated waste heat recovery.

Finally, this research is deeply motivated by the broader global directive to achieve the United Nations Sustainable Development Goals [69]. The foundational drive of this work directly aligns with Goal 7, Affordable and Clean Energy, by attempting to maximise the useful energy yield from hydrogen power plants. As this project develops methodologies to repurpose thermal waste from fuel cell electric vehicles, it concurrently supports Goal 11, Sustainable Cities and Communities, by promoting the adoption of zero emission public and private transportation within urban infrastructure. Furthermore, implementing these advanced fuel cell vehicles actively reduces global carbon emissions, providing a tangible contribution to Goal 13, Climate Action. The specific integrated heat recovery technology embraces the core principles of Goal 12, Responsible Consumption and Production, by actively scavenging and reusing waste heat that is traditionally discarded into the atmosphere. Ultimately, promoting enhanced fuel cell efficiency fosters the transition toward hydrogen as a primary energy vector, which invites continuous technological innovation and supports the development of robust new hydrogen infrastructures, strongly aligning with Goal 9, Industry, Innovation and Infrastructure.

1.3 Problem Statement

Video provides a powerful way to help you prove your point. When you click Online Video, you can paste in the embed code for the video you want to add. You can

also type a keyword to search online for the video that best fits your document as shown in **Error! Reference source not found.**.

PEM fuel cells represent a promising alternative for vehicular power generation. However, the primary electrical efficiency of the polymer electrolyte membrane fuel cell remains constrained between 40% and 60% [70]. The remaining chemical energy from the consumed hydrogen reactant inherently converts into unutilised waste heat. Recovering this thermal energy presents a distinct opportunity to improve total system efficiency. However, open cathode variants operate at relatively low temperatures. Consequently, the system only produces ultra low grade waste heat bounded between 60 °C and 80 °C [71]. The fundamental physical challenge lies in determining how to effectively harvest and quantify this ultra low grade thermal energy, as the inherently low temperature gradient severely restricts the driving force required for secondary energy recovery.

Fuel cell electric vehicles operating in outdoor environments possess an untapped continuous convective cooling medium in the form of ambient cruising air [72]. Within the fuel cell stack, activation polarisation represents the dominant efficiency loss at low current densities, necessitating a significant fraction of chemical energy to overcome the reaction threshold. Heating the incoming hydrogen reactant offers a potential pathway to mitigate these activation losses and improve primary electrical output. Integrating hydrogen reactant preheating with solid state thermoelectric generation presents a highly promising recovery pathway by leveraging this cruising air to cool the external thermoelectric faces. However, the physical engineering complexity involves determining exactly how to combine these mechanisms simultaneously. There is significant uncertainty regarding what specific geometric type of heat exchanger and internal components are required to passively heat both the hydrogen gas and the thermoelectric modules, and simultaneously cool the opposing thermoelectric faces given the severely restricted low grade heat source.

Furthermore, mathematical models evaluating simultaneous thermal recovery mechanisms inherently rely on idealised mathematical assumptions. These computational models frequently fail to account for the physical realities of thermal contact resistance, structural heat leakages, and transient thermal lag within the physical mass. Relying exclusively on these mathematical predictions creates a critical engineering barrier when attempting to determine actual operational viability [73]. Therefore, preliminary physical evaluations under controlled steady state laboratory test

bench conditions are absolutely required to quantify the actual thermodynamic baseline and physical thermal losses of the selected heat exchanger geometry prior to vehicular integration.

Finally, transitioning this integrated system into a dynamic lightweight vehicle introduces severe environmental complexities that dictate actual physical performance [74]. Unstable ambient temperatures and fluctuating convective cruising air velocities during open road driving impose continuous transient boundaries that steady state laboratory testing inherently fails to replicate. Consequently, dynamic on road evaluations are strictly necessary to understand how chaotic environmental noise and transient driving conditions physically limit the maximum operational capacity of the recovery architecture.

1.4 Research Objectives

Based on the identified problems, the primary aim of this research is to develop, investigate, and experimentally evaluate an integrated passive heat recovery architecture designed to enhance the electrochemical and thermoelectrical performances of a PEM fuel cell. This aim is achieved through the following three specific objectives:

1. To develop and evaluate four integrated heat recovery architectures for a PEM fuel cell by quantifying the corresponding impacts on hydrogen reactant thermal elevation, primary fuel cell performance, secondary thermoelectric power generation, and overall waste heat utilisation (Technology Readiness Level (TRL) 2).
2. To experimentally validate the computational fluid dynamics models and to characterise the actual steady state performance of the physical system (TRL 4).
3. To evaluate the thermodynamic limitations and fuel cell performance of the physical system integrated onto a lightweight vehicle during transient dynamic driving cycles (TRL 6).

1.5 Research Question

To fulfil the stated problems, this research systematically investigates the following questions:

1. How do varying geometric configurations of the integrated architecture passively manage internal thermal partitioning to dictate hydrogen reactant thermal elevation, secondary thermoelectric generation, and overall waste heat utilisation for a low temperature polymer electrolyte membrane fuel cell?
2. How accurately does the physically fabricated recovery architecture validate the computational fluid dynamics models, and what is the actual steady state primary electrical power increment and secondary electrical generation when evaluated under controlled laboratory test bench conditions?
3. How do physical thermodynamic limitations, specifically the inherent reactant mass flow bottleneck and transient thermal saturation, restrict the actual fuel cell performance and absolute waste heat utilisation when integrated onto a lightweight vehicle during dynamic on road driving cycles?

1.6 Significance of Study

The research provides critical empirical data bridging the gap between idealized theoretical thermal recovery models and practical physical vehicular reality. The primary novelty of this research lies in the conceptualisation and physical design of a dual mode heat recovery architecture. While previous studies explore reactant preheating and solid state thermoelectric generation exclusively as independent systems, this study introduces a novel passive geometric design that simultaneously combines both mechanisms into a single heat recovery module. The integration of solid state TEG modules alongside recuperative hydrogen preheating establishes a novel framework for capturing ultra low grade waste heat from a PEM fuel cell without introducing parasitic mechanical components.

Furthermore, transitioning this dual architecture from mathematical modelling to physical experimental validation represents a significant methodological novelty. Crucially, by conducting physical on road evaluations utilising a lightweight fuel cell buggy across varying temporal durations, this research executes a novel dynamic assessment of the passive continuous recovery effect. The empirical data establishes that prolonged continuous vehicle operation allows the physical thermal mass of the recovery components to overcome initial thermal inertia and absorb latent heat more thoroughly. This finding is highly significant because it demonstrates that extended continuous driving yields a greater total accumulation of preheated hydrogen energy

and secondary TEG electrical output compared to short duration constant speed evaluations. This specific thermodynamic behaviour underscores the necessity of evaluating heat exchangers under extended dynamic cycles rather than brief, idealized testing intervals.

Finally, this research is equally significant for explicitly exposing the strict thermodynamic bottlenecks that fundamentally govern lightweight vehicle heat recovery. While computational models frequently assume perfect heat transfer, this empirical study physically quantifies the specific limitations inherent to vehicular applications. Highlighting the fundamental hardware constraints of low reactant mass flow rates, exposing severe upstream conductive heat losses, and identifying transient thermal saturation during high load accelerations provides future engineers with a realistic, grounded baseline. By thoroughly documenting these unavoidable physical flaws and operational uncertainties, this research actively redirects future thermal management design away from idealized steady state assumptions and toward practical physical vehicular constraints.

1.7 Limitation Scopes of Study

To ensure the research objectives remain achievable and experimentally valid, the boundaries of this investigation span three distinct methodological phases. The overarching scope encompasses the mathematical design, physical test bench validation, and dynamic on road evaluation of the integrated heat recovery architecture installed in a 2 kW polymer electrolyte membrane fuel cell buggy.

The thermodynamic evaluation throughout all three phases is strictly bounded by the First Law of Thermodynamics, focusing on quantifying the overall energy performance, macroscopic thermal partitioning, and secondary electrical generation. Exergy analysis and evaluations based on the Second Law of Thermodynamics are explicitly excluded from this study.

1.7.1 Scope for Objective 1: Mathematical and Numerical Design Investigation

For the first research objective, the mathematical and numerical design investigation evaluates four structural geometries. This geometric exploration focuses on balancing internal copper tube passes, solid heat pipes, and extended aluminium cooling fins alongside thermoelectric generator modules. The internal semiconductor junctions within the modules are explicitly excluded, restricting the computational domain to macroscopic solid bodies. The ultimate purpose of this phase is to evaluate the geometries and select a single finalised design.

The numerical evaluation utilises steady state one dimensional calculations based on thermal resistance and Number of Transfer Units methods. Subsequently, computational fluid dynamics investigations are bounded by steady state single phase conjugate heat transfer simulations utilising a k epsilon realizable turbulence model. The internal electrochemical mechanics of the fuel cell stack and the physical kinetic dynamics of the buggy are not mathematically modelled. Instead, operational metrics spanning 500 W to 2000 W serve as fixed boundary conditions. Environmental boundaries are fixed at a 30 °C ambient temperature and a 10 m/s convective cooling velocity. Direct simulation of secondary electrical generation is excluded; the software provides thermal mapping, while electrical outputs are projected utilising predictive mathematical equations.

1.7.2 Scope for Objective 2: Experimental Test Bench Validation

For the second research objective, the scope covers the physical manufacturing and steady state laboratory evaluation of the selected integrated heat recovery architecture. Physical fabrication encompasses the primary heating and secondary cooling chambers, integrating internal copper tubes, penetrating heat pipes, and aluminium cooling fins. This phase extracts empirical data representing the physical thermal behaviour, establishing a baseline reference for subsequent dynamic on road testing.

The experimental boundaries are constrained within a steady state laboratory environment, entirely excluding the physical traction motor. A programmable direct current electronic loader manipulates the fuel cell electrical power, restricting the current draw to increments between 1 A and 60 A. A dedicated direct current fan simulates cruising speeds by channelling external cooling air into the cooling chamber at constrained velocities between 0 and 10 m/s. The ambient laboratory environment is thermally bounded between 24 °C and 26 °C.

Data acquisition was strictly limited to extracting macroscopic steady state performance metrics (examples of macroscopic parameters measured Hydrogen temperature, hydrogen flow rate, fuel cell voltage and current), focusing exclusively on spatial surface temperatures, volumetric flow rates, and direct electrical outputs. Which provide a clear, controlled baseline to understand the fundamental thermodynamic behaviour of the PEM fuel cell under the direct influence of the novel IHR architecture. By isolating the system from unpredictable environmental factors, the core thermal and electrical interactions were systematically evaluated before introducing the chaotic transient conditions of dynamic on road testing. Consequently, complex internal thermodynamic variables within the fuel cell stack, such as internal gas pressures and microscopic membrane hydration behaviours, were explicitly excluded. Ultimately, the extracted macroscopic parameters served to reliably evaluate the total energy efficiency, fuel consumption, and waste heat utilisation under controlled laboratory test conditions.

1.7.3 Scope for Objective 3: Dynamic On Road Evaluation

For the final research objective, the scope transitions to a dynamic physical on road evaluation. The test platform is a 2 kW fuel cell buggy, propelled by an 800 W traction motor. Physical testing is confined to the flat tarmac environment of the Dewan

Tun Abdullah Mohd Salleh parking lot at Universiti Kebangsaan Malaysia. Data acquisition during these outdoor evaluations focuses exclusively on mapping the thermal distribution across the integrated architecture and measuring the corresponding electrical polarisation of the primary and secondary systems.

The on road testing methodology is partitioned into two operational phases. The first phase encompasses a constant speed evaluation restricted to a fixed 1 km distance. This scope limits the vehicle velocity to a cruising range between 10 km/h and 18 km/h, excluding transient thermal data generated during initial acceleration and final deceleration. This constant speed phase is bounded by three specific weight loading conditions utilising strictly controlled gross weights of 80 kg, 160 kg, and 240 kg.

The second phase follows a dynamic transient evaluation bounded by a modified New European Driving Cycle. Because the 800 W traction motor is mechanically limited to a maximum speed of 18 km/h and requires a minimum consistent cruising speed of 5 km/h, the standard cycle is mathematically scaled to operate strictly within these physical vehicular constraints. The adapted driving scope restricts the evaluation to four lower bound speed ranges simulating the Economic Commission for Europe 15 cycle and five upper bound speed ranges simulating the Extra Urban Driving Cycle, providing a highly bounded framework to evaluate outdoor transient thermal responses.

1.8 Limitations of Study

This research provides an empirically grounded evaluation of the integrated heat recovery architecture, however several inherent limitations and unavoidable experimental uncertainties require explicit acknowledgement. mathematical equations, numerical software, and physical manufacturing all carry inherent flaws that deviate from absolute physical reality. Furthermore, evaluating thermodynamic systems in open real world environments introduces continuous environmental noise and instrument error. This section outlines the specific mathematical assumptions, physical constraints, and uncontrolled thermodynamic leakages encountered across the three methodological phases that inherently influence the interpretation of the collected data.

1.8.1 Limitations for Objective 1: mathematical and Numerical Methodologies

The mathematical and numerical methodologies applied to fulfil the first objective involve inherent mathematical assumptions that deviate from physical reality.

A primary structural limitation involves the geometric simplification of the internal components. In actual physical operation, a heat pipe relies on highly complex two phase boiling and condensation mechanics to move thermal energy rapidly. However, within both the mathematical equations and the computational fluid dynamics software, these components are simplified and modelled entirely as solid copper cylinders. Simulating transient multi phase mechanics within a highly dense heat exchanger geometry exceeds standard computational limits. Similarly, modelling the thermoelectric generator modules as solid blocks of Bismuth Telluride completely omits the intricate microscopic thermal resistances introduced by the alternating positive and negative junctions, internal solder layers, and outer ceramic plates. Resolving these microscopic alternating junctions across millions of mesh elements introduces prohibitive computational overhead and frequently causes mathematical divergence. Therefore, these geometric simplifications serve strictly to maintain numerical stability.

A secondary structural assumption involves the physical interfaces between these components. Physical manufacturing necessitates the application of thermal paste to bridge microscopic air gaps between the copper tubes, aluminium fins, and thermoelectric generator surfaces. This thermal interface material is not modelled. Accurately modelling microscopic thermal paste thickness across macroscopic boundaries is computationally unfeasible. Instead, the simulations assume perfect heat transfer across all solid boundaries, operating with zero thermal contact resistance. Consequently, the software may overestimate how easily heat travels through these components and interfaces, serving as an idealised estimate rather than a perfect physical representation.

Furthermore, the computational fluid dynamics models operate under strict environmental assumptions that introduce unavoidable numerical uncertainties. The simulations utilise steady state and single phase fluid boundaries. By assuming a steady state, the software completely omits the transient thermal lag, deliberately ignoring the physical time required for the metal components to heat up or cool down during operation. The single phase assumption also ignores any potential water vapor condensation occurring within the primary exhaust stream. Additionally, the numerical models explicitly exclude radiative heat transfer, forcing the software to calculate energy exchange relying exclusively on conduction and convection.

Finally, a fundamental calculation limitation exists regarding the predicted electrical improvements. Because the complex internal electrochemical mechanics of the polymer electrolyte membrane fuel cell and the active Peltier cooling effect of the thermoelectric generator modules are not directly simulated in the software, the anticipated electrical increments are derived utilising mathematical equations from established literature. Projecting electrical power using predictive equations rather than employing a fully coupled multi physics simulation relies on historical data and generalized assumptions. This approach inherently fails to capture the unique electrochemical response, internal membrane degradation, and specific polarization behaviour of the exact physical units utilised later in the study.

1.8.2 Limitations for Objective 2: Experimental Test Bench Validation

Transitioning the mathematical IHR design into a physical prototype for the second objective introduces unavoidable manufacturing tolerances and material imperfections. Unlike the mathematically flawless surfaces modelled in the computational phase, the physical components inherently possess microscopic surface roughness, minor machining deviations, and imperfect component alignment. Consequently, relying on thermal paste to bridge these physical gaps introduces a realistic and unavoidable thermal contact resistance. This physical resistance inherently restricts the rate of heat conduction between the internal copper tubes, the exterior aluminium fins, and the TEG surfaces, resulting in physical thermal distributions that are slightly less efficient than the idealized numerical projections.

Evaluating the physical architecture within a laboratory test bench environment also introduces unavoidable thermodynamic leakages that analytical models frequently omit. While the laboratory room temperature is mechanically controlled, the physical metallic surfaces of the IHR system and the exposed connection manifolds inevitably experience continuous radiative heat loss to the surrounding environment. More severely, the system suffers from upstream conductive heat dissipation. Thermal energy is unavoidably lost along the physical length of the exhaust piping before the hot gas even enters the IHR recovery chamber, ensuring the physical recovery system operates on a significantly degraded thermal baseline.

Finally, data collection during the laboratory phase is constrained by the physical construction of the commercial fuel cell. The commercial stack functions as a

permanently enclosed unit. Opening the physical casing to install internal sensors for measuring exact membrane hydration or localised internal temperatures would permanently damage the hardware and violate laboratory safety guidelines. Therefore, the experimental methodology strictly relies on external measurement tools, specifically surface mounted thermocouples and external fluid flow meters. While this external approach safely preserves the structural integrity of the fuel cell, evaluating performance exclusively from the outside creates an unavoidable experimental limitation. The external sensors only capture the overall bulk performance of the system and cannot detect localised internal phenomena, such as microscopic dry spots on the polymer membrane or uneven internal gas distribution. Consequently, calculating the system efficiency utilising only external readings introduces minor experimental uncertainties when compared to idealised mathematical models.

1.8.3 Limitations for Objective 3: Dynamic On Road Evaluation

Transition of the IHR evaluation to an outdoor physical environment introduces thermodynamic complexities and experimental uncertainties compared to laboratory test benches. The primary limitation of his dynamic phase is the transient thermal lag induced by the physical metallic mass of the IHR architecture. The dense copper and aluminium components inherently possess a heavy thermal mass. Consequently, during acceleration phase, the resulting spike in waste heat takes considerable time to soak into the metal structure. Because of this thermal inertia, the surface mounted temperature sensors inherently lag behind the actual instantaneous electrical spikes, meaning the recorded data represents a delayed historical thermal response rather than a perfect real time thermodynamic mapping.

Furthermore, conducting physical evaluations in an open track (parking lot) introduces environmental noise. Unlike the perfectly smooth, mechanically controlled cooling fan utilised in the laboratory phase, the physical vehicle is continuously subjected to unpredictable ambient wind gusts and fluctuating natural convection rates. These erratic weather variables continuously disrupt the external boundary conditions, severely impacting the cold side heat rejection of the TEG modules and creating scattered thermal data.

Additionally, executing the highly specific scaled dynamic driving cycle relies entirely on a human driver, introducing operational errors. Manual throttle variations,

minor delays in human reaction time, and micro gradients in the parking lot tarmac introduce continuous transient noise into the 800 W motor load. This creates an erratic power demand profile full of sudden current spikes and drops that standard theoretical driving cycles simply do not predict.

Finally, the absolute waste heat utilization recorded during these extended dynamic evaluations is fundamentally restricted by the permanent physical bottleneck of the fuel cell system itself. The selected 2 kW architecture dictates an inherently low mass flow rate for the hydrogen reactant gas. Regardless of how efficiently the IHR internal geometry is designed, this tiny physical volume of gas possesses a severely limited thermal absorption capacity. Therefore, the mathematically low energy recovery percentages documented during the on road testing do not represent a failure of the heat exchanger design, but rather physically demonstrate the strict fundamental thermodynamic limitations inherent to lightweight, low temperature PEM fuel cell applications with low hydrogen fuel flowrate.

1.9 Thesis Overview

The primary novelty of this thesis lies in the simultaneous integration of hydrogen reactant preheating and solid state thermoelectric generation into a single passive heat recovery module, and the subsequent empirical evaluation of this dual architecture under dynamic outdoor vehicular conditions. By expanding the evaluation framework beyond idealised steady state mathematical models to explicitly quantify the physical thermodynamic bottlenecks and transient thermal lag experienced during actual on road driving, this research establishes a grounded empirical baseline for understanding practical vehicular thermal dynamics. To systematically detail this investigation, the thesis is structured into five distinct chapters which is simplified figure 1.1.

Chapter 1 introduces the research background and formulates the primary engineering challenges regarding ultra low grade heat recovery. The chapter proceeds to define the core research objectives, highlight the novelty of the integrated approach, align the project with global sustainability goals, and explicitly outline the scopes and boundaries of the physical investigations.

Chapter 2 provides a comprehensive review of existing academic literature. The review critically evaluates prior studies concerning polymer electrolyte membrane fuel

cell thermal management, hydrogen reactant preheating, and solid state thermoelectric generation. Furthermore, the chapter critically examines the boundaries of current mathematical evaluation methodologies and justifies the strict necessity for dynamic physical testing.

Chapter 3 details the experimental methodology and physical apparatus utilised throughout the research. The text describes the three sequential phases of evaluation encompassing mathematical, computational fluid dynamics modelling, the controlled steady state laboratory test bench configuration, and the dynamic outdoor fuel cell buggy integration, while explicitly acknowledging the inherent physical uncertainties of the deployed measurement instruments.

Chapter 4 presents the empirical data and critically analyses the physical results. The analysis compares the initial computational models against the actual steady state baseline performance. Furthermore, this chapter evaluates the transient thermal responses and electrochemical efficiencies recorded during dynamic on road evaluations, specifically highlighting the physical limitations, experimental errors, and thermodynamic bottlenecks observed during physical outdoor testing.

Chapter 5 summarises the primary research findings and draws cautious conclusions regarding the operational viability of the integrated recovery module. The thesis concludes by proposing strategic recommendations for future research to address the observed physical constraints and to mitigate experimental flaws in larger scaled applications.

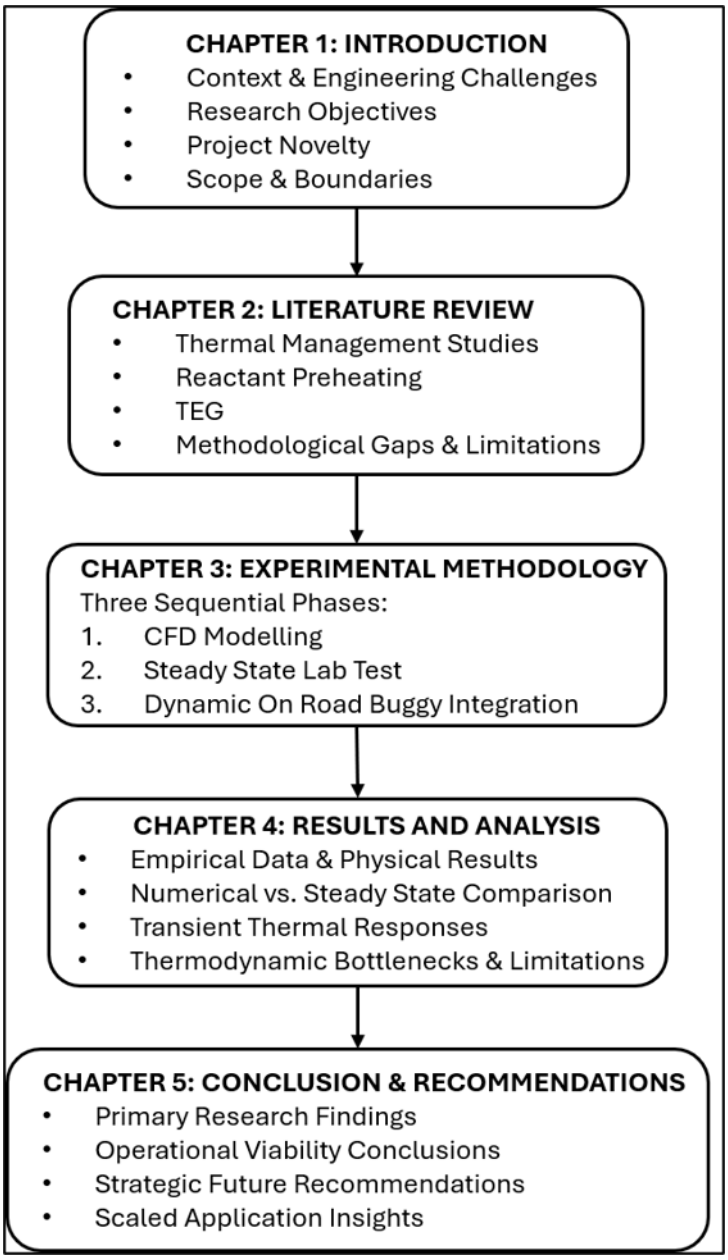

Figure 1.1 Thesis Overview Flowchart

CHAPTER 2
LITERATURE REVIEW

2.1 Introduction

Recent advancements in PEM fuel cells yielded significant progress in isolated thermal management and waste heat recovery (WHR) architectures, their dynamic integration under transient automotive conditions appeared to benefit from further exploration. Existing literature indicated that robust thermal regulation played a critical role in mitigating material degradation and sustaining primary electrical power output. Approximately 30 to 50% of the input chemical energy was typically dissipated as low-grade waste heat within a narrow optimal operating window of 60 to 80 °C [75]. To repurpose this thermal liability and boost overall system net power, WHR technologies gained significant traction. Systems such as the Organic Rankine Cycle (ORC), which were fundamentally bounded by Carnot limits to an average practical thermal efficiency of roughly 7.4% [76], alongside combined heat and power networks, attempted to capture this loss and theoretically improved the overall electrical efficiency of the system.

Concurrently, the evolution of realistic Accelerated Stress Tests (AST) provided valuable frameworks for isolating specific degradation mechanisms under standardised driving profiles, such as the Worldwide Harmonized Light Vehicles Test Cycle (WLTC) or the NEDC [77]. However, the exploration of the intersection of these domains suggested specific methodological limitations. Existing dynamic testing protocols largely assumed isolated thermal environments, which may not have fully accounted for the complex thermal and electrical coupling induced when active recovery systems altered the inherent thermal inertia of the primary stack. In lightweight vehicular applications characterized by aggressive sub-second load transients, such as sudden current density shifts from 800 to 1400 mA/cm² [78], alongside frequent start-stop cycles, this altered thermal impedance potentially destabilized the delicate internal hydration equilibrium.

Consequently, such imbalances are observed to exacerbate micro-scale vulnerabilities, potentially inducing localised reactant starvation and rapid liquid water accumulation near the active catalyst layers. These phenomena typically manifest as

severe voltage drops, which significantly restrict the electrical power performance of the vehicle. Therefore, establishing unified system-level dynamic testing frameworks capable of empirically quantifying the transient hydrothermal penalties associated with integrated WHR was suggested as a valuable pathway for optimizing the electrical durability and viability of next-generation vehicular PEM fuel cells. Before evaluating these complex recovery architectures, researchers found it necessary to first bound the fundamental thermodynamic limits and polarization mechanisms that governed the baseline power generation of the primary stack.

2.2 PEM Fuel Cell Thermodynamics and Performance Limitations

2.2.1 Operating Principles and Energy Partitioning

The fundamental operation of a PEM fuel cell is the direct electrochemical conversion of chemical energy into electrical work, driven by the hydrogen oxidation reaction (HOR) at the anode and the oxygen reduction reaction (ORR) at the cathode. The absolute thermodynamic limit of this energy conversion is governed by the change in standard Gibbs free energy, which dictated a theoretical reversible Nernst potential of 1.229 V and established a maximum theoretical thermal efficiency ceiling of approximately 83% [79]. Furthermore, thermodynamic models indicate that the reversible Nernst potential is inversely proportional to the operating temperature. As the thermal state of the cell elevate, the theoretical maximum voltage consistently decline [79].

However, in practical vehicular applications the operational power efficiency often diverge significantly from this thermodynamic ceiling. Empirical energy partitioning analyses, such as those conducted on the 114 kW stack utilised in the Toyota Mirai across ambient testing environments of −18 to 35 °C, consistently demonstrate that 40 to 60% of the input chemical energy was inherently dissipated as low-grade waste heat [70]. This profound thermal loss restricted the optimal operation of the stack to a narrowed thermal window, typically between 60 and 80 °C [80]. This massive energy dissipation was interpreted not as an anomalous byproduct but as a fundamental physical consequence of the electrochemical irreversibility’s within the system. This generated heat was generally partitioned into two distinct categories.

The first category, reversible entropic heat, is a consequence of the overall reaction and is predominantly localised at the cathode catalyst layer due to the specific dynamics of the ORR. The second category, irreversible heat, stems directly from the operational overpotentials of the system. The activation heat generated by the kinetic energy barriers of reaction initiation at the catalyst-ionomer interface, which dominated at low current densities below 0.2 A/cm². It also include Ohmic Joule heating induced by resistance to protonic transport through the polymer membrane and electronic transport through solid components, which typically dictate losses between 0.2 and 1.0 A/cm². Finally, it accounts for mass transport heat emerging from reactant diffusion limitations within the porous media under high current densities exceeding 1.0 A/cm².

Crucially, these irreversible losses compounded as the electrical demand escalated where the rate of localised heat generation scale linearly with the decline in cell voltage efficiency. Under high-load operations, such as the rapid current density steps typical of aggressive vehicular accelerations, the rate of waste heat generation frequently equalled or exceeded the net electrical power output of the PEM fuel cell [81]. This severe thermal partitioning suggest that the physical durability and electrical performance of high-power automotive stacks rely heavily on advanced thermal management architectures. These systems need to be capable of rejecting or recovering this heat load before it destabilizes the internal multi-phase transport. If these aggressive thermal transients are not regulated, they trigger localised hot spots, sometimes exceeding 95 °C, which induce severe membrane dehydration, drops in ionic conductivity, and irreversible electrical power degradation.

2.2.2 Polarization Losses

The operational voltage of a PEM fuel cell consistently deviate from the theoretical reversible Nernst potential due to three fundamental irreversible polarization phenomena: activation, ohmic, and mass transport overpotentials [70]. These collective voltage losses dictate the morphology of the polarization curve and serve as the primary mechanisms for internal waste heat generation, thereby inextricably coupling the baseline electrochemistry of the cell to the system-level hydrothermal management. Because these polarizations restrict the useful electrical power of the stack, researchers explore methods to mitigate their impact as a primary objective of advanced thermal conditioning.

Activation polarization dominate performance degradation at low current densities and represent the kinetic energy barrier required to initiate electrochemical reactions. The magnitude of this voltage loss is fundamentally governed by the sluggish kinetics of the ORR at the cathode, while the HOR at the anode contributed negligibly to the overall kinetic impedance. Quantified by Butler-Volmer kinetics or the simplified Tafel equation, the energy is expended to overcome this barrier manifested as localised activation heat. Because the ORR limited the overall reaction rate, this heat generation is concentrated at the cathode catalyst layer, suggesting a need for targeted thermal mitigation strategies to help avert accelerated catalyst degradation and preserve initial voltage outputs.

As the current density transitions into the moderate operating regime, ohmic polarization emerges as the defining performance constraint. This voltage loss stemmed from the intrinsic resistance to charge transport across the fuel cell assembly. It comprised both the electronic resistance encountered by electrons migrating through solid components, such as the GDL and bipolar plates, and the ionic resistance impeding proton transport through the polymer electrolyte membrane. Crucially, ohmic losses exhibit dynamic coupling with the hydration state of the membrane. Inadequate water management or excessive thermal loads increases the saturated vapor pressure, which likely dehydrate the ionomer and curtail its proton conductivity. This establishes a potentially detrimental thermodynamic feedback loop where elevated ionic resistance amplified Joule heating, which further desiccate the membrane and led to significant drops in electrical power output.

Under high-load conditions, electrochemical kinetics are bottlenecked by mass transport polarization. This overpotential manifested when the rapid consumption of reactants outpaced their diffusion rate through the porous transport layers to the active catalyst sites. Concurrently, the accelerated production of liquid water at the cathode during peak current densities precipitated localised flooding. Liquid water physically occluded the pores of the GDL and catalyst layer, which impeded oxygen diffusion and induced reactant starvation. Consequently, this localised reactant depletion triggered a sharp voltage drop that defined the limiting current density and peak power boundary of the PEM fuel cell. Mitigating these mass transport losses necessitated the deployment of advanced architectures engineered to expel liquid water without desiccating the reactant gas streams [70].

2.2.3 Temperature Dependency of Cell Performance

The reversible Nernst potential of a PEM fuel cell is inversely proportional to its operating temperature. Thermodynamic models indicate that as the thermal state elevates, the theoretical maximum voltage strictly decline [82]. Despite this fundamental thermodynamic penalty, empirical data consistently demonstrated that operating the stack at elevated temperatures, specifically within the optimal window of 60 to 80 °C, increased the operational electrical power output [83]. This enhancement occurred because higher thermal states significantly accelerated the intrinsically sluggish kinetics of the cathodic ORR, thereby reducing activation polarization and raising the functional output voltage.

However, the most profound and volatile temperature dependency within the PEM fuel cell governed the proton conductivity of the perfluoro sulfonic acid (PFSA) membrane [79]. Protonic transport through these polymers strictly require a high degree of water saturation. Because the saturated vapor pressure of water rose exponentially with temperature, excessive internal stack heat drove rapid evaporation, forcing the local relative humidity to plummet. This thermally induced dehydration could severely diminish the ionic conductivity of the membrane, often dropping below 1 S/m at critical thermal thresholds, which typically resulted in massive ohmic polarization and severe electrical power loss [84].

Crucially, this dynamic could establish a highly destructive thermodynamic feedback loop. As membrane dehydration elevate ohmic resistance, the restricted charge transport generated intense localised Joule heating. Without rapid thermal mitigation, these concentrated hot spots might further desiccate the surrounding ionomer and induce severe mechanical stresses, potentially accelerating degradation mechanisms such as membrane thinning and pinhole formation [84].

Conversely, operating at suboptimal temperatures or failing to properly thermally condition incoming reactants triggers the opposite extreme of localised subcooling. Under these conditions, the product water vapor generated by the ORR rapidly condense into liquid droplets within the GDL and micro channels. This flooding physically occluded the porous media and stifled oxygen diffusion to the active catalyst sites, which could induce an acute and exponential mass transport voltage drop [85]. Consequently, the overall electrical power degradation of a PEM fuel cell operate as a highly sensitive non linear function of its internal hydrothermal balance. In lightweight

vehicular applications where rapid load transients constantly disrupt the localised heat generation rate, finding ways to precisely manage the profound temperature dependency of these coupled kinetic and transport phenomena might offer critical improvements to this operational challenge.

2.3 Conventional Thermal Management Architectures and Operational Bottlenecks

Mitigating the thermodynamic bottlenecks within PEM fuel cells require conventional thermal management systems (TMS) rejecting between 40% and 60% of the input chemical energy inevitably dissipated as low grade waste heat, while maintaining a strictly uniform operating temperature bounded between 60 °C and 80 °C. Failure to achieve this macroscopic temperature uniformity directly induces localised hot spots, which might accelerate membrane desiccation, exacerbate non uniform current density distributions, and trigger irreversible material failures [5]. Historically, TMS architectures is branched by power output scale into air cooled and liquid cooled paradigms [11]. Ultimately, while these conventional cooling strategies provide the necessary bulk heat dissipation for automotive applications, their reliance on parasitic power and their vulnerability to localised thermal gradients leads to a critical performance ceiling [70] [86].

2.3.1 Current Cooling Strategies: Overview of Passive and Active Architectures

Current literature suggested that the selection of an appropriate cooling strategy is strictly dictated by the rated power capacity of the stack, specific volumetric constraints, and the transient demands of the intended application [87].

Passive TMS architectures operate without mechanical components, relying predominantly on natural convection and high thermally conductive materials, such as pyrolytic graphite sheets or metallic foams, alongside the latent heat absorption of phase change materials (PCM) to dissipate thermal energy [88], [89]. While offering architectural simplicity and zero parasitic power consumption, their reliance on natural heat dissipation restricted their viability to micro PEM fuel cell applications. For lightweight vehicular environments, rapidly fluctuating heat fluxes fundamentally exceeded the thermal transport capacity of passive conduction, rendering standalone passive systems thermodynamically inadequate for automotive scales [88].

For intermediate power ranges, typically operating below 5 kW, active air cooling frequently served as the baseline thermal regulation strategy [90]. This architecture utilise blowers or fans to force ambient air across open cathode structures. While this open cathode air cooled strategy is highly effective for low power vehicular chassis and eliminate the need for secondary liquid coolant loops, its scalability is severely restricted. Air possesses a critically low specific heat capacity of approximately 1.005 J/g°C. Consequently, rejecting massive heat loads require high capacity compressors that impose substantial parasitic power penalties, rendering standalone air cooling thermodynamically restrictive for full scale heavy duty applications [91].

Given these thermodynamic constraints, active liquid cooling emerge as the definitive industry standard for high power vehicular PEM fuel cell architectures exceeding 5 kW [11]. Circulating a dielectric coolant, frequently deionized water or a water ethylene glycol mixture, through miniature channels embedded within the bipolar plates enable aggressive heat extraction [92]. Because liquid coolants possessed significantly higher specific heat capacities, such as 4.186 J/g°C for water, they provided a highly robust thermal buffer against the aggressive load transients characteristic of automotive drive cycles [93].

2.3.2 Limitations of Conventional Thermal Management: Parasitic Power and the Boundaries of Heat Rejection

Despite its dominance in commercial platforms, conventional active liquid cooling leads to substantial systemic trade offs. A primary constraint identified across contemporary literature was the severe parasitic power penalty imposed by coolant pumps and radiator fans, which directly cannibalised the net electrical output of the stack [94]. In heavy duty automotive applications, overcoming the hydraulic resistance of intricate channels and rejecting absorbed heat to the ambient environment demanded staggering balance of plant (BoP) parasitic loads [95]. Projections indicated that the radiator fan alone in a 313 kW PEM fuel cell truck could consume up to 27 kW of parasitic electrical power, severely throttling system level efficiency [82].

Furthermore, conventional parallel and serpentine channel architectures inherently develop significant inlet to outlet temperature gradients. Empirical infrared measurements of large scale 110 kW automotive stacks revealed maximum surface

temperature differences reaching up to 20 K [5]. This macroscopic gradient severely compromises optimal hydration across the membrane electrode assembly (MEA), leaving downstream regions highly susceptible to localised reactant starvation and accelerated material degradation [96]. Additionally, a critical methodological limitation across much of the literature evaluating these cooling architectures was a historical reliance on steady state boundary conditions [97]. Such mathematical assumptions frequently fail to accurately capture the severe thermal inertia, localised flow maldistributions, and delayed temperature responses that manifested during rapid real world driving load shifts. This highlighted the reality that dynamic physical evaluations inherently carried experimental uncertainties and unavoidable transient flaws [98].

Because a PEM fuel cell had to operate within a strictly narrow and relatively low thermal window, the mean temperature difference (MTD) between the heat source and the ambient environment is remarkably small compared to traditional internal combustion engines [80]. Consequently, adequately rejecting the massive thermal load require disproportionately high coolant mass flow rates and expansive radiator frontal areas. Discarding roughly half of the chemical energy of the fuel directly to the ambient atmosphere strictly capped the theoretical ceiling of vehicular electrical efficiency. Recent critical analyses suggested that transitioning from pure heat rejection to integrated WHR architectures might offer a superior pathway [99]. Rather than expending additional BoP electrical power to forcefully reject thermal energy, actively repurposing this low grade heat for reactant conditioning or auxiliary systems could theoretically elevate the total energy utilization of fuel cell hybrid electric vehicles (FCHEV) up to 90%. Therefore, the physical boundaries of conventional active cooling suggested that future TMS design might benefit from evolving toward multi physics approaches that actively harvested thermal liabilities to preserve primary electrical power, while rigorously acknowledging the physical uncertainties inherent to dynamic on road systems [29].

2.4 Waste Heat Recovery Strategies in Fuel Cell Systems

Building upon the established reality that 40 to 60% of the input chemical energy in PEM fuel cells is dissipated as low grade waste heat, contemporary literature increasingly reframe this thermal liability as a secondary energy resource. The integration of WHR architectures presented a critical frontier for maximizing system

level electrical efficiency. Systemic evaluations suggest that capturing and repurposing this thermal output could theoretically elevate the overall energy utilization of FCHEV platforms to approximately 90% while simultaneously extending cold weather driving ranges by roughly 11% [99]. Current WHR methodologies were broadly synthesized into three dominant paradigms: direct solid state energy conversion, thermodynamic power cycles, and latent thermal storage or cogeneration networks.

A comprehensive synthesis of recent literature, as detailed in Table 2.1, revealed a diverse array of physical configurations engineered to capture low grade waste heat from fuel cell vehicles. Researchers predominantly explored two distinct recovery pathways consisting of reactant preheating and secondary thermoelectric generation. For reactant thermal conditioning, the literature indicated a profound reliance on complex internal heat exchanger geometries evaluated shell and tube designs featuring corrugated knotted tubes to preheat hydrogen [100], while [101] investigated heat exchangers coupled with external electric heaters to condition incoming cathode air. Similarly, [17] utilised finned multi tube pass architectures to elevate hydrogen temperatures, reporting a broad waste heat utilization spectrum of 3 to 24 %. While these highly engineered geometries successfully transferred sensible heat, implementing tortuous flow paths like swirl nozzles or corrugated tubes inherently introduced aerodynamic pressure drops that might inadvertently increase parasitic pumping loads on the balance of plant.

Table 2.1
Comprehensive Comparison of Waste Heat Recovery Strategies and System Configurations in Fuel Cell Application

Parameter	[102]	[103]	[104]	[9]	[39]	[105]	[100]	[101]	[17]
Heat Recovery Method	Nozzle heating and Heat Pipe Heatsink cooling	Swirl nozzle heating and Heat Pipe Heatsink cooling	Heat Pipe heatsink cooling	Heat Pipe heatsink cooling	Heat Pipe cooling	Multi Pass Finned Tube heating and Heat Pipe Heatsink cooling	Shell and Tube and Corrugated Knotted Tubes	Heat Exchange and External Electric Heater	Finned and Multi Tube Pass Heat Exchanger
Application	Parallel and series FCV power train WHR	FCV WHR	FCV WHR	FCV WHR	PEMFC WHR	FCV WHR	Hydrogen Preheating For FC	Preheat Inlet Air Of PEMFC	Hydrogen Preheating Of PEMFC
Heat Source	PEMFC operating from 1540 to 2150 W	PEMFC operating from 1200 to 2000 W	PEMFC operating at 2000 W	PEMFC operating at 1000 W	PEMFC operating at 900 W	PEMFC operating from 500 to 2000 W	Fuel Cell Engine PT100	PEMFC Waste Heat	PEMFC Waste Heat
Heat Source Temperature	40 to 60 °C	45 to 60 °C	53 to 58 °C	24 to 37 °C	24 to 37 °C	29 to 51 °C	−30 to +70 °C	−50 to +30 °C	40 to 60 °C
Cooling Temperature	25 °C	28 °C	Ambient	23.5 °C	23.5 °C	30 °C	N/A	N/A	N/A
Cooling Fins Number	55	55	55	55	N/A	50	N/A	N/A	N/A
Cruising Speed	100 km/h	0 to 36 km/h	0 to 36 km/h	20 km/h	4 to 8 km/h	36 km/h	N/A	N/A	N/A
Number of TEG Cells	1 and 16	1	4	1	1	6 and 12	N/A	N/A	N/A
Methodology	Numerical	Experimental and Mathematical	Experimental	Experimental	Experimental	Numerical and Mathematical	Experimental Test Bench and Numerical Model	Numerical Model and Mathematical Calculation	Experimental and Mathematical Model
Waste Heat Utilization	2% with 16 TEG cells	N/A	N/A	N/A	N/A	< 1.6%	N/A	N/A	3 to 24 %
Power Generated from TEG	3400 µW	3000 µW at 1.6 swirl number	1900 µW	218 mW	110 mW	1400 µW	N/A	N/A	N/A

Beyond reactant heating, extracting secondary electrical power via thermoelectric generators heavily dictated the external cooling architecture. The comparative matrix highlighted an overwhelming reliance on heat pipe heatsink assemblies to manage the critical cold side boundary. Studies such as [9] [104], and [39] explicitly integrated heat pipes and extended aluminium cooling fins to aggressively draw thermal energy away from the solid state semiconductor modules. Despite these advanced cooling mechanisms, the absolute electrical generation remain physically constrained by the low temperature boundaries of the primary fuel cell. For example, mathematical models by Saufi et al. [9] scavenging ultra low waste heat near 37 °C yielded a maximum generation of merely 218 mW. Other numerical and experimental investigations, such as those by citations operating under simulated vehicular cruising speeds, reported even lower outputs strictly in the microwatt range. These consistently minimal yields confirmed that solid state recovery operating under suboptimal low grade thermal boundaries struggled to overcome fundamental Carnot limitations.

Attempting to combine these independent recovery pathways into a single physical unit introduced severe internal thermal competition. Numerical investigations of dual systems, such as the multi pass finned tube and heat pipe heatsink configuration evaluated in the [105], indicated a total waste heat utilization of less than 1.6 % while generating marginal thermoelectric power. This extremely low utilization factor exposes a critical physical bottleneck. The inherently low mass flow rate of the reactant gas severely restricted its thermal absorption capacity, while the limited physical surface area of the thermoelectric modules restricts secondary electrical conversion.

Furthermore, synthesizing the methodologies listed in Table 2.1 revealed a heavy reliance on numerical simulations or idealized steady state mathematical models. While experimental test bench validations were present, they frequently utilised static convection rates that failed to replicate the highly transient aerodynamic cooling boundaries experienced during actual moving vehicle operation. Ultimately, this comparative analysis confirmed that while independent waste heat recovery mechanisms provided measurable theoretical benefits, their physical implementation in lightweight vehicles was severely restricted by thermodynamic boundaries. The prevailing reliance on steady state assumptions suggested that evaluating integrated recovery architectures strictly required a methodological shift toward dynamic on road physical testing. Moving beyond idealized mathematical models to capture the transient thermal lag and chaotic aerodynamic interference of actual driving environments

remained an absolutely necessary step to quantify the true viability of these complex thermal networks.

2.4.1 Overview of Heat Recovery Architectures: Organic Rankine Cycles, Cogeneration, and Solid-State Conversion

To elevate overall system efficiency, current WHR methodologies attempted to capture the thermal effluent of the PEM fuel cell and convert it into either functional secondary electricity or useful thermal work [106]. For thermodynamic electrical conversion, the ORC remained the most extensively modelled WHR architecture. Unlike traditional steam cycles, an ORC utilised organic working fluids with low boiling points, such as R123, R245fa, and R134a, to capture the low grade heat of the primary stack. To circumvent the inherent complexities of converting low grade heat back into electricity using secondary fluid loops, recent studies increasingly advocated for the direct thermal utilization of waste heat. In stationary and heavy duty domains, CCP architectures routed stack waste heat to drive absorption chillers, providing essential cooling capabilities. Conversely, CHP cogeneration systems directly repurposed the thermal effluent for critical BoP operations, such as passenger cabin climate control, preheating of incoming reactants, or facilitating hydrogen desorption from metal hydride storage tanks [99]. Furthermore, integrating PCM into the liquid cooling loop allowed excess operational heat to be stored as latent energy and subsequently discharged to preheat the stack during sub zero conditions. Empirical validations on a commercial scale 370 cell stack demonstrated that a PCM assisted cooling loop successfully sustained internal temperatures above 0 °C for 63.4 hours in −20 °C ambient environments, thereby accelerating subsequent cold startup times by 11.7% without drawing auxiliary electrical power [107].

Finally, for direct solid state conversion, TEG exploited the Seebeck effect to convert thermal gradients directly into electrical power, offering the architectural advantage of possessing absolutely no moving parts [88]. A comparative relational analysis of these distinct thermal management and WHR architectures was synthesized in Table 2.2 to highlight their operational boundaries.

Table 2.2
Comparative Analysis of Thermal Management and WHR Architectures

No	Architecture	Application Scale	Key Advantages	Major Limitations and Bottlenecks
1	Active Air Cooling [90]	2 to 5 kW	Low architectural complexity, lightweight, eliminates liquid coolant leak risks.	Low specific heat capacity of air (1.005 J/g°C) requires high volumetric airflow, causing severe parasitic blower power penalties.
2	Active Liquid Cooling [11]	> 5 kW (Automotive)	High specific heat capacity (4.186 J/g°C for water) provides a robust thermal buffer against load transients.	Introduces massive parasitic power loads from mechanical pumps and radiator fans and is prone to spatial temperature gradients.
3	Thermoelectric Generators (TEG) [88]	Micro to Low Power	Solid state conversion with no moving parts directly converts thermal gradients to electrical power.	Capped at 5 to 8% conversion efficiency for low grade heat, producing marginal yields of 5 to 20 W under a 40 to 50 °C gradient.
4	Organic Rankine Cycle (ORC) [82]	Mid to Large Scale	Extensively modelled thermodynamic conversion system capable of secondary electrical generation.	Bottlenecked by Carnot limits (4.7 to 7.4% efficiency) and introduces severe volumetric and mass penalties to the vehicle chassis.
5	Combined Heat and Power (CHP) [99]	Vehicle and System Level	Theoretically elevates overall energy utilization up to 90% and extends cold weather range by 11%.	Lack of dynamic physical on road validation, as over 70% of studies evaluate in strict steady state isolation.

2.4.2 Challenges in Low Grade Heat Recovery: Thermodynamic Bottlenecks and Spatial Constraints

Although the substantial thermal dissipation of a PEM fuel cell presented a theoretical opportunity for WHR, its practical implementation is severely constrained by fundamental thermodynamic bottlenecks [99]. The primary challenge originated from the intrinsically low grade nature of the thermal effluent. Because optimal stack performance is strictly restricted to a narrow thermal window of 60 to 80 °C to prevent membrane dehydration, the MTD between the heat source and the ambient environment is relatively small. As established by fundamental thermodynamic principles, this narrow temperature gradient strictly bounded the maximum recoverable work by the Carnot efficiency limit. Consequently, thermodynamic power cycles frequently struggle to achieve economic and operational viability in these low temperature regimes. Empirical validations and thermodynamic models of mid to large scale systems, such as a simulated 49.8 kW fuel cell stack, indicated that ORC systems utilising low boiling point organic refrigerants achieved a maximum thermal to electrical conversion efficiency of merely 4.7 to 7.4%. This typically resulted in a marginal absolute net system efficiency gain of only 2 to 3% [106].

Similarly, direct solid state energy conversion utilising TEG arrays faced profound inefficiencies when subjected to low thermal driving potentials. Experimental validations [9] utilising a 2 kW open cathode PEM fuel cell coupled with a TEG demonstrated that scavenging ultra low temperature waste heat, producing a 37 °C effluent, yielded a negligible maximum electrical output of just 218 mW. Even under idealized testing conditions leveraging a larger 40 to 50 °C temperature gradient. Current semiconductor materials typically capped TEG conversion efficiencies at 5 to 8% for low grade heat, generated a nominal 5 to 20 W of electrical power per module.

Beyond these strict thermodynamic limitations, integrating WHR architectures into lightweight vehicular platforms introduced severe spatial and parasitic mass penalties. The complex multi-phase fluid loops, evaporators, and condensers required for ORC systems, or the extensive surface areas mandated for TEG integration, significantly inflated the BoP volume and weight of the vehicle [82]. Comprehensive reviews revealed that over 70% of existing studies evaluated these thermal recovery subsystems in strict isolation under steady state boundary conditions [99]. Consequently, current models largely failed to capture the transient thermal inertia, localised flow maldistributions, and delayed temperature responses that manifested during the aggressive sub second load shifting characteristic of automotive drive cycles. Therefore, evaluating the true technical and economic viability of WHR architectures suggested a methodological shift toward physical dynamic on road testing frameworks capable of empirically validating these transient hydrothermal penalties, while rigorously acknowledging the physical uncertainties inherent to outdoor vehicular testing [108].

2.4.3 Heat Exchangers and Heat Pipes for Thermal Management

Contemporary literature increasingly investigated advanced heat exchangers and passive two phase architectures, predominantly focusing on heat pipes (HP), as an alternative for the severe parasitic electrical power penalties imposed by the mechanical pumps and radiator fans of conventional active cooling systems. By theoretically reducing parasitic pumping loads, these advanced components offered a more efficient thermal routing mechanisms. However, evaluating their integration into heavy duty vehicular stacks suggests that standalone passive components were frequently constrained by physical limits, necessitating highly optimised hybrid approaches [109].

2.4.3.1 Classification and Mechanisms of Heat Exchangers: Compact Architectures in Gas to Gas and Solid to Gas Transfer

Managing the stringent thermal boundaries of PEM fuel cells heavily rely on optimised compact heat exchanger architectures, especially since the MTD between the optimal 70 °C stack coolant and ambient air remain relatively small. The prevailing standard for high power automotive bulk heat rejection is the cross flow fin and tube radiator. Recent parametric optimizations focused on manipulating micro geometries, such as louvered fins. Which artificially disrupted boundary layers and maximized the convective heat transfer coefficient without inducing prohibitive aerodynamic pressure drops. For instance, Ionescu [93] evaluated the thermofluids performance of a louvered fin and tube radiator explicitly designed for an automotive liquid cooled stack. Operated under rigorous vehicular boundary conditions processing water glycol coolant flow rates of 1.0 to 2.0 L/min and frontal ambient air velocities up to 14 m/s, the study demonstrated that minimizing the louver pitch to fin pitch ratio maximizes the overall surface goodness factor.

However, as noted by D'Adamo et al. [110], modelling these complex multi scale finned structures computationally frequently required simplifying the radiator into a homogenized porous media. This methodological simplification represented a critical gap because it often obscured the localised micro scale thermal fluid maldistributions that occurred during the sudden ambient airflow changes characteristic of aggressive vehicular acceleration. Beyond primary liquid to air radiators, contemporary thermal management increasingly integrated specialized compact heat exchangers for gas to gas and solid to gas thermal transfer within WHR and reactant conditioning subsystems. Shell and tube or compact plate fin heat exchangers were frequently employed for transferring sensible exhaust heat directly into incoming reactant gases, thereby mitigating the risk of localised subcooling or condensation flooding at the cell inlets.

Furthermore, in solid state WHR applications, the heat exchanger architecture had to be intrinsically coupled with TEG arrays. While this highly integrated architecture theoretically maximized the interfacial heat flux necessary for driving the Seebeck effect. The immense volumetric and mass penalties associated with metallic plate fin blocks fundamentally restrict their deployment in lightweight space constrained vehicles. A prevailing limitation across the current heat exchanger literature is that most performance evaluations relied strictly on steady state boundary conditions.

This left their dynamic thermal inertia and delayed response times toward the high frequency thermal transients of real world driving cycles largely unvalidated. This confirmed that physical evaluations inherently carried experimental uncertainties and transient flaws that steady state models often ignored [97], [108].

2.4.3.2 Heat Pipe Integration for Enhanced Thermal Transport

Seeking a solution for the inherent thermal resistance of solid conductive materials and the severe parasitic power penalties of forced liquid cooling, contemporary literature increasingly investigated the integration of two phase HP arrays within PEM fuel cells. Operating on the thermodynamic principle of the latent heat of vaporization, a HP offers a nearly isothermal thermal transport mechanism [95]. Thermal energy at the active sites is absorbed at the evaporator section, causing the internal working fluid to vaporize. This vapor travels rapidly toward the condenser section where it releases the latent heat into a rejection sink or WHR zone before returning as a liquid via capillary action or gravitational forces. By theoretically reducing the equivalent thermal resistance into a fraction of that of solid copper or graphite, HP architecture served as highly efficient passive thermal bridges.

Recent structural optimizations focused on integrating micro HP arrays directly into the flow field plates, minimizing contact resistance and addressing localised thermal gradients. Empirical validations by Singh et al. demonstrated that mounting cylindrical HP arrays onto the bipolar end plates of a modified PEM fuel cell successfully reduced localised operating temperatures by 12 °C, simultaneously enhancing the hydrogen storage density of the integrated carbon electrode by 40% [73] [97]. Similarly, advanced numerical models indicated that hybridizing ultra thin HP arrays with conventional liquid cooling significantly homogenized the in plane temperature distribution across the MEA, suppressing the formation of isolated hot spots [92].

Beyond mere heat dissipation, heat pipes were increasingly deployed as critical thermal conduits within vehicular WHR networks. Tetuko et al. [5] experimentally validated the use of passive HP arrays that routed low grade stack waste heat directly into metal hydride storage canisters, demonstrated that rapid phase change transport successfully sustained the required endothermic hydrogen desorption rates without the parasitic burden of auxiliary electric heaters [81], [98]. In a micro scale solid state WHR

application, Saufi Sulaiman et al. coupled a 2 kW open cathode PEM fuel cell with an HP, heat sink, and TEG assembly. The study revealed that while the HP effectively scavenged ultra low temperature effluent, produced a 37 °C boundary condition. The thermodynamic limitations of the TEG yielded a marginal maximum electrical output of only 218 mW.

Despite their thermodynamic elegance, a relational analysis of the HP literature revealed significant methodological and practical gaps regarding automotive scalability. Most current studies evaluated HP performance under idealized steady state conditions, falling short at fully capturing the transient thermal lag and severe flow maldistributions that manifested during sub second load shifting. Furthermore, the operational envelope of an HP was strictly bounded by the capillary limit. Under the aggressive high density heat fluxes typical of heavy duty vehicular stacks exceeding 100 kW, the working fluid risked sudden dry out at the evaporator, which could trigger catastrophic thermal runaway. This highlighted that static laboratory models might not accurately predict the chaotic transient flaws inherent to dynamic on road applications.

2.4.3.3 Air as a Primary Heating and Cooling Medium: Convective Bottlenecks and Mobile Applicability

While active liquid cooling dominate high power automotive applications, ambient air remain extensively investigated as a primary thermal cooling medium, specifically within open cathode architectures or low to medium power PEM fuel cells typically rated under 5 kW [111]. Utilising air simultaneously as a reactant and a cooling medium offers architectural elegance by eliminating complex leak prone dielectric liquid loops and reducing overall system mass. However, current literature consistently identified severe thermodynamic and convective bottlenecks inherent to air cooled systems. Air possesses a fundamentally low specific heat capacity of approximately 1.005 J/g°C and a poor convective heat transfer coefficient relative to liquid media, therefore, maintaining the strict optimal operating temperature window strictly require excessive volumetric airflow rates during high current operation. Consequently, extracting massive heat fluxes purely via forced air convection imposed substantial parasitic power penalties from high capacity axial blowers, which directly reduced the net electrical output of the stack [112].

To mitigate these severe convective limitations, contemporary research increasingly focused on modifying internal flow field geometries to artificially enhance the heat transfer surface area. For instance, Merdjani and Kizilova [86] investigated the integration of advanced flow fields and porous metallic foams into the cathode channels. The study demonstrated that highly optimised geometric intrusions and tortuous metallic ligaments significantly amplified the convective heat removal efficiency, yielding a far more homogeneous temperature distribution across the active area compared to conventional parallel channels without exponentially increasing the compression work required by the fan.

Beyond heat rejection, air was also deployed as an active heating medium to combat sub zero transient challenges. During cold starts, the accumulation and subsequent freezing of product water within the porous GDL physically occluded oxygen transport, which can trigger rapid electrochemical failure. Experimental validations proved that preheating the incoming reactant air significantly elevated the localised thermal state of the GDL, thereby successfully delaying catastrophic ice crystallization and extending the operational envelope of the stack in sub zero environments [113]. Despite these architectural advancements, a relational analysis of the literature reveals a critical methodological gap. The heavy reliance on ambient air strongly coupled the internal hydrothermal stability of the fuel cell to highly volatile external environmental conditions, such as ambient temperature, air density, and relative humidity. Dynamic voltage responses were highly sensitive to the delayed thermal inertia of the air supply during sudden load changes [111]. Furthermore, over 70% of current studies evaluating air cooled or air heated enhancements relied strictly on steady state or mild step load boundary conditions, leaving their viability under the chaotic transient flaws of real world driving largely unvalidated [97].

2.4.4 Reactant Thermal Conditioning and Hydrogen Preheating

The profound temperature sensitivity of PEM fuel cells extended beyond the internal stack assembly to the thermal state of incoming reactants, particularly when subjected to sub zero operational environments [82]. Although the HOR at the anode was intrinsically orders of magnitude faster than the cathodic ORR, the thermal conditioning of incoming hydrogen remained a critical determinant of overall electrochemical efficiency. Contemporary thermodynamic models established that the

activation overpotential is highly sensitive to localised temperature gradients. When reactants enter the stack at ambient or sub zero temperatures without adequate preheating, they acted as a parasitic thermal sink that actively depressed the local temperature of the catalyst layer. As dictated by fundamental Butler Volmer kinetics, this localised subcooling exponentially decreased the exchange current density and elevated the activation energy barrier, culminating in a pronounced and immediate voltage drop.

When a vehicular stack was initiated below 0 °C, the product water generated by the ORR rapidly crystallized within the porous GDL and active catalyst sites [114]. To mitigate these kinetic losses and sub zero transient bottlenecks, current literature increasingly evaluated active reactant preheating methodologies. Zhan et al. [40] experimentally investigated various cold start preheating strategies on a 2 kW PEM fuel cell stack subjected to rigorous −10 °C and −20 °C ambient conditions. Their empirical validation revealed that while actively heating the incoming reactant air successfully elevated internal temperatures and prevented catastrophic phase change failures, utilising air preheating in isolation was thermodynamically slow due to the low specific heat capacity of air. Instead, combining reactant heating with direct end plate heating proved significantly more time efficient. Expanding on this, numerical investigations by Yang et al. indicated that synergistic reactant heating mitigated the severe in plane temperature gradients that otherwise exacerbated non uniform current distributions during a cold start [115].

Beyond the necessity of cold start mitigation, thermally conditioning reactants during standard operation presented a critical frontier for WHR and system level exergy optimization. Because 40 to 60% of the input chemical energy was inherently dissipated as low grade heat, repurposing this thermal liability to preheat incoming hydrogen and air significantly curtailed thermodynamic losses within the BOP. Furthermore, reactant thermal conditioning was deeply intertwined with hydrogen storage dynamics, particularly in systems utilising solid state MH canisters. Because the desorption of hydrogen from MH canisters was a highly endothermic process, it dictated a continuous thermal supply to maintain adequate fuel flow rates. Tetuko et al. experimentally simulated a symbiotic thermal loop utilised passive two phase heat pipes to route low grade PEM fuel cell waste heat directly to MH canisters [116]. Their results proved that phase change thermal bridging successfully sustained the requisite hydrogen discharge

rates without incurring the severe parasitic electrical penalties associated with auxiliary heaters.

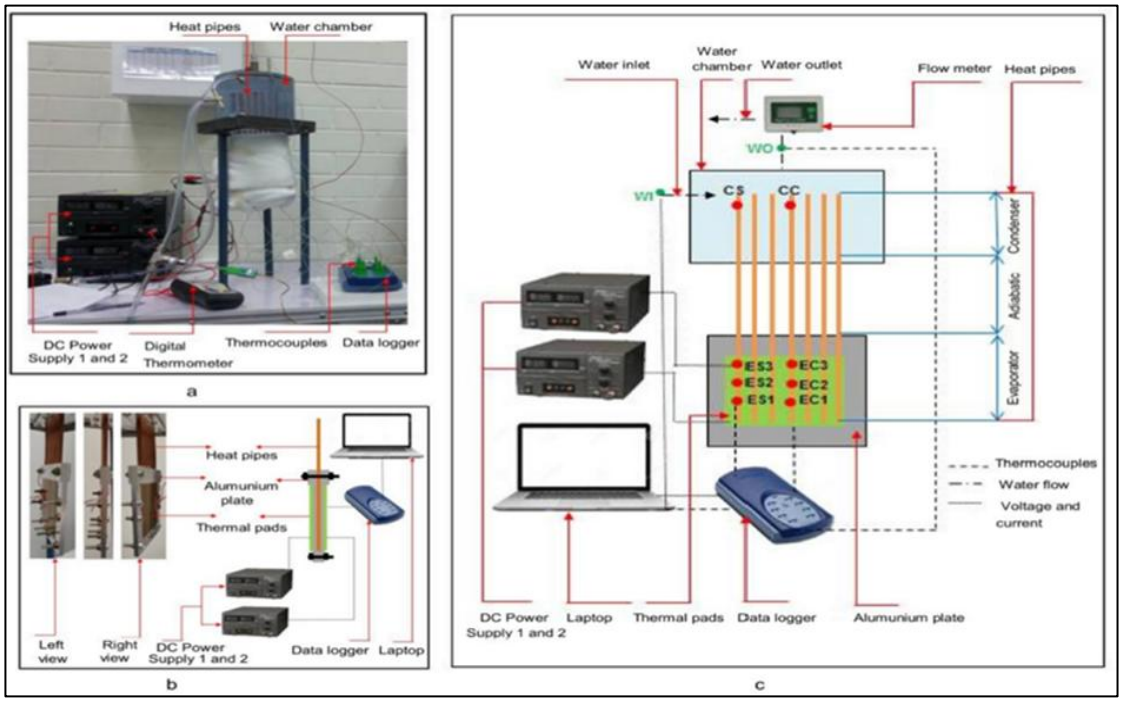

Figure 2.1 (a) Experimental Setup of an MH Canister Studying Hydrogen Discharge Rate Behavior With Heat Addition Mimicking the Heat Supplied by A Fuel Cell. (b) Schematic Diagram of the Experimental Setup Used to Study the Hydrogen Discharge Rate of the MH Canister Utilising Thermal Management [114]

Despite these architectural advancements in thermal coupling, a relational analysis of the current WHR and reactant conditioning literature exposed a profound critical gap. Synthesizing these findings revealed a methodological constraint were researchers frequently extrapolated specific heating rates from low power or isolated air cooled test benches directly to high power automotive architectures. Comprehensive reviews indicated that a vast majority of existing studies evaluated thermal recovery subsystems under strict steady state isolation [99]. This fundamentally failed to account for the dynamic thermal interdependencies of the hybrid powertrain, suggesting that evaluating reactant conditioning required a shift toward physical dynamic on road testing that inherently captures experimental uncertainties and environmental volatility.

2.4.4.1 Electrochemical Impact of Preheated Reactants: Kinetics and Voltage Drop Mitigation

Although the HOR at the anode of a PEM fuel cell was intrinsically orders of magnitude faster than the cathodic ORR, the thermal conditioning of incoming hydrogen remained a critical determinant of overall electrochemical efficiency. Contemporary thermodynamic models established that the activation overpotential, which represents the kinetic energy barrier required to initiate electrochemical reactions, was highly sensitive to localised temperature gradients at the triple phase boundaries. When reactants entered the stack at ambient or sub zero temperatures without adequate preheating, they acted as a parasitic thermal sink that actively depressed the local temperature of the catalyst layer. As dictated by fundamental Butler Volmer kinetics, this localised subcooling exponentially decreased the exchanged current density and elevated the activation energy barrier, culminating in a pronounced and immediate voltage drop.

To mitigate these kinetic losses, recent literature increasingly advocated for active reactant preheating, frequently achieved by routing low grade stack waste heat to the reactant inlet streams. The electrochemical benefits of hydrogen preheating were particularly pronounced during sub zero cold starts, where reactant thermal conditioning actively prevented catastrophic phase change failures. Experimental validations utilising 2 kW PEM fuel cell stacks subjected to rigorous −10 °C and −20 °C ambient conditions revealed that actively heating the incoming gases helped rapidly elevate internal stack temperatures, thereby preventing the freezing of product water that physically occludes the GDL and induced acute reactant starvation [113]. Expanding on this, numerical investigations by Yang et al. indicated that synergistic reactant heating mitigated the severe in plane temperature gradients that otherwise exacerbated non uniform current distributions during a cold start [115].

2.4.4.2 Previous Implementations and System Complexities: Flow Rate Dependencies and Thermodynamic Limitations

Although theoretical frameworks consistently advocated for the kinetic and operational benefits of reactant preheating, the practical implementation of these architectures introduced profound systemic complexities and physical constraints [82].

Contemporary empirical studies predominantly attempted reactant preheating through two primary pathways. These included active electric heating elements integrated directly upstream of the GDL, or passive heat exchangers that scavenged low grade thermal effluent from the primary cooling loop of the stack. However, synthesizing the results of these physical setups revealed severe thermodynamic limitations intricately tied to the fundamental thermo physical properties of the reactant gases.

Because ambient air possessed a critically low specific heat capacity of approximately 1.005 J/g°C and a fundamentally poor convective heat transfer coefficient, its ability to act as a rapid thermal vector was severely restricted [113]. Attempting to warm the stack strictly by preheating the incoming reactant air was thermodynamically sluggish because the low thermal mass of the gas flow was vastly insufficient to rapidly elevate the internal temperatures of the MEA before localised product water crystallized. Consequently, gas preheating had to typically be physically coupled with direct conductive end plate heating to achieve viable cold start times. Furthermore, extrapolating the efficacy of these gaseous heating mechanisms from low power open cathode models directly to high power liquid cooled automotive stacks remained methodologically uncertain. In a liquid cooled architecture, the massive thermal inertia of the bipolar plates and dielectric coolant vastly overshadowed the thermal capacity of the incoming air.

Crucially, the integration of reactant preheating subsystems introduced severe transient flow rate dependencies that were frequently underreported in the literature [81]. In fully integrated vehicular BoP setups, the mass flow rate of incoming reactants fluctuated violently in response to sub second driver load demands. During rapid transient acceleration, the sudden influx of high velocity cold reactants fundamentally outpaced the delayed thermal inertia of the upstream heat exchangers. This phenomenon induced temporary localised subcooling at the catalyst layer and triggered immediate voltage undershoots, emphasizing that dynamic testing frameworks were strictly necessary to capture these volatile physical interactions [97].

2.4.5 Thermoelectric Generators for Solid State Energy Recovery

Direct solid state energy conversion via TEG arrays represent an architecturally elegant WHR paradigm for PEM fuel cells. Exploiting the Seebeck effect, a TEG converts interfacial thermal gradients directly into electrical power without the parasitic

mechanical loads, complex fluid loops, or moving parts required by thermodynamic power cycles [88]. However, a critical synthesis of contemporary literature indicate that their empirical viability in lightweight vehicular platforms is fundamentally constrained by strict thermodynamic bottlenecks. Because optimal low temperature PEM fuel cells operated within a narrow thermal boundary of 60 to 80 °C, the MTD available to drive the TEG remain critically small. Consequently, current semiconductor materials typically capped thermal to electrical conversion efficiencies at a mere 5 to 8% for low grade heat. Veza noted that under an idealized 40 to 50 °C temperature gradient, a TEG module operating on a 70 °C PEM fuel cell stack generated a nominal output of only 5 to 20 W [88]. This underscored a physical limitation, suggesting that solid state recovery at suboptimal thermal boundaries yielded marginal returns that struggled to justify the integration cost and weight penalties at automotive scales.

To circumvent these inherent material inefficiencies, recent research increasingly focused on highly optimised polygeneration architectures. Rather than simply routing recovered power back into the electrical bus of the vehicle, Lan et al. [118] proposed a novel integrated system routing PEM fuel cell exhaust gas through TEG modules directly coupled to a water electrolysis cell, actively repurposing the recovered power for secondary hydrogen production [117]. Expanding on these dual mode architectures, researchers also investigated unitized regenerative fuel cells capable of alternating between power generation and water electrolysis within a single assembly. However, evaluating the performance and durability of vapor fed regenerative systems frequently revealed significant material degradation, suggesting that experimental uncertainties and structural flaws still hindered their long term viability in dynamic vehicular applications. Through multi objective parametric optimization, they demonstrated that tailoring the micro geometry of the thermoelectric legs, specifically optimizing the height to a range of 1.01 to 1.3 mm and the cross sectional area to 2.52 to 3.28 mm^2, could theoretically elevate the net output power by up to 39.4% compared to standard commercial modules. Furthermore, extracting sufficient heat to drive a TEG dictated the use of sophisticated heat exchanger networks. Gao et al. [119] theoretically modelled a setup where TEG elements are sandwiched directly within the walls of a compact plate fin heat exchanger to maximize the interfacial heat flux required to drive the Seebeck effect.

2.5 Computational Fluid Dynamics in Thermal System Design and Multi Physics Coupling

Because the internal operational environment of a PEM fuel cell was characterized by severe spatial constraints and optical opacity, empirical observation of localised thermal fluid phenomena remained profoundly limited. Consequently, Computational Fluid Dynamics (CFD) emerged as an indispensable methodological framework for elucidating the complex coupled thermal water electrical mechanisms governing stack performance [110]. Contemporary literature indicated a definitive transition from early lumped parameter zero dimensional (0D) or one dimensional (1D) models toward highly resolved three dimensional (3D) multi physics simulations utilising commercial finite element platforms. For instance, Tran et al. Developed a comprehensive 3D finite element model of a 5 cell PEM stack operating at current densities up to 1.0 A/cm², enabling precised spatial visualization of internal temperature gradients and theoretically validating that up to 76% of generated waste heat could be recovered via optimised coolant routing [91]. Similarly, Cao et al. utilised 3D CFD modelling to evaluate the integration of solid liquid PCM within metallic bipolar plates, demonstrating computationally that a PCM can sustain localised cooling effects for over 120 seconds post shutdown [107].

Despite the high spatial fidelity of isolated 3D CFD models, simulating a full scale high power automotive PEM fuel cell stack alongside its dynamic BoP introduced prohibitive computational overhead. To circumvent this bottleneck, recent researched increasingly advocated for 1D and 3D co simulation architectures. Huo et al. addressed this by developing an integrated framework to evaluate high precision simulations of large size stacks, demonstrating that complex thermal management architectures can be evaluated at the system level without the crippling computational cost of resolving every individual micro channel [120].

Nevertheless, a relational synthesis of the current CFD literature exposed a methodological gap regarding transient automotive dynamics. While steady state optimization of flow fields and cooling channels was extensively documented, simulating the aggressive sub second load shifting and severe thermal shocks characteristic of real world driving cycles remained exceptionally challenging [110]. Pushing these boundaries, Seddiq et al. Utilised high fidelity transient simulations to model a PEM fuel cell subjected to sudden thermal shocks, wherein the bipolar plate

walls experienced abrupt temperature drops to 10 °C for durations of 3 to 19 seconds [121]. The transient simulation captured a critical 15% degradation in current density alongside severe oxygen concentration depletion in the catalyst layer and localised liquid water saturation spikes that required over 4 seconds of recovery time.

While such advanced models provided unprecedented insight into transient penalties, scaling this level of transient multi-phase fidelity to a full scale automotive stack remained fundamentally constrained by current computational limits. Furthermore, it had to be acknowledged that numerical CFD simulations inherently carried experimental uncertainties and theoretical assumptions. Mathematical models often failed to capture the chaotic unpredictable flaws of real world environments, such as ambient wind shear, road vibrations, and sensor latency. Therefore, physical dynamic on road testing remained an indispensable methodology for validating the true operational viability of integrated thermal management systems.

2.5.1 Mathematical Modelling of Heat Exchangers: Numerical Approaches for Compact Geometries

Compact heat exchangers, such as louvered fin and tube radiators and plate fin structures, are characterized by highly intricate micro geometries and severe spatial constraints. Therefore, empirical visualization of localised thermal fluid phenomena remain exceptionally difficult. Consequently, mathematical and numerical modelling emerged as the prevailing methodological framework for predicting temperature distributions, pressure drops, and thermal transfer rates within the BoP. Historically, researchers relied on foundational one dimensional analytical tools, such as the Effectiveness Number of Transfer Units method, to evaluate bulk heat flux across these components. For example, Ionescu utilised this approach to conduct a parametric thermodynamic analysis of a cross flow louvered fin and tube radiator explicitly designed for a liquid cooled automotive PEM fuel cell stack [92].

To move beyond the limitations of bulk mathematical calculations and capture precise spatial thermal gradients, recent research increasingly employed 3D CFD and finite element modelling. Gao et al. applied this approach to a WHR subsystem, developing a numerical model wherein TEG elements were sandwiched directly within the walls of a compact plate fin heat exchanger [119]. Their high fidelity model mapped the localised interfacial heat flux transferred from the high temperature exhaust gas to

the semiconductor legs, mathematically validating the specific geometries required to maximize the Seebeck driving potential.

2.5.2 Validating Fuel Cell Thermal Models: CFD Capabilities and Inherent Numerical Uncertainties

Despite these highly resolved diagnostic capabilities, a critical synthesis of the modelling literature revealed that numerical thermal predictions were intrinsically bounded by the severe simplifying assumptions required to achieve computational convergence. As D'Adamo et al. critically highlighted, achieving time efficient 3D simulations of multi phase transport frequently mandated treating the GDL and catalyst layers as homogenized isotropic porous media [110]. This foundational mathematical assumption fundamentally failed to capture the true anisotropic complexity of compressed carbon fibres and localised polytetrafluoroethylene distributions. This inevitably introduced significant theoretical uncertainties regarding actual liquid water accumulation and localised thermal contact resistance. Consequently, a numerical model might accurately predict the bulk temperature gradient of a multi cell stack while entirely obscuring micro scale thermal fluid blockages that could trigger catastrophic failure in a physical prototype.

Furthermore, the prevailing methodology for validating these CFD models exposed a profound systemic gap. As established by Xie et al. [122], the historical reliance on validating computational domains solely against macroscopic steady state polarization curves was methodologically insufficient. A computational model could mathematically replicate a bulk 100 kW polarization curve through fortuitous parameter cancellation while entirely misrepresenting the internal spatial distributions of ohmic resistance and localised temperature gradients. To bridge the widening gap between idealized numerical predictions and the highly volatile realities of vehicular operation, recent scholarship increasingly advocated for digitally assisted surrogate modelling combined with rigorous multi parameter validation [120]. However, these computational frameworks must always be paired with an acknowledgment that mathematical models inherently carried physical flaws and could not perfectly simulate environmental noise.

2.6 Experimental and Dynamic Testing Protocols for Fuel Cells

To accurately capture the profound electro thermal and hydrothermal transients inherent to vehicular applications, evaluating the true technical and economic viability of PEM fuel cells strictly required moving beyond idealized steady state boundary conditions. Consequently, contemporary empirical frameworks increasingly relied on standardised dynamic testing protocols, such as the Fuel Cell Dynamic Load Cycle derived from the NEDC, and the WLTC [123]. Long term empirical validations utilising dynamic load cycles on single PEM setups, often subjected to continuous testing exceeding 3000 transient cycles, revealed that aggressive load shifting fundamentally altered the internal degradation landscape. This precipitated irreversible voltage decay that steady state models systematically fail to predict. However, conducting real time lifespan testing to meet the heavy duty automotive target of 25,000 to 30,000 hours was economically and temporally prohibitive.

To circumvent this logistical bottleneck, researchers frequently employed Accelerated Stress Tests (AST) designed to artificially intensify the specific hydrothermal and mechanical stressors experienced during dynamic operation. For example, Thiele et al. [123] formulated an operation condition dependent load profile optimization by adapting the WLTC into a realistic AST. By subjecting commercial PEM fuel cell stacks to this optimised AST under variable cathode air inlet relative humidities, the study successfully accelerated the manifestation of mass transport resistance and platinum dissolution, recording severe degradation rates at high current densities in merely 173 hours. Similarly, Birkner et al. [124] developed a dynamic AST coupling varying temperature, humidity, and load shifts capable of aging a commercial MEA to its end of life state within 1000 hours.

While Accelerated Stress Tests are useful for quickly evaluating materials, comparing different global testing standards indicate that performance degradation depends heavily on how long the fuel cell operates at maximum power [125]. This revealed a major testing limitation. Utilising data from short 1000 hour laboratory tests to predict a 30,000 hour lifespan in unpredictable real world environments proved mathematically unreliable and experimentally uncertain. Furthermore, isolating the micro scale transient phenomena during these high frequency load shifts revealed severe internal flow maldistributions. Experimental characterizations of water gas heat synergistic transport by Luo et al. [78] demonstrated that subjecting a PEM fuel cell to

an abrupt transient current load step, shifting from 800 to 1400 mA/cm² at 65 °C under zero backpressure, triggered acute localised reactant gas starvation. The sudden influx of current outpaced the delayed mass transport of the gas supply, driving the minimum reactant gas concentration in the anode and cathode catalyst layers down to critically low levels. This induced immediate voltage undershoots and exacerbated localised membrane dehydration, conclusively proving that observing the physical realities of transient loading was necessary for validating next generation thermal recovery architectures.

2.6.1 Controlled Laboratory Bench Testing: Polarization Curve Extraction and Steady State Thermal Mapping

To establish the foundational electrochemical and thermal boundaries of PEM fuel cells, contemporary empirical research relied heavily on controlled laboratory bench testing. The primary diagnostic tool utilised across these experimental setups was the extraction of macroscopic steady state polarization curves. Standardised testing protocols, such as those established by the United States Department of Energy Fuel Cell Technical Team, dictated rigorous steady state data collection procedures. Under these protocols, operational variables such as an 80 °C cell control temperature, precisely metered inlet dew points, and absolute outlet pressures were strictly regulated while the current density was incrementally stepped and stabilized. While the resultant polarization curves were indispensable for quantifying bulk activation, ohmic, and mass transport overpotentials under idealized conditions, a critical synthesis of the literature indicated that relying solely on these macroscopic outputs might fundamentally obscure localised internal phenomena. As Xie et al. established, validating computational models strictly via bulk polarization curves was methodologically flawed because a model can mathematically replicate a macroscopic output while entirely misrepresenting the internal spatial distributions of localised temperature gradients and ohmic resistance [122].

To circumvent the limitations of bulk data extraction and achieve higher spatial resolution, researchers increasingly integrated steady state thermal mapping methodologies within customized Fuel Cell Test Stations (FCTS). Because the opaque nature of standard metallic or graphite bipolar plates prevented direct internal observation, specialized test benches frequently employed modified transparent cell

architectures coupled with high resolution infrared thermography. For instance, Arif utilised an in house FCTS to simultaneously map liquid water accumulation and temperature distribution across the active area [126]. By replacing standard end plates with thinned transparent polycarbonate materials, the study successfully visualized severe localised temperature stratifications and water flooding under varied reactant flow rates. Similarly, Meyer et al. conducted combined current and electro thermal performance mapping on an air-cooled open cathode PEM fuel cell [127]. Their steady state thermal mapping revealed that localised temperatures consistently peaked near the cathode outlet due to the cumulative effects of reactant depletion, exothermic water formation, and inadequate convective cooling.

Despite these advancements in spatial diagnostics, a relational analysis of the laboratory testing literature exposed a methodological gap regarding transient vehicular applicability. Most standard bench tests and thermal mapping experiments were conducted under highly controlled steady state boundary conditions or utilised slow incremental step load changes to allow internal heat and mass transfer to reach equilibrium [126]. These static frameworks frequently failed to capture the high frequency thermal shocks, severe localised subcooling, and transient liquid water saturation spikes that manifested during the aggressive sub second load shifting characteristic of real world automotive drive cycles.

2.6.2 Dynamic Drive Cycles and Real World Environmental Effects: Transient Loads and Convective Variables

Transitioning from highly controlled steady state laboratory bench testing to establishing the true technical and economic viability of vehicular PEM fuel cells fundamentally depended on analysing their resilience to real world transient loads. Long term empirical validations, such as the dynamic durability test conducted by Zuo et al. [128] utilising over 3000 transient cycles on a single cell, revealed that aggressive transient loading induces severe irreversible voltage degradation. Specifically, their data demonstrated that repetitive cycling triggered significant localised voltage drops, primarily driven by sub second reactant starvation and rapid fluctuations in membrane hydration. Similarly, Thiele et al. adapted the WLTC into a condensed AST for commercial stacks, empirically proving that dynamic vehicular cycling drastically accelerated mass transport resistance and catalyst dissolution [123]. However,

synthesizing these foundational studies exposed a systemic methodological constraint. Most of these standardised dynamic cycles were executed within strictly controlled climatic chambers. Consequently, they mathematically and physically decoupled the electrical load transients of the stack from the highly volatile stochastic external environmental conditions the powertrain inherently faced on the road.

In practical automotive applications, the stability of the TMS and subsequent WHR potential were continuously perturbed by fluctuating ambient variables, most notably varying ambient temperatures and vehicle speed dependent convective airflows. During actual driving conditions, the frontal ram air velocity directly modulated the heat rejection capacity of the primary vehicle radiator, introducing a highly transient convective boundary that steady state models failed to capture. Han and Yu [129] highlighted this critical dependency through a ram air compensation analysis, demonstrating mathematically that vehicle aerodynamics and dynamic speed shifts fundamentally dictated the localised response times of the cooling loop and the parasitic power consumption of the coolant pumps and fans.

Furthermore, Katayama et al. [48] explored the evolution of MEA degradation through actual driving tests, confirming that volatile ambient temperatures severely disrupted the maximum power point of the stack and exacerbated catalyst degradation during sudden start stop events. The vulnerability of the thermal network was particularly pronounced under extreme climatic boundaries. Empirical chassis dynamometer testing of a commercial fuel cell vehicle by Lohse-Busch et al. across a drastic ambient spectrum of −18 °C to +35 °C illustrated the profound non linear impact of ambient thermal boundaries on net system efficiency and BoP parasitic loads.

2.7 Summary and Research Gaps: Toward Integrated Dynamic Validation

The transition toward sustainable energy systems positioned PEM fuel cells as a primary zero emission powertrain for heavy duty and lightweight vehicular applications. However, this comprehensive review of the literature revealed that the true technical and economic viability of these systems remained fundamentally bottlenecked by the complex multi physics interplay between thermal management, mass transport, and transient vehicular loads.

A critical synthesis of the thermal management and WHR literature demonstrated that the pursuit of elevated system efficiency was severely constrained by

the intrinsically low grade nature of PEM fuel cell thermal effluent. Because optimal stack performance and membrane hydration strictly dictated a narrow operating temperature window of 60 to 80 °C, the MTD between the fuel cell and the ambient environment was relatively small. Consequently, thermodynamic power cycles, such as the ORC, and solid state TEG architectures were strictly bound by Carnot limitations. Current semiconductor materials utilised in TEG arrays capped thermal to electrical conversion efficiencies at merely 5 to 8% for low grade heat. The reviewed literature consistently indicated that while these WHR architectures provided marginal absolute efficiency gains, their integration introduced severe volumetric, gravimetric, and parasitic mass penalties that were mathematically difficult to justify within space constrained lightweight vehicular chassis.

Furthermore, evaluating the diagnostic tools utilised to optimise these complex thermal networks exposed a profound reliance on computational homogenization. While 3D CFD models provided unprecedented spatial resolution of internal temperature gradients, achieving time efficient simulations frequently mandated treating complex geometries, such as compact heat exchanger fins or porous GDL structures, as isotropic homogenized media [46]. This mathematical necessity inherently obscured the localised micro scale thermal fluid maldistributions and transient flow blockages that triggered catastrophic cell failure during physical operation.

Most importantly, a relational analysis of the experimental and dynamic testing literature revealed the most critical methodological gap hindering commercialisation. Comprehensive reviews highlighted an overwhelming segregation of subsystem evaluation, where over 70% of current studies evaluated thermal management and reactant conditioning subsystems in strict steady state isolation. This fundamentally ignored the dynamic interdependencies of hybrid powertrains. Even when researchers employed standardised dynamic load profiles, such as the WLTC, these tests were overwhelmingly executed within highly controlled laboratory climatic chambers [81].

While high frequency step load changes had been empirically proven to induce localised reactant gas starvation and severe voltage undershoots, these laboratory bench tests mathematically decoupled internal electrochemical transients from external stochastic environmental variables. In real world applications, fluctuating ambient temperatures and variable ram air velocities directly dictated the parasitic load of the cooling pumps and the delayed thermal inertia of the BoP [99]. Therefore, evaluating

the true viability of advanced thermal recovery architectures strictly required a methodological shift toward physical dynamic on road testing. Future research had to embrace the chaotic transient flaws inherent to outdoor vehicular environments to capture the integrated hydrothermal penalties that idealized laboratory models systematically failed to predict.

CHAPTER 3
RESEARCH METHODOLOGY

3.1 Introduction

This chapter systematically details the methodology utilised to elevate the integrated heat recovery architecture from a mathematical concept to a validated vehicular application for a low temperature open cathode polymer electrolyte membrane fuel cell. The overarching research framework, illustrating the progression from conceptual formulation to environmental demonstration, was structured across three overarching scientific pillars encompassing eight distinct operational phases. This sequential progression is comprehensively mapped in Figure 3.1a) detailing the master methodology fishbone diagram and b) illustrating the research methodology flowchart. The research flow was deliberately designed to progressively increase empirical rigor and thermodynamic complexity, fundamentally recognising that transitioning from idealised mathematical models to physical vehicular reality inherently introduces compounding experimental uncertainties, transient thermal lag, and unavoidable thermodynamic leakages.

The initial segment of the methodology, encompassing Phase 1 and Phase 2, focused strictly on theoretical design and computational boundaries. This first pillar directly addressed the complex problem of thermal partitioning, with the primary objective of balancing internal reactant heat absorption against the secondary thermoelectric generator temperature difference. The approach evaluated four preliminary geometries utilising one dimensional thermal resistance networks and three dimensional steady state computational fluid dynamics simulations. By establishing numerical stability and executing a mathematical model cross verification, this phase culminated in an optimised, mathematically bounded technological concept, formally achieving technology readiness level (TRL) 2. While this phase provided a foundational design, it is cautiously acknowledged that these numerical models relied on idealised boundaries, completely omitting physical contact resistances and real world manufacturing imperfections.

Upon achieving numerical alignment, the methodology transitioned into the second pillar, spanning Phase 3 through Phase 6, which governed the physical test bench

validation. This intermediate stage necessitated the rigorous physical fabrication of the optimised computational geometry, precise sensor instrumentation, systematic pretesting for instrument calibration, and the finalisation of the steady state laboratory experimental protocols. By subjecting the fabricated architecture to steady state electrical sweeps and mechanically simulated convective cooling, a physical empirical baseline was established to quantify the reduction in activation polarisation and the generation of secondary power. Successfully validating the physical components within a controlled laboratory environment advanced the system to TRL 4. However, as established in the study limitations, the data acquired during this phase inherently absorbed minor physical machining defects, localised thermal contact resistances, and instrument resolution limits.

Finally, the methodology culminated in the dynamic on road evaluation pillar, encompassing Phase 7 and Phase 8. This advanced phase shifted the physical integrated heat recovery system onto a mobile 2 kW fuel cell buggy platform. The sequence required the physical pre commissioning of the prototype onto the vehicular chassis, crossing the TRL 5 threshold by ensuring environmental and mechanical stability. This was sequentially followed by formal on road driving evaluations utilising constant speed tests with variable weight loadings and tracking performance across a scaled dynamic New European Driving Cycle (NEDC) route. This final phase specifically investigated the dynamic limitations of the architecture, primarily focusing on the inherent mass flow bottlenecks of the hydrogen reactant and the transient thermal saturation experienced during prolonged continuous driving. By explicitly mapping the dynamic thermodynamic limitations within this simulated relevant environment, the integrated architecture successfully achieved TRL 6. It was strictly emphasised that the empirical data collected during this phase was subjected to severe environmental noise, unpredictable external aerodynamic turbulence, and unavoidable human driver inconsistencies.

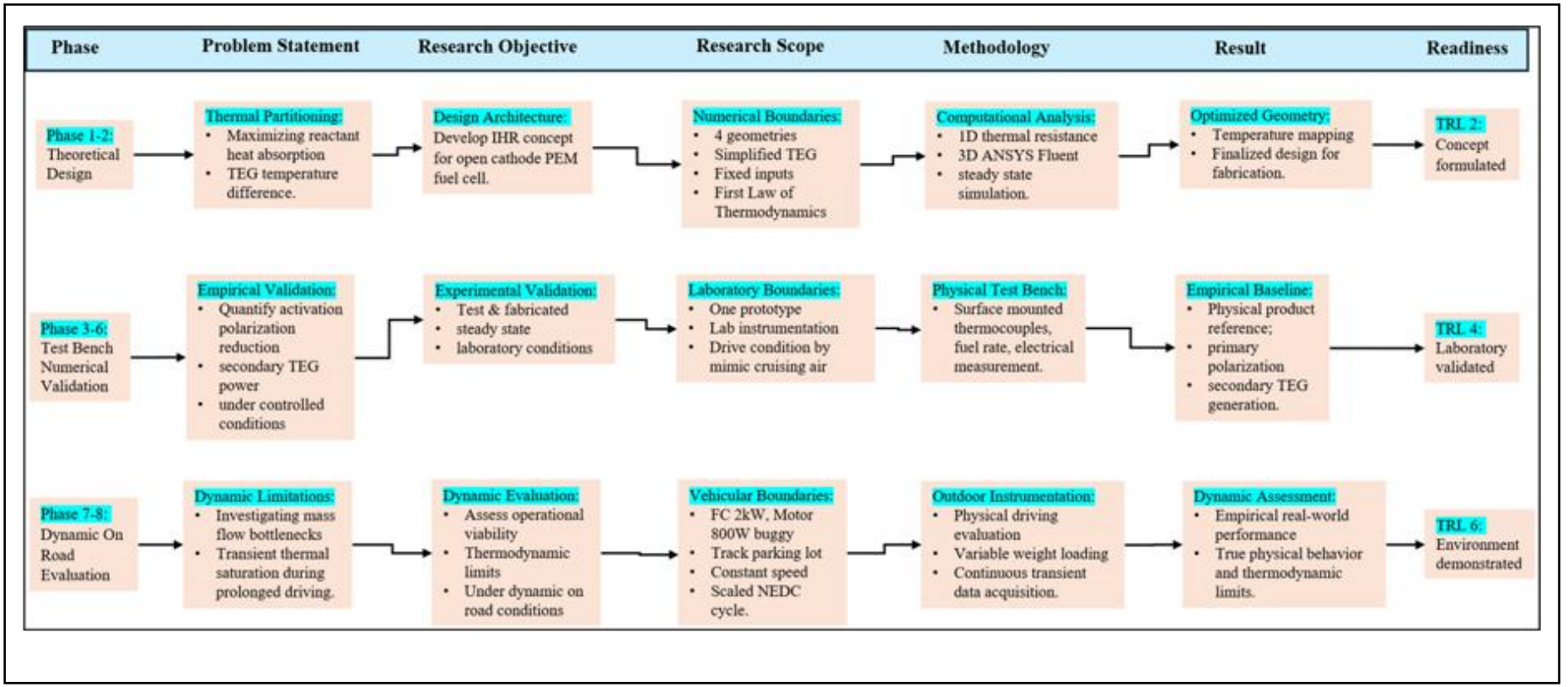
Phase
Problem Statement
Research Objective
Research Scope
Methodology
Result
Readiness
Phase 1-2: Theoretical Design
Thermal Partitioning:
• Maximizing reactant heat absorption
• TEG temperature difference.
Design Architecture:
Develop IHR concept for open cathode PEM fuel cell.
Numerical Boundaries:
• 4 geometries
• Simplified TEG
• Fixed inputs
• First Law of Thermodynamics
Computational Analysis:
• 1D thermal resistance
• 3D ANSYS Fluent
• steady state simulation.
Optimized Geometry:
• Temperature mapping
• Finalized design for fabrication.
TRL 2: Concept formulated
Phase 3-6: Test Bench Numerical Validation
Empirical Validation:
• Quantify activation polarization reduction
• secondary TEG power
• under controlled conditions
Experimental Validation:
• Test & fabricated
• steady state
• laboratory conditions
Laboratory Boundaries:
• One prototype
• Lab instrumentation
• Drive condition by mimic cruising air
Physical Test Bench:
• Surface mounted thermocouples, fuel rate, electrical measurement.
Empirical Baseline:
• Physical product reference;
• primary polarization
• secondary TEG generation.
TRL 4: Laboratory validated
Phase 7-8: Dynamic On Road Evaluation
Dynamic Limitations:
• Investigating mass flow bottlenecks
• Transient thermal saturation during prolonged driving.
Dynamic Evaluation:
• Assess operational viability
• Thermodynamic limits
• Under dynamic on road conditions
Vehicular Boundaries:
• FC 2kW, Motor 800W buggy
• Track parking lot
• Constant speed
• Scaled NEDC cycle.
Outdoor Instrumentation:
• Physical driving evaluation
• Variable weight loading
• Continuous transient data acquisition.
Dynamic Assessment:
• Empirical real-world performance
• True physical behavior and thermodynamic limits.
TRL 6: Environment demonstrated

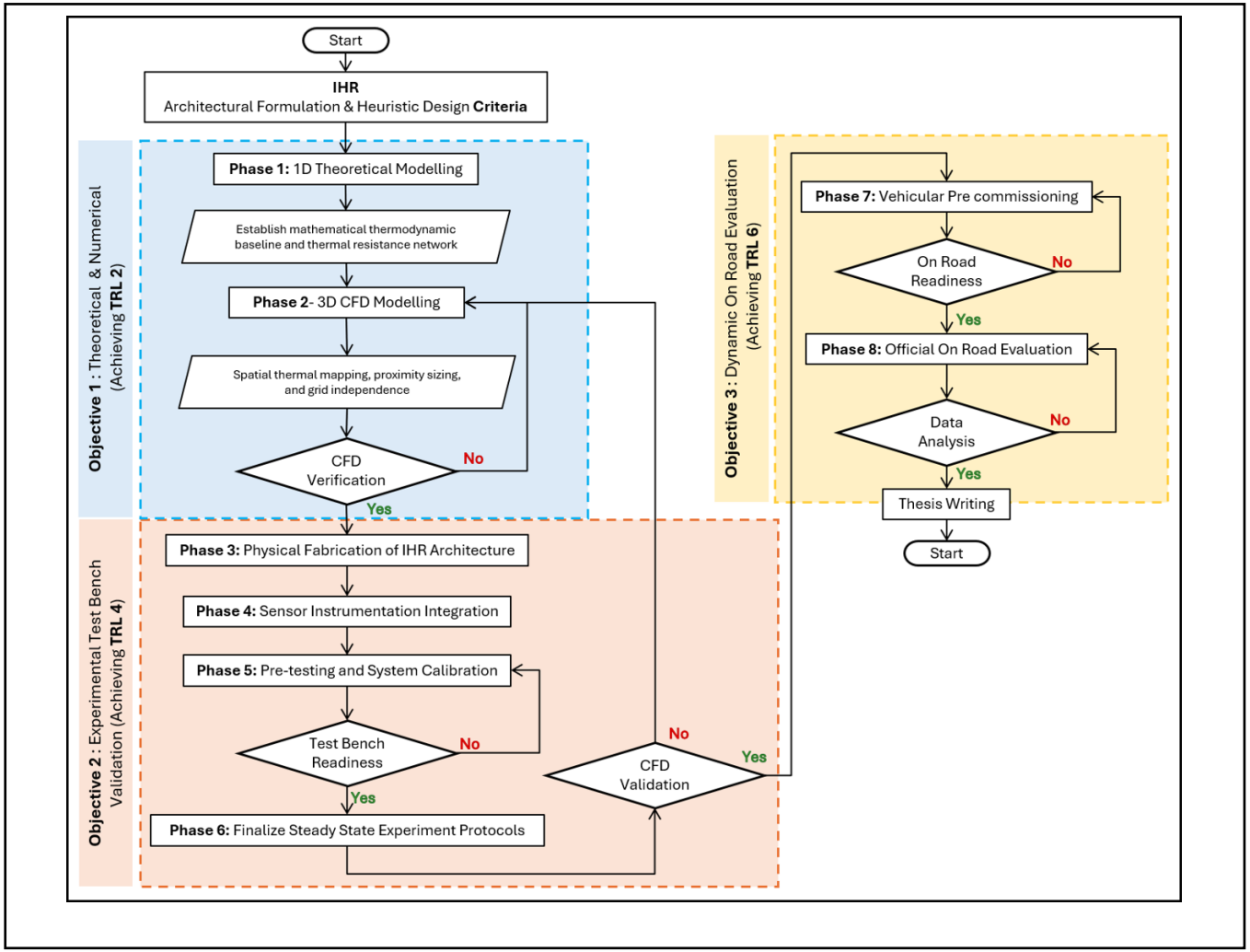

Figure 3.1 Master Methodology (a) Fish Bone Diagram (b) Flowchart

3.1.1 Methodological Novelty and Empirical Contributions

The primary empirical contribution of this methodology resided in the physical fabrication and evaluation of a combined waste heat recovery architecture. This novel system simultaneously preheated the incoming hydrogen fuel reactant and utilised solid state TEG modules as an additional secondary power producer. Previous methodologies typically evaluated these thermal recovery pathways in strict isolation. Conversely, this research deliberately integrated them into a single synergistic unit. Consequently, the methodology rigorously evaluated the complex thermal sharing dynamics, demonstrating that a single low grade waste heat stream could successfully sustain dual recovery functions despite inherent thermodynamic leakages and experimental uncertainties.

Furthermore, the methodology bypassed the limitations of relying on a singular validation tool by forcing the conceptual design through a rigorous chronological pipeline. The architecture was sequentially evaluated through one dimensional mathematical modelling, three dimensional computational fluid dynamics, and steady state physical test bench validation. This multistage cross verification framework explicitly bridged the critical gap between idealised numerical assumptions and actual physical manufacturing realities. It formally acknowledged that computational models frequently obscured minor machining defects, physical flaws, and localised thermal contact resistances that manifest during physical prototyping.

Ultimately, the methodology distinguished itself from standard literature by transitioning the physical integrated system out of a highly controlled indoor climatic chamber and mounting it directly onto a mobile 2 kW PEM fuel cell buggy. This dynamic on road vehicular validation safely exposed the novel architecture to stochastic real-world variables, including unpredictable aerodynamic turbulence, mechanical vibrations, and transient driver load shifts. By systematically mapping the thermodynamic limitations within this volatile relevant environment, the methodology successfully demonstrated the technology at TRL 6. This rigorous approach captured the chaotic experimental uncertainties and transient thermal flaws that standard steady state laboratory methodologies fundamentally failed to predict.

3.2 Mathematical Modelling and Numerical Methodology (Achieving TRL 2)

The first phase of the methodology was initiated by this section. A detailed mathematical formulation and numerical investigation of the IHR were conducted. The sequential approach was initiated through the establishment of strict heuristic design criteria to physically bound the geometry prior to any mathematical modelling. Following this architectural formulation, a fundamental one-dimensional analytical model was developed to estimate the baseline thermodynamic potential. Subsequently, three-dimensional computational fluid dynamics simulations captured the complex spatial thermal distribution. Cross-verifying both mathematical approaches provided the numerical stability to confirm design viability, achieving TRL 2 prior to manufacturing.

3.2.1 Design Criteria and Architectural Baseline

The methodology's foundational phase first established a novel conceptual baseline for simultaneous hydrogen fuel preheating and direct secondary electrical power production. To bypass exhaustive computational parametric sweeps for internal micro dimensions, commercial off the shelf component constraints systematically bounded geometric development. Consequently, strict heuristic design criteria dictated by primary power plant operational limits and lightweight vehicular kinetic constraints defined the architectural baseline. Derived from these constraints, the fundamental system concept (Figure 3.2) comprised distinct primary heating and secondary cooling chambers. The heating architecture adapted a compact, multiple-tube pass finned heat exchanger to capture hot fuel cell exhaust. Conversely, the cooling heat exchanger utilised a solid copper block with embedded heat pipes and extended aluminium fins, relying entirely on ambient cruising air. Centrally sandwiched solid-state TEG modules continuously exploited the temperature differential between the exhaust and ambient environments.

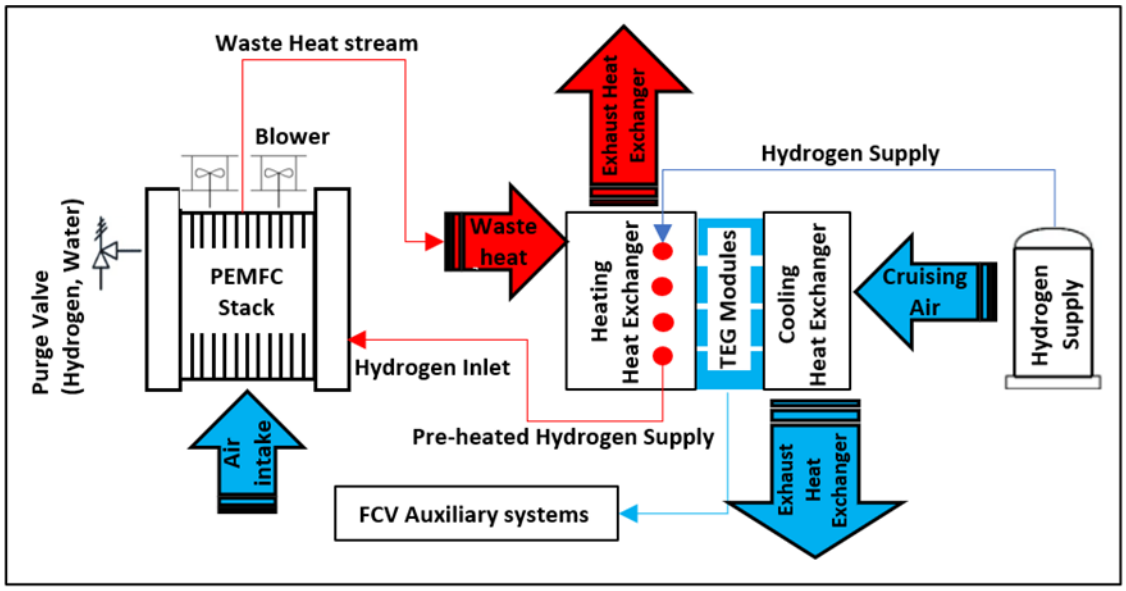

Figure 3.2 Schematic Diagram of the IHR System Concept

This integrated recovery concept was specifically formulated for implementation on a lightweight buggy platform operating at a nominal maximum cruising speed of approximately 10 km/h (2.78 m/s). The designated primary power plant for this application was a commercial 2000 W open-cathode PEM fuel cell. The physical and operational specifications of this specific stack, as detailed in Table 3.1, dictated the absolute thermodynamic boundaries of the available waste heat.

Table 3.1
Specifications of the Selected PEM Fuel Cell

Parameter	Specification
Fuel Cell Type	Open cathode, air cooled
Manufacturer	Horizon
Maximum Power Output	2000 W
Number of Cells	48 cells
Maximum Operating Temperature	65°C
Physical Dimensions (H x W x L)	35 cm x 31 cm x 18.5 cm

Guided by the operational limits of this selected fuel cell, specific engineering design criteria were established, as outlined in Table 3.2. These specific parameters were not selected arbitrarily rather they were derived from a combination of established operational boundaries and theoretical thermodynamic limits to ensure practical physical viability.

Table 3.2
Integrated Heat Recovery System Design Criteria

Parameters	Unit	Stack Power (2000W)
Open-cathode PEM fuel cell	kW	2
Fuel cell Exit air Velocity	m/s	2.4-3.23
Fuel cell Exit air temperature (waste heat)	°C	23-65
Hydrogen Preheating Target	°C	10
Hydrogen outlet temperature target	°C	29 - 53
Target fuel cel Output Power Increment (from hydrogen preheating)	%	4 – 8
Number of TEG cells	cells	<12
Target Thermoelectric Generation	W	< 3
IHR Heat Exchanger type for heating	-	Compact multiple tube pass-finned
IHR Heat Exchanger type for cooling		Copper plate embedded heat pipe with fins
Target Energy utilization	%	1-3

Operational limits of the selected 2 kW open-cathode stack dictated the primary thermodynamic boundary. While it provided sufficient traction power for a lightweight mobility platform, this open-cathode architecture inherently restricted waste-heat properties. Exit air velocity ranged strictly between 2.0 and 2.5 m/s, yielding fluctuating exhaust temperatures of 23 to 65 °C. Because this represented an ultra-low-grade thermal source at low convective velocities, the architectural baseline mandated a compact, multiple-tube pass finned heat exchanger. This geometry maximised the surface-area-to-volume ratio required to capture sensible heat within the confined vehicular chassis.

For reactant conditioning, the primary recovery objective aimed to elevate the incoming hydrogen temperature. The design specified a modest 10 °C preheating increment, yielding an absolute outlet target between 29 °C and 53 °C. This thermal limit lowered internal activation energy barriers and improved reaction kinetics without risking localised membrane dehydration. [17]. By targeting this conservative thermal rise, the system attempted to secure an analytical primary electrical power increment of 4 to 8 % while strictly preserving the long-term hydration stability of the internal polymer membrane.

To further maximise the utility of the captured waste heat, the architecture incorporated secondary solid-state thermoelectric generation. The physical criteria limited the inclusion to fewer than 12 TEG modules, ensuring adequate physical surface area for heat absorption while preventing excessive spatial expansion. The target for the mathematical model's generation was established to exceed 5 W of continuous

secondary power. While small in absolute magnitude, recovering this 5 W passively provided sufficient electrical energy to sustain auxiliary balance of plant components, such as microcontrollers or diagnostic sensors. Generating this auxiliary power entirely from waste heat prevented additional parasitic loads from draining the primary traction battery.

Finally, acknowledging the inherent flaws and thermodynamic limitations of passive recovery mechanisms, the comprehensive target for overall waste heat utilisation was established strictly between 1 and 3 %. Although mathematical models frequently projected higher recovery efficiencies, this cautious target explicitly reflected the severe physical bottlenecks present in vehicular applications. The absolute thermal absorption capacity was fundamentally bottlenecked by the extremely low mass flow rate of the hydrogen reactant gas. Furthermore, physical vehicular operation introduced unavoidable conductive thermal losses and contact resistances across the heat exchanger assemblies. Setting this conservative target provided a highly realistic, physically grounded engineering baseline to evaluate the subsequent computational optimisations and dynamic on-road validations.

3.2.2 Geometric Specifications of the Evaluated Architectures

By locking the foundational physical constraints and conceptual design baseline established in the previous section, four distinct geometric iterations were subsequently developed. These four conceptual designs represented a bounded comparative matrix. Rather than relying on infinite analytical software sweeps, these geometries were formulated heuristically to ensure practical physical manufacturability, utilising standard off-the-shelf material dimensions.

The geometric variations across the four designs focused exclusively on altering the macroscopic internal flow paths, the spatial arrangement of the semiconductor modules, and the balance between the heating and cooling surface areas to identify the optimal thermal equilibrium. Each iteration was deliberately configured to test a specific thermodynamic priority:

- **Design 1 (Maximized TEG Capacity):** This architecture prioritizes secondary electrical generation by maximizing the semiconductor footprint, incorporating 12 TEG cells and a balanced six pass internal routing.

- **Design 2 (Maximized Thermal Transfer):** This iteration focuses on maximizing both the primary heat capture and the secondary heat rejection. It utilised the largest primary heatsink surface area and an extended eight pass tube configuration to maximize fluid residence time in the heating chamber. Simultaneously, it integrates 24 solid heat pipes within the cooling chamber to aggressively draw heat away from the semiconductor cold side.
- **Design 3 (Maximized Cold Side Dissipation):** To artificially force a steeper thermal gradient across a reduced number of TEG cells, this design prioritizes the secondary cooling domain, deploying a massive cooling fin surface area to rapidly reject heat into the ambient air.
- **Design 4 (Compact Lightweight Baseline):** Acting as the spatially constrained control, this design mirrors the internal configuration of Design 3 but significantly reduces the external cooling fin mass to evaluate the thermodynamic penalty of prioritizing a lightweight vehicular footprint.

To ensure absolute transparency and reproducibility of the subsequent numerical evaluations, the specific physical dimensions distinguishing these four heuristic IHR architectures were summarized in Table 3.3. These macroscopic geometric parameters served as the unyielding physical boundaries for both the one-dimensional mathematical thermal network and the three-dimensional CFD modelling.

Table 3.3
Summary of Macroscopic Geometric Specifications for the Four Evaluated Architectures

IHR Parameters	Design 1	Design 2	Design 3	Design 4
Overall system size mm width x length x thickness	530 x 265 x 82	300 x 300 x 96	250 x 171 x 154	250 x 171 x 154
Num. Heatsink fins	29	34	29	29
Tubes Pass	6	8	4	4
Num. Heat Pipes	8	24	15	15
Num. Cooling fins	200 (4 sets of 50)	376 (8 sets of 47)	50	50
TEG cells	12	8	6	6
Hydrogen Tube heating surface area (m^2)	0.076	0.151	0.0577	0.0577
Heatsink Heating surface area (m^2)	0.968	1.3242	0.595	0.595
cooling Fins Total surface area (m^2)	0.768	0.6392	1.559	0.892

Difference	More TEG	More heat pipe	Compact + more cooling fins	Compact + lightweight

For comprehensive empirical reproducibility, the exhaustive detailed dimensions, material properties, and specific component spacing tolerances for each individual design were provided in Appendix A. It was fundamentally acknowledged that while the dimensions tabulated in Table 3.3 represent idealized computational geometries, physical manufacturing inherently introduces minor spatial deviations. However, establishing these rigid geometric boundaries provided the necessary mathematical foundation to initiate the analytical thermodynamic modelling phase.

3.2.3 Mathematical Thermodynamic Modelling

To establish a mathematically bounded thermodynamic baseline prior to executing the complex three-dimensional computational fluid dynamics, a fundamental one-dimensional mathematical model was developed. The primary objective of this analytical phase was to obtain generalised geometrical guidelines and to provide a stable mathematical foundation to cross-verify the subsequent simulation results.

As illustrated in Figure 3.3, the mathematical model bifurcated the system into two distinct analytical domains: the primary hydrogen preheating domain, governed by the effectiveness-NTU method, and the secondary thermoelectric cooling domain, governed by a one-dimensional thermal resistance circuit. To evaluate the architecture across a realistic operational spectrum, the mathematical model was executed under four distinct boundary conditions representing 500, 1000, 1500, and 2000 W of fuel cell operation. The hot air temperatures, ranging from 29 °C to 51 °C, corresponded to stack power outputs between 500 W and 2000 W. These thermal boundaries were derived from empirical mappings of the exit air across varying stack loads, where the transfer of the chemical energy of the fuel directly to the ambient atmosphere strictly capped the theoretical ceiling of vehicular electrical efficiency. This exhausted hot air functioned as the primary waste heat source, which was subsequently absorbed by the integrated heat recovery system within the heat exchanger domain. Drawing upon previous literature, the external cooling air velocity was constrained to a simulated vehicle cruising speed of 36 km/h, operating under an assumed ambient environmental temperature of 30 °C. Furthermore, the mass flow rates for the incoming hydrogen

reactant were adapted from empirical data established by Mohamed et al. [17]. The hydrogen supply within the analytical model was maintained at a constant temperature of 30 °C directly from the storage tank. Finally, the specific empirical boundary parameters extracted from the literature, which served as the unyielding inputs for the solver, were detailed in Table 3.4, which were extracted from the aforementioned studies, [17], [9].

Table 3.4
Input Parameters for the Integrated Heat Recovery System Based on PEMFC Operational Conditions

Domain/ streams	**Parameters**	**Unit**	**Symbol**	**Stack Power (W)**			
				500	**1000**	**1500**	**2000**
FC Stack Waste Heat Stream	Mass Flow Rate	kg/s	$\dot{m}_{FC}$	2.81	3.02	3.22	3.40
	Velocity	m/s	u_{FC}	2.48	2.73	2.98	3.23
	Temperature	°C	T_{FC}	29.23	36.53	43.83	51.13
Hydrogen Inlet	Mass Flow Rate	kg/s	$\dot{m}_{H2}$	9.04E-06	1.81E-05	2.71E-05	3.62E-05
	Velocity	m/s	u_{H2}	0.49	0.97	1.46	1.94
	Temperature	°C	T_{H2}	23	23	23	23
Cooling Stream	Cruising Velocity	m/s	u_{FCV}	10	10	10	10
	Temperature	°C	T_{FCV}	30	30	30	30

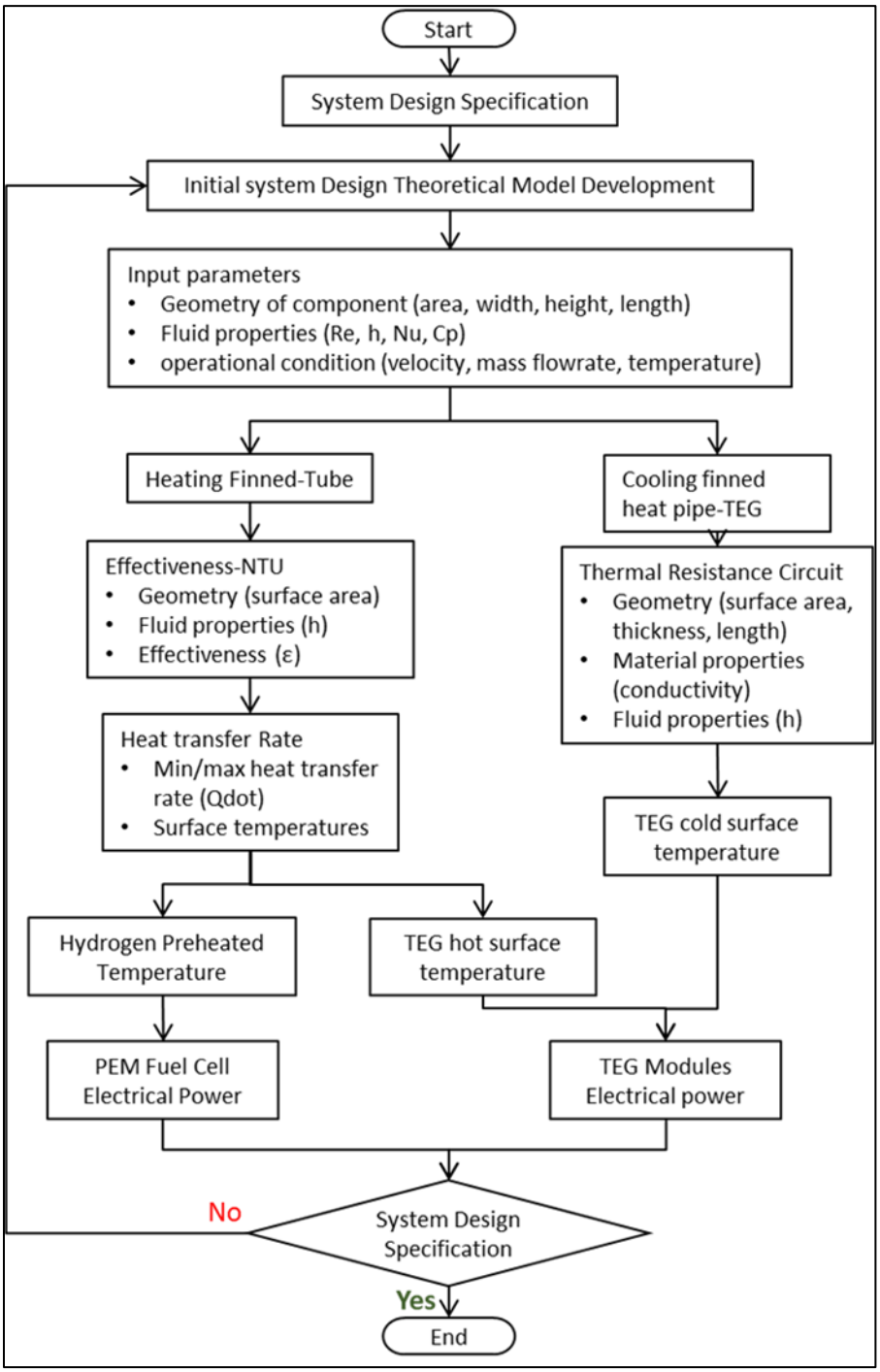

Figure 3.3 Mathematical Modelling Flowchart

3.2.3.1 Fundamental Mathematical Assumptions

To construct a functional one-dimensional network, several strict modelling assumptions were mandated. First, the system operated under absolute steady-state conditions, ignoring transient thermal lags. Second, thermal radiation was neglected, leaving convection and conduction as the sole energy transfer mechanisms. Third, solid

interfaces between metallic components and semiconductor modules possessed perfect thermal contact. Although physical fabrication required thermal grease which inherently introduced contact resistance establishing a zero-resistance baseline was necessary to evaluate the architecture's maximum analytical potential. Finally, material properties were perfectly isotropic, and parallel components maintained uniform spatial temperatures across their arrays.

3.2.3.2 Primary Heating Domain: Effectiveness-NTU Method

The sizing and thermal capacity of the hydrogen preheating heat exchanger were heavily influenced by the macroscopic geometry parameters, specifically the number of fins, tube passes, and overall fluid residence lengths. To predict the outlet state of the internal reactant, the *effectiveness-NTU* method was deployed. The localised Reynolds numbers for the internal hydrogen flow Re_{H^2} and the external waste heat stream Re_{WH} were calculated as follows [130]:

$$Re_{H^2} = \frac{u_{H^2}.\ D_i}{v_{H^2}} \tag{3.1}$$

$$Re_{WH} = \frac{u_{WH}.\ H_{fin}}{v_{WH}} \tag{3.2}$$

where D_i represents the inner diameter of the multiple tube pass (0.01704 m), H_{fin} was the height of the primary heatsink fin, u was the respective velocity, and v represented the respective kinematic viscosities. The subsequent Nusselt numbers required to determine the convective heat transfer coefficients were then established [131]:

$$Nu_{H2} = \frac{h_i.\ D_i}{k_{H^2}} \tag{3.3}$$

$$Nu_{WH} = 0.228 \cdot \mathrm{Re}_{\mathrm{WH}}^{0.731}.\mathrm{Pr}_{\mathrm{WH}}^{0.33} \tag{3.4}$$

Because the extremely low velocity hydrogen flow within the narrow tube remains strictly laminar, the internal Nusselt number (Nu_{H2}) was assigned a constant value of 4.36, representing a uniform heat flux boundary condition [132]. The overall heat transfer coefficient (U) across the thin tube boundary was cautiously approximated by ignoring the negligible conductive resistance of the thin metallic tube wall, [131]:

$$\frac{1}{U} \approx \frac{1}{h_i} + \frac{1}{h_o} \qquad [W/m^2\text{K}] \qquad (3.6)$$

where h_o is the forced convection coefficient at the external fin side. To bridge this overall heat transfer coefficient to the actual thermal recovery, the dimensionless number of transfer units NTU was calculated. This parameter inherently relies on the total heat transfer surface area A_s and the minimum heat capacity rate C_{min}, representing the product of mass flow rate and specific heat capacity of the limiting fluid) between the hydrogen and waste heat streams [133]:

$$NTU = \frac{U \cdot As}{C_{min}} \qquad (3.6)$$

Subsequently, the heat exchanger effectiveness ε was determined utilising the fundamental NTU relationship [133]:

$$\varepsilon = 1 - \exp(-NTU) \qquad (3.7)$$

By defining this effectiveness, the actual rate of thermal transfer to the hydrogen stream $\dot{Q}_{actual}$ was calculated based on the maximum possible thermodynamic transfer capacity $\dot{Q}_{max}$. $\dot{m}_{H2}$ was mass flow rate of hydrogen supply, $C_{p,H2}$ was the specific heat capacity of hydrogen, T_{WH} was the waste heat temperature and $T_{H2,in}$ was the inlet temperature of hydrogen [134]:

$$\dot{Q}_{actual} = \varepsilon \dot{Q}_{max} \qquad [\text{W}] \qquad (3.8)$$

$$\dot{Q}_{max} = \dot{m}_{H2} \cdot C_{p,H2} \cdot (T_{WH} - T_{H2,in}) \quad [\text{W}] \quad (3.9)$$

This fundamentally yields the preheated outlet temperature of the hydrogen gas $T_{H2,out}$, which served as the primary cross verification parameter against the subsequent numerical simulations.

$$T_{H2,out} = T_{H2,in} + \frac{\dot{Q}_{\text{actual}}}{\dot{m}_{H2} \cdot C_{p,H2}} \quad [°\text{C}] \quad (3.10)$$

3.2.3.3 Secondary Cooling Domain

The secondary cooling domain with one-dimensional thermal resistance network to predict the operational temperatures of the solid state semiconductor surfaces, a generalized one-dimensional thermal resistance circuit was established. While it was acknowledged that the four distinct conceptual architectures (detailed in Table 3.3) possess varying physical dimensions and parallel component arrays, the universal governing thermal pathway remains mathematically identical across all designs. Figure 3.4 and Figure 3.5 illustrate this universal network, simplified from a complex parallel and series combination into a direct linear circuit [134].

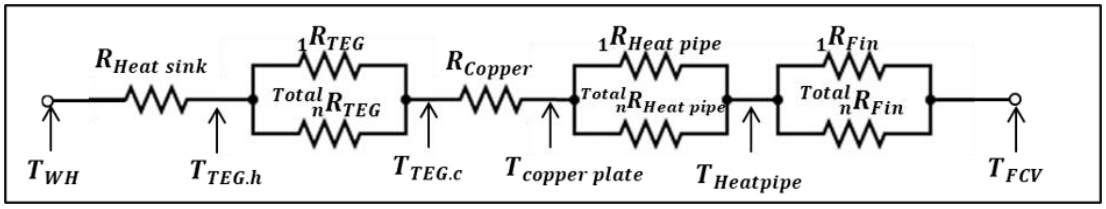

Figure 3.4 Example of Universal Thermal Resistance Network for IHR Architecture

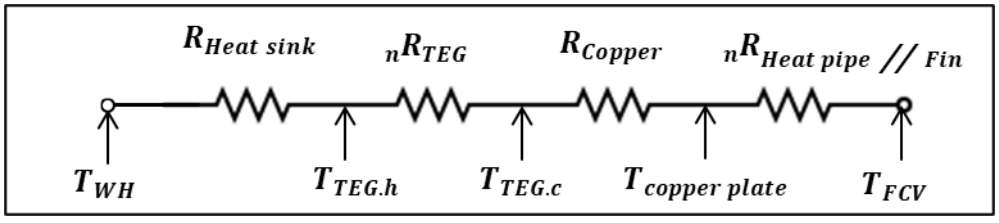

Figure 3.5 Simplified Linear Thermal Resistance Circuit

The critical hot surface $T_{TEG,h}$ and cold surface $T_{TEG,c}$ temperatures of the bismuth telluride modules were predicted by determining the total continuous heat transfer rate $\dot{Q}_{\mathrm{T,C}}$ traversing the solid assembly. The fundamental thermodynamic thermal resistance equations (equation 3.11 to 3.21) were referred from [134]:

$$\dot{Q}_{\mathrm{T,C}} = \frac{T_{WH} - T_{FCV}}{R_{T,C}} \quad [\mathrm{W}] \qquad (3.11)$$

where the total universal resistance $R_{T,C}$ was the sum of the individual conductive and convective resistances:

$$R_{T.C} = R_{Heat\ sink} + R_{Copper} + {}^{n}_{12}R_{TEG} + R_{Copper} + {}^{n}_{4}R_{Heat\ pipe\ //\ Fin} \quad [\mathrm{K/W}] \qquad (3.12)$$

where $R_{Heat\ sink}$, R_{Copper}, ${}^{n}_{12}R_{TEG}$, ${}^{n}_{4}R_{Heat\ pipe\ //\ Fin}$ were the total resistance for the heatsink, copper plate, combined heat pipe and fins. ${}^{n}_{4}R_{Heat\ pipe\ //\ Fin}$ were the sum of $R_{Heat\ pipe}$ and $R_{Heat\ sink}$ from the parallel thermal resistance accounting the actual number of fins and heat pipes. The individual macroscopic thermal resistances for the distinct physical components were calculated utilising standard Fourier and Newton cooling conduction and convection formulations:

$$R_{copper\ block} = \frac{t_{copper\ block}}{k_{copper\ block} A_{copper\ block}} \quad [\mathrm{K/W}] \qquad (3.13)$$

$$R_{Heat\ pipe} = \frac{L_{Heat\ pipe}}{k_{copper} A_{Heat\ pipe}} \quad [\mathrm{K/W}] \qquad (3.14)$$

$$R_{Fin} = \frac{L_{Fin}}{k_{Aluminium} A_{Fin}} + \frac{1}{h_{FCV} A_{Fin}} \quad [\mathrm{K/W}] \qquad (3.15)$$

$$R_{TEG} = \frac{t_{TEG}}{k_{Bismuth\ telluride} A_{TEG}} \quad \text{[K/W]} \quad (3.16)$$

$$R_{Heat\ sink} = \frac{L_{Heat\ sink}}{k_{Aluminium} A_{Heat\ sink}} + \frac{1}{h_{WH} A_{Heat\ sink}} \quad \text{[K/W]} \quad (3.17)$$

Once the total continuous heat transfer rate $\dot{Q}_{\mathrm{T,c}}$ and the discrete macroscopic thermal resistances were established, the mathematical model extracted the localised surface temperatures by calculating the sequential thermal drop across the network nodes. Initially, the boundary temperature of the primary heatsink fin $T_{Heatsink.fin}$ and the solid heatsink base T_{base} were calculated by sequentially subtracting the convective and conductive thermal drops from the primary waste heat source T_{WH} :

$$T_{Heatsink.fin} = T_{WH} - \frac{\dot{Q}_{\mathrm{actual}}}{h_{WH} \cdot A_{Heatsink\ fin}} \quad \text{[°C]} \quad (3.18)$$

$$T_{base} = T_{Heatsink.fin} - \frac{\dot{Q}_{actual} \cdot t_{base}}{k_{alumnium} \cdot A_{Heatsink\ fin}} \quad \text{[°C]} \quad (3.19)$$

where t_{base} represents the physical thickness of the heatsink base and $k_{alumnium}$ was the isotropic thermal conductivity of the aluminium structure. By establishing this foundational base temperature, the critical hot surface $T_{TEG,h}$ and cold surface $T_{TEG,c}$ temperatures of the bismuth telluride modules were predicted by subtracting the specific conductive temperature drop from the preceding boundary temperature:

$$T_{TEG,h} = T_{Base} - (\dot{Q}_{\mathrm{T.c}} \cdot R_{copper}) \quad \text{[°C]} \quad (3.20)$$

$$T_{TEG,c} = T_{TEG,h} - (\dot{Q}_{\mathrm{T.c}} \frac{R_{TEG}}{nTEG}) \quad \text{[°C]} \quad (3.21)$$

3.2.3.4 TEG Power Evaluation and Empirical Mapping

Upon deriving the discrete boundary temperatures from the thermal resistance network, the secondary electrical generation of the TEG cells, P_{TEG}, was estimated. The established method by Mohamed et al. [102] was adopted, where the peak power output obtainable from the potential of a TEG was theoretically restricted to 25% of the optimum TEG power. This optimum condition occurred when the short-circuit current was multiplied by the open-circuit voltage, with both parameters being dependent on the surface temperatures of the TEG cell. Therefore, the TEG power output was predicted using Equations 3.22 to 3.24, which were obtained from previous literature, [135].

$$P_{TEG} = \frac{1}{4} . I_{SC} . OCV \quad \text{[W]} \quad (3.22)$$

$$OCV = \alpha . \Delta T_{TEG} \quad \text{[V]} \quad (3.23)$$

$$I_{SC} = (1.44 . T_{h.}) - 48.3 \quad \text{[A]} \quad (3.24)$$

The I_{SC} was defined as the short circuit current obtained when the cell voltage was zero, while OCV was the open circuit voltage that occurred when the cell current was zero. The value of the hot side and cold side TEG surfaces from the simulation was used to calculate the temperatures difference for the TEG module, ΔT_{TEG} and the OCV. The hot side TEG surface temperature, $T_{h.}$ from the simulation was used to calculate $I_{SC.}$ The Seebeck coefficient, α, was equal to 24.7 mVK^{-1} that shows the constant temperature thermoelectric potential of the semiconductor material.

3.2.3.5 PEM fuel cell performance analysis

The IHR designs were evaluated on the hydrogen temperature difference, hydrogen heat absorption, TEG power generation, power enhancement of PEMFC and waste heat utilization. The numerical model provided temperature values for the hydrogen stream as well as the surface temperatures of the TEG cells under variable

waste heat stream temperatures. These temperatures were then translated to calculate the rate of heat absorption by the hydrogen stream as well as the TEG electrical power outputs. To predict the fuel cell power enhancement due to hydrogen preheating, a simplified method was used by referring to the results of a previous study by Mohamed and Kamil [17], who mapped the enhancement of a PEM fuel cell stack power output against the hydrogen preheating degree. Experimental data from [17] were mapped, as shown in figure 3.6, and a correlation was obtained (Equation. 3.25) as reference to calculate the fuel cell enhancement for this study.

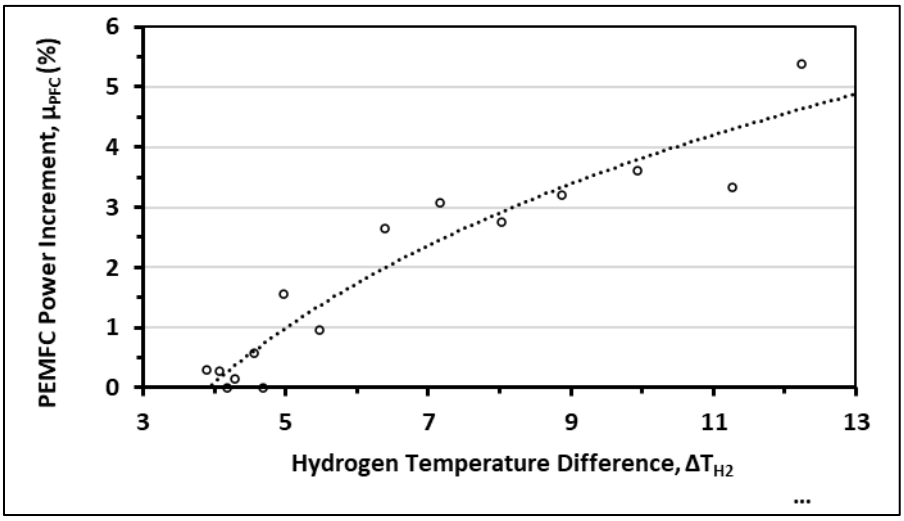

Figure 3.6 PEM fuel cell power output increment per degree of fuel preheating (extracted from literature [17])

From the exponential profile in Figure 3.6, the percentage of PEMFC power increment relative to the degree of preheated hydrogen temperature can be expressed as [17]:

$$\mu_{PFC} = (4.072 \cdot ln \cdot \Delta T_{H2}) - 5.5595 \qquad [\%] \qquad (3.25)$$

where ΔT_{H2} was the inlet and outlet temperature difference of the hydrogen stream at the heating heat exchanger, which was then used to predict the PEMFC power output enhancement [17]:

$$\Delta P_{el,FC,analytical} = P_{el,FC} \cdot \mu_{PFC} \qquad [W] \qquad (3.26)$$

where $P_{el,FC,ANALYTICAL}$ was the nominal electrical power output from the fuel cell (500 W to 2000 W).

From the hydrogen temperature difference, the preheating rate of hydrogen was, [13]:

$$\dot{Q}_{H2,analytical} = \dot{m}_{H2} \cdot C_{p.\ H2} \cdot (\Delta T_{H2}) \quad [\text{W}] \quad (3.27)$$

The mass flow rate of hydrogen relative to the stack power output, $\dot{m}_{H2}$ and the heat capacity of hydrogen, $C_{p,H2}$.

The waste heat utilization factor, μ_{WH} was the ratio of combined heating rate of hydrogen preheating and TEG power generation, P_{TEG} to the thermal power generated from the stack, $P_{th.FC}$ relative to the fuel cell power output [17]:

$$\mu_{WH,analytical} = \frac{\dot{Q}_{H2,analytical} + \dot{Q}_{T.c}}{P_{th.\ FC}} \cdot 100 \quad [\%] \quad (3.28)$$

In this work, the $P_{th,FC,analytical}$ was assumed similar in magnitude to the electrical power generated (a 50% energy conversion efficiency assumption) [17].

3.2.4 Computational Fluid Dynamics Setup and Discretization

Following the foundational one dimensional mathematical modelling, a comprehensive three-dimensional computational fluid dynamics investigation was executed utilising ANSYS Fluent 2024 R1. While the theoretical thermal resistance circuits and *E-NTU* methods provided generalized thermal boundaries, the numerical software was utilised to resolve the complex spatial heat transfer and fluid maldistributions inherent to the physical geometries. Crucially, the surface temperatures and hydrogen outlet temperatures extracted from these spatial simulations were subsequently applied to the exact same predictive performance models derived from established literature equations. This ensured that the predicted primary fuel cell power increments and secondary solid state thermoelectric generation were evaluated

consistently across both analytical phases. The overall numerical process flow chart was illustrated in Figure 3.7.

The numerical progression initiated with the computer aided design modelling of the four distinct IHR architectures and was systematically evaluated. A structured computational workflow was established, as outlined in the numerical flow chart. Following the initial geometric modelling, the process required discretising the solid and fluid domains through a rigorous meshing process. Ensuring mesh quality operated as a repetitive refinement cycle, where the element skewness was continuously monitored and adjusted until a highly reliable grid was successfully achieved. Upon securing adequate skewness, the computational setup progressed to declaring the specific solid bodies, fluid domains, inlet boundaries, and outlet boundaries, while carefully defining the conjugate heat transfer interfaces between the interacting components.

Subsequently, the specific material properties and operational boundary conditions were applied to the model. The physical solver was then configured, selecting a steady state formulation coupled with the appropriate energy and turbulence models to capture the aerodynamic convection. Prior to executing the full computational run, a preliminary mass balance validation was performed to mathematically verify that the domain setup and flow trajectories remained scientifically logical. Following a successful mass balance check, the numerical solver was initiated. During the computation, the iteration convergence criteria were strictly monitored. If the residuals exhibited mathematical instability, the setup was halted, and the mesh or boundary definitions were iteratively refined to eliminate errors.

Once absolute mathematical convergence was secured, the resulting spatial data underwent a critical pre validation phase. The extracted hydrogen and thermoelectric surface temperatures were cross referenced against the baseline values established by the earlier one dimensional mathematical model. The computational results were only accepted if the comparative deviation remained strictly below a 10% threshold, and if the corresponding pressure profiles demonstrated scientifically sound aerodynamic behaviour. Ultimately, by successfully fulfilling these rigorous verification steps, the four conceptual designs were objectively analysed to determine the highest overall thermal performance. Based on this final comparative analysis, a single optimal design was selected to proceed toward physical fabrication and subsequent steady state test bench validation.

To facilitate the interpretation of the four distinct integrated heat recovery architectures, the internal assemblies and system components were visualised in three dimensions across Figure 3.8 to Figure 3.11. All four evaluated designs incorporated three completely separate fluid domains, comprising the internal hydrogen reactant gas, the hot exhaust air stream discharged from the fuel cell, and the cold ambient air stream intercepted from the cruising vehicle.

The thermal energy transfer initiated with the hot exhaust air exiting the primary fuel cell stack. This high temperature stream was channelled directly into an impinging jet configuration to simultaneously heat the primary heatsink and the integrated multiple tube pass pipe. Because the multiple tube pass network physically penetrated through the thickness of the heatsink fins, the thermal absorption occurred concurrently. Consequently, the heated tube walls actively preheated the internal hydrogen gas, while the primary heatsink conducted thermal energy directly to the hot surface of the solid state TEG. After transferring this thermal energy, the exhaust air exited through the rear of the heatsink without ever making direct physical contact with the TEG modules. Concurrently, the hydrogen fuel gas entered the multiple tube pass network, which served as the reactant inlet for the heating system. As the gas traversed this heated pipe network, it absorbed the necessary thermal energy before exiting and continuing its trajectory directly into the inlet of the primary fuel cell stack.

The TEG modules functioned as a physical separation barrier sandwiched centrally between the primary heating and secondary cooling systems, relying entirely on indirect conductive heat transfer. The TEG surface touching the primary heatsink became the designated hot side, while the opposing surface touching the secondary copper plate acted as the cold side. The thermal energy travelled conductively from the hot TEG surface to the cold TEG surface, and subsequently into the solid copper plate. Because the heat pipes were physically embedded within this copper plate, the absorbed heat was rapidly conducted into the heat pipe network, transported to the extended aluminium fins, and ultimately convected away by the cold cruising air stream.

Therefore, the overall chronology of thermal transfer cascaded sequentially from the stack exhaust air into the combined heatsink and copper tube, transferred to the TEG hot surface, traversed to the TEG cold surface, conducted into the copper plate and heat pipes, and was finally dispersed through the aluminium fins into the cold air stream. The specific design parameters defining these integrated architectures were summarised in Table 3.3, with an exhaustive engineering catalogue being safely

provided in Appendix B. Figures 3.8 through 3.11 illustrated the specific three-dimensional geometries for each design iteration, with isometric, top, and side views being presented alongside a detailed exploded view. The intended fluid flow directions across the three primary subassemblies were mapped by these visual representations: the hydrogen preheating system comprising the finned tube network, the TEG heating assembly featuring a finned flat plate, and the secondary cooling system integrating extended fins with solid heat pipes. The four evaluated designs were deliberately differentiated through the manipulation of specific geometric parameters to evaluate thermal scaling. For the primary heating system, the overall heatsink dimensions, the number of heatsink fins, the total number of tube passes, and the total physical length of the tubing were included as variable parameters. The intermediate solid-state conversion stage was varied strictly by the total number of TEG modules and their spatial arrangement. Finally, the secondary cooling system was differentiated by altering the dimensions of the copper plate, the total number of embedded heat pipes, and the total number of extended cooling fins.

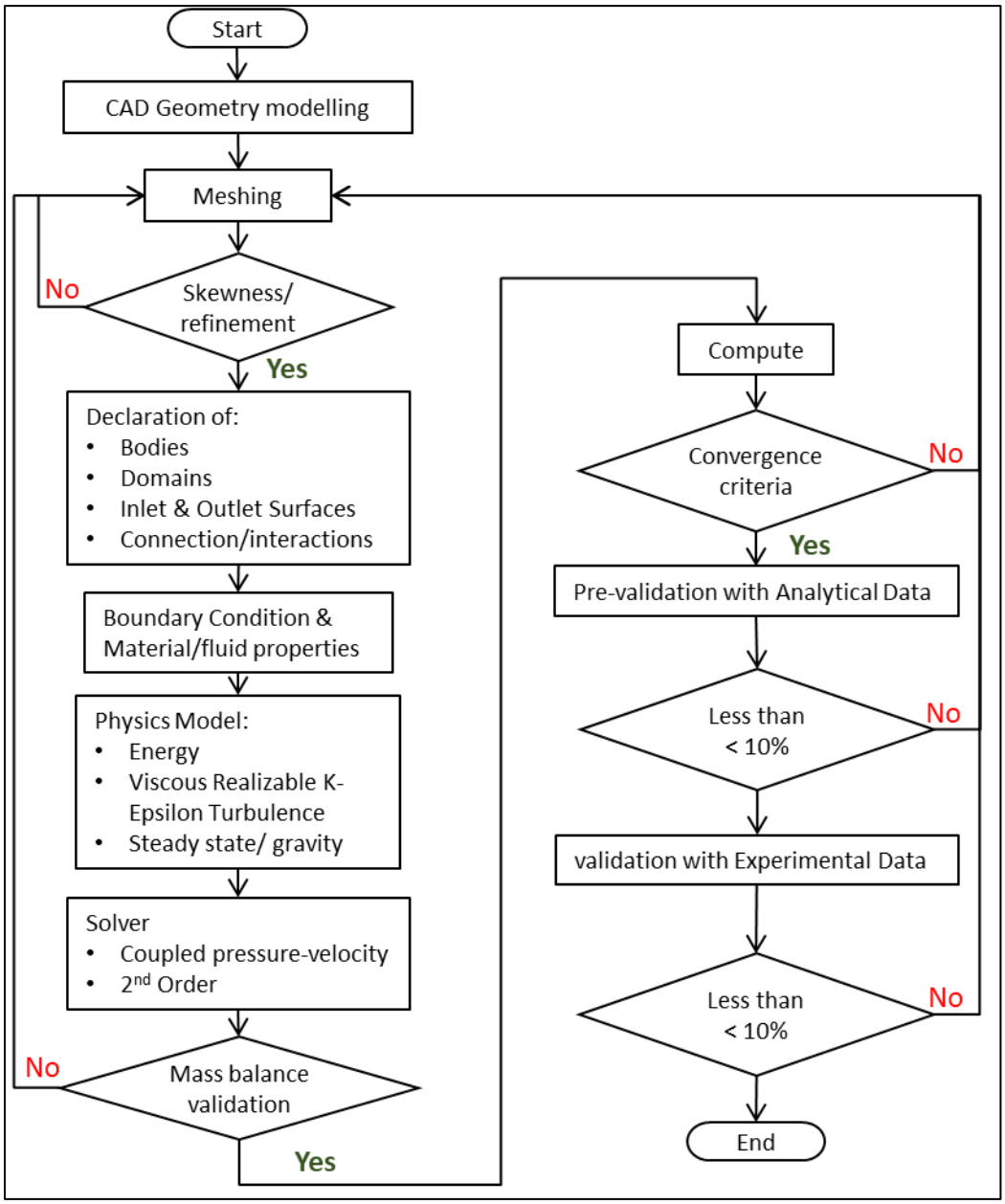

Figure 3.7 Workflow for Phase 2 Computational Numerical Modelling

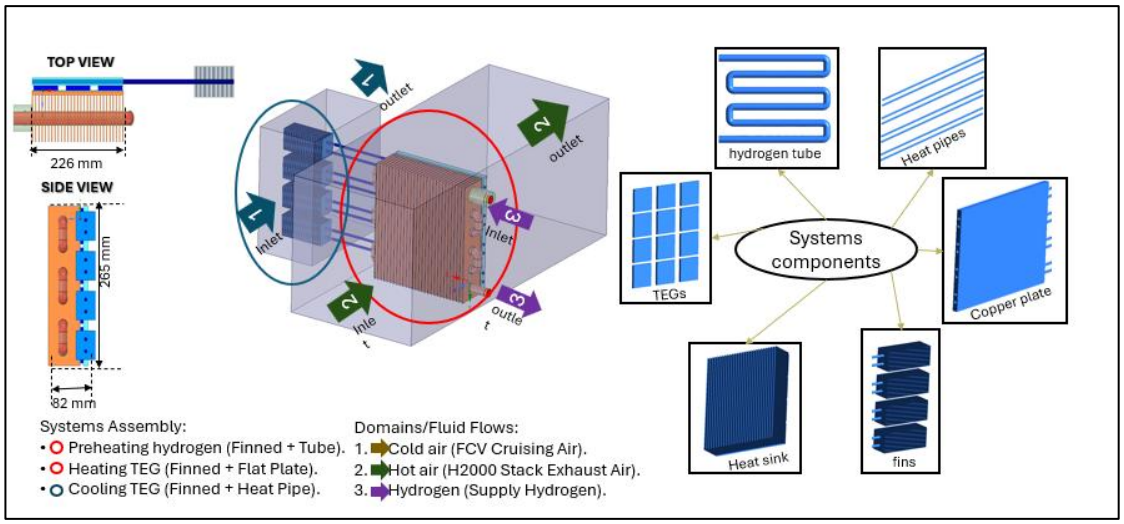

Figure 3.8 IHR Design 1 Assembly and Systems Component

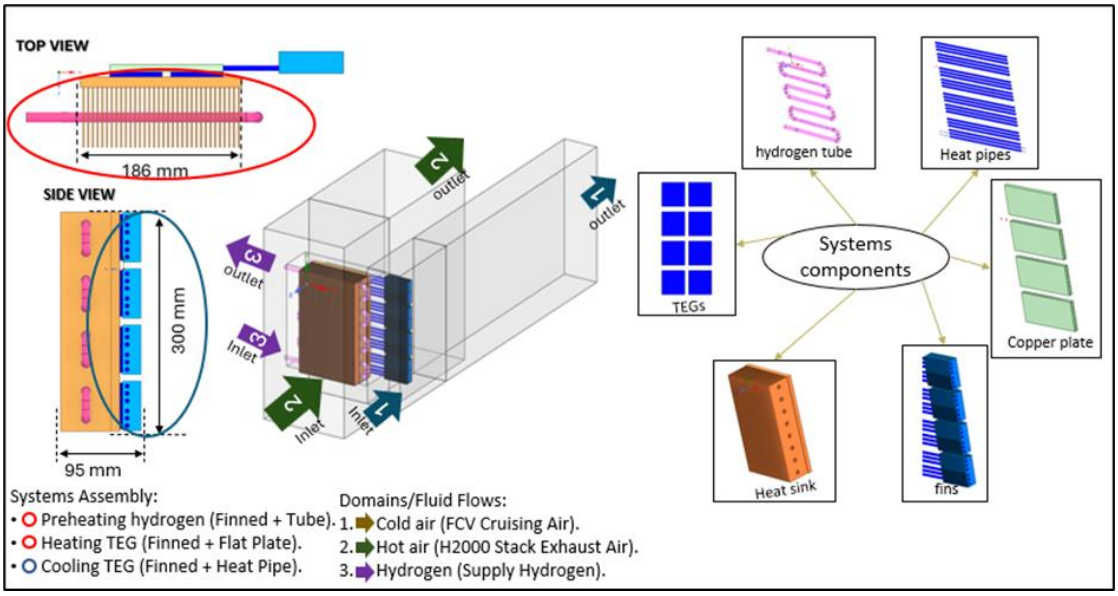

Figure 3.9 IHR Design 2 Assembly And Systems Component

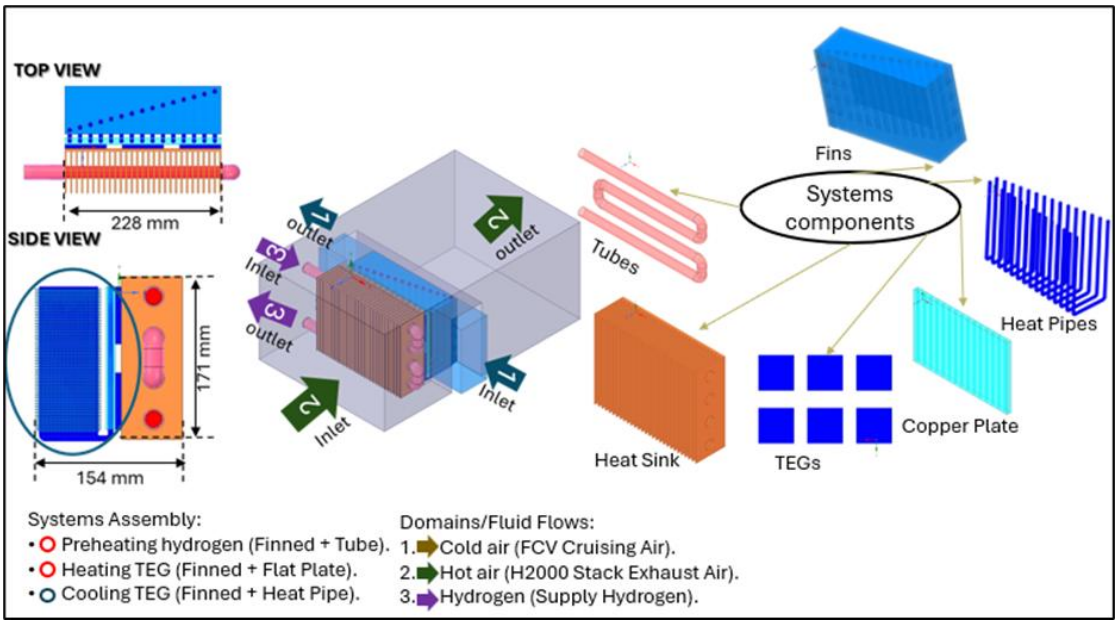

Figure 3.10 IHR Design 3 Assembly and Systems Component

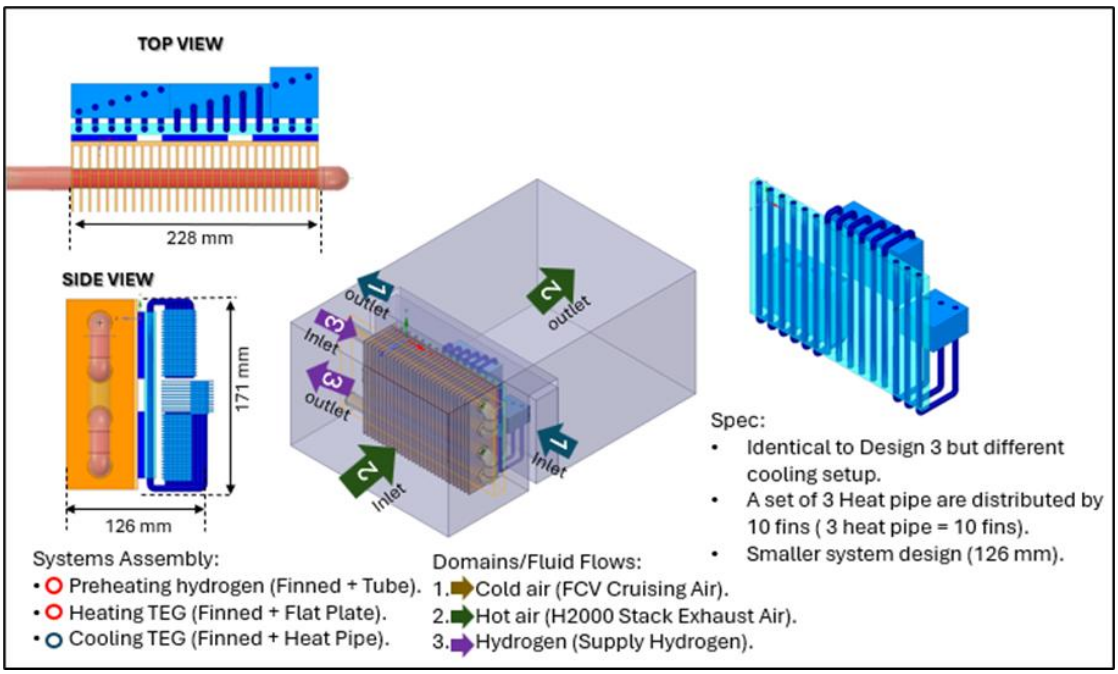

Figure 3.11 IHR Design 4 Assembly and Systems Component

3.2.4.1 Computational Domains and Boundary Conditions

The simulation environment was structured around three interacting fluid domains. First, the primary heating domain evaluated the fuel cell waste-heat air stream, dynamically varying the mass flow rate and inlet temperature to reflect stack operations from 500 W to 2000 W. Second, the primary internal flow domain evaluated the hydrogen reactant stream, scaling its inlet velocity relative to the identical stack power

spectrum. Finally, the secondary cooling domain evaluated the ambient atmospheric air, which was maintained at a constant 10 m/s to simulate the continuous cruising velocity of the lightweight vehicle under a fixed ambient inlet temperature of 30 °C. The exact numerical boundaries utilised for these computational inlets were locked to the literature values previously established in Table 3.4.

To ensure computational stability, the three-dimensional models were simulated under absolute steady state conditions, assuming incompressible fluid streams for both the air and hydrogen domains. Crucially, due to the severe computational expense and numerical instability inherent to modelling internal multiphase boiling and condensation, the internal fluid dynamics of the solid heat pipes were bypassed. Instead, the heat pipes were simplified and modelled as highly conductive solid copper rods, ensuring conductive thermal extraction was maintained without crashing the fluid solver. The assigned material properties for the solid and fluid domains were summarised in Table 3.5.

To ensure the numerical accuracy of the conjugate heat transfer simulations, the thermophysical properties for all interacting solid and fluid domains required strict definition prior to executing the solver. The properties for most standard components were extracted directly from the predefined materials database embedded within the ANSYS Fluent software. Specifically, the solid copper plate and the simplified solid heat pipes were assigned default copper properties. The plate fins and the heatsink structures utilised default aluminium properties, while the thermal insulator was assigned standard glass wool. Similarly, the fluid domains were defined utilising standard software fluids: the internal reactant domain was assigned hydrogen gas, and both the hot and cold external fluid streams were assigned air. Conversely, the specialised semiconductor material required for the TEG modules, bismuth telluride, was not available as a standard default option. Consequently, the exact density, specific heat capacity, and thermal conductivity for the solid-state bismuth telluride were manually defined based on empirical values established in prior peer-reviewed literature [136]. While utilising these standardised database values and established literature parameters provided a stable mathematical foundation for the computational solver, it was cautiously acknowledged that physical manufacturing materials inevitably possessed microscopic impurities or minor structural variations that these idealised uniform properties could not perfectly replicate.

Table 3.5
Material Properties Assigned for the Computational Fluid Dynamics Domains

Properties	Unit	Symbol	Material					
			Copper Plate/ Heat Pipe	Glass Mineral Wool Insulator	Air Hot Stream/ Cold Stream	Hydrogen	TEG Bismuth Telluride	Aluminium Plate Fins/ Heatsink
Density	kg/m^3	ρ	8978	20	1.059	0.08189	7730	2719
Specific Heat Capacity	J/kg.K	C_p	381	1030	1007	Piecewise polynomial	157.35	871
Thermal Conductivity	W/m.k	k	387.6	0.35	0.02808	0.1672	1.2	202.4
Source			ANSYS	ANSYS	ANSYS	ANSYS	[136]	ANSYS

3.2.4.2 Governing Equations and Physics Models

The computational solver dictated distinct flow regime models based on the physical limits of the interacting fluids. Due to the exceptionally low mass flow rate of the hydrogen supply, the internal tube flow maintained a maximum Reynolds number strictly below 300. Thus, hydrogen domain favoured a laminar flow model but the external fluid streams impinging upon the heavily finned primary heatsink and secondary cooling fins generated severe turbulence, with Reynolds numbers exceeding 30,000. To accurately capture these highly turbulent external convective interactions, the Reynolds-Averaged Navier-Stokes equations were deployed utilising the *k-ε* turbulence model.

Although the *k-ω* Shear Stress Transport model was recognised as a historically favoured option for conjugate heat transfer due to its direct mathematical resolution of the viscous sublayer, its application strictly required a near-wall grid with a non-dimensional wall distance approaching unity [137]. Given the vast and intricate surface areas inherent to the heat sink and tube fin configurations, achieving this level of microscopic geometric resolution across all fluid-solid interfaces would have induced a prohibitive computational burden on the overall cell count. Consequently, the Realizable k-ε model was selected as a necessary and pragmatic numerical compromise, relying on wall functions to adequately bridge the flow regime between the fully turbulent free stream and the solid boundaries [133]. Because the overarching objective of this loosely coupled thermal analysis was to evaluate the macroscopic thermal energy balance and bulk heat transport, this boundary approximation was considered sufficiently representative of the physical system. Furthermore, the Realizable k-ε offered superior mathematical stability when calculating the complex flow separation and bulk fluid mixing characteristic of the external finned domains, thereby ensuring a robust iterative convergence for the overall energy recovery assessment [133].

The governing physical equations governing the conservation of mass (Continuity), Momentum, and Energy across the computational domains were expressed as follows [133]:

Continuity equation,

$$\nabla \cdot (\rho \vec{u}) = 0 \tag{3.29}$$

Momentum equation,

$$\nabla \cdot (\rho \vec{u} \vec{u}) = -\nabla P + \mu \nabla^2 \vec{u} + \rho \vec{g} \tag{3.30}$$

Energy equation,

$$\nabla \cdot \left(C_P \rho \vec{u} T \right) = k \nabla^2 T \tag{3.31}$$

where *u, P, T, μ, g* and *ρ* represent the velocity vector, static pressure, temperature, dynamic viscosity, gravitational acceleration, and fluid density, respectively. To resolve the specific turbulent kinetic energy k and the turbulent dissipation rate ε, the respective transport equations were engaged:

$$\frac{\delta k}{\delta x_j} \cdot \left(\rho \cdot \bar{u}_j \right) = \frac{\delta}{\delta x_j} \cdot \left(\frac{\mu_t}{\sigma_k} \cdot \frac{\delta k}{\delta x_j} \right) + \mu_t \left(\frac{\delta \overline{\mu}_i}{\delta x_j} + \frac{\delta \overline{\mu}_j}{\delta x_i} \right) \frac{\delta \overline{\mu}_i}{\delta x_j} - \rho \cdot \varepsilon \tag{3.32}$$

For ε,

$$\frac{\delta \varepsilon}{\delta x_j} \cdot \left(\rho \cdot \overline{u}_j \right) = \frac{\delta}{\delta x_j} \cdot \left(\frac{\mu_t}{\sigma_\varepsilon} \cdot \frac{\delta \varepsilon}{\delta x_j} \right) + C_1 \mu_t \frac{\varepsilon}{k} \left(\frac{\delta \overline{\mu}_i}{\delta x_j} + \frac{\delta \overline{\mu}_j}{\delta x_i} \right) \frac{\delta \overline{\mu}_i}{\delta x_j} - C_2 \cdot \rho \cdot \frac{\varepsilon^2}{k} \tag{3.33}$$

The model constants for the Realizable *k-ε* formulation were locked at standard empirical defaults C_1=1.44, C_2=1.92, C_μ= 0.09, σ_k= 1, σ_ε=1.3. The overarching parameters governing the computational solver setup were detailed in Table 3.6.

Table 3.6
Parameters for Computational Fluid Dynamics Setup

Parameters	**Selection**
Solver	
Type	Coupled, Pressure- Based
Velocity Formulation	Absolute

Models	
Energy	On
Viscous	Realizable K- epsilon
Solution Methods	
Momentum	2nd order upwind
Turbulent Dissipation Rate	2nd order upwind

3.2.4.3 Meshing Strategy and Grid Independence Test

The physical geometries of the evaluated architectures contained highly complex fluid pathways, including tortuous multiple tube passes and elbows, intersecting with exceptionally thin extended aluminium fins possessing a physical thickness of 0.6 mm. Structured hexahedral elements theoretically offer superior numerical accuracy and faster convergence for simple linear geometries. However, attempting to force a structured hexahedral grid onto these highly irregular spatial boundaries induced severe element distortion. Forcing hexahedral elements around the cylindrical copper tubes and sharp fin intersections frequently degraded orthogonal quality and elevated skewness to mathematically unacceptable levels, which inherently destabilised the fluid solver. Consequently, an unstructured tetrahedral meshing technique was deliberately selected. Tetrahedral elements provided the essential topological flexibility required to adapt smoothly to the complex geometric transitions without compromising the fundamental cell quality.

Utilising default automated meshing algorithms on these narrow boundaries inherently generated severe element skewness across the fluid-solid interfaces. To mathematically compensate for this geometric bottleneck, manual refinement focussing on both global and local sizing was enforced. The global mesh parameters were initially set with a maximum element size of 500 mm, a minimum size of 0.2 mm, and a constant growth rate of 1.2. For localised refinement, the through-thickness element divisions for the highly conductive solid components were specifically targeted. Because the extended aluminium plate fins and the hydrogen copper tubes possessed minimal physical thicknesses of 0.6 mm and 1.0 mm respectively, alongside exceptionally high thermal conductivities, their through-thickness divisions were restricted to a single

element. Through-thickness thermal behaviour was adequately captured by this specific approach without an unnecessary computational burden being imposed. Conversely, a significantly higher spatial resolution was required by the solid-state TEG modules to accurately capture the steep temperature gradients necessary for secondary power generation. To achieve this, a localised edge sizing of five divisions was applied, whereby four distinct elements were successfully incorporated across the component thickness.

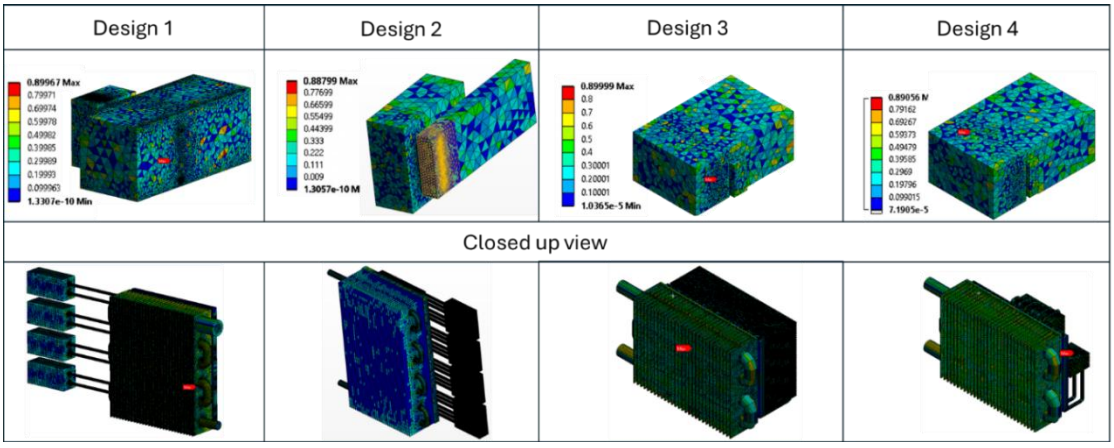

Figure 3.12 Overall Mesh Quality for the 4 Evaluated Architectures

To ensure the numerical outcomes were strictly a product of the physical geometry and not an artifact of the computational grid, a rigorous grid independence study was executed. The fundamental objective of this study was to identify the optimal computational cost to accuracy ratio. The initial coarse mesh generated approximately 8 million elements. However, the computational results for the critical parameters exhibited severe mathematical fluctuations at this density, indicating inadequate spatial resolution. Consequently, the grid was systematically refined by reducing the maximum and minimum global element sizes by half during each subsequent iteration. This progressive refinement swept the total element count from the initial 8 million up to an exceptionally dense 23 million elements. Furthermore, addressing the relationship between computation time and mesh resolution, the computational time was actively monitored alongside the mesh size during the grid independence study. Documenting this temporal relationship was necessary to objectively justify the computational cost to accuracy ratio. It empirically demonstrated that the selected optimal mesh density provided the required spatial accuracy without imposing an unnecessarily severe or prohibitive central processing unit time penalty on the overall simulation process.

Figure 3.13 displayed the computational cost taken for each mesh refinement iterated. The shortest was on the first iteration which was 8 million element and the longest was 23 million elements, 1 hour and half and almost 4 hours, respectively.

Throughout this progressive refinement, physical stability parameters, specifically the hydrogen pressure drop and the thermoelectric generator temperature difference, were continuously monitored. The empirical data indicated that an intermediate grid density of approximately 17 million elements provided absolute mathematical stability without altering the critical thermodynamic outputs. This optimal computational sweet spot was achieved utilising a maximum global element size of 60 mm and a minimum size of 0.02 mm. Further spatial decrements beyond 17 million elements yielded completely stagnant thermodynamic outcomes, confirming that asymptotic numerical convergence had been achieved. The visual convergence profiles confirming this asymptotic stabilisation were explicitly illustrated in Figure 3.14 a, and b. Furthermore, the exhaustive raw data matrices detailing the domain specific pressure drops were safely catalogued in Appendix B to maintain narrative focus.

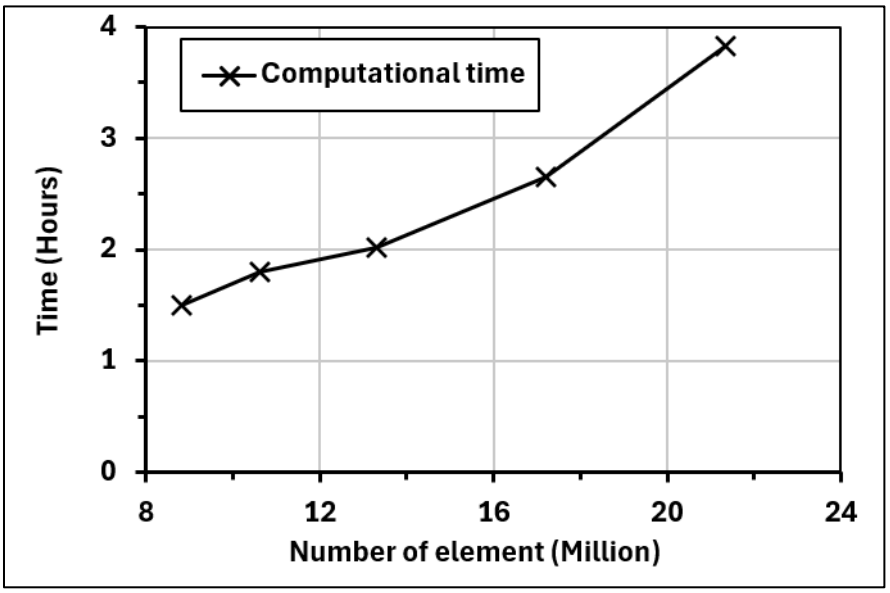

Figure 3.13 Grid Independence Test Computational Time

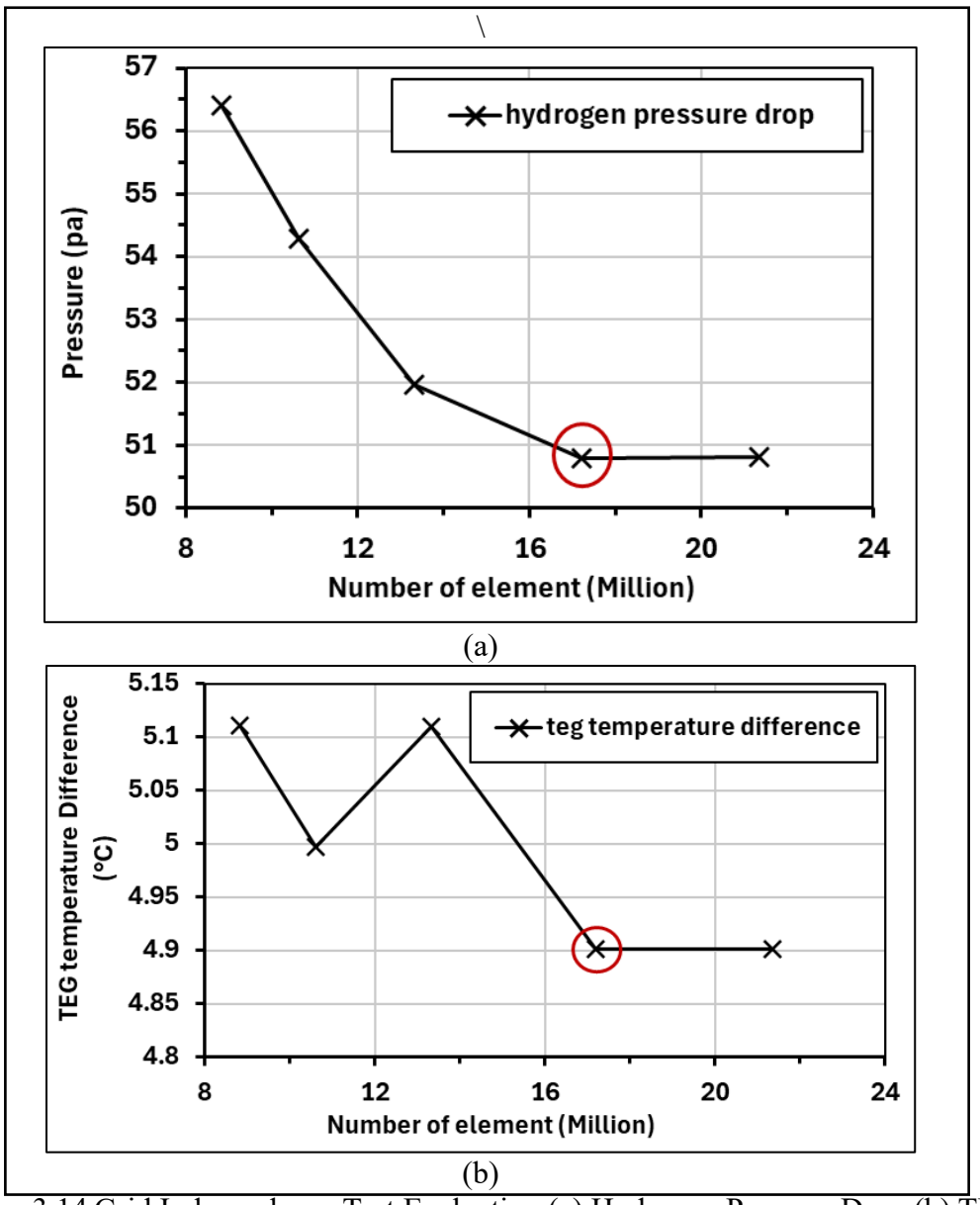

Figure 3.14 Grid Independence Test Evaluating (a) Hydrogen Pressure Drop (b) TEG Temperature Difference

3.2.4.4 Solver Execution and Convergence Criteria

The numerical computation method employed a pressure-based coupled algorithm. This approach was considered appropriate as it was generally well-suited for flows where pressure variations were not primarily driven by density changes, thereby assisting in the management of the complex velocity and density gradients associated with the highly refined computational grid. To pursue a higher degree of mathematical precision within the domain discretisation, a second-order upwind scheme was utilised for the pressure, momentum, turbulent kinetic energy, turbulent dissipation rate, and

energy equations. While these configurations aimed to reduce discretisation errors, it must be acknowledged that numerical uncertainties and minor approximation flaws inherently remain within any complex fluid model.

The evaluation of the computational iteration performance was presented to illustrate the relative mathematical stability of the numerical simulation routine. In computational fluid dynamics, variations in solver configuration or mesh quality can frequently induce mathematical fluctuations. In potentially unstable setups, residuals may initially appear steady before exhibiting erratic spikes as the iterations progress. Furthermore, during the grid independence study, central processing unit time was monitored alongside mesh density. Documenting this temporal relationship provided a means to evaluate the computational cost-to-accuracy ratio. Observations suggested that the chosen optimal mesh density offered a suitable level of geometric resolution without imposing a strictly prohibitive computational time penalty on the overall simulation process, though practical compromises between computational expense and absolute precision were invariably necessary in numerical studies.

The determination of computational convergence was guided by two primary criteria. First, mathematical residuals were monitored against stringent, pre-defined thresholds. As depicted in Figure 3.15, the convergence criterion was established to achieve a minimum residual of 1E-3 for the continuity equation, directional velocity components (x, y, and z), and the turbulence model parameters. Conversely, the temperature residual was subject to a stricter minimum threshold of 1E-6. The iterative process was executed with the objective of solving the equations to achieve these established criteria. The iteration history recorded in Figure 3.15 displays a consistent, non-linear decrease in residuals until they approximated a steady asymptote. This behaviour suggested that the numerical solver had likely reached a reasonable mathematical equilibrium.

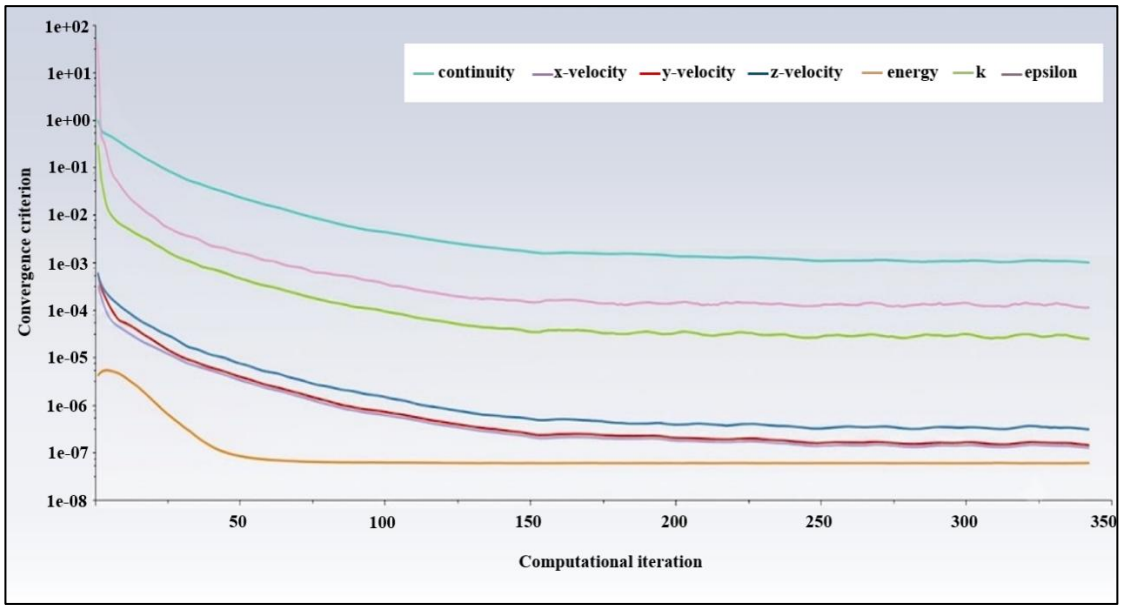

Figure 3.15 Convergence Residuals Versus Iteration Sequence

Furthermore, the physical thermodynamic stability of the model was continuously monitored alongside the mathematical residuals. To facilitate this rigorous monitoring, user-defined mathematical output parameters were established within the solver to systematically track core physical variables. The stabilisation of these targeted outputs served as an indicator that the extracted data represented a confident, albeit approximate, numerical solution. Furthermore, given the steady-state nature of the simulation, observing these parameters reach a constant plateau provided reasonable assurance that a steady flow condition had been effectively captured within the computational domain. Consequently, iterations were typically concluded only when these targeted boundary parameters appeared to flatten into steady-state asymptotes.

The stabilisation of the numerical were monitored by the crucial fluid domains, which were the pressure drop across cold chamber, hydrogen preheating tube and hot chamber. The cold chamber, serving as the cruising air domain, was tracked throughout the iteration sequence as the primary representative metric. As presented in Figure 3.16, this cold chamber pressure drop approached a generally constant asymptote, indicating a satisfactory level of mathematical equilibrium for the current study. Other continuously monitored physical parameters, including the primary hot chamber pressure drop, the internal hydrogen domain pressure drop, and the representative thermoelectric generator boundary temperatures, exhibited similar asymptotic tendencies. To maintain narrative focus, the graphical convergence profiles for these supplementary parameters were catalogued in Appendix C. It remains important to note

that while these measures indicate a robust computational solution, inherent modelling approximations mean that absolute physical convergence remains an idealised concept subject to a degree of experimental and numerical uncertainty.

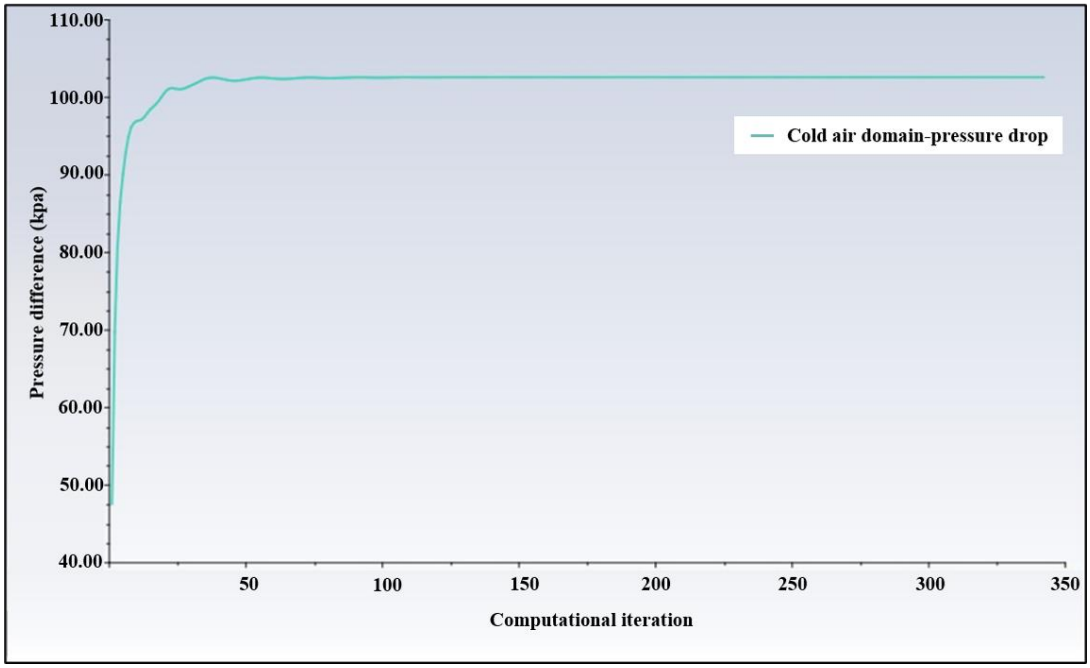

Figure 3.16 Thermodynamic Stability Profile of the Cold Chamber Pressure Drop Versus Iteration Sequence

3.2.5 Mathematical Verification of Numerical Models

Before advancing to the physical manufacturing phase, a rigorous analytical model cross verification was mandated to ensure the three-dimensional computational fluid dynamics did not generate nonphysical numerical artifacts. This was achieved by systematically comparing the primary thermodynamic outputs of the complex CFD simulations against the mathematically bounded baseline established by the one-dimensional mathematical thermal resistance network.

To quantify the mathematical alignment between these two distinct analytical methods, the absolute relative deviation was calculated for the critical boundary parameters, specifically targeting the hydrogen reactant outlet temperature $T_{H2.\ out}$ and the discrete TEG surface temperatures $T_{TEG,h}$ and $T_{TEG,c}$. The general equation utilised to calculate this comparative deviation was expressed as:

$$Deviation = \left| \frac{\emptyset_{cfd} - \emptyset_{analytical}}{\emptyset_{analytical}} \right| x\ 100 \qquad [\%] \qquad (3.34)$$

where ∅ represents the specific thermodynamic variable being monitored.

It was fundamentally acknowledged that achieving a zero percent deviation between these two methods was physically impossible and thermodynamically unrealistic. The one-dimensional mathematical model relies on highly idealized assumptions, including perfectly uniform flow distribution, isotropic thermal conduction, and the complete absence of localised thermal bottlenecks. In stark contrast, the three-dimensional computational fluid dynamics actively resolves complex spatial phenomena, including localised boundary layer separation, turbulent wake vortices behind the extended fins, and non-uniform flow maldistribution across the tube bundles.

Consequently, the CFD outcomes were inherently expected to predict slightly lower, more conservative thermal transfer rates compared to the idealized one-dimensional mathematical ceiling. To account for these expected spatial variances while maintaining strict scientific rigor, an acceptable relative deviation threshold was strictly bounded at a maximum of 10% as dictated by the pre validation loop in the computational flowchart (Figure 3.7). Successfully yielding a comparative deviation of less than 10% between the analytical linear math and the complex three-dimension simulation formally confirms numerical reliability. Achieving this critical threshold verifies that the simulated architectures adhere rigorously to the foundational laws of thermodynamics, effectively culminating the first methodological pillar and successfully securing TRL 2 prior to the initiation of physical prototype fabrication.

3.3 Experimental Test Bench Validation (Achieving TRL 4)

Upon securing numerical stability and mathematical verifying the computational fluid dynamics models in the first methodological phase, the investigation transitioned into the second overarching pillar: experimental test bench validation. The primary objective of this phase was to translate the optimised analytical model geometry into a functional physical prototype and subject it to controlled steady state laboratory conditions. Establishing this controlled empirical baseline was an absolute prerequisite prior to vehicular integration. Because actual on road driving inherently introduces chaotic environmental noise, erratic convective cooling rates, and

highly transient electrical loads, isolating the physical capabilities of the recovery architecture from these external variables was necessary. By securing a steady state baseline first, the subsequent dynamic on road data can be accurately interpreted, allowing a manageable comparative evaluation to differentiate between true system thermodynamic behaviour and transient environmental disturbances. By empirically quantifying the actual reduction in activation polarization and the secondary electrical generation under these isolated conditions, this phase effectively elevates the system to TRL 4.

3.3.1 Physical Fabrication of the Integrated Architecture

Following the successful mathematical cross verification, a singular architecture was mandated for physical manufacturing. Based on the comparative thermodynamic outcomes of the four computationally evaluated geometries, Design 2 was designated as the optimal configuration for physical testing. While previous numerical evaluations indicated that Design 1 yielded a marginally higher absolute hydrogen temperature, Design 2 successfully provided the second highest hydrogen preheating capacity while simultaneously securing a significantly larger temperature difference across the TEG surfaces. This specific thermal balance theoretically yields a substantially higher secondary TEG power generation alongside a highly comparable primary fuel cell power increment. Consequently, to maximize the overall dual recovery potential, Design 2 was selected to serve as the physical baseline.

The sequential physical fabrication process for this selected architecture was illustrated in Figure 3.17. To maintain practical manufacturing feasibility and reliability, several highly complex components were procured as commercial off the shelf units, specifically the TEG modules, the primary aluminium heatsink, the solid heat pipes, and the extended cooling fins. Therefore, custom physical manufacturing was strictly focused on developing the external fluid chambers, the internal multiple tube pass piping, the intermediate copper plate, and the structural mountings required to securely integrate these disparate components into a singular architecture. The manufacturing sequence was systematically divided into two parallel phases: the primary heating assembly and the secondary cooling assembly.

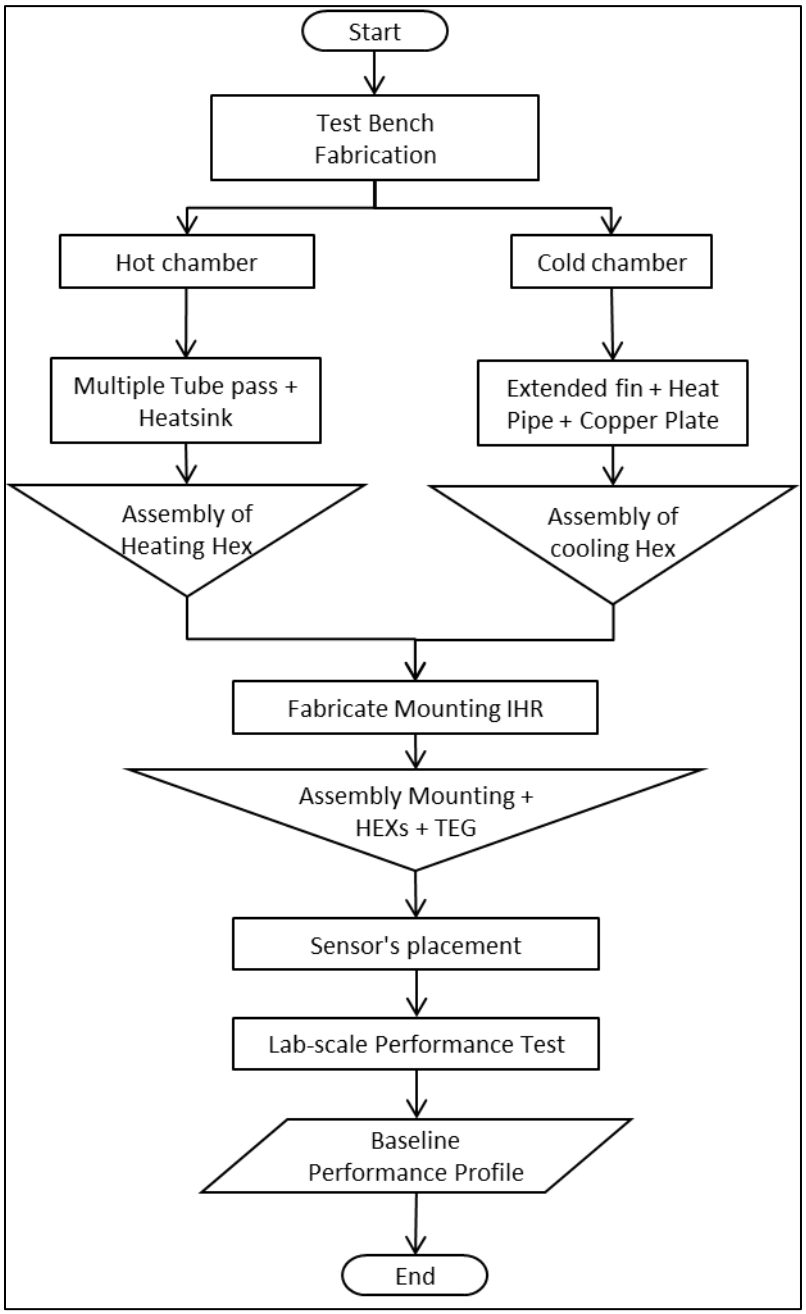

Figure 3.17 Sequential Physical Fabrication And Assembly Process Flowchart

The first fabrication phase focused on the primary heating side of the architecture. The external hot chamber was constructed utilising stainless steel sheet metal, which underwent manual cutting, precision drilling, physical metal forming, and mechanical riveting to achieve the desired geometric boundary. The fundamental physical purpose of this enclosed hot chamber was to securely channel the primary waste heat stream directly from the fuel cell exhaust manifold into the extended aluminium heatsink housing the multiple tube passes, effectively preventing premature thermal diffusion into the ambient laboratory environment. The exhaustive two-

dimensional engineering drawings detailing the precise sheet metal dimensions and folding tolerances for both the hot and cold chambers were catalogued in Appendix D. To construct the internal multiple tube pass architecture, a continuous highly conductive copper tube was prepared and cut into eight individual straight segments. The commercial heatsink fins were carefully measured and manually drilled to allow these straight copper segments to physically penetrate the aluminium structure. Following insertion, fourteen distinct copper elbows were manually soldered to the straight exposed ends, successfully forming a continuous serpentine fluid pathway through the heatsink. This sequence of physical machining, precise drilling, copper tube brazing, and preliminary leak testing for the primary heating heat exchanger was visually documented in Figure 3.18. It was fundamentally acknowledged that manual drilling and mechanical soldering inherently introduce minor microscopic surface deviations and slight geometric tolerances that perfectly symmetric computational models do not possess.

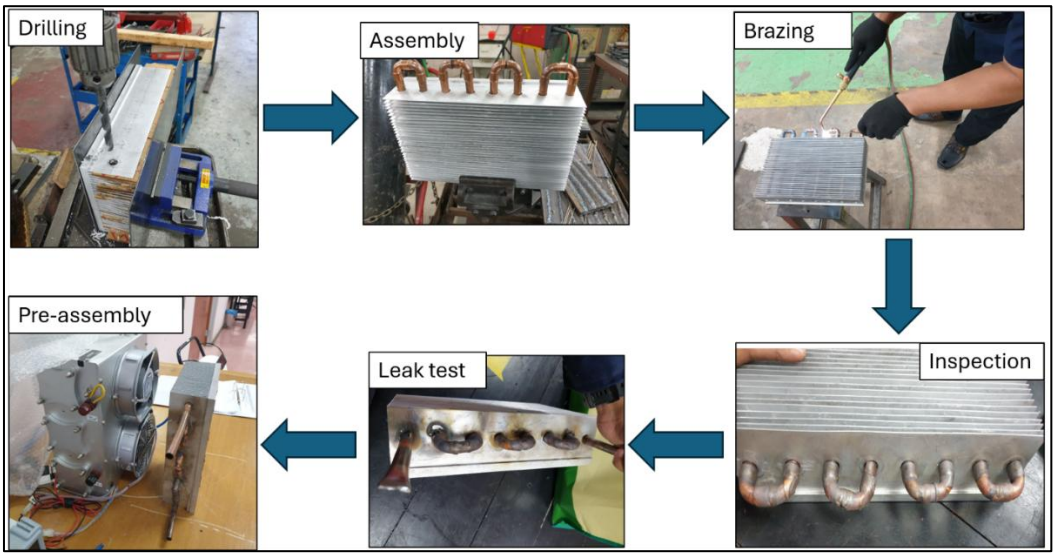

Figure 3.18 Fabrication Process For IHR Heating Heat Exchanger (Tube-Heatsink)

Simultaneously, the second fabrication phase focused on the secondary cooling side of the architecture. The external cold chamber was constructed utilising the identical sheet metal forming and riveting processes applied to the hot chamber. To facilitate efficient thermal conduction away from the TEG modules, a solid copper plate was utilised as the primary cold interface. This plate was mechanically drilled to create precise internal channels, allowing the commercial heat pipes to physically penetrate the structure. These embedded heat pipes were subsequently integrated with

the extended aluminium cooling fins to ensure the thermal energy was effectively passed into the convective cold air stream.

Following the independent fabrication of the heating and cooling heat exchangers, the entire architecture was structurally assembled. A set of eight commercial TEG modules was positioned centrally between the heating and cooling assemblies. To mitigate the unavoidable thermal contact resistance caused by microscopic machining roughness, a thin layer of thermal interface paste was manually applied to both the hot and cold TEG surfaces. The hot side of each module was pressed directly against the base of the primary aluminium heatsink, while the cold side was physically clamped against the intermediate copper plate housing the heat pipes. Figure 3.19 illustrates the IHR cooling heat exchanger and the IHR preassembly, visually demonstrating the component stacking and the cool side clamping mechanism prior to the integration of the channelling hot and cold air chambers.

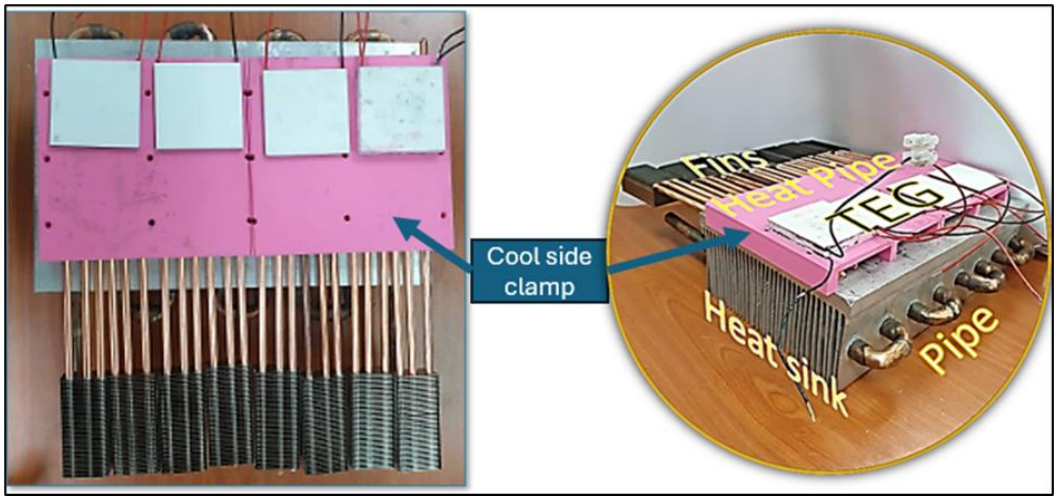

Figure 3.19 IHR Cooling Heat Exchanger And IHR Preassembly Without the Channelling Hot and Cold Air Chambers

Custom structural mounting brackets were fabricated to firmly hold the integrated heating and cooling units together, providing a secure physical clamp to attach the hot chamber directly to the primary fuel cell exhaust manifold. To minimize uncontrolled thermodynamic leakages to the surrounding ambient laboratory environment, the external stainless-steel chambers and the exposed copper elbows of the multiple tube pass were wrapped with external thermal insulation material. The final physically integrated and fully insulated architecture, complete with the external fluid

channelling chambers, is presented in Figure 3.20, effectively marking the completion of the fabrication phase.

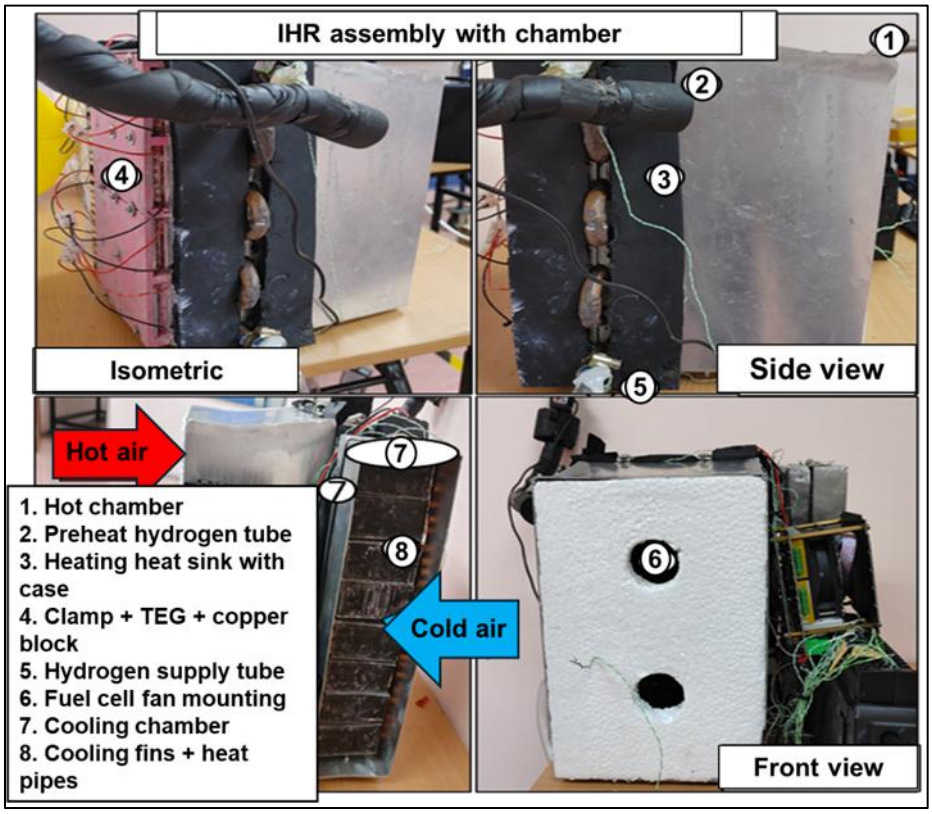

Figure 3.20 Fully Integrated And Insulated Physical Prototype With External Fluid Chambers

3.3.2 Instrumentation and Data Acquisition Setup

To systematically quantify the thermodynamic performance and electrical recovery potential of the fabricated prototype, the physical architecture was integrated into a fully instrumented laboratory test bench. The fundamental objective of this setup was to secure highly precise, steady state empirical data regarding spatial temperature gradients, fluid velocities, and electrical polarization prior to initiating chaotic on road dynamic testing. The fully instrumented experimental test bench, detailing the precise physical integration of the data acquisition sensors and the environmental control apparatus, was visually documented in Figure 3.21.

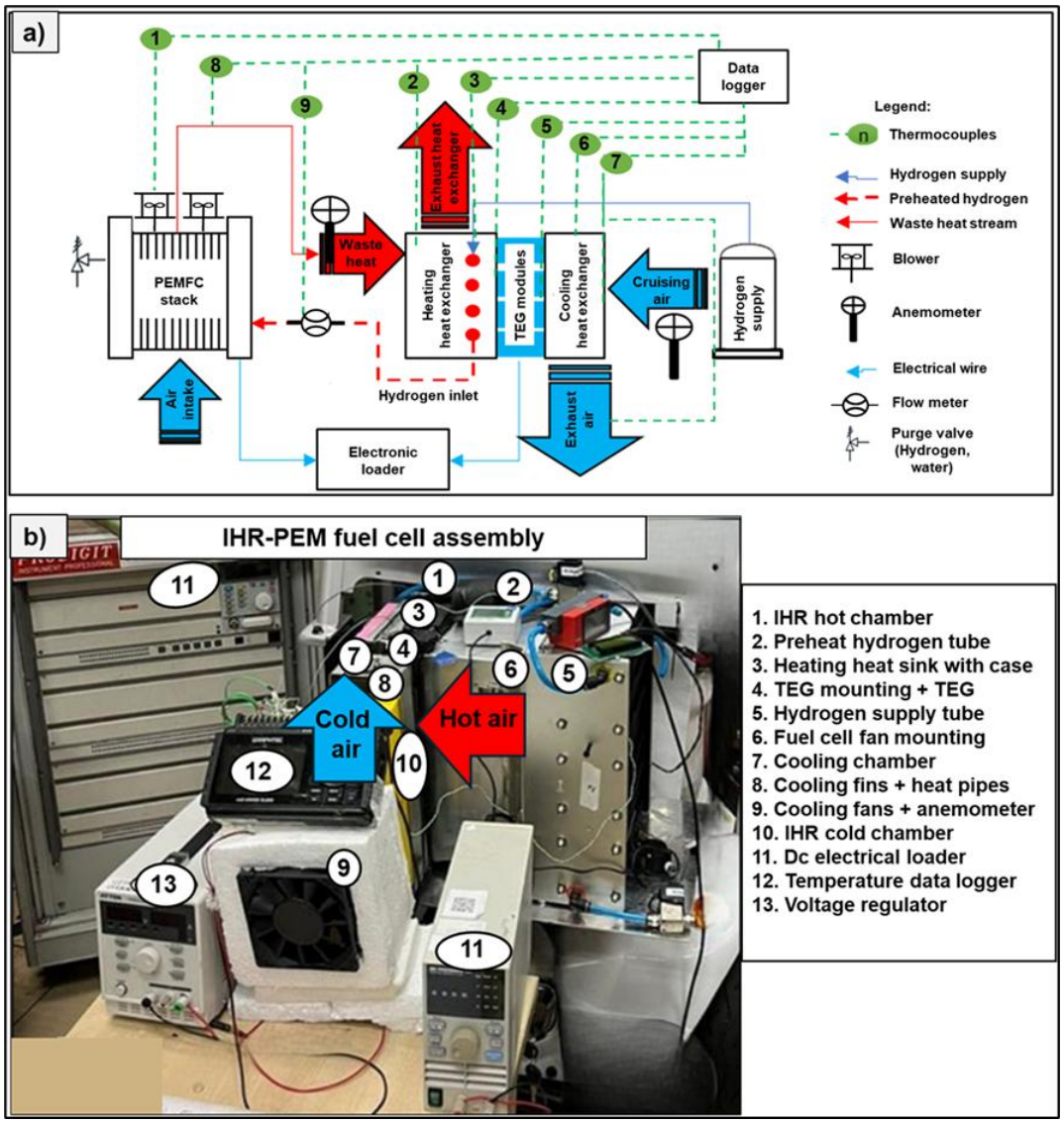

Figure 3.21 a) Schematic and b) Photographic Representation of the Fully Assembled Laboratory Test Bench and IHR Architecture

To map the comprehensive dimensionless temperature distribution profile (X/L) across the integrated architecture, a highly strategic thermal sensor placement strategy was executed. Seven distinct spatial locations were monitored, tracking the thermal energy transfer from the primary fuel cell exhaust ($X/L = 0$) completely through the system to the secondary cold chamber exit ($X/L = 1$). A three-dimensional physical mapping of these specific sensor locations was illustrated in Figure 3.22, while the exact dimensionless extraction distances were catalogued in Table 3.7.

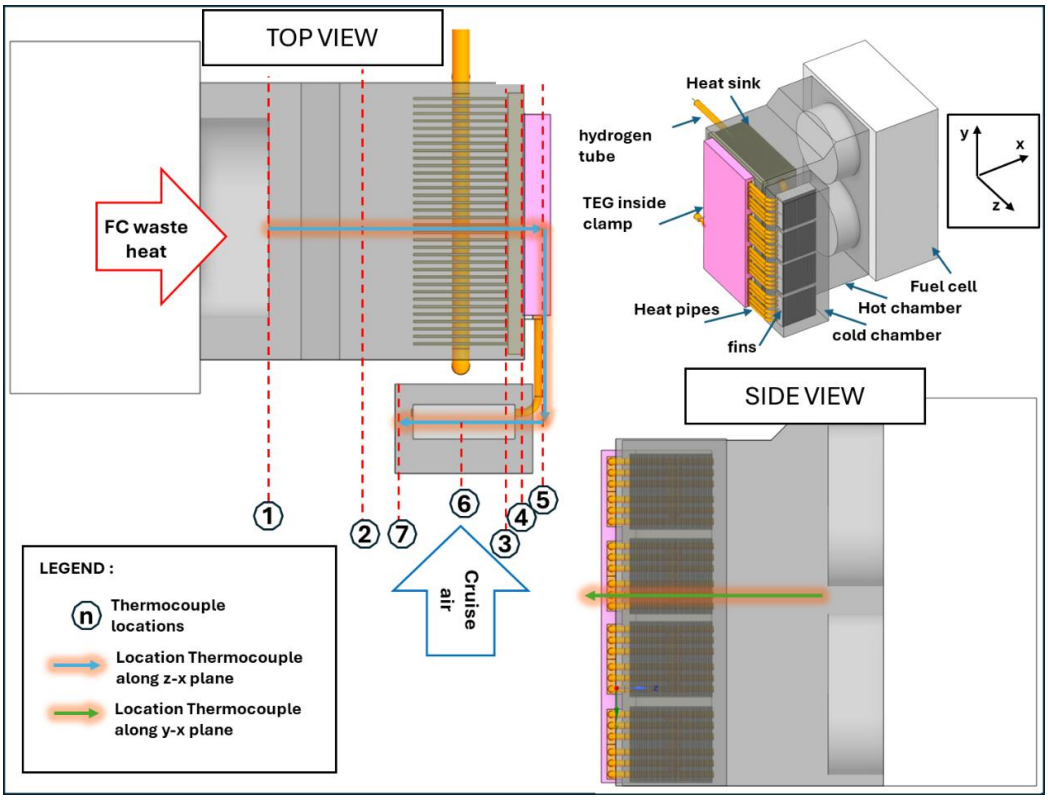

Figure 3.22 Three-Dimensional Spatial Mapping of Thermocouple Locations

Table 3.7
Spatial Mapping of Temperature Sensor Distribution Across the Integrated Architecture

Num.	Location	Distance from reference point (mm)	(X/L)
1	FC	0	0
2	Hot chamber	65	0.14
3	Heat sink top base	175	0.38
4	TEG hot	187	0.4
5	TEG cold	193	0.42
6	Fins	425	0.92
7	Cold chamber	463	1

In addition to the primary spatial nodes mapping the macroscopic thermal gradient, the absolute inlet and outlet temperatures of the internal hydrogen reactant stream were also continuously monitored. Because these specific sensors functioned solely to capture the discrete fluid boundary conditions at the physical extremities of the internal copper tube passes, they were explicitly excluded from the dimensionless

spatial mapping illustrated in Figure 3.22 to maintain visual clarity of the primary heat exchanger profile.

The localised temperatures at all designated physical nodes, including both the solid components of the IHR assembly surfaces and the internal fluid boundaries (hydrogen and air), were measured utilising 0.4 mm twisted K type thermocouples, constructed from nickel chrome and nickel aluminium conductors capable of withstanding up to 250 °C The transient thermal signals from these collective sensors were continuously monitored and recorded simultaneously using a Graphtec GL220A midi data logger. While these specific sensors provide rapid thermal response times, it was fundamentally acknowledged that all physical thermocouples possess inherent manufacturing calibration tolerances. Furthermore, microscopic contact resistances between the sensor tip and the measured solid surfaces inevitably introduce minor experimental uncertainties that deviate from idealized computational boundary conditions.

To strictly monitor and control the fluid dynamics traversing the system, highly specialized delivery and volumetric instruments were deployed. The fundamental hydrogen reactant supply originated from a high-pressure storage cylinder. To ensure safe and stable gas delivery to the integrated architecture during the steady state evaluations, a mechanical pressure regulator was utilised to step down and constantly maintain the physical delivery pressure at a strict 0.5 bar threshold, as demanded by the fuel cell stack. Because the supply pressure was mechanically locked at this constant baseline throughout the laboratory testing, transient tank pressure drop was not a monitored variable during this specific phase. Following this steady pressure regulation, the primary reactant mass flow of the hydrogen gas was precisely measured utilising a Vogtlin Instruments red y compact mass flow meter (GCM G1/4). Simultaneously, the convective velocities of the hot waste heat air stream and the secondary cold cooling air were continuously measured utilising a GM8903 digital anemometer, capable of resolving velocities up to 30 m/s. It must be noted, however, that utilising a handheld point measurement anemometer within a confined duct inherently captures localised streamline velocities, serving as a practical approximation of the total bulk fluid flow rather than an absolute uniform measurement.

To capture the dual electrical power recovery of the system, two distinct programmable direct current electronic loads were integrated into the test bench. To simulate the highly variable current demand typically imposed by a fuel cell electric vehicle traction motor, a high power 33512F DC electronic load (rated for 60 V, 360 A, 5400 W) was directly connected to the primary fuel cell stack. Concurrently, a secondary BK Precision 8540 electronic load (rated for 150 W, 0 to 60 VDC, 1 mA to 30 A) was specifically dedicated to the TEG module array, precisely sweeping the circuit to determine the absolute peak secondary power generation. The exhaustive technical specifications of all deployed measurement instruments and data acquisition hardware were summarized in Table 3.8.

Table 3.8
Technical Specifications of Experimental Instruments and Sensors

Instrument	Specification	Description
Thermocouple	Type, temperature range	K-type (twisted), 250 / °C
	(conductor material) size	(nickel chrome, nickel aluminium), 0.4 / mm
Data logger	Type	Graphtec midi logger GL220A
	No. of channel	20
Electronic Load FC	Model	33512F high power DC electronic load
	Operation Range	60 / V, 360 / A, 5400 / W
Electronic Load TEG		BK PRECISION 8540 150W
	Operation Range	0-60 VDC, 1 mA-30A
DC fan	Model, airflow	Delta electronics DC brushless Fans
	Size (height x diameter x width)	120 x 38 x 120 / mm
	Voltage	12 / V
Flow meter	Manufacturer	Vogtlin instruments
	Model	red-y compact meter GCM G1/4
	Measurement	Hydrogen gas
Anemometer	Model	GM8903
	Velocity, temperature range	0-30 / m s^{-1}, 0-45 / ℃

Instrument	Specification	Description
Pressure regulator	Model	SG2 two-stage
	Inlet, outlet range	310bar, 0-17.2 bar

Finally, to simulate the convective cooling effect of the vehicle cruising velocity within a stationary laboratory environment, an external environmental control apparatus was established. A 12 V DC brushless fan (Delta Electronics, 120 x 38 x 120 mm) was physically aligned with the inlet of the secondary cold chamber to channel ambient air across the extended cooling fins. While this apparatus successfully provides a steady state convective flow for the test bench validation, it was cautiously recognized that a compact axial fan cannot perfectly replicate the uniform, laminar, infinite boundary wind fields experienced by an actual moving vehicle, inherently introducing a margin of aerodynamic deviation into the laboratory baseline.

Crucially, it should be noted that the core physical instrumentation suite detailed herein, encompassing the thermocouples, data logger, and primary flow meters, was deliberately established as a portable, fully integrated data acquisition architecture. This strategic implementation ensured that the identical measurement apparatus could be subsequently deployed for the dynamic on road vehicular testing phase, effectively eliminating instrument based physical variance when comparing the stationary steady state laboratory baseline against the chaotic on road performance data.

To provide a comprehensive macro-level overview of the physical experimental architecture, all previously detailed fluidic, thermal, and electrical subsystems were physically integrated onto a centralized laboratory test bench. Figure 3.21 illustrated the complete schematic and physical configuration of the primary fuel cell coupled with the secondary IHR system, explicitly detailing the routing of the hydrogen reactant lines, the positioning of the K-type thermocouples, and the integration of the data acquisition hardware prior to the commencement of the steady-state testing matrix.

3.3.3 System Pretesting and Calibration Protocols

Prior to initiating the steady state electrical sweeps and introducing live hydrogen reactant into the integrated architecture, a rigorous series of pretesting and calibration protocols were mandated. These preparatory procedures were essential to mitigate critical hardware failures, ensure personnel safety, and establish a verifiable

zero load baseline for the data acquisition suite, thereby minimizing experimental uncertainties before active testing commenced.

The primary safety and operational prerequisite involved a comprehensive fluidic leak evaluation of the customized hydrogen delivery network. Given that the internal copper tube passes were manually routed through the primary hot chamber and secured via mechanical fittings, ensuring hermetic sealing was paramount. A pressurized inert gas test was initially conducted, utilising a localised application of leak detection fluid across all joints, valves, and the pressure regulator interfaces. Following the verification of structural integrity under inert conditions, a highly cautious, low pressure hydrogen sweep was executed while actively monitoring the exterior assembly boundaries with a portable combustible gas detector. While the leak testing protocols effectively ensure operational safety and bulk mass flow continuity, it was acknowledged that microscopic, negligible permeation at the physical material boundaries remains an inherent characteristic of any assembled gas delivery architecture.

Simultaneously, mitigating parasitic thermal losses and ensuring precise thermal transfer across the secondary recovery array required a strict mechanical inspection. The physical interfaces between the primary aluminium heat sink, the hot side of the TEG array, and the secondary cold chamber were systematically evaluated. To minimize localised contact thermal resistance, high performance thermal paste was uniformly applied across all microscopic surface asperities joining the solid-state modules to the metallic boundaries. Furthermore, to rigorously restrict parasitic thermal leakages, a dedicated 3 mm thickness of thermal insulation material was physically applied to both the internal and external surfaces of the primary hot chamber. The structural integrity of this dual boundary insulation was systematically verified to ensure the transient waste heat was directionally channelled through the TEG array rather than dissipating into the ambient laboratory environment. It was cautiously recognized, however, that perfect adiabatic insulation was physically impossible; minor ambient convective heat losses from the exterior chassis inherently exist and form part of the laboratory boundary condition.

Finally, immediately prior to the activation of the fuel cell electronic load, a comprehensive zero load sensor baseline calibration was executed. The Graphtec data logger and all corresponding 0.4 mm K type thermocouples were activated and left to record the stationary laboratory environment for a continuous 15 minute duration. This

specific protocol verified that all spatial temperature nodes uniformly registered the identical ambient room temperature baseline, confirming that no localised sensor degradation, wiring faults, or electromagnetic interference from the powered (but inactive) electronic load were skewing the data acquisition system. Only after this stabilized thermal equilibrium and zero power electrical baseline were empirically verified, was the primary reactant flow initiated, and the testing matrix commenced.

3.3.4 Experimental Procedure and Testing Matrix

To systematically capture the thermodynamic and electrical performance of the system, a highly structured experimental testing matrix was executed. The empirical procedure was fundamentally divided into two primary operational configurations to allow for direct comparative analysis: an isolated baseline utilising only the primary fuel cell stack without the recovery architecture, and the fully integrated dual recovery prototype (FC and IHR).

For each specific testing configuration, the primary fuel cell was subjected to a highly controlled electrical current sweep utilising the programmable DC electronic load. To capture the full operational bandwidth of the system while mimicking the variable demand of an electric traction motor, the electrical sweep was initiated at a minimal draw of 1 A, progressed to 5 A and 10 A, and subsequently increased in precise 5 A increments until the maximum operational threshold of 60 A was achieved.

At each discrete current increment, a strict temporal holding protocol was enforced prior to data acquisition to ensure the physical system achieved a quasi-steady thermodynamic state. The real time thermal stabilization of the TEG surface temperatures was selected as the primary empirical indicator for this equilibrium condition. Observations indicated that achieving this quasi-steady state required a temporal duration of approximately 4 to 5 minutes per increment. However, it was fundamentally acknowledged that this stabilization period inherently varied across different testing phases, as the specific transient thermal response was deeply dependent on both the magnitude of the applied electrical load and the instantaneous convective cooling rate.

Crucially, throughout these prolonged stabilization windows, the proprietary internal controller of the fuel cell autonomously commanded a mechanical solenoid valve to execute an instantaneous hydrogen reactant purge every 10 seconds. This

factory calibrated sequence, lasting only on the order of milliseconds, was a mandatory operational constant designed to forcibly clear accumulating liquid water from the internal flow channels to prevent membrane flooding. While this rapid valve actuation induced microscopic, millisecond scale fluctuations in the hydrogen mass flow meter readings, the physical flow rate instantly restabilized. Because this periodic purging was a hardcoded mechanical necessity, and its transient duration fell well below the macroscopic sampling resolution required for steady state analysis, its localised physical effects were inherently absorbed and averaged into the overarching 4 to 5 minute quasi steady state stabilization window.

To systematically evaluate the secondary influence of the vehicle cruising velocity, the integrated architecture was subjected to three distinct convective cooling scenarios utilising the external environmental control fan. The testing matrix recorded the complete current sweep under external cooling velocities of 0, 5, and 10 m/s. This comprehensive multidimensional matrix successfully isolates the specific impact of the simulated aerodynamic wind on the secondary TEG power generation and the primary fuel cell polarization. The complete specifications of these fundamental experimental parameters were summarized in Table 3.9.

Table 3.9
Specifications of the Experiment Parameters

Parameter	**Value**	
	Baseline (PEM fuel cell only)	PEM fuel cell + IHR
Cruising air velocity (replicated only for IHR cooling)	Nil	(0, 5, 10) $m\ s^{-1}$
PEM fuel cell current load	(0 – 60) A	(0 – 60) A
PEM fuel cell purging interval	10 s	10 s

By enforcing the 4 to 5 minute thermal stabilisation window at every discrete testing node, the transient physical lag inherent to the massive aluminium heatsink was effectively mitigated, yielding a highly reliable steady state baseline. Nevertheless, to maintain absolute academic rigor, it must be cautiously recognized that achieving a mathematically perfect thermal equilibrium was practically impossible within a physical laboratory setting. Minor, unavoidable ambient room temperature fluctuations

and subtle aerodynamic boundary layer disruptions inherently ensure that the recorded data represents a highly controlled quasi steady state rather than an absolute idealized steady state.

3.3.5 Experimental Repetition

To ensure absolute empirical reliability and mitigate the inherent uncertainties associated with physical laboratory testing, a rigorous protocol of experimental repetition was deliberately enforced throughout the methodology. The repetition was executed across two distinct operational phases. Initially, during the pre-testing and calibration phase, the baseline zero load sequences were repeated multiple times. This specific repetition was necessary to perfectly synchronise the data acquisition instruments, ensuring that the environmental control fan speeds, ambient room temperatures, and the primary fuel cell sensor readings achieved a consistent, stable baseline prior to introducing the active electrical loads.

Subsequently, during the active testing matrix, every individual case parameter configuration specifically, the discrete current sweeps under the 0, 5, and 10 m/s cooling velocities was deliberately repeated three separate times. The thermodynamic and electrical data recorded during these three independent physical trials were subsequently aggregated, and the arithmetic mean was calculated to generate the final reported empirical values. By executing this systematic repetition, the methodology successfully filtered out anomalous transient spikes, unpredictable ambient laboratory fluctuations, and minor human operational errors. While this rigorous repetition significantly enhanced the overall statistical confidence of the results, it was cautiously acknowledged that minor variance between individual physical runs remained an unavoidable characteristic of experimental thermodynamics.

3.3.6 Mathematical Formulation of Performance Metrics

Following the successful acquisition of the raw empirical data across the steady state stabilization windows, a rigorous mathematical framework was established to process the localised temperature and electrical measurements into macroscopic performance metrics. This data processing phase was systematically divided into three

primary evaluative domains: thermal heat transfer analysis, electrical power generation, and overall system efficiency.

3.3.6.1 Thermal Performance and Heat Recovery Analysis

The localised thermocouple readings were initially translated to quantify the absolute heat transfer performance of the integrated primary and secondary recovery processes. To establish the total baseline thermal energy available within the system, the simplified primary fuel cell thermal power generation was calculated. This specific formulation was predicated on the theoretical assumption that the generated product water exists entirely as saturated vapor at the stack exhaust outlet. While this provides a highly standardised theoretical baseline, it was cautiously acknowledged that practical multiphase fluid dynamics may introduce minor deviations from this idealized saturated state. The thermal power generation was evaluated based on the total number of cells, the total stack voltage, and the stack output current [30].

$$P_{th,stack} = (1.25n - V_{stack})I_{stack} \quad \text{[W]} \quad (3.35)$$

To quantify the primary recovery mechanism, the absolute hydrogen preheating degree was evaluated. The rate of thermal energy successfully absorbed by the internal hydrogen reactant gas within the multiple tube passes was calculated utilising the measured mass flow rate, the specific heat capacity of hydrogen, and the physical temperature differential between the inlet and outlet boundaries.

$$\dot{Q}_{H2} = \dot{m}_{h2}\, C_{P,H2}\, \Delta T_{H2} \quad \text{[W]} \quad (3.36)$$

Subsequently, the secondary thermal recovery mechanism facilitated by the solid-state arrays was analysed. The fundamental Seebeck coefficient, representing the magnitude of the induced thermoelectric voltage relative to the measured physical temperature difference across the modules, was established first [46].

$$\alpha = \frac{V_{TEG}}{\Delta T_{TEG}} \quad [\text{W/K}] \quad (3.37)$$

The distinct heating and cooling heat transfer rates across the physical module surfaces were adapted from established thermoelectric evaluation models. These boundary rates were deeply influenced by this Seebeck coefficient, alongside the localised surface temperature differentials, the circuit amperage, the material thermal conductivity (standardised at 1.2 W/mK) , and the internal ohmic resistance (standardised at 0.8 ohms). The discrete heating absorption rate at the hot surface was calculated accordingly [46].

$$\dot{Q}_{h_{TEG}} = \alpha T_{h_{TEG}} I_{TEG} - \kappa_{TEG} \Delta T_{TEG} - 0.5 I^2{}_{TEG} R_{TEG} \quad [\text{W}] \quad (3.38)$$

Conversely, the discrete cooling rejection rate at the cold surface, which dictates the necessary sizing of the extended external fins, was calculated by accounting for the resistive Joule heating effect [46].

$$\dot{Q}_{c_{TEG}} = \alpha T_{c_{TEG}} I_{TEG} - \kappa_{TEG} \Delta T_{TEG} + 0.5 I^2{}_{TEG} R_{TEG} \quad [\text{W}] \quad (3.39)$$

The total effective heat transfer rate for the secondary recovery array was subsequently defined as the mathematical summation of these boundary heating and cooling rates [132].

$$\dot{Q}_{TEG} = \dot{Q}_{c_{TEG}} + \dot{Q}_{h_{TEG}} \quad [\text{W}] \quad (3.40)$$

Finally, the overarching capacity of the integrated recovery architecture was quantified utilising a dimensionless waste heat utilization factor. This metric establishes the direct ratio between the total recovered thermal power (the summation of the hydrogen preheating rate and the secondary array heat transfer rate) and the total baseline thermal power generated by the primary stack [17].

$$\mu_{WH} = \frac{\dot{Q}_{H2} + \dot{Q}_{TEG}}{P_{th.FC}} \text{ x } 100 \quad [\%] \quad (3.41)$$

3.3.6.2 Electrical Performance Analysis

The baseline evaluation of the electrical performance relies entirely upon fundamental Ohms law principles, utilising the precise voltage and current parameters recorded by the programmable DC electronic loads. To establish the absolute benchmark, the electrical power production of the primary fuel cell stack operating independently, without the integrated recovery architecture, was calculated first [12].

$$P_{el,stack} = V_{stack} I_{stack} \quad [W] \quad (3.42)$$

To capture the primary performance enhancement, the identical formulation was applied to the data acquired when the primary stack was physically integrated with the recovery architecture, denoted utilising the superscript IHR [12].

$$P_{el,stack}^{IHR} = V_{el,stack}^{IHR} I_{el,stack}^{IHR} \quad [W] \quad (3.43)$$

Concurrently, the secondary electrical power directly generated by the recovery array was calculated utilising its independently measured voltage and precisely swept current [136].

$$P_{el,TEG} = V_{TEG} I_{TEG} \quad [W] \quad (3.44)$$

The fundamental enhancement in the primary stack power output, strictly resulting from the elevated internal reaction kinetics facilitated by the preheated hydrogen, was evaluated as the fractional ratio between the absolute power increase and the isolated benchmark in power percentage points (pp).

$$\Delta P_{el_{stack}} = \frac{P_{el,stack}^{IHR} - P_{el,stack}}{P_{el,stack}} \quad [pp] \quad (3.45)$$

3.3.6.3 System Efficiency and Reactant Consumption Analysis

To thoroughly evaluate the true thermodynamic efficiency of the system, the precise consumption of the hydrogen reactant must be mathematically reconciled against the electrical output. The fundamental mass flow rate required to sustain the primary stack operation was derived utilising a standard electrochemical consumption constant alongside the measured electrical power and individual cell voltage [12].

$$\dot{m}_{h2} = \frac{1.05 \text{ x } 10^{-8} \ P_{el,stack}}{V_{cell,stack}} \quad [kg/s] \quad (3.46)$$

To evaluate the cumulative efficiency, the total theoretical hydrogen consumption was calculated over the targeted 180 second steady state data extraction window utilised for each specific test case [12].

$$m_{h2} = \dot{m}_{h2} \text{ x } t \quad [kg] \quad (3.47)$$

Crucially, this idealized steady state consumption must be modified to account for the physical reactant lost during the automated mechanical purging cycles. Over the designated 180 second extraction window, the 10 second autonomous purge interval results in precisely 18 discrete purge events, each lasting an estimated 0.5 seconds. By applying the previously established mass flow rate to these transient purge durations, the physical mass of the lost hydrogen was accurately quantified. The absolute total consuming hydrogen mass was therefore defined as the summation of the steady state reacted mass and this calculated purge loss mass. The total theoretical energy consumed from the stack was subsequently calculated utilising this absolute total mass and the specific Higher Heating Value (HHV) of hydrogen (1.43 x 10^8 J/kg)[12]. It was noted that utilising the HHV assumes complete theoretical condensation of the product water, serving as a maximum thermodynamic ceiling rather than a perfectly attainable practical limit [12].

$$E_{h2} = m_{h2,total} \text{ x } HHV \quad \text{[J]} \quad (3.48)$$

The actual physical energy generated by the primary stack over this identical temporal window was calculated based on the sustained electrical power output as a function of time [12].

$$E = P_{el,stack} \text{ x } t \quad \text{[J]} \quad (3.49)$$

The absolute baseline energy efficiency of the primary stack was thus defined as the ratio of the generated electrical energy to the total theoretical energy potential of the consumed hydrogen mass [12].

$$\eta_{stack} = \frac{E}{E_{h2}} \text{ x } 100 \quad \text{[\%]} \quad (3.50)$$

Ultimately, the comprehensive efficiency enhancement achieved by the integrated dual recovery architecture was evaluated as the fractional ratio between the calculated efficiency increase and the original benchmark efficiency presented as the unit of percentage points [12].

$$\Delta\eta_{stack} = \frac{\eta_{stack}^{IHR} - \eta_{stack}}{\eta_{stack}} \quad \text{[pp]} \quad (3.51)$$

3.3.7 Experimental Uncertainty and Error Propagation

To maintain absolute academic rigor and transparency, it was fundamentally acknowledged that no physical empirical measurement was completely devoid of error. Every recorded data point inherently possesses a margin of uncertainty dictated by the manufacturing tolerances, calibration drift, and finite digital resolution limits of the deployed instrumentation. Consequently, to mathematically validate the fidelity of the reported performance metrics, a comprehensive uncertainty analysis was executed across the entire testing matrix.

The uncertainty analysis was systematically divided into two distinct layers. The first layer quantified the independent absolute and relative uncertainties of the primary measurement hardware, including the K type thermocouples, the mass flow meter, and the precision digital multi-meter. The absolute uncertainty was fundamentally constrained by the fixed resolution of the instrument itself. However, the relative (percentage) uncertainty dynamically fluctuates based on the magnitude of the measured value. Table 3.10 catalogues these independent hardware uncertainties, specifically comparing the deviations at the lowest baseline load (1 A) against the peak operational load (60 A).

Table 3.10
First Layer Independent Measured Parameters and Hardware Uncertainty

Measured Parameter	**Instrumentation / Sensor Type**	**Operational Range**	**resolution instrument**	**Absolute Uncertainty**		**Relative Uncertainty**	
				FC lowest Load at 1 A	FC Peak Load at 60 A	FC lowest Load at 1 A (%)	FC Peak Load at 60 A (%)
Spatial Surface Temperatures (IHR & TEG) (°C)	K-type Thermocouple	23 to 65 °C	± 0.01 °C	± 4.3E-4	± 1.5E-4	0.04	0.02
Hydrogen Flow Rate (LPM)	Digital Mass Flow Meter	0 to 32 LPM	± 0.01 LPM	± 1.0E-2	± 3.1E-4	1.00	0.03
Fuel Cell Voltage (V)	Digital Multimeter	23 to 45 V	± 0.01 V	± 4.3E-4	± 2.2E-4	0.04	0.02
Fuel Cell Current (A)	Digital Multimeter	1 to 60 A	± 0.01 A	± 1.0E-2	± 1.7E-4	1.00	0.02
TEG Voltage (V)	Precision Digital Multimeter	0.028 to 0.7 V	± 0.001	± 3.6E-2	± 1.4E-5	3.57	0.14
TEG Current (A)	Precision Digital Multimeter	0.028 to 0.3 A	± 0.001	± 3.6E-2	± 3.3E-5	3.57	0.33

Due to hardware limits, the relative uncertainty was inherently magnified at the lowest operational boundaries. For instance, at the 1 A baseline, the primary fuel cell produces an ultra low grade heating condition. Consequently, the TEG generates microscopic voltage and current outputs (e.g., approximately 0.028 V and 0.028 A) that fall precariously close to the fixed ±0.001 resolution limit of the precision multimeters. Measuring values so near to the absolute detection threshold of the instrument mathematically yields a relatively high 3.57% uncertainty for both voltage and current. However, as the physical thermal gradients intensify at the 60 A peak load, the measured electrical outputs significantly expand, subsequently collapsing the relative instrument error to a negligible 0.14% and 0.33%, respectively. This physical phenomenon dictates that the experimental data yields its highest mathematical confidence precisely at the peak performance limits where the recovery architecture was most active.

The second layer of the analysis evaluated how these localised independent errors compounded when processed through the mathematical performance equations established in Section 3.2.4. To accurately quantify this compounding effect, the standard Root Sum Square (RSS) method for error propagation, originally formulated by Kline and McClintock, was deployed. For a calculated dependent performance metric R derived from a set of independent measured variables (x_1, x_2, …, x_n) the total propagated uncertainty ω_R was calculated utilising the partial derivatives of the function alongside the individual variable uncertainties (ω_1, ω_2, …, ω_n), as expressed in Equation 3.52, [31].

$$\omega_R = \left[\left(\frac{\partial R}{\partial x_1}\omega_1\right)^2 + \left(\frac{\partial R}{\partial x_2}\omega_2\right)^2 + \cdots + \left(\frac{\partial R}{\partial x_n}\omega_n\right)^2\right]^{\frac{1}{2}} \tag{3.52}$$

Applying this rigorous mathematical propagation to the primary calculated metrics yields the final experimental uncertainty matrix, catalogued in Table 3.11.

Table 3.11
Second Layer Propagated Uncertainty for Calculated Performance Metrics

	Absolute Uncertainty	**Relative Uncertainty**

Propagation Uncertainty Parameter	FC lowest Load at 1 A	FC Peak Load at 60 A	FC lowest Load at 1 A (%)	FC Peak Load at 60 A (%)
TEG Electrical Power (We)	± 5.1E-2	± 36.3E-4	± 5.05	± 0.36
Fuel Cell Electrical Power (We)	± 1.0E-2	± 2.8E-4	± 1.00	± 0.03
TEG Heat transfer (W)	± 6.2E-2	± 1.4E-5	± 6.19	± 0.14
Fuel Cell Thermal Power (W)	± 1.0E-2	± 2.8E-4	± 1.00	± 0.03
Hydrogen Heat Transfer (W)	± 1.0E-2	± 3.5E-4	± 1.00	± 0.03
Fuel cell efficiency (%)	± 1.4E-2	± 2.8E-4	± 1.41	± 0.03
waste heat utilization (%)	± 6.3E-2	± 1.5E-5	± 6.35	± 0.15

The propagated data firmly supported the structural integrity of the experimental methodology. The maximum compounded uncertainty occurs within the calculated Waste Heat Utilization and the TEG Electrical Power at the absolute lowest 1 A load, peaking at safely acknowledged thresholds of 6.35% and 5.05%, respectively. Crucially, as the primary stack achieved its maximum thermal and electrical output at 60 A, the propagated relative uncertainties for all critical system performance metrics organically drop well below the 1.00% threshold. This comprehensive mathematical bounding ensured that the final steady state data utilised for the subsequent numerical validation and comparative performance analysis represents a highly reliable, mathematically defended empirical baseline.

3.3.8 Numerical Calibration Feedback Loop

Following the acquisition of the steady state empirical data, a critical numerical calibration feedback loop was executed. While the initial CFD model of the selected Design 2 architecture was utilised to guide the physical fabrication process, verifying the computational fidelity of this model against physical reality was a mandatory academic requirement. To accomplish this, the empirical boundary conditions recorded during the physical test bench phase were systematically fed back into the ANSYS Fluent solver to evaluate the predictive accuracy of the numerical simulation.

To subject the computational model to the most rigorous validation standard, the peak operational case consisting of the 60 A electrical load coupled with the maximum 10 m/s convective air velocity was selected for the rerun. This specific operational extreme was intentionally chosen because it represents the highest thermal gradients, the maximum internal reactant mass flow rate, and the most aggressive external aerodynamic cooling scenario. If the numerical model successfully resolves the complex multiphase conjugate heat transfer at this extreme boundary, its fundamental reliability across the lower operational spectrum can be confidently inferred.

The calibration process focused strictly on the critical thermal parameters that dictate the secondary recovery performance and the primary internal reactant heating. The simulated results were extracted and directly compared against the localised thermocouple test bench data for four primary metrics: the absolute hydrogen preheated temperature, the discrete TEG physical surface temperatures (hot and cold sides), the total TEG temperature difference across the solid-state modules, and the net hydrogen temperature difference between the inlet and outlet boundaries.

To mathematically quantify the agreement between the physical laboratory prototype and the computational model, the standard absolute relative percentage error was calculated for each targeted parameter. This deviation evaluates the numerical prediction (V_{num}) against the established experimental baseline (V_{exp}), as expressed in Equation 3.53.

$$Error\ validation\ (\%) = \left|\frac{V_{exp} - V_{num}}{V_{exp}}\right| x\ 100 \qquad [\%] \qquad (3.53)$$

While this numerical calibration feedback loop ensured a highly refined computational tool, it must be cautiously acknowledged that achieving a zero percent deviation was practically impossible. The CFD environment inherently relied upon mathematically idealized boundary conditions, perfect material homogeneity, and strictly defined adiabatic walls. Conversely, the physical test bench data inherently absorbed minor manufacturing defects, subtle ambient convective heat losses, and localised contact thermal resistances. Therefore, an acceptable error threshold, typically bounded within 10% for complex thermal systems, was established to validate the model while respecting the unavoidable presence of physical experimental uncertainty.

3.4 On Road Dynamic Testing

3.4.1 Lightweight Vehicle Specifications and System Integration

To evaluate the integrated recovery architecture under realistic transient boundary conditions, the physical test bench was transitioned onto a mobile platform. A commercial lightweight electric vehicle was procured to serve strictly as a dynamic vehicular test bed. Specifically, a GRF-04 Minibus E900 four-wheel scooter (Dezhou Yisen New Energy Auto Co., Ltd.) was utilised. The primary academic focus of this phase remained exclusively on the thermodynamic and electrical performance of the fuel cell and the secondary IHR system; consequently, specific vehicular propulsion metrics, such as traction motor efficiency or drivetrain torque, were intentionally excluded from the measurement scope.

To physically accommodate the experimental architecture, custom structural mountings and a semi-enclosed protective casing were fabricated and integrated onto the buggy chassis. These dedicated fixtures securely anchored the primary fuel cell stack, the IHR hardware, the thermodynamic sensor arrays, and the fluidic delivery network, attempting to ensure structural rigidity against induced road vibrations. Furthermore, the external front casing was specifically constructed to provide rudimentary environmental shielding for the sensitive electrochemical and digital components against light precipitation and physical debris. It was cautiously acknowledged, however, that this custom enclosure does not constitute a fully weatherproof barrier, inherently leaving the experimental architecture vulnerable to heavy rain or severe outdoor elements. Figure 3.23 visually documents this complete physical integration, explicitly illustrating the custom instrument dashboard and the spatial compactness required to house the dual recovery architecture within the physical boundaries of the mobile platform.



Figure 3.23 Photographic Representation of The Fully Assembled Fuel Cell Buggy, Detailing The Physical Integration of The Primary Stack, IHR System, Protective Casing, and Instrumentation

For the mobile reactant supply, a standard 9 L high pressure hydrogen cylinder, structurally rated for a maximum capacity of 300 bar, was securely mounted to the rear vehicle framework. However, as a strict operational safety precaution for dynamic on road testing, the physical cylinder was intentionally pressurized to a maximum threshold of only 120 bar.

To establish an accurate baseline for the subsequent variable weight loading evaluations, the cumulative mass of the physical modifications was meticulously documented. Rather than detailing the negligible mass of individual microscopic sensors, the total instrumented curb weight was aggregated by primary subsystems. The physical capabilities of the 800 W traction motor inherently bound the kinetic limits of the testing cycle, and it was required to overcome a total baseline instrumented weight of 196 kg prior to the addition of any human payloads. The comprehensive vehicle specifications and this grouped baseline mass were summarized in Table 3.12.

Table 3.12
Specifications and Baseline Instrumented Mass of the Mobile Test Platform

Parameter	Specification / Mass (kg)
Vehicle Platform Specifications	
Manufacturer	Dezhou Yisen New Energy Auto Co., Ltd.
Model	GRF-04 Minibus E900 Four-Wheel Scooter
Dimensions (L x W x H)	2.1 m x 0.96 m x 1.6 m
Seating Capacity	3
Traction Motor	60 V, 500 to 800 W (Battery Powertrain)
Instrumented Mass Breakdown	
Raw Buggy Chassis	150 kg
Fuel Cell and IHR System	18 kg
Data Acquisition and Auxiliary 12 V Battery	20 kg
Hydrogen Cylinder (120 bar) and Mounts	8 kg
Total Baseline Instrumented Weight (0p)	**196 kg**

3.4.2 Mobile Instrumentation and Data Acquisition

The electrical architecture of the mobile platform necessitated a specialized integration strategy to ensure absolute data fidelity. Powering the delicate instrumentation or the initial startup sequence directly from the primary fuel cell would introduce a parasitic load, mathematically skewing the experimental performance metrics. Consequently, an independent 12 V automotive battery was installed to isolate the data acquisition circuit. As illustrated in the electrical schematic diagram (Figure 3.24), this 12 V source supplied the initial transient power required by the proprietary fuel cell controller. Crucially, once the fuel cell stack achieved operational status, a manual switch was utilised to physically sever this 12 V connection. This specific mechanical intervention guaranteed that the fuel cell operated entirely independently during the driving cycle. Furthermore, the traction motor required a 60 V operating threshold while the fuel cell open-circuit voltage peaked at 43 V. A DC/DC step-up

inverter was successfully integrated into the primary powertrain to bridge this strict voltage differential.

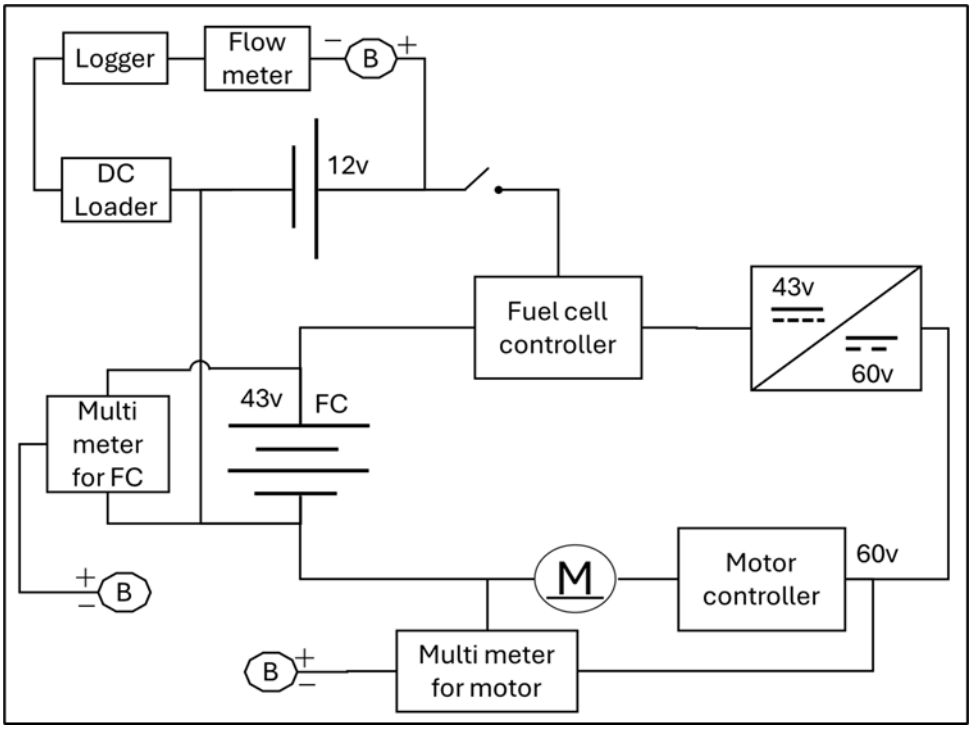

Figure 3.24 Electrical Schematic Diagram of the Mobile Fuel Cell Buggy Illustrating the Isolated 12V Instrumentation Circuit and the Primary Motor Powertrain

Maintaining experimental consistency between the laboratory phase and the mobile evaluations was a primary methodological objective. The core instrumentation suite, comprising the K-type thermocouples, the Graphtec data logger, and the digital hydrogen mass flow meter, was directly transferred from the stationary test bench and mounted onto the buggy. Digital multimeters equipped with continuous file-logging capabilities were added to the sensing matrix to accurately capture the dynamic electrical power generation of the fuel cell, the TEG array, and the traction motor demand. Because the transient current loads experienced during the outdoor driving cycles never exceeded the maximum 60 A boundary previously evaluated on the test bench, the comprehensive error propagation and hardware uncertainty limits established in Section 3.2.6 remain mathematically valid. Therefore, these pre-established limits conservatively bound the mobile performance data without requiring redundant recalculation.

Tracking the physical cruising velocity and the corresponding hydrogen consumption required practical adaptation for the outdoor environment. Vehicle speed and live GPS coordinates were continuously logged utilising a mobile software application (Zeopoxa cycling app). Simultaneously, the digital display of the hydrogen mass flow meter was visually recorded via a mounted camera. Extracting continuous instantaneous data from massive video files across prolonged driving cycles was highly prone to synchronization errors. Therefore, a stabilized averaging method was deployed. During both the 1 km constant speed runs and the short intervals of the scaled New European Driving Cycle (NEDC) cycle, the flow readings were allowed to stabilize following an initial 2-minute purging phase. The maximum and minimum values of this stabilized, low-fluctuation window were extracted and averaged. This cautious methodology yields a highly reliable mean consumption rate while actively filtering out erratic transient measurement spikes.

Finally, the physical transition to the mobile buggy necessitated an expanded spatial temperature mapping strategy. Unlike the enclosed laboratory bench, the on-road architecture interacted heavily with the varying ambient environment. The dimensionless extraction profile (X/L) was subsequently expanded from seven to ten discrete measurement nodes. This new distribution specifically added critical tracking points at the fuel cell air intake (X/L = 0), the heat pipe boundary, and the external cruising air boundary (X/L = 1). This expanded thermal mapping accurately captures the total thermodynamic envelope of the moving vehicle. The updated spatial locations were visually represented in Figure 3.25 and mathematically catalogued in Table 3.13.

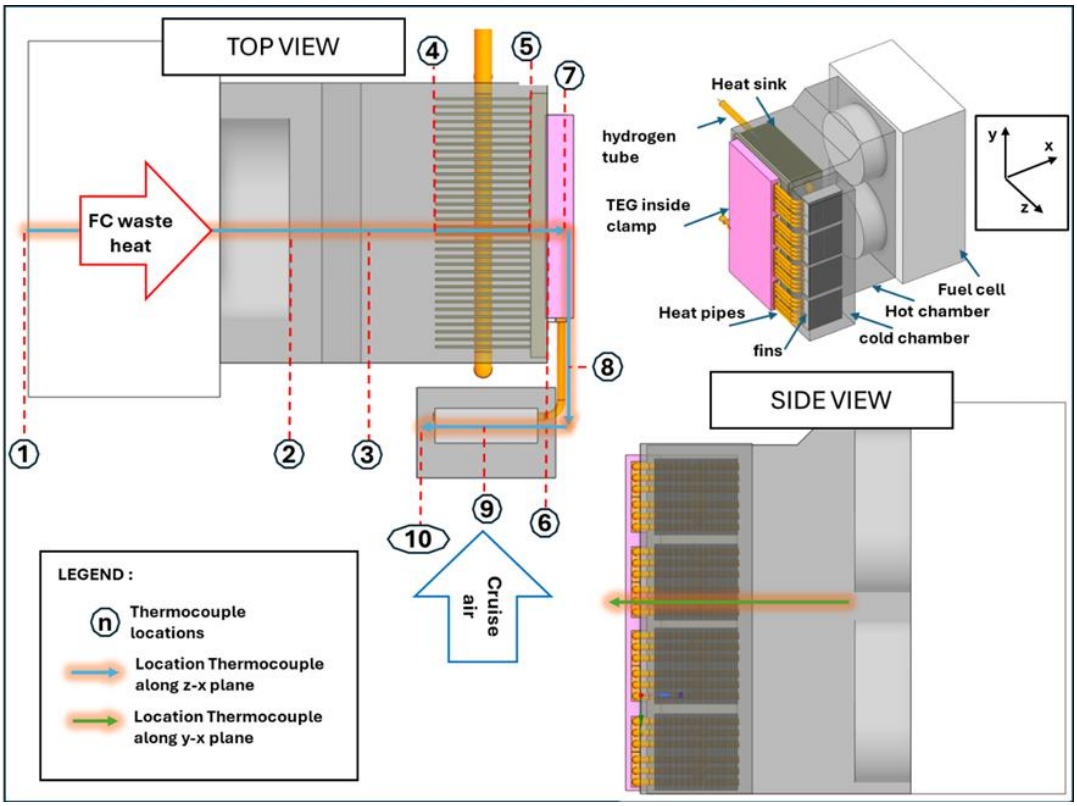

Figure 3.25 Three Dimensional Spatial Mapping of the Ten Thermocouple Locations for the Mobile Architecture

Table 3.13
Spatial Mapping of Temperature Sensor Distribution Across the Mobile Architecture

Num.	Location	Distance from reference point (mm)	(X/L)
1	FC air intake	0	0
2	FC waste heat	230	0.33
3	Hot stream	295	0.43
4	Hot fins	385	0.56
5	Hot base	405	0.59
6	TEG hot side	417	0.6
7	TEG cold side	423	0.61
8	Heat pipe	584	0.84
9	Cold fins	655.1	0.95
10	Cruising air	692.1	1

3.4.3 Environmental Boundary Conditions and Test Location

Establishing a reliable physical baseline for the dynamic evaluations required a controlled outdoor environment. The on-road testing was conducted at the Tun Abdullah Mohd Salleh Hall parking lot facility, located within the UKM campus. Figure 3.26 provides an aerial geographical mapping of this selected test location. The physical driving route consisted of a closed rectangular circuit circulating the perimeter of the main building. A single complete lap along this defined trajectory measured precisely 333 m. Consequently, executing a standard 1 km continuous driving cycle required the vehicle to complete three consecutive laps followed by an additional 100 m linear straightaway. Utilising a closed perimeter circuit on relatively flat tarmac was a deliberate methodological choice, actively minimizing the erratic influence of severe elevation gradients and unpredictable public traffic on the 800 W traction motor load.

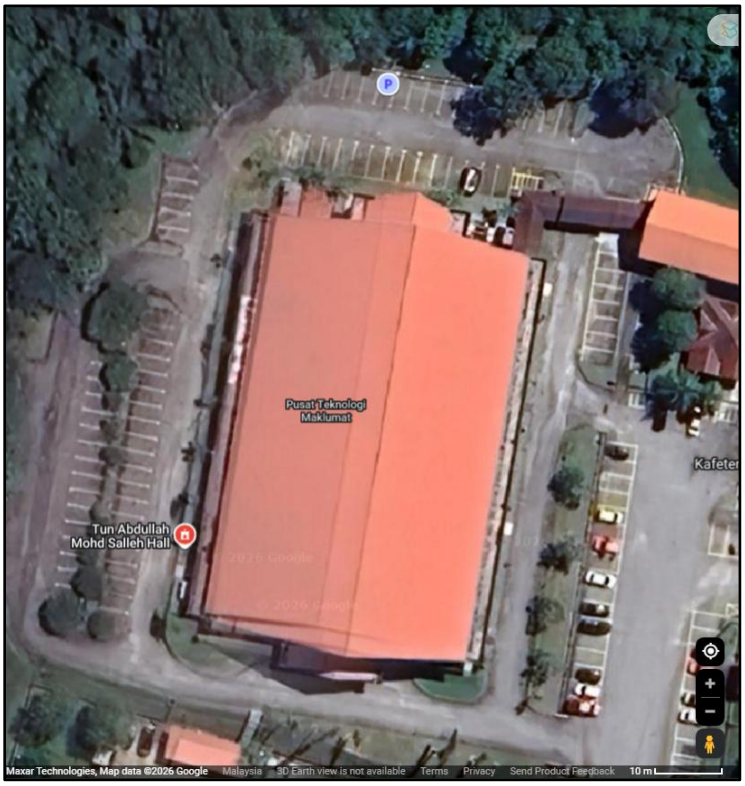

Figure 3.26 Aerial Geographical Mapping of the Tun Abdullah Mohd Salleh Hall Parking Lot Driving Circuit at UKM

The physical data acquisition was systematically executed over an extended five month timeframe, spanning from May 15 to October 10, 2024. Conducting evaluations across this prolonged temporal span inherently exposes the thermal architecture to

natural meteorological fluctuations. Because the secondary solid-state TEG generation relies entirely on successful convective heat rejection from the external cooling fins to the surrounding air, the ambient weather conditions fundamentally dictate the absolute efficiency limits of the recovery system.

To rigorously evaluate this environmental dependence, the dynamic test protocols were strictly segregated into defined daytime and nighttime operational windows. The daytime evaluations were conducted during peak thermal hours, specifically between 9:30 AM and 11:30 AM, and later between 3:00 PM and 6:00 PM. These specific windows deliberately subjected the IHR architecture to high ambient atmospheric temperatures and direct solar radiation, representing the most aggressive thermal stress test for the cold side heat sink. Conversely, the nighttime cases were executed between 8:00 PM and 11:00 PM. Operating during this nocturnal window provided a significantly cooler ambient boundary entirely free from solar radiation interference, maximizing the natural convective cooling potential.

While segregating the data into Day and Night operational profiles provides a highly structured comparative matrix, evaluating thermodynamic systems in an open outdoor environment carries inherent experimental caveats. It was fundamentally acknowledged that these ambient weather variables cannot be mechanically locked or perfectly replicated like a climate-controlled laboratory test bench. Unpredictable crosswinds, fluctuating relative humidity, and micro-variations in the daily atmospheric temperature continuously disrupt the external boundary conditions, inevitably introducing a degree of transient thermal noise into the empirical data recorded during these real-world driving cycles.

3.4.4 Constant Speed Evaluation Protocols

The initial phase of the dynamic on road testing focused exclusively on evaluating the system under steady cruising velocities. This specific protocol was designed to isolate the physical thermodynamic limits of the recovery architecture over a continuous 1 km driving distance. The 800 W traction motor capabilities dictated the kinetic boundaries of the test, restricting the absolute maximum vehicle velocity. Consequently, the constant speed evaluations were executed across three defined cruising targets: a low speed of 10 km/h (designated as 1S), an intermediate speed of 15 km/h (designated as 2S), and a peak velocity of 18 km/h (designated as 3S). During

these specific runs, the initial transient acceleration phase and the final deceleration phase were explicitly excluded from the averaged data extraction to ensure the analysis focused purely on the stabilized cruising thermal equilibrium.

Crucially, to establish a definitive comparative baseline, the entire constant speed testing matrix was executed under two distinct hardware configurations. The physical vehicle was initially evaluated utilising the standard baseline fuel cell without the thermal recovery components. Subsequently, the identical driving protocols were repeated utilising the fully integrated IHR architecture. Furthermore, to accurately capture the influence of ambient thermal boundaries on continuous recovery performance, this complete comparative matrix was executed during both the established daytime and nighttime operational windows. This structured approach ensured that the empirical analysis could accurately isolate and quantify the specific thermodynamic and electrical impacts directly attributable to the passive recovery mechanisms across diverse environmental conditions.

Simulating varying passenger payloads across these speeds required a highly repeatable and mechanically stable method. Utilising actual human passengers introduces unpredictable biological variables such as shifting body weight and inconsistent mass profiles across different testing days. Therefore, calibrated iron dumbbell plates ranging from 5 kg to 20 kg increments were utilised as static payloads. The evaluations were categorized into three distinct passenger equivalents: 1P representing an 80 kg payload, 2P representing a 160 kg payload, and 3P representing a 240 kg payload. To accurately mimic the physical centre of gravity of a fully occupied vehicle, these static plates were strategically distributed across the passenger seats and the lower footwells. This careful spatial distribution ensured the chassis maintained realistic balance and provided a consistent rolling resistance against the traction motor. Table 3.14 and Figure 3.27 detailed the comprehensive experimental test matrix utilised for this steady cruising phase. The total gross weight represents the combined mass of the baseline instrumented buggy (196 kg) and the respective static dumbbell payload. Every case listed in this matrix was performed for the baseline fuel cell and the IHR configuration across both day and night environments.

Table 3.14
Experimental Test Matrix for the 1 Km Constant Speed Evaluations

Payload Designation	Added Static Mass (kg)	Total Gross Vehicle Weight (kg)	Target Cruising Velocity Designation (km/h)			Driving Distance (km)
			1S	2S	3S	
1P	80	276	10	15	18	1.0
2P	160	356	10	15	18	1.0
3P	240	436	10	15	18	1.0

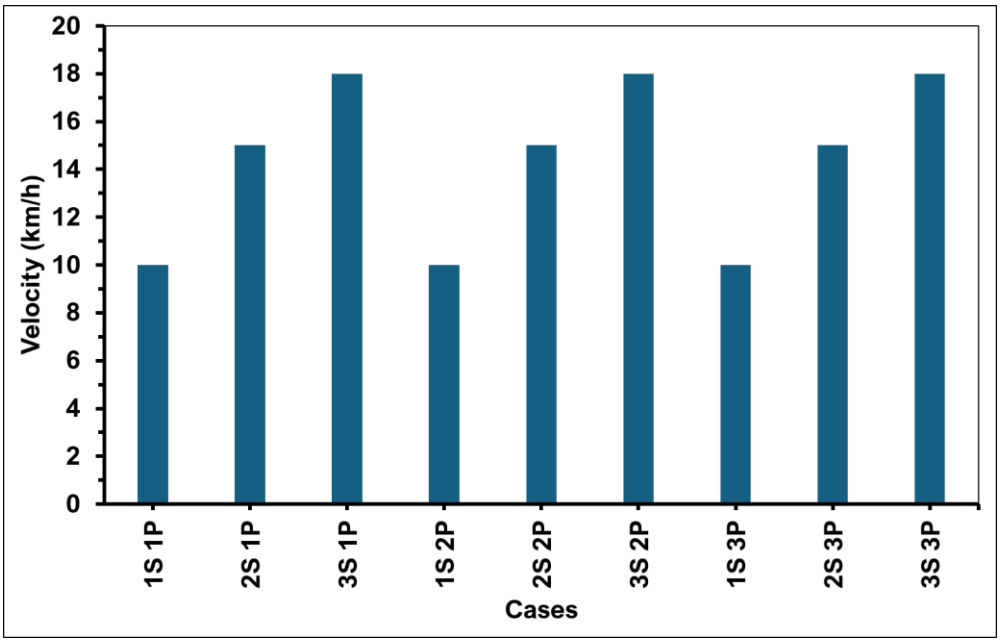

Figure 3.27 Experimental Test Matrix for the 1 Km Constant Speed Evaluations

Throughout these dynamic evaluations, continuous high resolution data acquisition was critical to capture the rapid transient shifts in the mobile system. Consequently, all synchronized recording instruments, encompassing the multichannel thermal data loggers and the digital electrical multimeters, were programmed to capture physical measurements at a strict 1 second interval. This exact temporal resolution ensured that every microscopic fluctuation in spatial temperature gradients, fuel cell voltage, and secondary TEG current was comprehensively logged for the entire duration of the driving cycle.

While this constant speed methodology provides a highly structured comparative matrix, evaluating a moving physical vehicle fundamentally differs from a mechanically locked laboratory dynamometer. It was cautiously acknowledged that maintaining a perfect, unyielding velocity on an outdoor tarmac circuit was practically impossible. Minor gradient imperfections in the parking lot surface, subtle shifts in aerodynamic wind resistance, and the inherent micro-adjustments required by manual

human throttle control continuously disrupt the traction motor. Therefore, the defined 1S, 2S, and 3S speed targets represent the stabilized mean velocities, inherently containing minor transient current spikes and minor voltage drops within the raw continuous data

3.4.5 Scaled Dynamic Driving Cycle Protocols

To evaluate the integrated recovery architecture under realistic transient boundaries, the testing protocol progressed from constant speed runs to a continuous dynamic driving cycle. The standard New European Driving Cycle (NEDC) provides an internationally recognized transient profile, designed to simulate the continuous stop and go nature of urban traffic coupled with high speed extra urban cruising. However, the physical kinetic limitations of the 800 W traction motor fundamentally restrict the buggy from achieving the velocities dictated by the standard cycle. Therefore, a mathematically scaled dynamic profile was formulated to replicate the transient acceleration, and deceleration loads of the NEDC while strictly remaining within the physical limitations of the mobile platform.

Crucially, to establish a definitive comparative baseline for this transient evaluation, the dynamic driving cycle was executed under two distinct hardware configurations, mirroring the comparative approach utilised during the prior 1 km constant speed runs. The physical vehicle was first evaluated executing the scaled NEDC utilising the standard baseline fuel cell without the thermal recovery components. Subsequently, the identical dynamic driving protocol was repeated utilising the fully integrated IHR architecture. Furthermore, to accurately capture the influence of ambient thermal boundaries on transient recovery performance, this complete comparative matrix was executed during both the established daytime and nighttime operational windows. This structured approach ensured that the empirical analysis could accurately isolate and quantify the specific thermodynamic and electrical impacts directly attributable to the passive recovery mechanisms under highly fluctuating loads and varying environmental conditions.

The scaling methodology was anchored by the absolute maximum velocity limits. The standard NEDC reaches a peak terminal velocity of 120 km/h, whereas the experimental buggy was physically constrained to a maximum speed of 18 km/h. This establishes a baseline linear reduction ratio of 0.15 (15%). Applying this exact

mathematical ratio to the lower urban speeds, however, yields target velocities below 3 km/h. Because the traction motor requires a minimum threshold of approximately 5 km/h to maintain a steady rolling momentum without stalling, precise integer rounding was deployed to establish practical, drivable targets. In standard automotive methodology, driving cycles were fundamentally composed of four transient states: idling (resting), acceleration, steady cruising, and deceleration. To rigorously maintain the highly transient nature of the standard cycle, the scaled profile utilised in this study preserved the exact temporal durations (in seconds) for every resting, acceleration, and deceleration phase dictated by the standard NEDC. Only the absolute peak velocity targets were mathematically scaled.

The standard NEDC was partitioned into two distinct phases: the urban ECE-15 cycle and the Extra Urban Driving Cycle (EUDC). For the four repeated ECE-15 phases, the standard cruising targets were proportionally scaled down to four drivable low speed intervals: 5, 7, 10, and 8 km/h. For the high speed EUDC phase, the five standard cruising peaks were scaled to provide a diverse transient power profile near the motor limits, resulting in target velocities of 13, 11, 14, 15, and 18 km/h. The complete mapping of these scaled target speeds against the total standard NEDC phase durations (which encapsulate the acceleration, cruising, and deceleration ramps) was detailed in Table 3.15 and Figure 3.28.

Throughout these dynamic NEDC evaluations, continuous high resolution data acquisition was critical to capture the rapid transient shifts in the mobile system. Consequently, all synchronized recording instruments, encompassing the multichannel thermal data loggers and the digital electrical multimeters, were programmed to capture physical measurements at a strict 1 second interval. This exact temporal resolution ensured that every microscopic fluctuation in spatial temperature gradients, fuel cell voltage, and secondary TEG current was comprehensively logged for the entire 1180 second duration of the scaled driving cycle.

Table 3.15
Scaled NEDC Dynamic Driving Profile Mapped to Buggy Physical Limits

Driving Phase	Standard NEDC Cruising Target (km/h)	Scaled Buggy Target (km/h)	Total Phase Duration including Accel/Decel/Cruise (Seconds)

Driving Phase	Standard NEDC Cruising Target (km/h)	Scaled Buggy Target (km/h)	Total Phase Duration including Accel/Decel/Cruise (Seconds)
Profile 1	15	5	17
Profile 2	32	7	47
Profile 3	50	10	46
Profile 4	35	8	21
EUDC (Extra-Urban)			
Profile 5	70	13	91
Profile 6	50	11	69
Profile 7	70	14	93
Profile 8	100	15	65
Profile 9	120	18	82

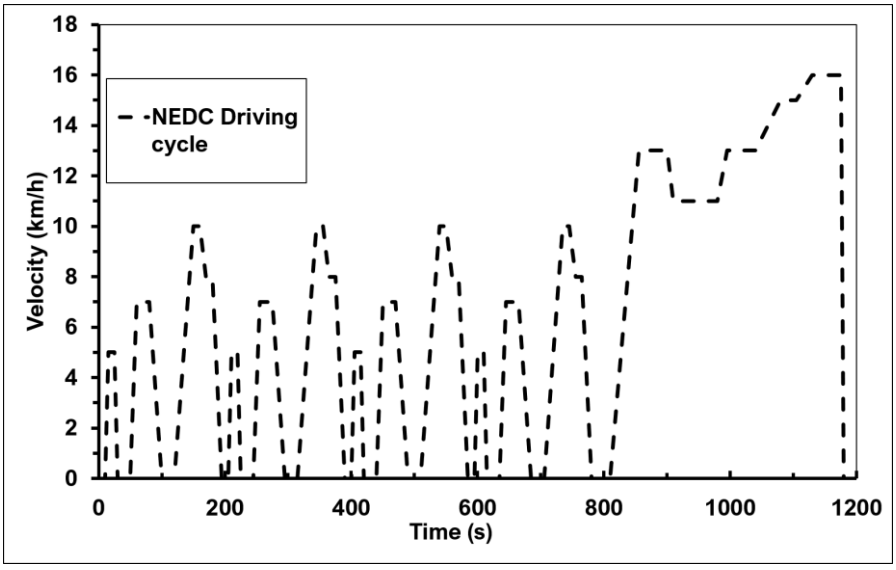

Figure 3.28 Scaled NEDC Dynamic Driving Profile

Executing this complex transient profile on an outdoor circuit introduces significant experimental uncertainty. Unlike a vehicle locked onto a highly calibrated chassis dynamometer, the experimental buggy was manually operated by a human driver utilising physical visual cues and the mobile GPS logger to track the target speeds. It was cautiously acknowledged that perfectly maintaining these exact target velocities for the precise second intervals dictated by the standard cycle was physically

impossible without automated speed monitoring and drive-by-wire instrumentation. Human reaction delays during acceleration, transient overshooting of target speeds, and the unpredictable rolling resistance of the tarmac inevitably caused minor misalignments in the actual physical driving speeds and phase timings.

Consequently, the raw continuous data extracted from these outdoor runs inherently contained temporal and velocity deviations from the mathematical model profile. To ensure a structured and accurate comparative analysis, this raw dynamic data was carefully filtered and mathematically mapped during the post-processing phase to align specifically with the exact standard NEDC timing intervals. Therefore, the presented data does not represent a mathematically flawless driving execution, but rather a realistic physical approximation of transient vehicular thermal stress that has been rigorously mapped onto a standardised temporal framework.

3.4.6 Dynamic Data Processing and Transient Uncertainty

The mathematical formulation utilised to process the raw dynamic data into macroscopic performance metrics, including thermal heat transfer rates and baseline electrical power generation, largely mirrors the governing equations previously established during the laboratory test bench phase in Section 3.2.4. To maintain structural conciseness and avoid mathematical redundancy, those fundamental steady state thermodynamic equations were not reproduced in this section. However, evaluating empirical data collected from an uncontrolled physical environment required a specialized data alignment and statistical verification strategy.

Because the scaled NEDC dynamic profile fluctuates severely compared to the relatively stable 1 km constant speed evaluations, comparing instantaneous power traces introduces significant analytical noise. To resolve this, the macroscopic performance was evaluated utilising the total accumulated energy. Given that the mobile data acquisition system continuously monitored the electrical power at a strict 1 second interval, the total electrical energy generated by the fuel cell (E_{FC})and consumed by the traction motor (E_{motor}) was mathematically derived by summating the discrete instantaneous power readings ($P_{FC,i}$ or $P_{motor,i}$) over the total driving duration (t_{total}):

$$E = \sum_{i=1}^{t_{total}} P_i \cdot \Delta t \qquad \text{[J]} \qquad (3.54)$$

Where E represents the specific total energy being calculated (E_{FC} or E_{motor}), P_i represents the corresponding instantaneous power reading for that system ($P_{FC,i}$ or $P_{motor,i}$), and Δt represents the 1 second logging interval.

Similarly, the continuous secondary recovery performance of the solid state thermoelectric modules was evaluated by summating the instantaneous data points. The total thermal energy transferred across the array ($Q_{TEG,total}$) was calculated by integrating the instantaneous heat transfer rates ($\dot{Q}_{TEG,i}$) over the identical driving duration:

$$Q_{TEG,total} = \sum_{i=1}^{t_{total}} \dot{Q}_{TEG,i} \cdot \Delta t \qquad \text{[J]} \qquad (3.55)$$

Furthermore, the total secondary electrical energy generated by the thermoelectric array ($E_{TEG,total}$) was quantified by summating the instantaneous electrical power readings ($P_{TEG,i}$). To standardize this specific electrical output for comparative analysis, the accumulated energy was mathematically converted into watt hours (Wh) utilising the standard temporal conversion factor of 3600 seconds per hour:

$$E_{TEG,total} = \frac{\sum_{i=1}^{t_{total}} P_{TEG,i} \cdot \Delta t}{3600} \qquad \text{[Wh]} \qquad (3.56)$$

Prior to evaluating the primary thermodynamic and electrical enhancements, a statistical verification methodology was mandated to ensure absolute fairness between the comparative on road driving cases, explicitly encompassing both the 1 km constant speed evaluations and the highly transient NEDC dynamic cycles. Because physical driving inevitably introduces external variables such as minor human throttle corrections, uneven road surfaces, turning losses, and transient wind disturbances, perfectly matching the instantaneous traction demand between a baseline fuel cell run and an integrated architecture run was physically impossible. To confirm that the

evaluated performance differences were not artificially dominated by unequal vehicular traction demands, the summated total motor electrical energy (E_{motor}) was designated as the primary verification metric. A relative deviation acceptance criterion of strictly less than 5% was established to validate the comparative fairness of the matched test cases, calculated as follows:

$$\text{Deviation} = \left|\frac{E_{motor,IHR} - E_{motor,Base}}{E_{motor,Base}}\right| x\ 100 \qquad [\%] \qquad (3.57)$$

Furthermore, because the dynamic data fluctuates badly over the extended route, descriptive statistical metrics were systematically applied to the total fuel cell energy and total motor energy datasets to evaluate their ultimate reliability. The overall energy performance for each specific operational condition was summarized utilising the mean value ($\overline{x}$), the standard deviation (STD) to reflect short term on road fluctuations, the coefficient of variation (CV), the standard error (SE), and the relative standard error (RSE). These metrics were mathematically defined utilising the following standard statistical formulations:

$$\overline{x} = \frac{1}{N}\sum_{i=1}^{N} x_i \qquad [J] \qquad (3.58)$$

$$STD = \sqrt{\sum_{i=1}^{N} \frac{(x_i - \overline{x})^2}{N-1}} \qquad [J] \qquad (3.59)$$

$$CV = \left(\frac{STD}{\overline{x}}\right) \cdot 100 \qquad [\%] \qquad (3.60)$$

$$SE = \frac{STD}{\sqrt{N}} \qquad [J] \qquad (3.61)$$

$$RSE = \frac{SE}{\overline{x}} \quad [\%] \quad (3.62)$$

where x_i represents the individual recorded total energy value for a specific run and N represents the total number of evaluation iterations.

Following this statistical verification to ensure comparable physical traction demand, executing a direct comparative analysis between the highly varied on road driving cases required a specialized data alignment strategy. During the 1 km constant speed evaluations, the physical traction demand dictated that the fuel cell operated within relatively narrow and isolated current bands for each specific weight and speed combination. For instance, the current drawn during a low speed 1P test does not naturally overlap with the massive current drawn during a high speed 3P test. Consequently, directly comparing the raw power outputs across different cases proved mathematically inconsistent. To overcome this disjointed data spread, the extracted power profiles were systematically plotted against the drawn current and subsequently normalized utilising a singular physical reference point. This critical normalization anchor point was established at the fuel cell open circuit voltage under a constant minimal current draw (specifically 45 V at 1 A). By mathematically normalizing the narrow dynamic data bands to this fixed open circuit boundary, a continuous and comparable normalized power profile was successfully established for every evaluated constant speed configuration.

Conversely, the highly transient scaled NEDC evaluations naturally encompassed a massive operational current span due to the continuous sequence of rapid accelerations, high speed cruising, and decelerations. Because this dynamic profile inherently generated data points across the entire fuel cell load spectrum, normalizing the data to the open circuit voltage was mathematically unnecessary. The raw dynamic data independently provided a sufficiently broad and continuous power profile to establish reliable operational trends.

Regardless of the evaluation type, raw data points extracted from different physical driving runs rarely align at the exact same instantaneous current values due to minute throttle variations. To resolve this, mathematical trendlines representing the power versus current relationship were generated for each specific test case. To ensure strict analytical rigor and prevent mathematical overestimation, only trendline equations demonstrating a coefficient of determination (R^2) strictly exceeding 92% were accepted

into the final analysis. The coefficient of determination evaluating the fitness of these predictive trendlines was calculated utilising the following standard formulation:

$$R^2 = 1 - \frac{\sum(P_i - \widehat{P}_i^{\,2})}{\sum(P_i - \bar{P})^2} \quad [\%] \quad (3.63)$$

where $P_i$represents the actual raw electrical power recorded during the physical on road evaluation, $\widehat{P}_i$ represents the predicted electrical power derived from the generated mathematical trendline, and $\bar{P}$ represents the mean average of all actual recorded power values within that specific dataset.

Finally, to evaluate the overall system efficiency for the entire physical on road testing matrix, encompassing both the 1 km constant speed evaluations and the scaled NEDC profiles, determining the exact reactant consumption was necessary. While the instantaneous hydrogen flow rate was monitored during the evaluations as previously discussed, integrating flow data over extended physical driving cycles inherently introduces compounding measurement noise due to vehicle vibrations and sensor sensitivity. To avoid this uncertainty and secure a more reliable macroscopic metric, the absolute hydrogen consumption was determined utilising the storage tank pressure drop method. By recording the initial tank pressure ($p_{initial}$) before the drive and the final tank pressure (p_{final}) after cycle completion, the absolute pressure differential (Δp) was established. This pressure drop was mathematically converted into the absolute on road consumed hydrogen mass ($m_{H2,on\,road}$) utilising the ideal gas formulation adapted for the fixed 9 L storage cylinder volume ($V_{H2,on\,road}$) and the specific ambient temperature (T) [12]:

$$m_{H2,on\,road} = \frac{\Delta p \cdot V_{H2,on\,road}}{R_{H2} \cdot T} \quad [\text{kg}] \quad (3.64)$$

where R_{H2} represents the specific gas constant for hydrogen. The total theoretical on road energy input supplied to the system ($E_{in,on\,road}$) was subsequently calculated by multiplying this absolute consumed mass by the Higher Heating Value (HHV) of hydrogen [12]:

$$E_{in,on\ road} = m_{H2,on\ road} \cdot HHV \qquad [J] \qquad (3.65)$$

The overall on road system efficiency ($\eta_{on\ road}$) was determined by comparing the summated total electrical energy output of the fuel cell (E_{FC}) against this total theoretical energy input [12]:

$$\eta_{on\ road} = \frac{E_{FC}}{E_{in,on\ road}} \cdot 100 \qquad [\%] \qquad (3.66)$$

Following the determination of the primary system efficiency, the overall thermodynamic effectiveness of the integrated recovery architecture was quantified. To accommodate the highly transient nature of the on road driving cycles, the waste heat utilization factor was calculated utilising the total accumulated thermal energies rather than instantaneous rates. The total thermal energy successfully absorbed by the hydrogen reactant gas ($Q_{H2,total}$) was mathematically derived by summating the instantaneous heat absorption rates ($\dot{Q}_{H2,i}$) over the identical total driving duration (t_{total}) [12]:

$$Q_{H2,total} = \sum_{i=1}^{t_{total}} \dot{Q}_{H2,i} \cdot \Delta t \qquad [J] \qquad (3.67)$$

Similarly, the total absolute thermal energy generated by the primary fuel cell ($Q_{FC,total}$) was quantified by summating the instantaneous thermal power generation readings ($P_{th,FC,i}$) [12]:

$$Q_{FC,total} = \sum_{i=1}^{t_{total}} P_{th,FC,i} \cdot \Delta t \qquad [J] \qquad (3.68)$$

Finally, the on road waste heat utilization factor ($\mu_{WH,on\ road}$) was established by calculating the direct percentage ratio of the total successfully recovered thermal

energy (comprising both the total TEG heat transfer and the total hydrogen heat absorption) against this total fuel cell thermal generation [17]:

$$\mu_{WH,on\,road} = \frac{Q_{TEG,total} + Q_{H2,total}}{Q_{FC,total}} \quad [\%] \quad (3.69)$$

This specialized calculation methodology intentionally avoids utilising instantaneous rates, providing a robust, macroscopically bounded utilization metric that remains resilient against the rapid physical flow and thermal fluctuations inherent to outdoor on road driving. While this rigorous data processing framework establishes a structured analytical baseline, it was cautiously acknowledged that empirical on road data inherently contains experimental noise, and the absolute physical reality remains subject to unavoidable environmental uncertainties.

CHAPTER 4
RESULTS AND DISCUSSION

4.1 Introduction

This chapter presents the comprehensive findings extracted from the mathematical modelling, physical laboratory validation, and dynamic vehicular evaluations of the integrated heat recovery architecture. To systematically address the core research objectives and navigate the highly complex thermodynamic data, the discussion was partitioned into three distinct subsections.

Section 4.2 details the preliminary computational fluid dynamics simulations utilised to evaluate four specific physical geometries. While this initial numerical phase successfully establishes the idealized thermal boundaries and selects the optimal configuration, it was explicitly acknowledged that these mathematical models inherently omit real world contact resistances and manufacturing flaws.

To bridge this mathematical gap, Section 4.3 transitions the analysis to a controlled steady state laboratory test bench. This intermediate phase empirically validates the primary electrical power increments and overall fuel cell efficiency improvements while rigorously quantifying the initial physical thermal leakages.

Finally, Section 4.4 exposes the physical prototype to dynamic on road testing utilising the lightweight fuel cell buggy. By evaluating the system under both constant speed and highly transient driving cycles, this final section deliberately embraces chaotic ambient wind shear, unavoidable sensor noise, and transient thermal lag. Ultimately, progressing sequentially through these three methodological phases provides a highly grounded and cautious evaluation that highlights both the electrochemical successes and the severe fundamental thermodynamic bottlenecks of the physical system.

4.2 IHR Design Evaluation for PEMFC Operation (results based on objective 1)

This section presents a comprehensive case study on novel IHR designs evaluated for a low-temperature PEM fuel cell operating at 500, 1000, 1500 and 2000

W. The aim of this analysis was to achieve Objective 1 by identifying the most suitable IHR configuration for subsequent prototype fabrication and experimental validation on the test bench and on road lightweight vehicle testing. The study combines mathematical calculations and CFD simulations to verify the thermal models, quantify hydrogen preheating performance, assess TEG thermal behaviour and electrical output, and evaluate the overall waste heat utilisation and net power enhancement achieved by each design. The results form the technical basis for selecting a final IHR configuration to be implemented in the laboratory and on-road experiments in later sections.

4.2.1 Full Domain Three Dimensional Computational Fluid Dynamics Visualisation

Prior to extracting the highly specific internal hydrogen reactant temperatures and the localised thermoelectric generator surface boundaries, a comprehensive macro level evaluation of the full computational domain was conducted. Addressing the necessity to verify the overall fluid solid interactions across the entire physical architecture, Table 4.1 was established to present the full three dimensional isometric visualisations of both the temperature and pressure profiles for all four evaluated designs. These visual profiles were deliberately extracted under the maximum 2 kW operational boundary condition to illustrate the physical system under the most severe thermal and aerodynamic stress.

As illustrated in the overall isometric view temperature profiles, the visual colour contours provided explicit confirmation that the spatial thermal distribution behaved according to fundamental thermodynamic principles. The four iterations were broadly categorized into two structural pairs. Design 1 and Design 2 shared similar fundamental configurations but differed in overall size and component quantity, whereas Design 3 and Design 4 possessed identical primary heating architectures but differed significantly in their secondary cold chamber designs. Across all four iterations, the primary structural heatsinks exhibited intense thermal absorption, visually denoted by the red and orange contours, reaching peak surface temperatures ranging between 51.2 °C to 48 °C. The secondary cooling structures, visualised by the cyan and blue contours, remained effectively isolated from the primary hot zone, the colour indicated the range between 23.5 °C to 28.5 °C respectively. This visual evidence confirmed that

the solid state TEG modules successfully functioned as a physical thermal barrier, effectively transferred the heat through conduction by thermal bridging between the hot exhaust chamber and the cold cruising air chamber.

Evaluating the specific thermal contours revealed distinct performance variations between the structural models. Overall, Design 2 recorded the highest absolute temperatures. Because Design 2 possessed a significantly larger primary heating surface area, it remained slightly hotter than Design 1, although this absolute thermal difference was minimal and did not exceed 1 °C (at 2000 W operation, 50.65 °C in Design 1 and in Design 2, 50.73°C). This specific thermal behaviour indicated that integrating additional heatsink fins successfully maintained the required heat absorption despite a significant reduction in the overall structural width of the heatsink. Design 1 possessed a substantially wider physical footprint compared to the highly compact architecture of Design 2. By packing a higher density of heating fins into this reduced space, Design 2 achieved an equivalent, and marginally superior, thermal capture within a much smaller spatial volume. However, this spatial compaction introduced a physical design compromise. Due to the reduced overall width of the primary heatsink, the available physical mounting boundary was constrained. This spatial limitation necessitated reducing the total number of solid state TEG modules to eight in Design 2, directly contrasting with the twelve modules accommodated by the wider footprint of Design 1.

On the cooling boundary, the integration of additional solid heat pipes and an expanded cooling fin array in Design 2 provided significantly more effective heat rejection compared to Design 1. This enhanced cooling capability was visually evident at the localized interface comprising the primary heatsink base, the solid state TEG modules, and the intermediate copper plate. Within this specific region, Design 1 exhibited a uniform orange coloured thermal profile corresponding to approximately 50 °C to 48°C. Conversely, Design 2 displayed a yellow to green coloured profile ranging from 42 °C to 44 °C, effectively achieving an approximate 6 °C to 8 °C temperature reduction. This is within the range achieved by previous work on a cooing TEG system utilising the heat pipe-plate fined heat exchanger which was a maximum of 7 °C of improvement [138]. This substantial thermal decrement indicated a highly efficient heat transfer mechanism. This superior cooling represented the exceptional thermal transport

capabilities of the embedded heat pipes, which are physically designed to rapidly extract localized heat through internal two-phase evaporation and capillary condensation cycles. Although the computational fluid dynamics models mathematically simplified these complex multi-phase mechanics into highly conductive solid structures to maintain numerical stability, the resulting thermal contours successfully demonstrated the theoretical cooling advantage of utilizing a high quantity heat pipe configuration [138].

Comparing the second structural pair, Design 3 and Design 4 exhibited highly similar heat absorption profiles due to their identical heating heat exchanger configurations. However, the extended cooling surface area integrated into Design 3 facilitated superior heat rejection. This design choice resulted in a temperature reduction of approximately 1.0 °C across the secondary cooling fins and yielded a visually more uniform spatial temperature distribution compared to Design 4. Ultimately, observing the macro level (isometric view) thermal contours suggested that Design 2 provided modest thermal absorption alongside the absolute best secondary cooling capabilities.

Furthermore, evaluating the full domain pressure profiles provided critical insights into the aerodynamic behaviour of the fluid streams interacting with the solid geometries. The consistent presence of high pressure stagnation zones at the inlets and low pressure wake zones at the outlets proved that the fluid simulation functioned technically and mathematically correctly. As the fluid streams collided with the frontal area of the primary heatsinks and the internal tube networks, distinct high pressure zones formed, represented by the red and yellow contours at the inlet faces. Consequently, turbulent wake regions exhibiting negative pressure boundaries, denoted by the dark blue contours, developed immediately downstream of the solid obstructions.

Comparing the pressure legends across the four iterations revealed significant variations in aerodynamic resistance directly tied to their geometric configurations. For example, Design 3 exhibited an exceptionally high peak stagnation pressure of 405 Pa. This severe aerodynamic resistance was caused by the narrow gaps between the extended cooling fins, which effectively choked the cold cruising air as it traversed the long tunnel like fluid pathways. In contrast, Design 4 compensated for these narrow gaps by utilizing significantly shorter fins, which drastically reduced the fluid choking effect and yielded a lower peak pressure of 202.8 Pa. Meanwhile, Design 2 demonstrated a significantly lower peak pressure of 191 Pa, suggesting a highly effective and aerodynamically efficient internal spacing. By presenting these full

domain macro level visualisations, the overall mathematical stability and physical logic of the conjugate heat transfer models were successfully validated. This macroscopic verification established a reliable foundation for subsequently extracting and analysing the microscopic internal fluid parameters and discrete surface temperatures required for the performance prediction models.

Table 4.1
Full Model Temperature and Pressure Profile

2 kW profiles	Design 1	Design 2	Design 3	Design 4
Temperature profile	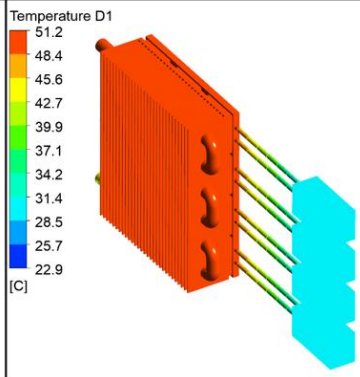	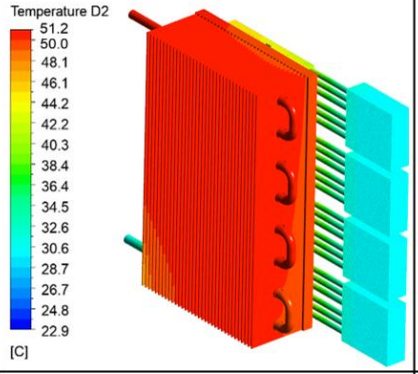	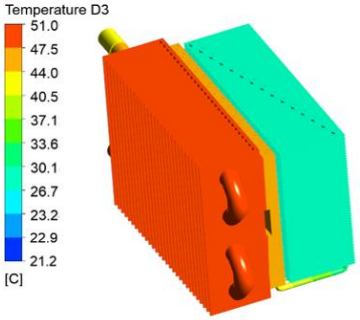	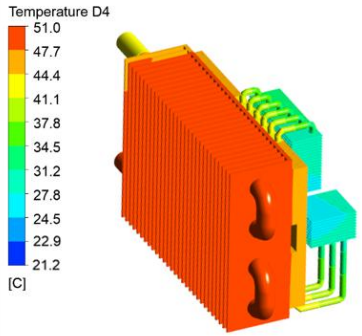
Pressure profile	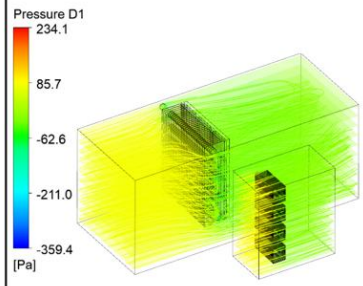	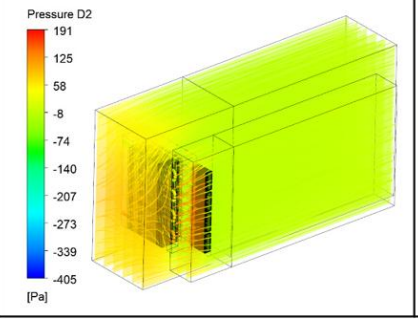	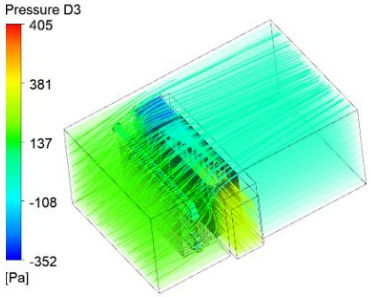	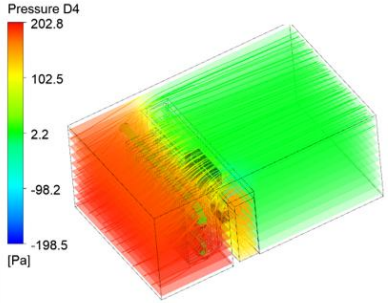

4.2.2 Verification of Hydrogen Preheated Temperature and TEG Temperatures Model

This section evaluated four integrated heat recovery designs to determine their temperature profiles across a polymer electrolyte membrane fuel cell operating range of 500 W to 2000 W. The analysis focused strictly on three primary parameters: the hydrogen preheated temperature, the TEG hot side temperature, and the TEG cold side temperature. These parameters were initially presented across Figure 4.1 to Figure 4.3. Crucially, this subsection was dedicated exclusively to the analytical and numerical verification of the computational fluid dynamics results against the one dimensional mathematical baseline using Equation 3.34. It is fundamentally clarified that this phase served to verify the mathematical reliability of the numerical codes prior to physical manufacturing, whereas empirical validation against physical experimental test bench data was reserved for subsequent sections under the secondary research objective. The objective of this preliminary verification was to identify a balanced physical design that provided the highest hydrogen heating alongside a maximised temperature gradient across the TEG module, specifically targeting the hottest possible TEG hot side and the lowest possible TEG cold side temperatures.

The computational model exhibiting the highest primary thermodynamic performance was selected for physical fabrication. This optimal prototype was subsequently analysed and compared against the empirical test bench results to formally validate the specific numerical model and the overarching computational routine. Because the universal numerical setup and boundary conditions were identical across all four configurations, successfully validating the optimal physical prototype theoretically verified the computational setup applied across the remaining three architectures that were not manufactured due to their inferior projected thermal performance.

Figure 4.1 a and b presented the hydrogen preheated temperatures derived from the theoretical mathematical model and the computational numerical approach, respectively. The extracted data indicated that the hydrogen temperature increased progressively across all design variations as the fuel cell power rose from 500 W to 2000 W. This continuous upward trend was physically justified by the primary energy partitioning of the fuel cell; escalating the electrical load inherently generated a proportionally larger volume of exothermic waste heat. This abundant thermal energy

strengthened the driving temperature gradient across the primary heating chamber, thereby facilitating a higher rate of conductive and convective heat transfer into the reactant gas. Furthermore, a distinct performance separation emerged between the evaluated architectures. Design 1 and Design 2 produced nearly identical, superior heating profiles, reaching computational numerical values of 50.6 °C and 50.7 °C at the 2000 W maximum boundary. In contrast, Design 3 and Design 4 generated lower temperature outputs, achieving 49.0 °C and 49.1 °C under the exact same peak load. This specific thermal variance was physically driven by the internal tube pass configurations. Design 1 and Design 2 incorporated higher numbers of internal copper tube passes, which significantly extended the physical residence time of the hydrogen gas within the hot chamber. This prolonged spatial exposure allowed the reactant to absorb thermal energy more thoroughly than in Design 3 and Design 4, which utilised fewer tube passes. Consequently, Design 2 maintained the highest hydrogen temperature throughout the entire operational sweep.

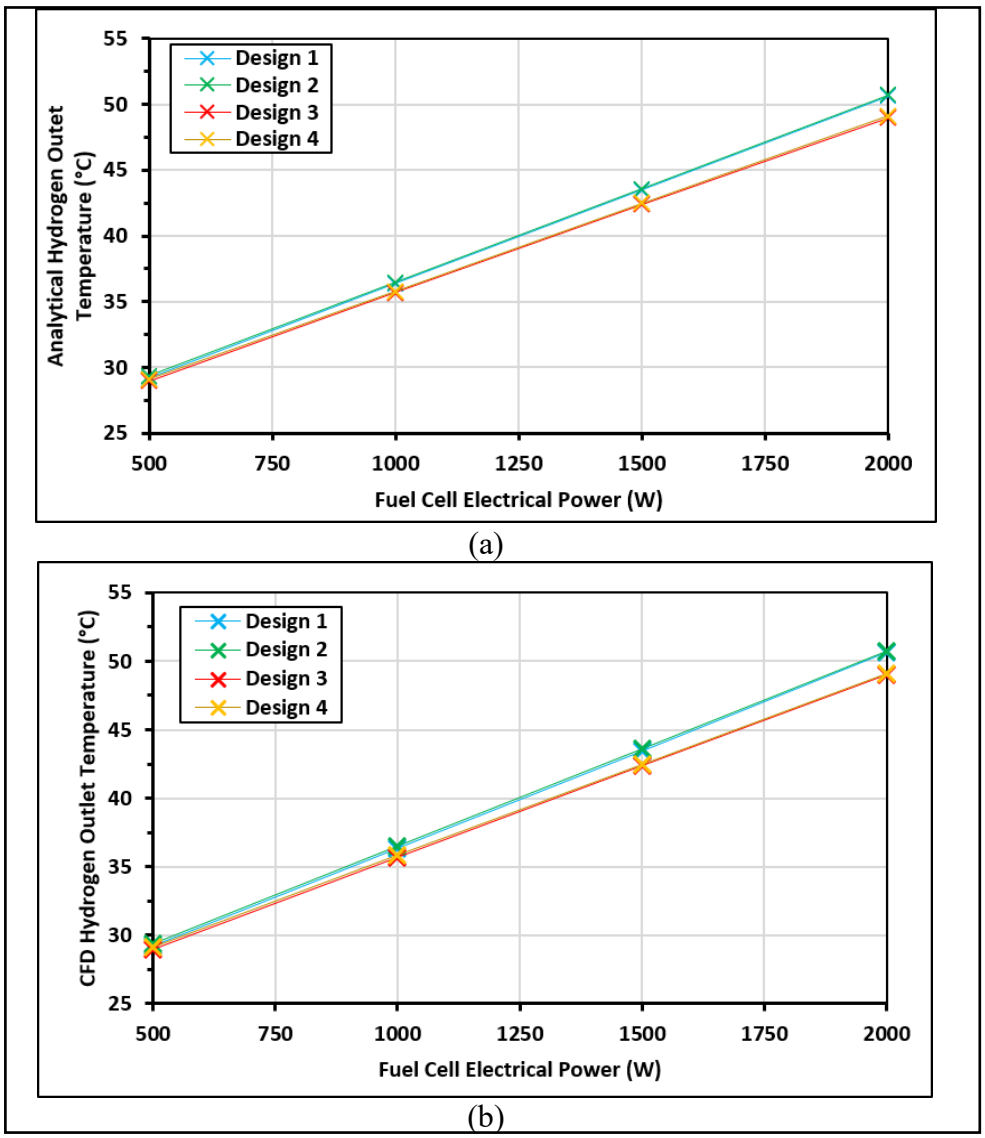

Figure 4.1 Preheated Hydrogen Temperature Predictions From (a) Mathematical Model (b) CFD Model

Figure 4.2a and Figure 4.2b displayed the TEG hot side temperature trends. Design 1 recorded the highest mathematical model hot side temperature at 49.6 °C for the 2000 W load, followed by Design 2 at 48.2 °C, Design 3 at 48.1 °C, and Design 4 at 47.7 °C. The computational fluid dynamics models mirrored this behaviour, with Design 1 reaching 50.4 °C and Design 4 reaching 47.8 °C. These metrics demonstrated that Design 1 and Design 2 captured the waste heat sufficiently, establishing a robust temperature foundation for secondary power generation. This thermal hierarchy was physically justified by the difference in geometric configurations of the primary heating chambers. Because Design 1 and Design 2 incorporated the largest primary heatsink surface areas and the highest number of internal copper tube passes, they absorbed a

significantly larger volume of sensible heat from the exhaust stream compared to the more compact footprint of Design 4.

Figure 4.3 a and b illustrated the corresponding TEG cold side temperature profiles. Maintaining a low temperature at this junction was necessary for optimal thermoelectric conversion. The extracted data revealed that Design 2 achieved the lowest cold side temperature, recording a computational value of 44.4 °C at 2000 W. Design 4 followed at 46.0 °C, then Design 3 at 46.2 °C, while Design 1 recorded the highest and least favourable cold side temperature at 50.1 °C. Despite Design 1 reaching the highest temperatures at the hot side, it failed to reject heat sufficiently, resulting in severely elevated cold side conditions. This distinct cooling behaviour was directly dictated by the secondary external cooling architectures. Design 2 demonstrated the most effective cooling capability because it integrated an expanded array of 24 solid heat pipes and 376 cooling fins. This massive physical surface area aggressively rejected thermal energy into the ambient cruising air stream. In contrast, Design 1 utilised only 8 solid heat pipes, which caused thermal saturation at the cold junction, allowing heat to accumulate faster than the system could physically reject it.

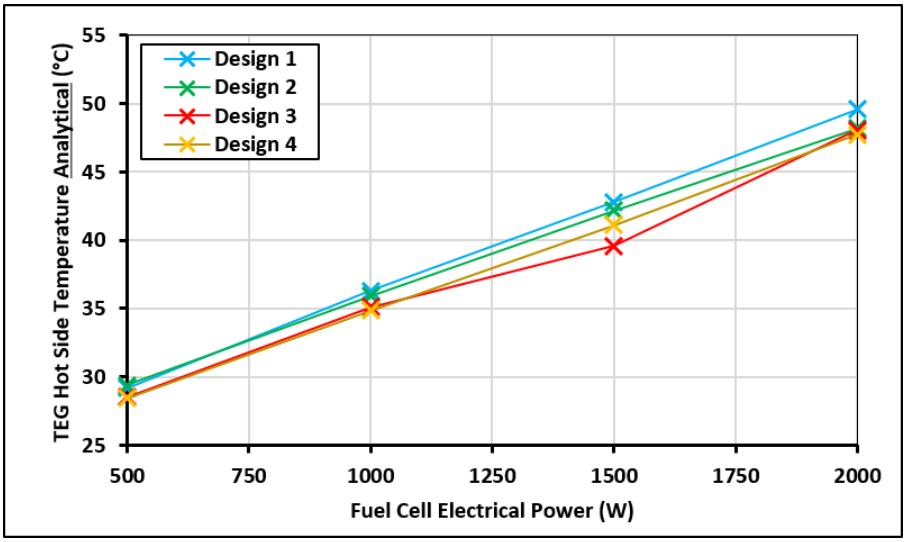

(a)

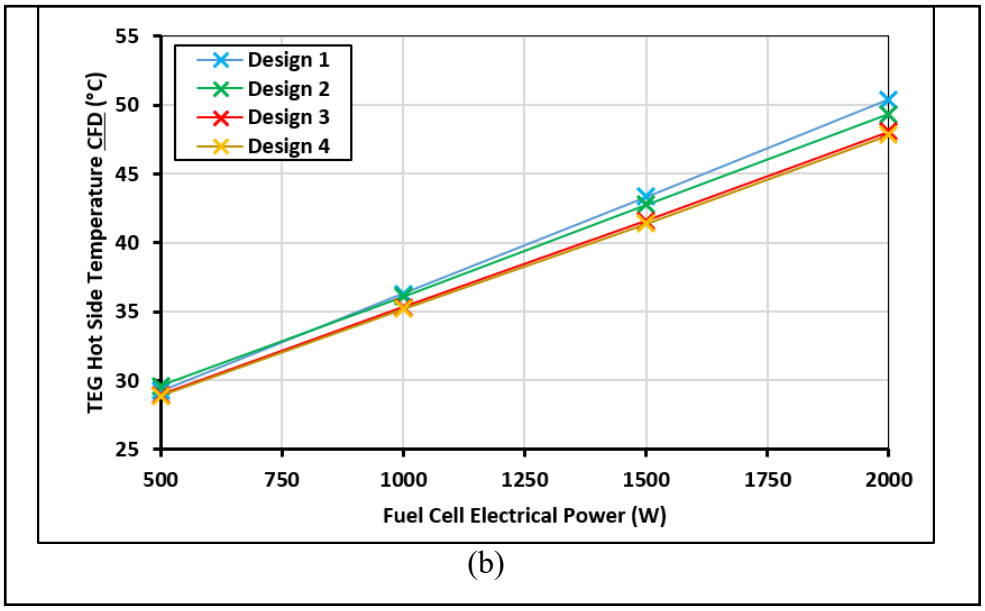

(b)

Figure 4.2 TEG Hot Side Surface Temperatures for (a) Mathematical Model (b) Numerical Model

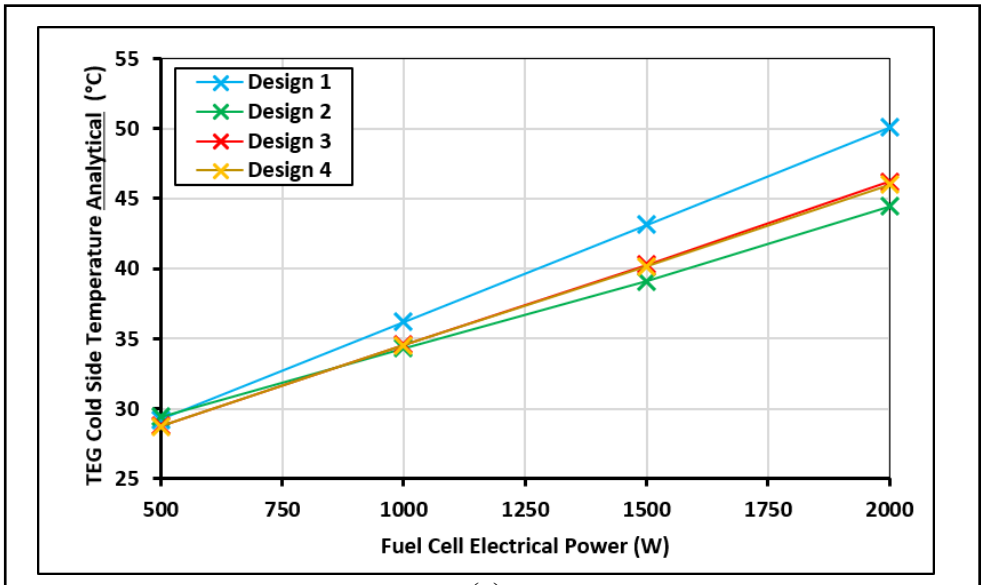

(a)

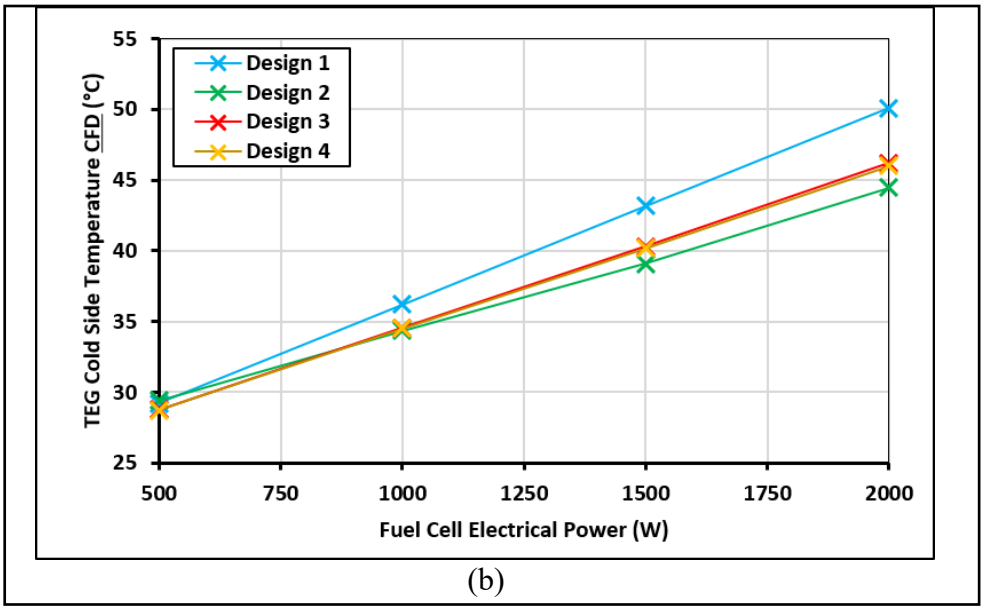

(b)

Figure 4.3 TEG Cold Side Surface Temperatures for (a) Mathematical Model (b) Numerical Model

To scientifically ensure these observed spatial trends and the thermodynamic discussion remained mathematically sound, the complex three dimensional computational fluid dynamics outputs were cross referenced against the one dimensional theoretical mathematical baseline. By confirming that the relative deviation between these two distinct analytical methods remained strictly below a 10% threshold, the numerical models and the resulting discussion were successfully verified. This close numerical alignment confirmed that the simulated thermal gradients accurately reflected the specific physical geometries, although it was cautiously acknowledged that idealised steady state boundaries inherently omit minor physical contact resistances and microscopic manufacturing flaws.

To precisely quantify this numerical error margin, the critical parameters of the integrated heat recovery architecture, specifically the hydrogen reactant temperature and the hot and cold TEG surface temperatures, were extracted. These computational parameters were compared against the analytical results, utilising the theoretical mathematical data as the foundational baseline via Equation 3.34. The resulting comparative parameters were visually mapped across Figure 4.4, Figure 4.5, and Figure 4.6, respectively.

The verification analysis calculated the percentage deviation. Across all evaluated designs and fuel cell power load iterations, spanning from 500 W to 2000 W, the relative differences for the TEG hot side, TEG cold side, and hydrogen preheated temperatures remained strictly below the 10 % threshold. For instance, the maximum

variance for the TEG cold side occurred in Design 4, recording a 2.4 % difference under the 500 W load condition. Concurrently, the TEG hot side exhibited a peak deviation of 5.1 % in Design 3 at the 1500 W operational point. These consistently low deviation values confirmed that the numerical models possessed an approximate 90 % reliability level. This established a highly favourable agreement between the preliminary mathematical predictions and the complex spatial simulations, matching the standard numerical verification thresholds established in literature [139]. However, it was cautiously acknowledged that minor numerical discrepancies inherently persist due to idealised mathematical assumptions and minor computational mesh diffusion errors. Consequently, the verified computational routine was confirmed as sufficiently robust to proceed to active experimental testing.

Synthesising these findings revealed the underlying engineering mechanisms driving the temperature behaviour of the varied configurations. The elevated hydrogen preheated temperatures observed across all configurations indicated that the copper tube fin structure absorbed the gas heat efficiently. The additional copper tube pass integrated specifically into Design 1 and Design 2 contributed to a measured computational increase of approximately 2 °C, over the configurations of Design 3 and Design 4. However, the critical performance differentiator emerged on the cooling boundary. The extra cooling surface area and the increased number of heat pipes utilised in Design 2 provided additional cooling leverage. This specific design advantage suppressed the TEG cold side temperature more effectively than the other variations. Consequently, Design 2 offered the most balanced temperature distribution by sustaining high reactant heating while preserving a wider gradient for TEG conversion. These geometric influences on temperature management and the necessity of maintaining wide spatial thermal gradients across dual recovery systems aligned strongly with the baseline architectural trends reported by Zamri et al. [45] alongside similar waste heat recovery simulations executed by [102] and [140].

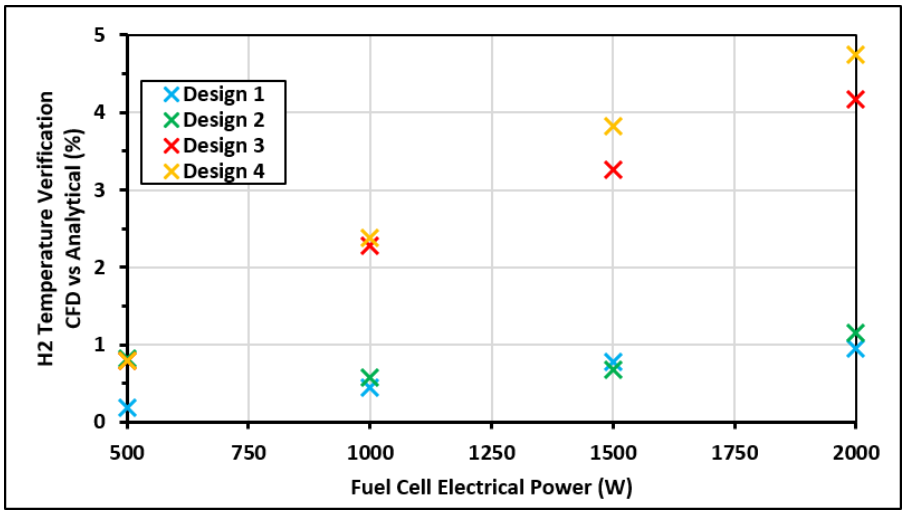

Figure 4.4 Comparison of Results Between CFD and Mathematical Modelling: Preheated Hydrogen Temperature

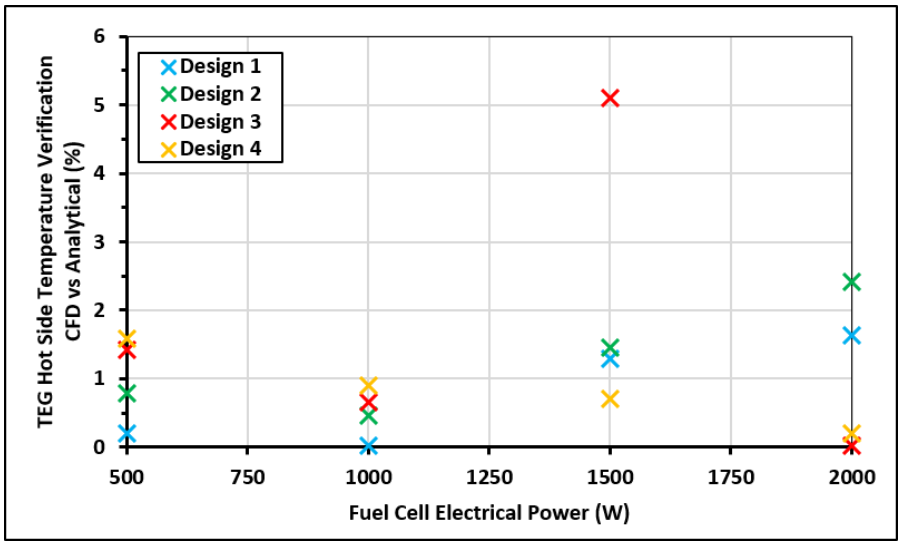

Figure 4.5 Comparison of Results Between CFD and Mathematical Modelling: TEG Hot Side Temperature

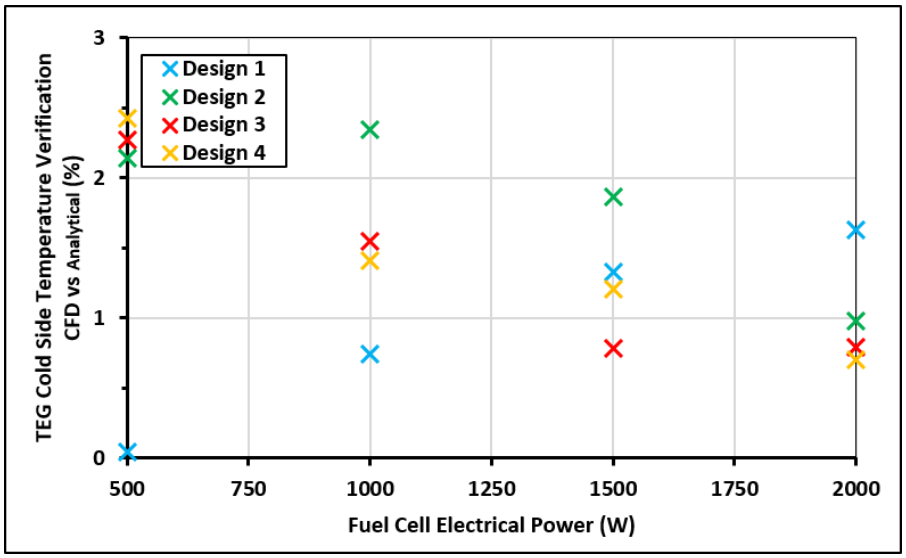

Figure 4.6 Comparison of Results Between CFD and Mathematical Modelling: TEG Cold Side Temperature

4.2.3 Hydrogen Preheating Performance

The primary objective of the heating chamber within the integrated configurations is to elevate the thermal state of the incoming reactant gas. To assess this capability across the four proposed designs, this subsection examines the temperature difference achieved between the hydrogen inlet and outlet boundaries. Furthermore, the analysis quantifies the corresponding total heat absorption as the PEM fuel cell scales from a 500 W to 2000 W operational load. Establishing these foundational heating metrics serves as a prerequisite for understanding the available thermal energy before evaluating the downstream TEG performance.

Figure 4.7 compares the temperature distribution of the hydrogen gas as it progresses along the copper tube fin heating pathway for all the evaluated designs. An analysis of the temperature propagation under fuel cell operational loads of 1500 W and above reveals a distinct saturation behaviour. The data demonstrated that the reactant gas achieved its maximum heated temperature by the completion of the second tube pass across all geometries. Consequently, the subsequent tube passes did not actively increase the gas temperature further; instead, they functioned to maintain the accumulated thermal state as the hydrogen traversed the remainder of the heating chamber.

Building upon this spatial distribution, Figure 4.8 presents the hydrogen temperature difference across the operational range. This metric represents the

calculated variance between the fixed 23 °C inlet boundary and the final heated outlet. As the PEM fuel cell power increased, greater waste heat generation drove a progressive rise in the hydrogen temperature difference.

The resulting temperature data clustered the four variations into two distinct performance categories based on their heating efficacy. Design 1 and Design 2 formed the upper tier, generating the highest overall temperature differences. At the 500 W load, these two configurations recorded 6.2 °C and 6.4 °C, respectively, which then escalated to 27.7 °C and 27.6 °C at the 2000 W upper boundary. Conversely, Design 3 and Design 4 exhibited slightly lower heating profiles. These geometries initiated at 6.0 °C and 6.1 °C under the minimum load and reached 26.0 °C and 26.1 °C at peak operation. Within each respective grouping, the internal variance remained minimal, maintaining a difference of less than 1 °C between Design 1 and Design 2, and similarly between Design 3 and Design 4 across all power settings. Design 3 and Design 4 had lower heating performance due to the reduction of heating surface area. Approximately 40 to 50% of heatsink size and preheating tube surface area and size reduction compared to Design 1 and Design 2 respectively. Thus incorporated lower capability of heating the hydrogen tube.

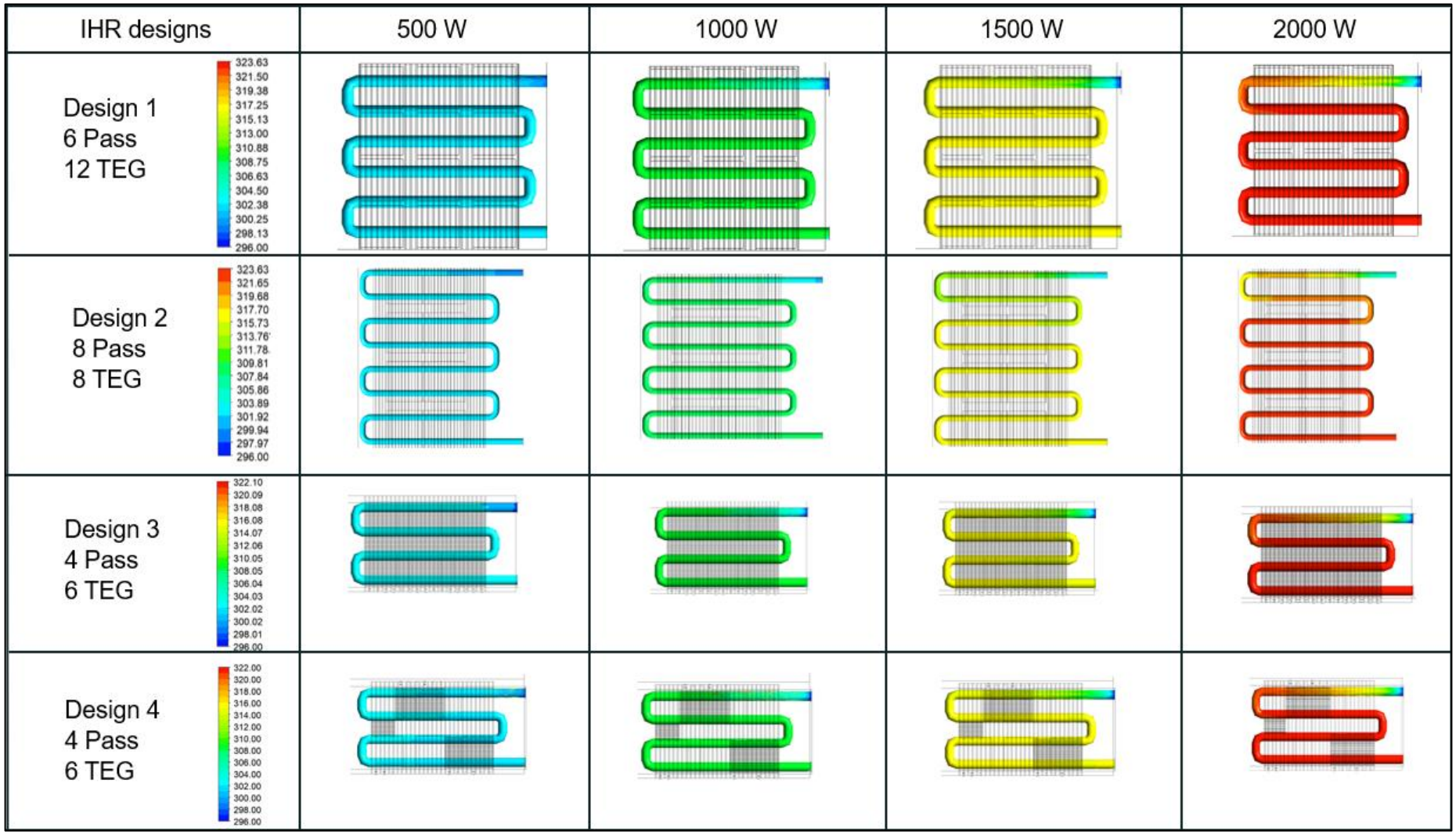

Figure 4.7 Numerical Analysis of Hydrogen Temperature Distribution During Preheating for the IHR Designs at 1500 W Fuel Cell Power

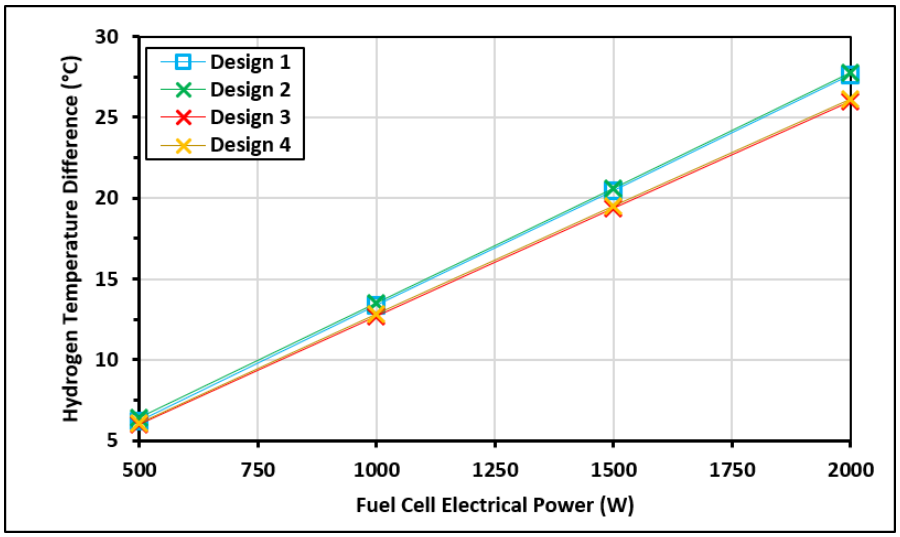

Figure 4.8 Hydrogen Temperature Rise (ΔT) Across the Preheater for Four IHR Designs At 500–2000 W Fuel Cell Power

This clustered behaviour correlates directly with the internal tube pass configuration. While the physical diameter of the copper tube remained constant across all cases, the number of tube passes and the available heating fin surface area differed. Design 1 and Design 2 utilised a higher number of tube passes, thereby prolonging the physical residence time of the gas within the heating chamber. Although Design 2 featured a larger overall heating surface area compared to Design 1, their identical number of tube passes yielded nearly identical temperature difference outcomes. This observation suggests that the internal residence time dictates the upper limit of gas heating more heavily than the external fin surface area alone.

Figure 4.9 illustrates the corresponding hydrogen heat absorption. Because thermal absorption directly depends on the temperature difference and the mass flow rate, these trends closely mirrored the temperature data. At the 500 W baseline, all four designs recorded an equal heat absorption of 0.8 W. As the operational load increased to 1500 W, the absorption values separated, reaching 7.9 W for Design 1, 8.0 W for Design 2, and 7.5 W for both Design 3 and Design 4. Under the maximum 2000 W condition, the absorption escalated to 26.3 W for the first group and 25.4 W to 25.5 W for the second group.

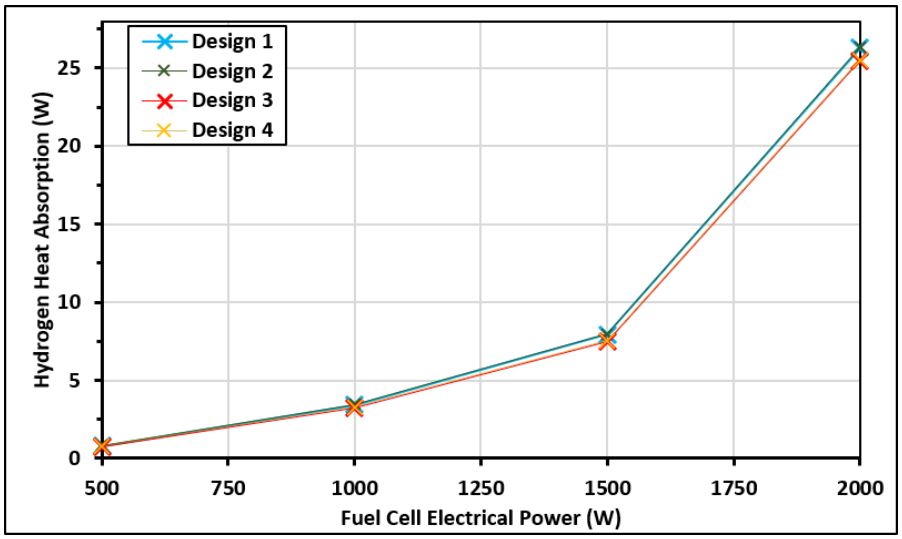

Figure 4.9 Hydrogen Heat Transfer Rate in the Preheating Section for Four IHR Designs at 500 to 2000 W Fuel Cell Power

These findings indicate that all four configurations successfully heated the reactant gas, confirming that the copper tube fin structure effectively absorbs waste heat from the surrounding fluid domain. While the additional tube passes in Design 1 and Design 2 contributed a measurable improvement, this increase in tube passes yielded only an extra 1.6 °C to 1.7 °C of temperature difference over Design 3 and Design 4 at the peak load. This small gain occurred despite Design 2 incorporating four extra tube passes relative to Design 3 and Design 4, and two additional tube passes relative to Design 1. The empirical data showed that the reduced surface area and fewer tube passes utilised in Design 3 and Design 4 remained sufficient for the primary goal of hydrogen heating. This aligns with the temperature distribution shown in Table 4.1, where the gas temperature saturated by the second tube pass, rendering the additional downstream tube passes geometrically redundant for primary heating purposes. However, utilising these smaller designs inherently reduces the physical surface area available for integrating the TEG modules. This physical trade off will inevitably limit the total secondary electrical production, an aspect addressed in the subsequent TEG performance evaluation. As with all numerical models, these values represent idealized steady state conditions and carry inherent computational uncertainties, necessitating physical validation.

4.2.4 Fuel Cell Predicted Performance

Heating the incoming hydrogen reactant before it enters the PEM fuel cell directly influences the internal electrochemical kinetics. Based on established predictive equations from previous literature, [17] the anticipated power improvement functions as a dependent variable of the hydrogen temperature difference. When the IHR system raises the hydrogen temperature, it lowers the activation energy required for the internal chemical reactions. This physical mechanism reduces polarization losses and theoretically yields a higher electrical output for the exact same operational fuel feed.

Figures 4.10 a and b present the predicted fuel cell power enhancement in absolute Watts and relative enhancement percentage, respectively. The power gain increased continuously as the baseline fuel cell power increased from 500 W to 2000 W. At the lowest 500 W load, the absolute power improvement remained small. Design 1 produced 9.4 W, Design 2 produced 10 W, Design 3 produced 8.7 W, and Design 4 produced 9 W. When the fuel cell operated at the 2000 W maximum load, the power gain reached 159.2 W for Design 1, 159.1 W for Design 2, 154.1 W for Design 3, and 154.5 W for Design 4. These absolute power outputs directly mirror the hydrogen temperature difference profiles established previously, where Design 1 and Design 2 generated the highest gas temperatures.

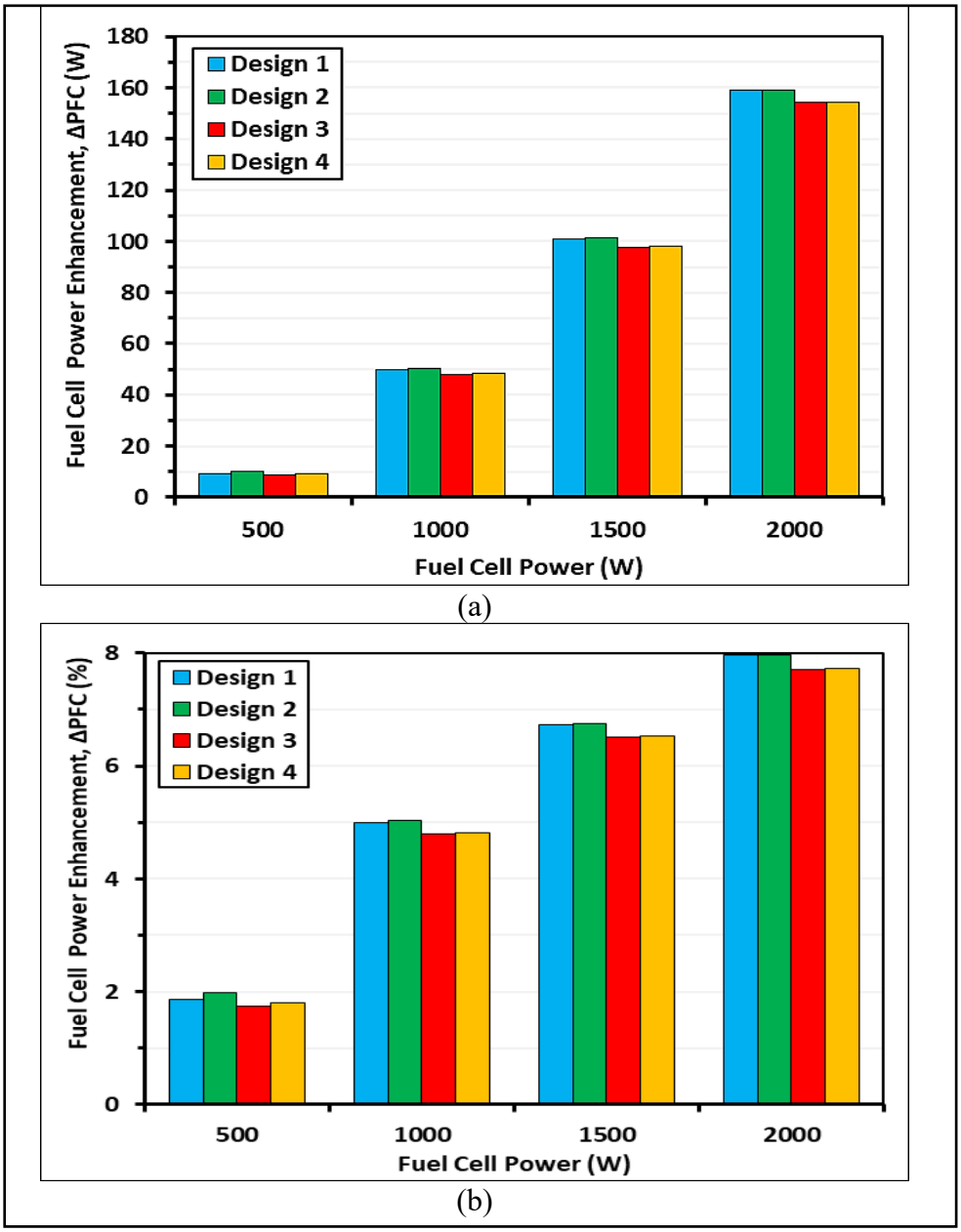

Figure 4.10 Predictions From Mathematical Electrochemical Model Based on Simulated Relative Hydrogen Preheated Temperatures (a) Fuel Cell Power Enhancement, (b) Enhancement Percentage From Base Output Without IHR.

The enhancement percentage provides a relative measure of the system performance benefits. The percentage enhancement starts at low values of 1.7% to 2% under the 500 W load across all cases. As the fuel cell power is scaled up to 2000 W, the relative gain increased to 8% for both Design 1 and Design 2, and 7.7% for Design 3 and Design 4. This upward trend suggests that hydrogen preheating provides a larger

benefit at higher current densities. At elevated hydrogen temperatures, the fuel cell electrochemical kinetics improves and reducing mass transport losses [17].

All evaluated IHR designs successfully produced a fuel cell power gain, achieving up to an 8% analytical improvement. While Design 1 and Design 2 produced the most promising primary power increments, selecting the optimal configuration for subsequent test bench and on road evaluations requires a further assessment on the TEG performance. Consequently, the TEG performance must be evaluated first to identify the most balanced physical design. Therefore, the subsequent section addresses these TEG electrical outputs before finalizing the configuration for further experimental testing.

4.2.5 TEG Thermal Behaviour and Electrical Power

The secondary electrical generation of the IHR system depends entirely on the thermal gradient maintained across the solid-state TEG modules. Based on the governing equations equation 3.22- 3.24 detailed in the methodology, the predicted TEG power output acts as a mathematical product of the short circuit current and the open circuit voltage. These electrical parameters function as direct responses to the absolute TEG surface temperatures and the resulting temperature difference between the hot and cold sides. Evaluating these thermal behaviors across the 500 W to 2000 W operational range reveals how effectively each physical geometry converts captured waste heat into usable electrical power.

Figure 4.11 compares the simulated TEG surface temperature profiles while Figure 4.12 profiles its relative surface temperature difference. The temperature difference increased for all configurations as the PEM fuel cell power increased. At the 2000 W maximum load, Design 2 achieved the highest difference at 4.90 °C. Design 3 and Design 4 followed with smaller differences of 1.87 °C and 1.83 °C, respectively. Design 1 recorded the lowest thermal separation, yielding only 0.31 °C at the peak operational load.

The temperature profiles for Design 1 exhibited very small separation between the hot and cold sides, resulting in thermal equalization rather than a useful gradient. In contrast, Design 2 displayed a clear thermal separation between the two module faces. This occurred because Design 2 combined a large internal heating surface area with an expanded external cooling architecture featuring more heat pipes and cooling fins. This

specific geometry maintained a high hot side temperature while simultaneously depressing the cold side temperature through external convection, thereby maximizing the thermal driving force. Design 3 and Design 4 lacked the extended heating fins of Design 2, which resulted in lower hot side temperatures and an overall smaller temperature difference.

Figure 4.13 details the resulting TEG electrical power generated in mW. At the low 500 W baseline, the available thermal energy across all designs was insufficient to overcome internal electrical resistances, resulting in 0 mW of production. As the operational power scaled to 2000 W, the power generation separated significantly and directly mirrored the thermal gradients. Design 2 produced the highest output at 5.51 mW. Design 3 and Design 4 generated 1.45 mW and 1.40 mW, respectively, while Design 1 produced a minimal 0.56 mW.

This electrical performance highlights a critical engineering mechanism. Power generation relies strictly on the physical temperature difference rather than the sheer quantity of thermoelectric material. Design 1 contained 12 TEG modules yet produced the lowest electrical power due to its inability to maintain a distinct cold side. Conversely, Design 2 utilised only 8 TEG modules but generated the highest electrical output because its physical geometry secured a much larger temperature difference. These findings establish that successful secondary power generation requires balancing heat absorption with effective heat rejection. This strongly aligns with parametric analyses by Zamri et al. [45] and Hasani and Rahbar, which demonstrate that convective cooling efficiency heavily dictates solid state generation. Maximizing the hot side temperature provides no electrical benefit if the cold side temperature rises proportionally. While Design 2 demonstrated the most effective thermal and electrical balance among the evaluated options, these computational values assume ideal contact resistances and steady state conditions As corroborated by Chen et al. [132] in their computational fluid dynamics approach for thermoelectric generators, numerical models effectively predict primary thermal gradients but frequently idealize physical interface boundaries. Therefore, physical experimental testing remains necessary to quantify the actual recoverable power under dynamic operating conditions. Moving beyond idealized mathematical assumptions is strictly required to capture the unpredictable thermal lag, structural flaws, and physical contact resistances inherent to actual vehicular operation [97].

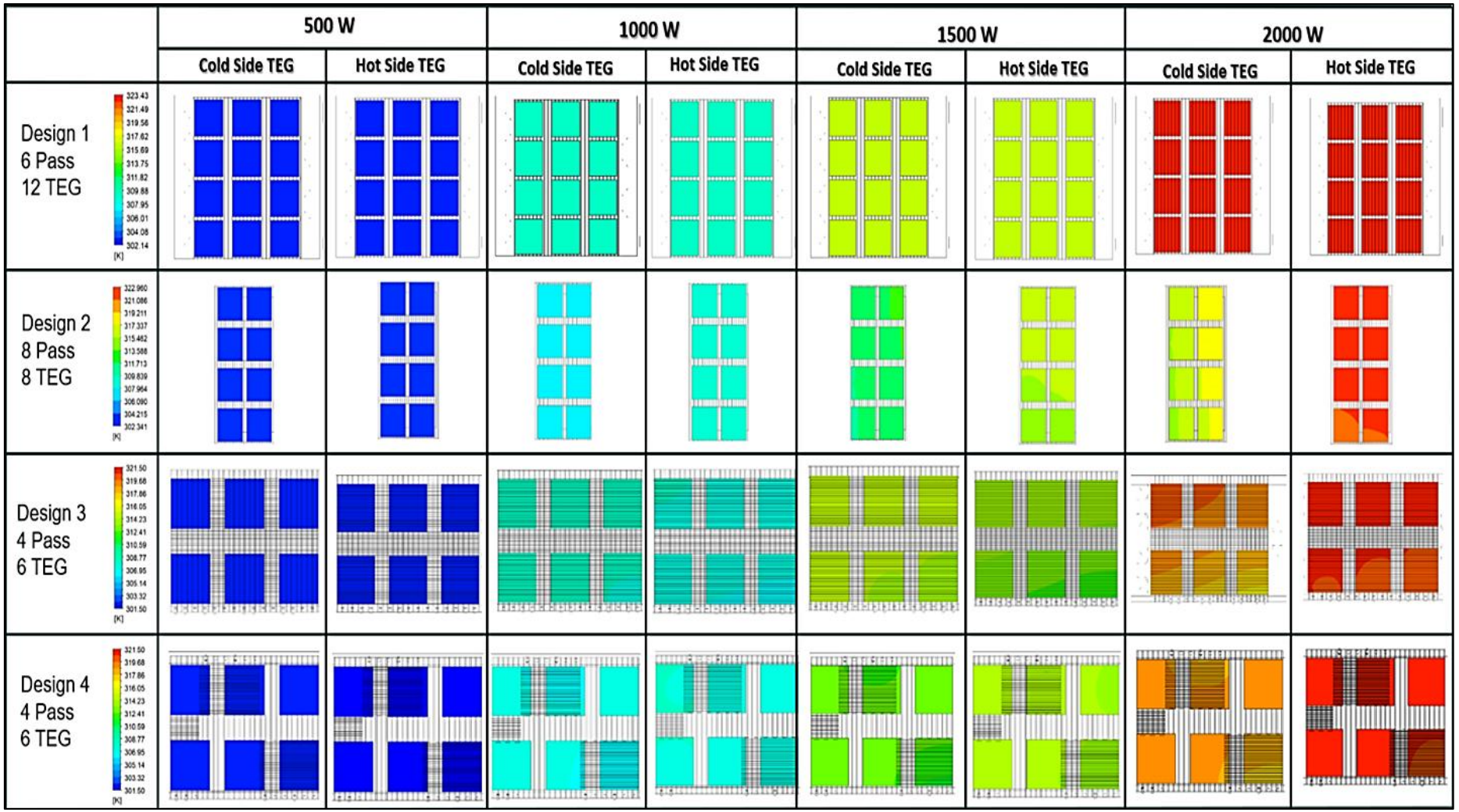

Figure 4.11 Simulated Temperature Contour of the TEG Hot and Cold Sides Under Variations of Fuel Cell Power

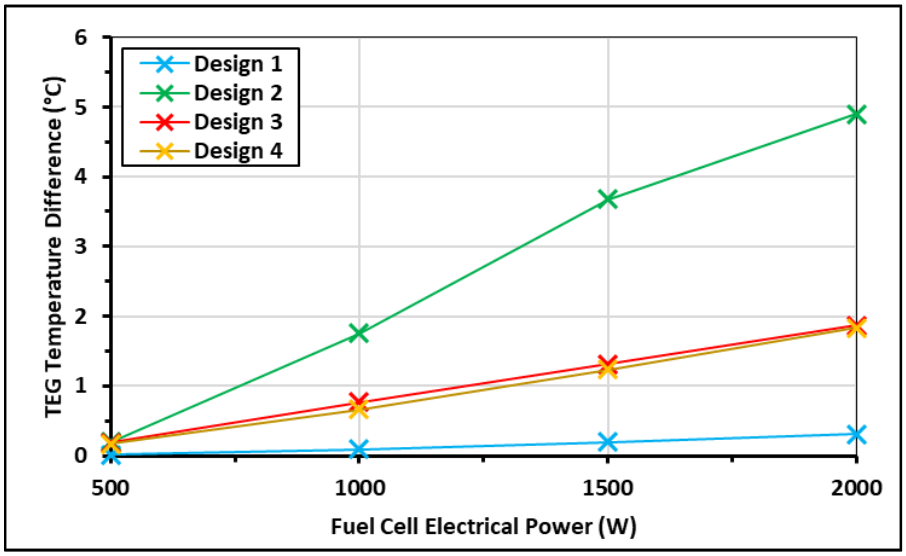

Figure 4.12 Simulated TEG Temperature Difference for the IHR Designs as a Function of Fuel Cell Power

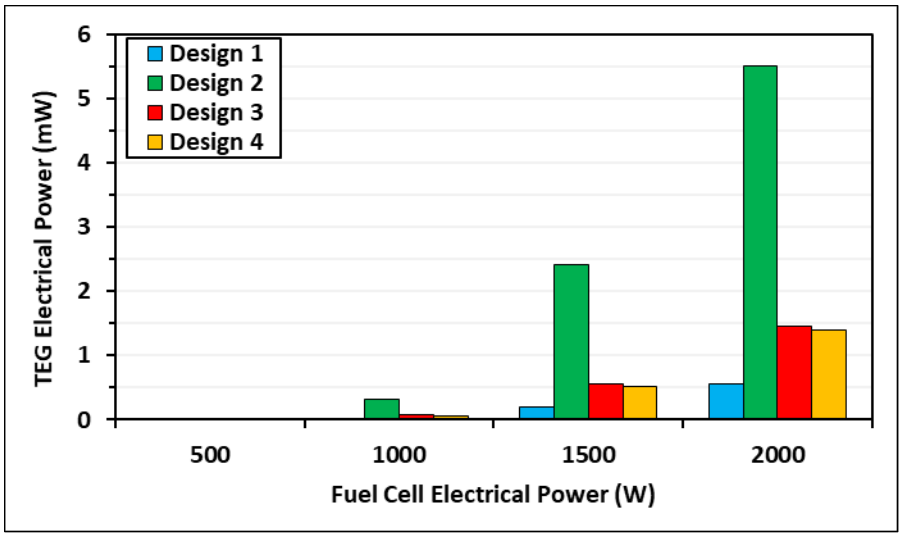

Figure 4.13 Estimated TEG Electrical Power Output Based on CFD-Predicted Temperature Differences at 500 to 2000 W Fuel Cell Power

4.2.6 Waste Heat Utilization (WHU)

The overall thermodynamic effectiveness of the IHR system is quantified through the WHU factor. This metric combines the recovered thermal energy from the hydrogen preheating process and the secondary electrical power generated by the TEG modules, expressing them as a fraction of the total available fuel cell waste heat.

Evaluating this parameter provides a complete system perspective on the recovery efficiency across the four proposed designs.

The calculated WHU percentages across the 500 W to 2000 W operational range was plotted on figure 4.14 and revealed consistent behaviour across all configurations. The recorded data showed that the utilization factor remained low, though it increased progressively with the fuel cell power load. At the 500 W baseline, the utilization recorded 0.16% for Design 1, Design 2, and Design 4, while Design 3 yielded 0.15%. As the fuel cell reached the 2000 W maximum load, the utilization factor improves to 1.31% for both Design 1 and Design 2. Design 3 and Design 4 recorded slightly lower values, each reaching a maximum of 1.27%.

These small utilization values originate from two primary physical constraints within the recovery architecture. First, the thermal energy absorbed during hydrogen preheating depends directly on the reactant mass flow rate. Because the maximum operational load of the PEM fuel cell is only 2000 W, the required hydrogen feed rate remains physically small. Consequently, the absolute heat absorption capacity of the gas is small relative to the total waste heat exhausted by the fuel cell. Second, the solid-state TEG modules contribute only a minor electrical output in the milliwatt range, as established in the previous section. This minimal secondary generation adds very little to the total recovered energy calculation.

Combining these two physical limits results in a low overall WHU. While the percentage appears small, this characteristic is expected for low power applications where the reactant flow rates fundamentally restrict the heat absorption capacity. The IHR system successfully demonstrates a physical method to capture otherwise wasted thermal energy, utilising it to enhance the primary fuel cell power and generate a small secondary electrical output. As with all mathematical and computational evaluations, these utilization metrics assume idealized environmental conditions and perfect insulation boundaries. As thoroughly documented by Qinguo Zhang et al. [67] in their specific evaluation of hydrogen preheating systems, idealized computational models frequently overestimate total recovery potential by ignoring ambient thermal leakages. This confirms that relying solely on software is insufficient, necessitating rigorous physical test bench validation to accurately account for actual thermal losses and inherent experimental uncertainties.

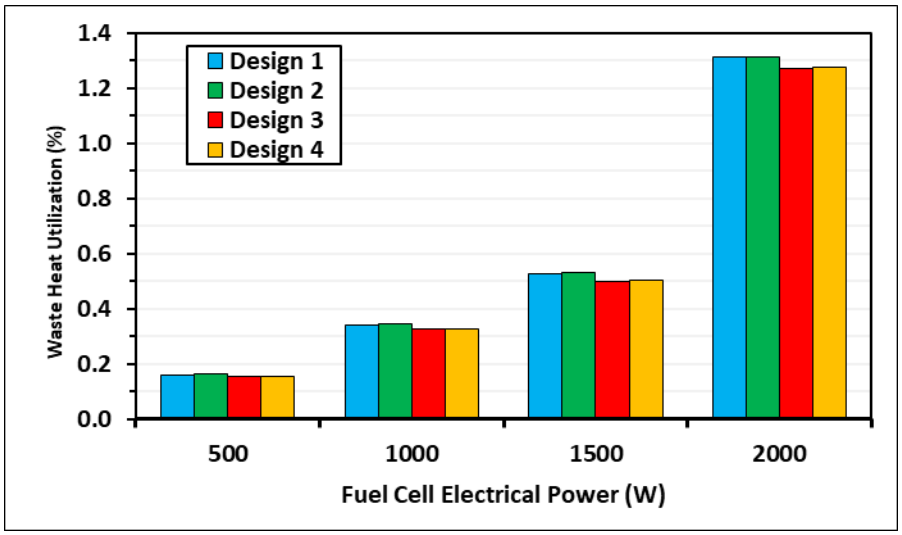

Figure 4.14 Waste Heat Utilisation of The IHR Designs as A Function of Fuel Cell Power at 500 to 2000 W

4.2.7 Summary

The preceding computational evaluations established the mathematical performance boundaries of four proposed IHR configurations. Because the overall waste heat utilization remained identically small across all geometries due to fundamental mass flow constraints, the final architectural selection relied entirely on maximizing the individual primary and secondary recovery pathways. The optimal design required a physical equilibrium, balancing the heat absorption necessary for reactant conditioning with the aggressive heat rejection needed to sustain solid state power generation.

While multiple configurations successfully elevated the hydrogen temperature to produce a analytical primary power gain, they frequently compromised the secondary recovery potential through inadequate cold side cooling. Design 2 emerged as the only configuration capable of satisfying both operational demands simultaneously. By effectively pairing high reactant heat absorption with an expanded external cooling architecture, it secured the highest TEG electrical output without sacrificing the primary hydrogen preheating performance. Consequently, because it provides the most effective dual recovery mechanism, Design 2 is selected as the designated architecture for the subsequent experimental test bench and on road evaluations. As these initial numerical conclusions rely on idealized steady state assumptions, physical testing remains necessary to quantify the actual recovery performance and account for unavoidable thermal losses within a dynamic operating environment. Furthermore, although the

computational results were verified against the mathematical baseline calculations, the computational fluid dynamics model requires empirical validation. The experimental test bench evaluations utilised to validate this numerical approach were discussed in Section 4.3.

4.3 Experimental Test Bench Results

The Design 2 configuration is selected for the laboratory test bench work and serves as the baseline architecture to compare the fuel cell integrated with the IHR subsystem against the standard fuel cell-only setup. This experimental phase is structured to quantify how the IHR system effects the hydrogen thermal condition, stack thermal behaviour, and overall electrical performance under a controlled, incremental current load. To emulate vehicle-induced convection on the cold-side chamber without altering the commanded electrical load, speed boundary conditions of 0, 5, and 10 m/s were imposed. Consequently, the system performance is assessed primarily as a function of the applied current. The ensuing analysis presents the fuel cell electrical performance first, followed by the hydrogen preheating response, the temperature distribution across the assembly, and concludes with the specific thermoelectric outcomes. Ultimately, this section establishes the experimental foundation required for subsequent computational validation and on-road testing.

4.3.1 Fuel Cell Electrical Performance

This subsection evaluates the electrical response by comparing the baseline configuration (without IHR) against the integrated setup under the three cooling speed conditions. The behaviour is assessed using the polarization profile, which encompasses the voltage-current and power-current relationships, alongside the resulting electrical power increments expressed in both absolute watts (W) and relative percentages increment (%).

Figure 4.15 illustrated the typical polymer electrolyte membrane fuel cell polarisation profiles of the baseline system compared against the integrated heat recovery configurations under simulated vehicle speeds. The recorded data exhibited a distinct non linear voltage response that decreased progressively with the drawn current, while the total electrical power rose accordingly. The voltage degradation across all evaluated cases was physically governed by three distinct electrochemical regions.

From the initial 1 A baseline up to approximately 10 A, the system experienced a steep initial voltage drop. This rapid decline was caused by activation polarisation, where a significant portion of the chemical energy was consumed strictly to overcome the kinetic activation barriers required to initiate the electrochemical reactions at the catalyst layer. Following this initial drop, the voltage decayed in a nearly linear, more gradual manner between 10 A and approximately 40 A. This intermediate region was dominated by ohmic resistance, which represents the physical opposition to protonic transport through the polymer membrane alongside the electronic resistance through the solid conductive plates. As the current demand escalated beyond 40 A toward the 60 A maximum boundary, the voltage profile exhibited a second steep decline. This final drop indicated the onset of mass transport limitations, where the rapid consumption of reactants outpaced their physical diffusion rate through the porous gas diffusion layers, inducing localized reactant starvation at the active catalyst sites.

When comparing the specific configurations, the baseline fuel cell exhibited the most severe voltage drop across the entire testing spectrum. Crucially, the voltage drop difference between the baseline system and the architectures featuring the integrated heat recovery began to display a significant mathematical separation at 30 A and above. For example, at the absolute maximum 60 A load, the baseline configuration experienced a severe voltage drop down to approximately 29.5 V. In contrast, the thermally conditioned system actively reduced this voltage drop, maintaining a higher operational potential of approximately 33.0 V.

This significant reduction in the voltage drop was driven by the physical availability of waste heat. At 30 A and above, the primary stack generated a substantially larger volume of exothermic thermal energy. This abundant heat strengthened the thermal driving potential through the recovery pathway, allowing the system to preheat the incoming hydrogen reactant much more aggressively. Elevating the reactant thermal state effectively lowered the internal activation energy required for the reactions to proceed. By improving the internal electrochemical kinetics exactly when ohmic and mass transport resistances typically dominate, the thermal conditioning directly mitigated the compounding polarisation losses, thereby reducing the overall voltage drop.

Because electrical power operates as the direct mathematical product of voltage and current, this reduced voltage drop directly allowed the integrated system to generate significantly more electrical power at the exact same current point. At the 60 A

boundary, this upward voltage shift resulted in the integrated system generating approximately 1950 W of primary electrical power, visibly outperforming the 1750 W produced by the unconditioned baseline setup. Although minor performance variations appeared among the three external cooling speeds, their overarching trajectories remained fundamentally similar. It is cautiously acknowledged that minor fluctuations in the high load data inherently exist due to transient localized water accumulation and minor experimental measurement noise common in physical testing. However, the pronounced mathematical separation between the baseline and the integrated cases clearly established that the thermal recovery architecture maintained a significantly more favourable internal operating state.

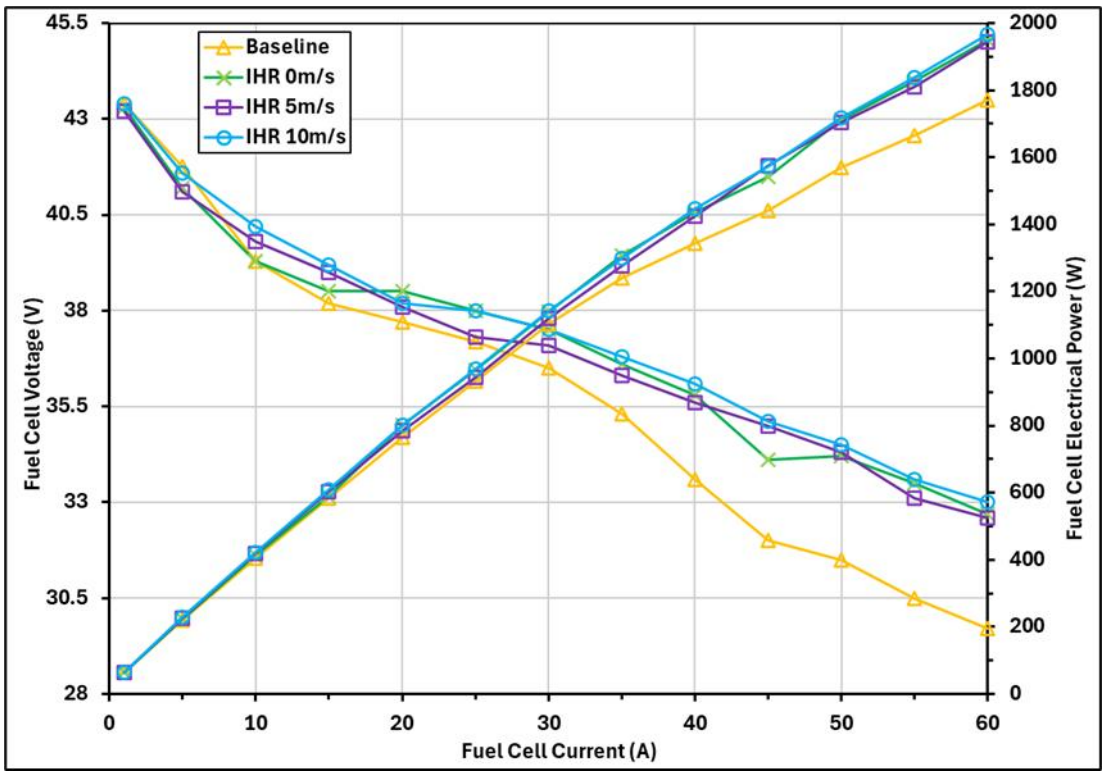

Figure 4.15 Fuel Cell Polarization Profiles of the Baseline System Compared With The Installation of IHR Under Simulated Vehicle Speeds

Figure 4.16 quantify this net electrical improvement. Both plots follow a comparable pattern where the increment remains modest at low currents and expands progressively, with the most pronounced benefits emerging at medium-to-high loads. The three speed cases track broadly similar trajectories, though small deviations exist. These minor differences appear consistent with practical experimental uncertainties, as nominally controlled variables, such as ambient room temperature stability and flow

sensitivities that cannot remain perfectly static throughout a full current sweep. Despite these dynamic variations, the integration provides a reliable electrical enhancement. Across the evaluated range, the maximum power increment occurs at the highest simulated vehicle speed of 10 m/s, achieving an increase of 196.7 W (11.1% compared to baseline) at 60 A. The increases at 60A for 0 m/s and 5 m/s conditions are approximately similar at 10.1% and 9.8%, respectively.

Below 25 A, the increment profiles display a fluctuating, non-monotonic pattern rather than a smooth upward curve. For instance, the 0 m/s case moves from a 7.9 W (1.94%) increment at 10 A down to 4.6 W (0.79%) at 15 A, before recovering between 20 and 25 A. Similarly, the 5 m/s profile rises to 20.04 W (3.43%) at 15 A but drops to 9.97 W (1.07%) at 25 A. Such behaviour is physically plausible under low-load conditions because the absolute waste heat generation and the resulting recovery driving potential were minimal. Consequently, small physical disturbances, such as transient thermal lag in the recovery path or minor variations in the reactant state, can yield disproportionate fluctuations in the calculated increments.

Beyond 25 A, the trends stabilize and demonstrate clear, non-linear growth. This shift indicates that higher current operation produces substantially more waste heat, which strengthens the thermal driving potential through the IHR pathway and enables more effective reactant conditioning. The 10 m/s case, for example, scales from a 41.45 W (3.76%) increment at 30 A up to 103.61 W (7.71%) at 40 A and reaches 149.40 W (9.52%) at 50 A before peaking.

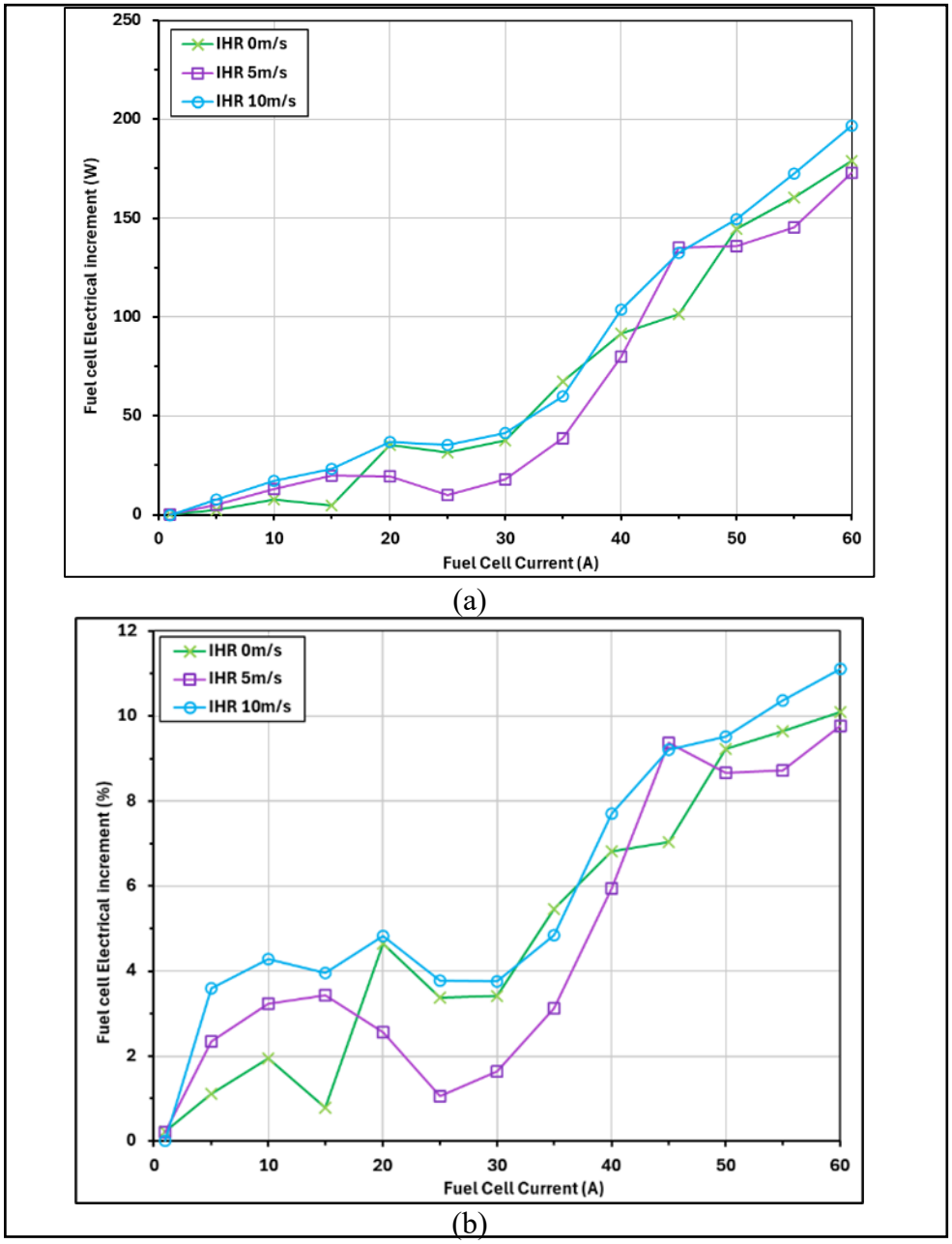

Figure 4.16 Fuel Cell Power Increment Compared to Baseline Case in (a) Unit Watts, and (b) Percentage Increment

From a thermodynamic and electrochemical standpoint, this performance improvement aligns with foundational theory. Fuel cell voltage is linked to the reaction's free energy and the thermal state of the reactants. During loaded operation, the actual stack voltage suffers from activation, ohmic, and mass-transport losses, all of which were temperature-sensitive through reaction kinetics and membrane conductivity. Integrating the IHR modifies the thermal state of the incoming hydrogen, which likely reduces effective polarization losses and supports a higher operating

voltage at equivalent currents. The observed pattern of modest gains at low loads and larger benefits at high loads generally reflects typical PEM fuel cell behaviour, where performance sensitivity to operating conditions increases as current density and polarization losses dominate.

4.3.2 FC and IHR System Thermal Performance

This section explores the thermal responses of the fuel cell stack. The analysis sequentially examines the fuel cell temperature rise, quantifies the associated rejected thermal power, and maps the dimensionless temperature distribution across the IHR spatial pathway. This progression establishes a thermal baseline that correlates with the electrical trends discussed previously.

Figure 4.17 shows the fuel cell stack temperature profile. It increases progressively with the increase in load current across all configurations, confirming that electrical demand acts as the primary driver of the thermal state. For the baseline setup without the IHR, the temperature rises from 23 °C at low loads (1 to 5 A) up to 50 °C at 60 A, logging intermediate values of 40 °C at 30 A and 46 °C at 50 A. When the IHR is active, the stack operates at an elevated thermal level, with the separation becoming distinct beyond the mid-load region. At 40 A, the baseline records 43 °C, while the three IHR cases converge at 49 °C, a consistent 6 °C elevation. At the 60 A maximum, the baseline hits 50 °C, whereas the IHR cases reach 53 °C at 0 m/s and 55 °C at both 5 and 10 m/s. These results indicate that the integrated IHR system retains a portion of the generated waste heat, leading to higher operating temperatures under heavy loads. However, a potential indicator of environmental influence appears at the lowest load of 1 A, where the baseline records a slightly lower initial temperature than the IHR cases prior to any substantial waste heat generation, suggesting ambient variations may also partially contribute to the overall thermal elevation.

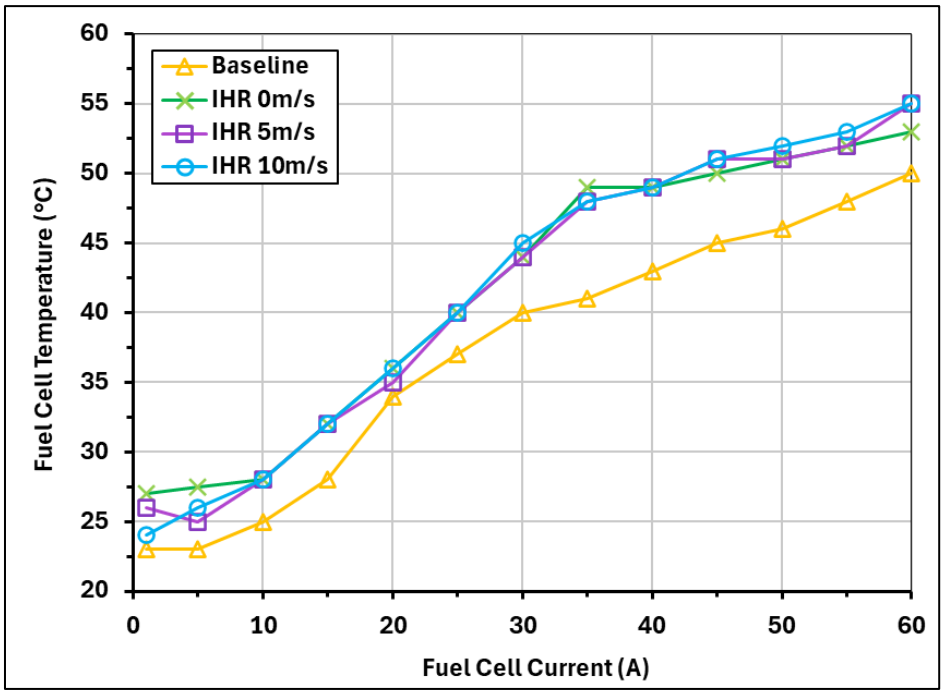

Figure 4.17 Effect of Fuel Cell Stack Current Load Variations to its Temperature Profiles

Figure 4.18 presents the profiles of the generated stack thermal power. The heat generated increases exponentially with current, expanding from approximately 24.4 W at 1 A and reaching a range between 1610 to 1810 W at 60 A, underscoring high-load operation as the dominant waste-heat resource due to greater irreversibilities. The baseline thermal power escalates to 1805.88 W at 60 A. Conversely, the IHR-integrated cases become systematically lower at medium-to-high loads. By 60 A, the thermal power calculates to 1627 W, 1633 W, and 1609 W for the 0, 5, and 10 m/s conditions, respectively. This reduction under IHR conditions mechanistically corresponds to the energy partitioning of the stack. Because the integrated cases experience a reduced voltage drop, a larger fraction of the chemical energy converts into electrical output, leaving proportionally less energy to be rejected as heat.

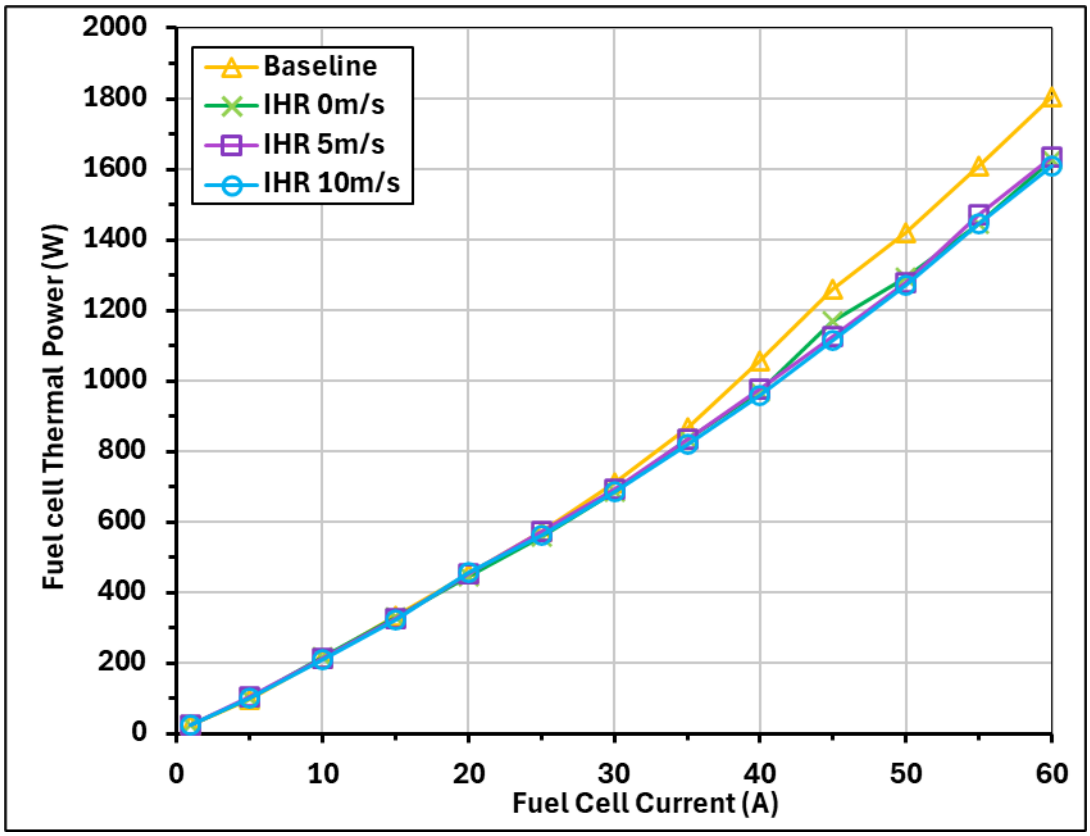

Figure 4.18 Generated Thermal Power Profiles of the Fuel Cell Stack

To map the spatial distribution of the thermal energy as it leaves the stack, Figure 4.19 profiles the temperature distribution at system-level along a dimensionless distance from the fuel cell stack to the cold chamber. The measured nodes trace the pathway from the stack to the ambient exit: (1) fuel cell waste heat, (2) hot stream, (3) IHR hot base, (4) TEG hot side, (5) TEG cold side, (6) cold-side fins, and (7) cold chamber outlet.

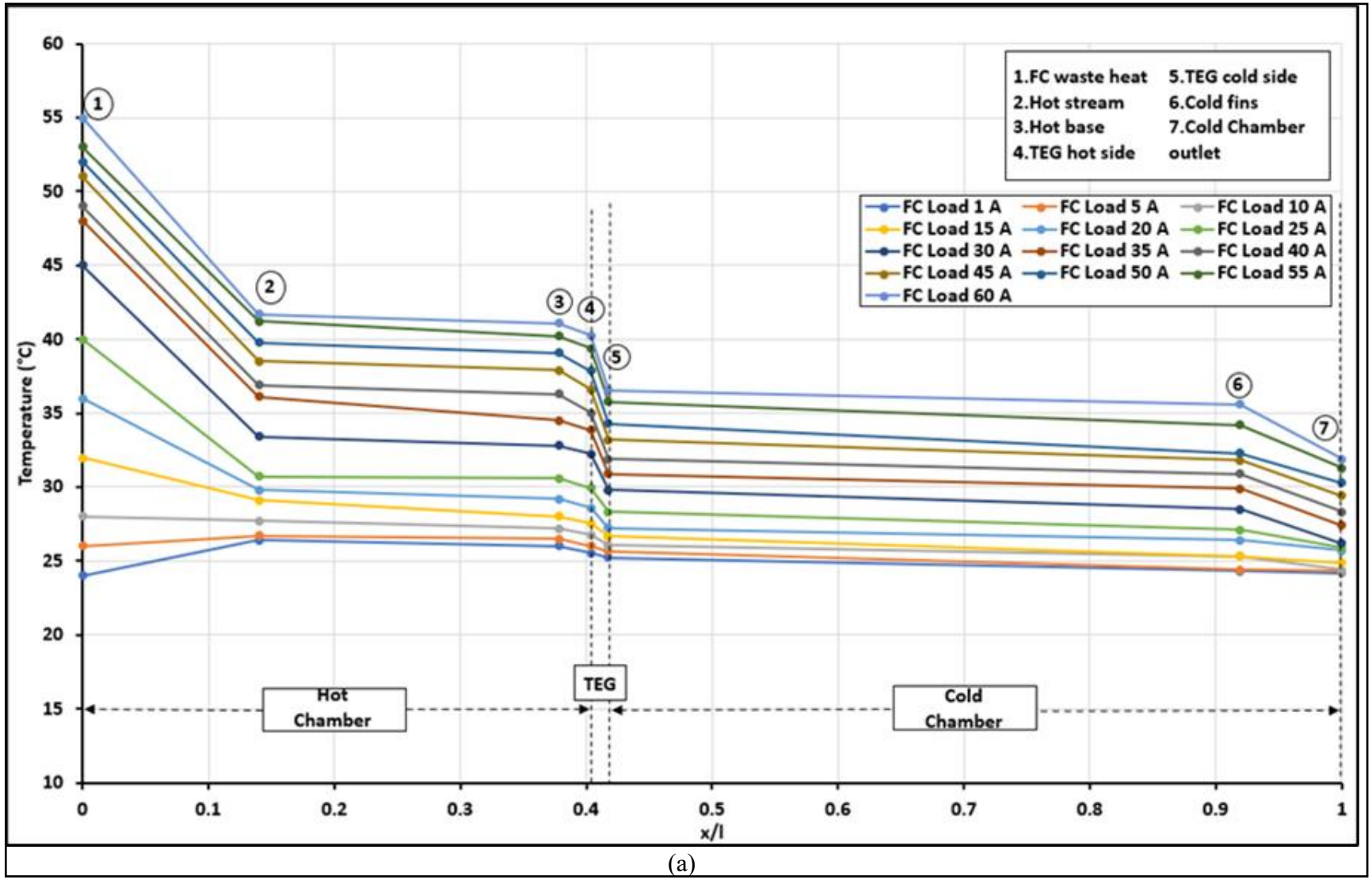
1.FC waste heat
2.Hot stream
3.Hot base
4.TEG hot side
5.TEG cold side
6.Cold fins
7.Cold Chamber outlet
FC Load 1 A
FC Load 5 A
FC Load 10 A
FC Load 15 A
FC Load 20 A
FC Load 25 A
FC Load 30 A
FC Load 35 A
FC Load 40 A
FC Load 45 A
FC Load 50 A
FC Load 55 A
FC Load 60 A
Temperature (°C)
x/l
Hot Chamber
TEG
Cold Chamber

(a)

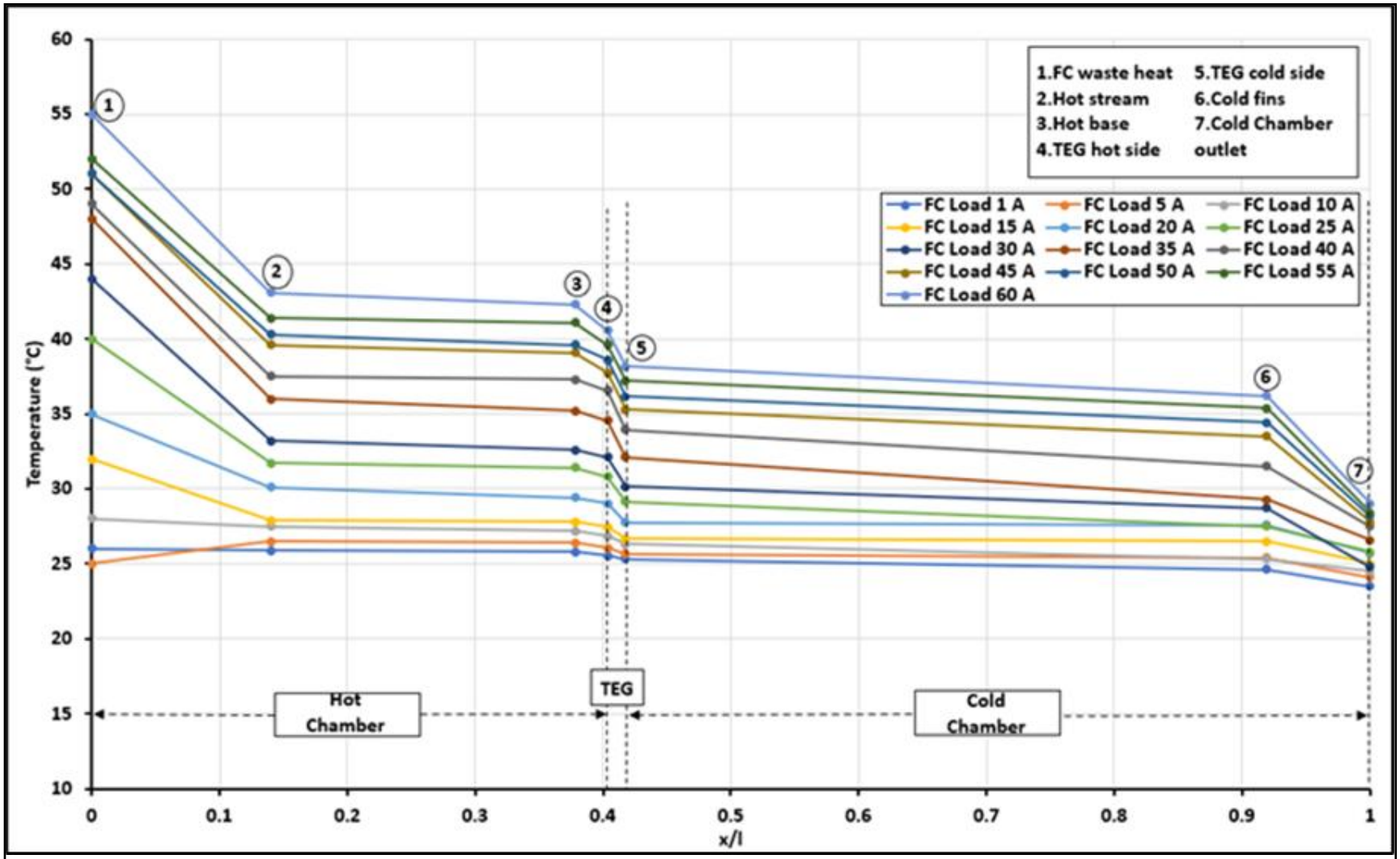
1.FC waste heat
2.Hot stream
3.Hot base
4.TEG hot side
5.TEG cold side
6.Cold fins
7.Cold Chamber outlet
FC Load 1 A
FC Load 5 A
FC Load 10 A
FC Load 15 A
FC Load 20 A
FC Load 25 A
FC Load 30 A
FC Load 35 A
FC Load 40 A
FC Load 45 A
FC Load 50 A
FC Load 55 A
FC Load 60 A
Temperature (°C)
x/l
Hot Chamber
TEG
Cold Chamber

(b)

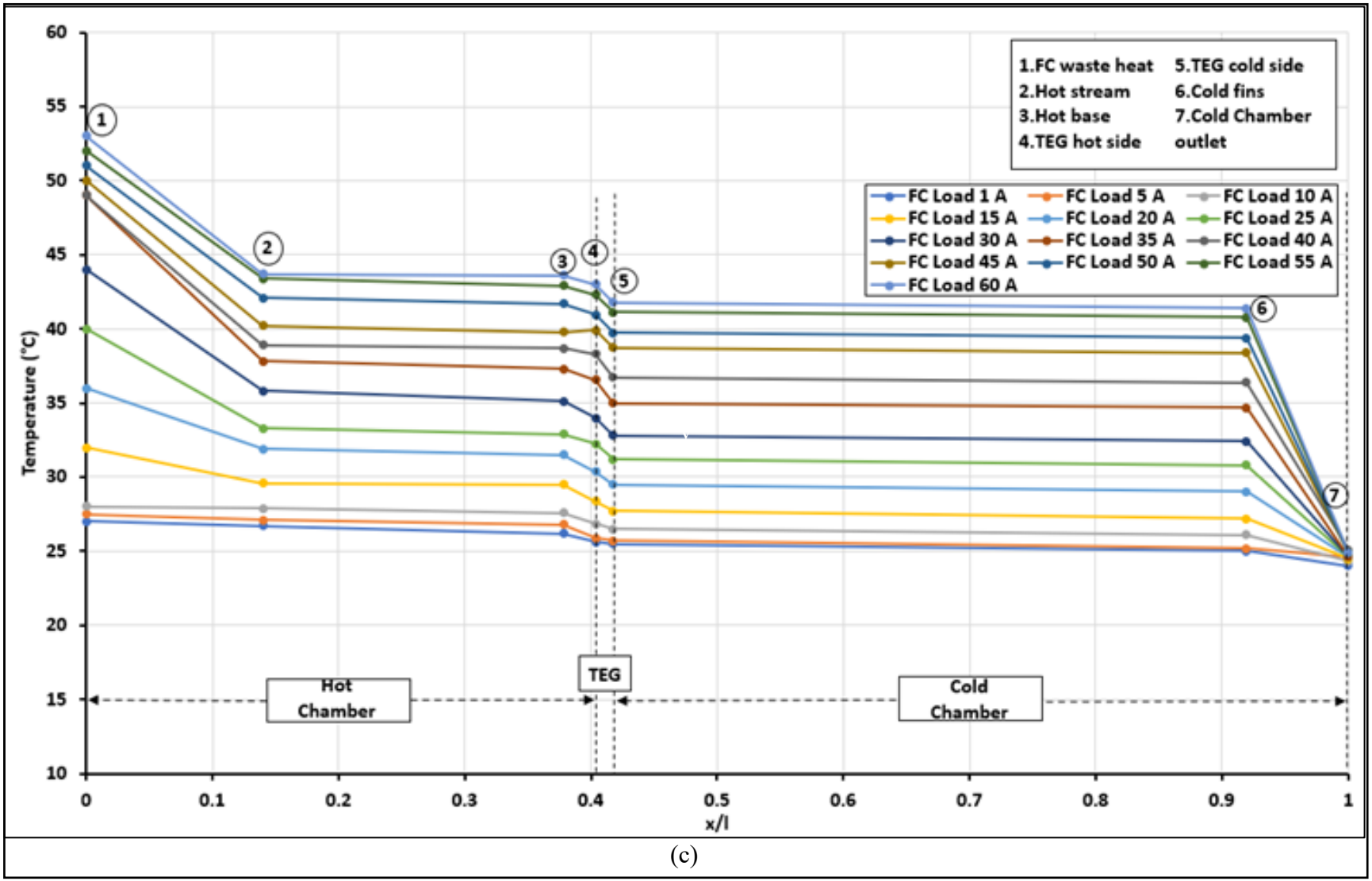
1.FC waste heat
2.Hot stream
3.Hot base
4.TEG hot side
5.TEG cold side
6.Cold fins
7.Cold Chamber outlet
FC Load 1 A
FC Load 5 A
FC Load 10 A
FC Load 15 A
FC Load 20 A
FC Load 25 A
FC Load 30 A
FC Load 35 A
FC Load 40 A
FC Load 45 A
FC Load 50 A
FC Load 55 A
FC Load 60 A
Temperature (°C)
x/l
Hot Chamber
TEG
Cold Chamber

(c)

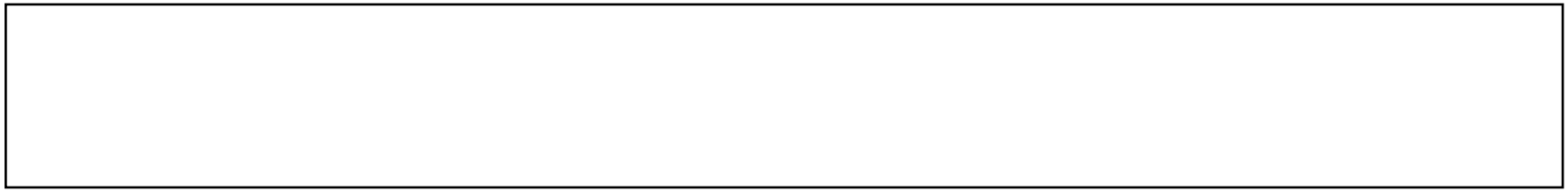

Figure 4.19 Spatial Temperature Distribution Across the IHR System Under Variations of Simulated Vehicle Speeds (a) 0 m/s (b) 5 m/s and (c) 10 m/s

Within the heating chamber (Points 1 to 2), a steep temperature drop emerges as the current increases. For example, at 60 A under the 10 m/s condition, the fuel cell (Point 1) records roughly 55 °C while the hot stream sensor (Point 2) reads 41.7 °C. This 13.3 °C differential represents an approximate 24% temperature drop relative to the source. While exact heat flux measurements would require direct flow meters, this steep gradient serves as a strong diagnostic indicator. It suggests that a substantial fraction of the source heat dissipates in the upstream coupling path, likely due to thermal contact resistance or structural conduction losses. Consequently, refining the hot chamber insulation and interface design appears favourable for mitigating this drop and improving thermal coupling in future iterations.

On the cooling side of the assembly, the gradients depend heavily on the imposed convection. The segment from the cold fins to the outlet (Points 6 to 7) is steep at 0 m/s, implying poor heat transfer to the stagnant ambient air. In contrast, this segment flattens considerably at 10 m/s, demonstrating robust heat removal driven by active convection. Similarly, the thermal relationship across the TEG module (Points 4 to 5) reveals that the 5 and 10 m/s cases sustain steeper gradients than the 0 m/s case. This dimensionless spatial mapping indicates that a stronger cold chamber assembly is needed to lower the cold side temperature and leads to larger thermal differential across the thermoelectric modules.

4.3.3 Hydrogen Flow Rate Profile

This This subsection assessed the reactant delivery response during the fixed current operation to empirically verify whether the physical addition of the integrated heat recovery pathway introduced any measurable flow restrictions. As illustrated in Figure 4.20, the recorded data demonstrated that the hydrogen flow rate scaled in a nearly linear fashion with the applied electrical current. The measured flow swept from a near zero state at the minimum load up to its absolute maximum boundary at 60 A, 15 L/M, confirming that the internal supply system responded proportionately and reliably to the programmed testing sequence.

The high current demand from the vehicle physically pulls electrons, which then forces the fuel cell to consume more hydrogen [141]. Because the high current demand continuously drains electrons from the anode, the hydrogen oxidation reaction must accelerate rapidly to keep up. This microscopic acceleration rapidly depletes the local

concentration of hydrogen gas at the catalyst sites. To prevent internal reactant starvation and a subsequent voltage collapse, the overarching electronic control system detects this rapid consumption and commands the injector valves to increase the macroscopic hydrogen volumetric flow rate. This precise relationship is mathematically governed by the Faraday law of electrolysis, which dictates that the molar consumption rate of the reactant is strictly proportional to the generated electrical current [12]. Consequently, at the macro level, as the external electrical load demanded a higher current, the internal fuel cell controller autonomously supplied a proportionally larger volumetric flow rate of hydrogen gas.

A critical secondary observation indicated that the hydrogen flow rate curves for the baseline fuel cell and all IHR speed conditions remained essentially identical across all physical configurations at any given electrical setpoint, the electrical performance improvements identified previously could not be attributed to an inadvertently enriched fuel supply. While the thermal preheating process actively altered the gas enthalpy and elevated its internal thermal state, it did not change the stoichiometric mass demand required for the reactions to proceed [67]. Therefore, the enhanced electrical output was isolated entirely to favourable changes in internal operating conditions, specifically the thermally induced voltage drop reduction, rather than an artificial increase in raw reactant volume. The linear relation of the hydrogen feed matching the applied current was fully expected under stoichiometric flow control. This empirical behaviour successfully confirmed that thermal conditioning improved the electrochemical performance without requiring an increased reactant mass supply.

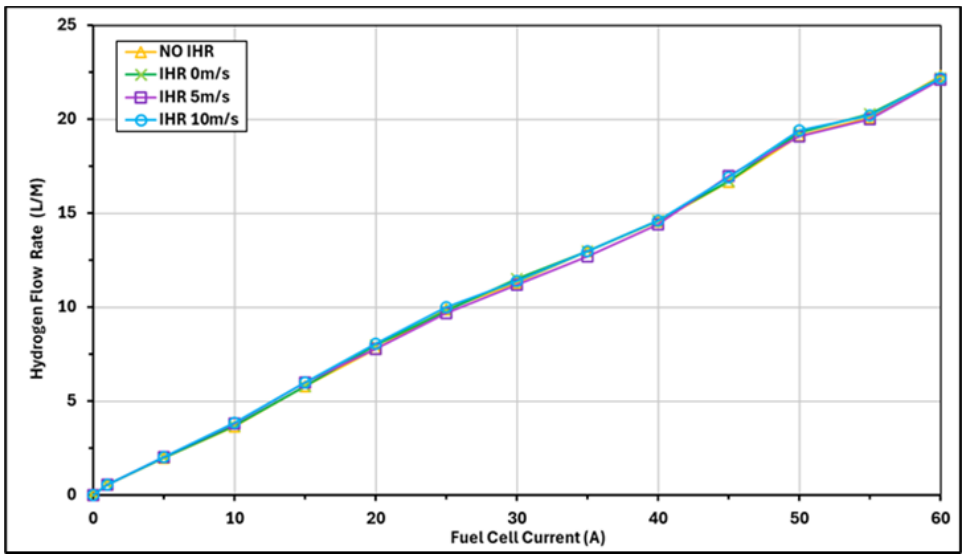

Figure 4.20 Measured Hydrogen Flow Rates Under Variations in Stack Current

4.3.4 Hydrogen Preheating Performance

The preheating behaviour of the integrated system is evaluated using three primary indicators - the inlet and preheated temperatures, the resulting temperature differential, and the total heat absorption. The objective is to determine if the recovery method provides a scalable hydrogen temperature rise linked to the fuel cell's waste-heat generation.

Figure 4.21a shows the hydrogen temperature profiles at the inlet and the exit (preheated condition) of the IHR. The analysis indicate that the hydrogen inlet temperature remains highly stable at approximately 23 °C across the full sweep, subject only to minor experimental noise. This stability is vital as it confirms the upstream supply condition acts as a constant baseline. Consequently, the distinct rise in the preheated temperature curve can be confidently attributed to the IHR heating chamber. The preheated hydrogen increases almost linearly, progressing from 24 to 27 °C at low loads up to approximately 41 °C at 60 A. Furthermore, the three speed profiles (0, 5, and 10 m/s) overlap closely. This indicates that preheating performance was influenced entirely by the fuel cell waste-heat, while the vehicle speeds have negligible influence on the hydrogen heating.

Figure 4.21b plots the resulting hydrogen temperature difference. The difference increases from roughly 2 °C at low loads to nearly 17 °C at 60 A. The increase confirms that the scale of hydrogen thermal heating was directly related to the waste heat intensity due to stack loadings. However, when evaluating the absolute energy transferred, Figure 4.22 reveals that the total hydrogen heat absorption remains below 8 W across all cases.

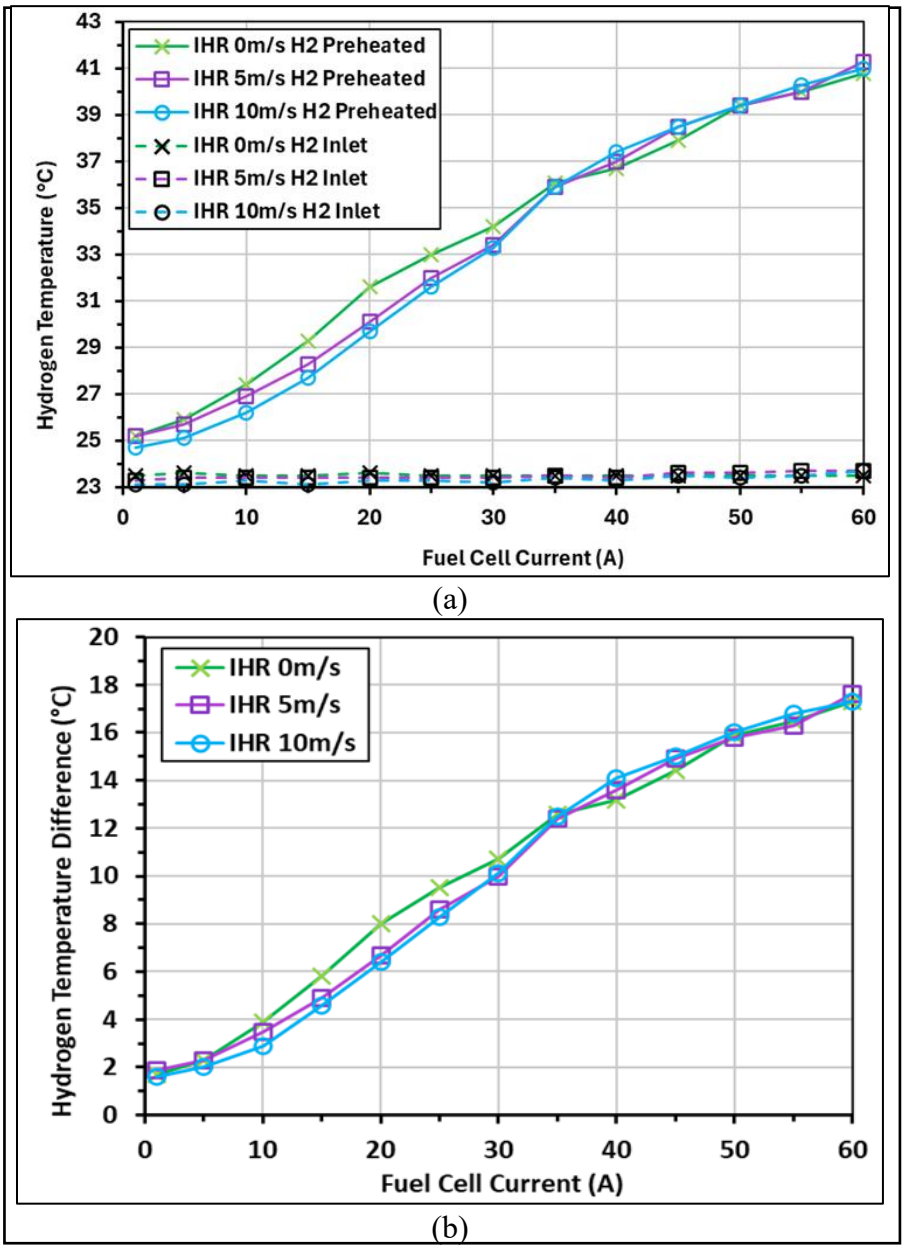

Figure 4.21 Hydrogen Temperature Profiles (a) at the Inlet and Exit of the IHR, and (b) Resulting Temperature Differences

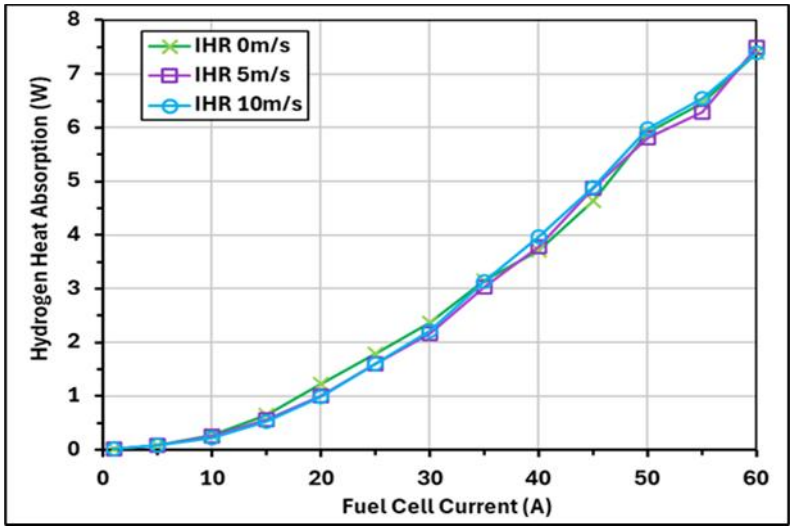

Figure 4.22 Heat Absorbed By Hydrogen Flow During Preheating at the IHR

Despite a substantial temperature difference approaching 17 °C, the relatively low heat absorption rate of less than 8 W aligns with the system's thermodynamic boundaries. The magnitude of heat transfer was limited by both the driving temperature and the fluid's mass flow rate. In this setup, the maximum hydrogen mass flow was extremely small, recorded at 2.80107 mg/s. According to the specific heat capacity relationship, the thermal absorption was mathematically constrained. This was a direct thermodynamic consequence of the low flow rate where a wide hydrogen temperature difference yields a modest absolute heat absorption if the mass being heated was minimal. The linear rise in preheated temperature supports the conclusion that the process was waste-heat limited and scales reliably with the load. Such preheating trends were typical when the heat source was directly proportional to the polarization heat generated by the stack.

4.3.5 TEG Thermal and Electrical Performance

This subsection evaluates the TEG response within the heat recovery pathway using three core metrics: TEG temperature difference, TEG total heat transfer rate, and TEG electrical power output. The analysis explores how the rising fuel cell load supplies thermal potential, and how the vehicle speeds influence external convection rates and dictate heat rejection as well as subsequent module performance.

Figure 4.23 illustrates that TEG temperature difference increases with stack output current for all cases, establishing that a higher electrical load yields a stronger

thermal driving potential. At low currents up to 10 A, the difference remains marginal, staying below 0.70 °C. As the load advances, the speed cases diverge clearly. Reaching 30 A, TEG temperature difference expands to 1.20 °C (0 m/s), 1.95 °C (5 m/s), and 2.45 °C (10 m/s). By the 60 A boundary, the values hit 1.20 °C, 2.43 °C, and 3.70 °C, respectively. These metrics demonstrate that higher cooling speeds successfully lower the cold-side temperature, thereby sustaining a steeper gradient across the TEG. Free convection at 0 m/s speed exhibits a partially saturating TEG temperature difference beyond the mid-load region, an outcome consistent with a weak cold-side sink that limits thermal separation despite abundant waste heat.

Figure 4.24 tracks the corresponding TEG total heat transfer. The total heat transferred increases with current across all setups, proving that elevated loads drive greater heat flux through the module. The magnitude of this transfer also scales with convection speed. Operating at 40 A, the calculated heat transfer was 5.3 W (0 m/s), 9.4 W (5 m/s), and 11.1 W (10 m/s). Pushing the load to 60 A yields an increased heat transfer rate of 6.9 W (30% increase), 10.2 W (9%), and 12.8 W (15%), respectively.

A distinct behavioural shift occurs in the 0 m/s profile, which flattens between 35 A and 50 A (hovering between 5.24 to 5.30 W) before a final slight rise. This plateau characterizes a cold-side physical limitation: when ambient heat rejection was poor, the cold-side temperature creeps upward, eroding the driving gradient and constraining incremental heat flow. Conversely, the 10 m/s case rises steadily, confirming that active cooling satisfies the thermal demand required to pull heat through the module.

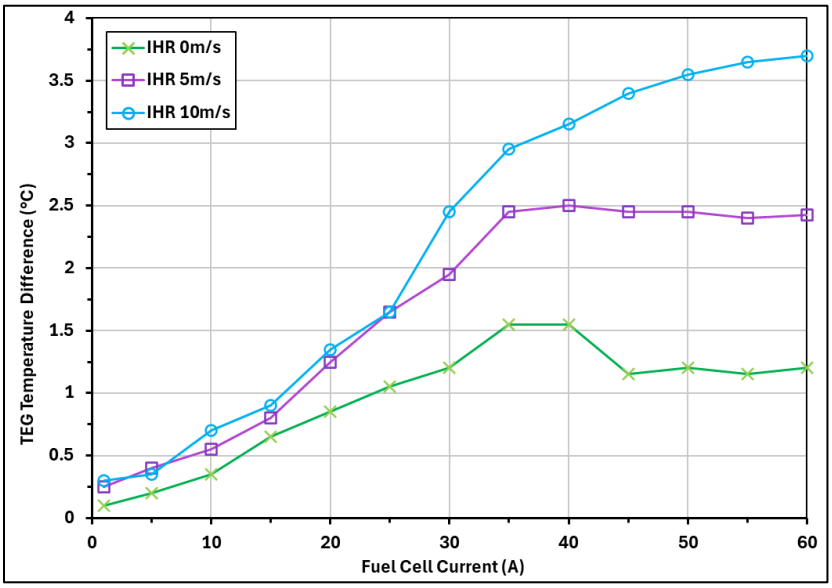

Figure 4.23 TEG Temperature Difference Trend Relative To Fuel Cell Stack Current Variation

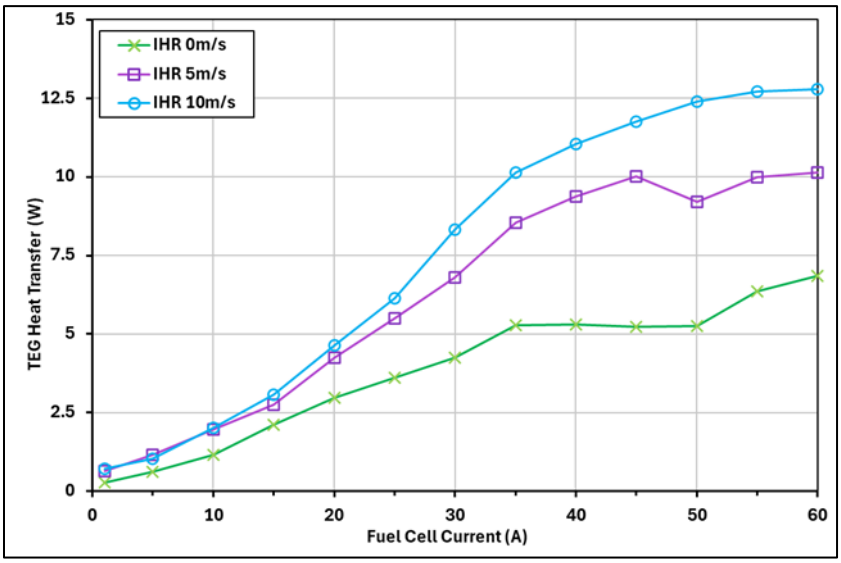

Figure 4.24 Heat Transfer Rate Across the TEG

Figure 4.25 displays the resulting electrical power. The generation response accelerates strongly with current, and the separation between the varied cooling conditions becomes stark at high loads. Below 15 A, generation was near zero, as the minimal gradient cannot overcome the module's internal electrical resistance. Advancing to 40 A, the output jumps to 32.6 mW (0 m/s), 120.1 mW (5 m/s), and 164.2 mW (10 m/s). The absolute maximum occurs under the 10 m/s condition, approaching 192.5 mW at 55 A and stabilizing above 187.0 mW at 60 A. This confirms that robust cold-side heat rejection is integral to maximizing thermoelectric conversion.

Notably, the active cooling profiles exhibit a degree of non-linear behaviours. The 5 m/s case shows slight fluctuations between 45 A and 60 A, where TEG electrical power peaks at 138.7 mW, dips to 108.8 mW, and recovers between 132.2 to 133.3 mW range. Reviewing the corresponding temperature data reveals that the 5 m/s TEG temperature difference also begins to stabilize in this exact span. This fluctuation highlights an experimental discrepancy common in dynamic test benches, where minor shifts in contact thermal coupling or transient ambient drifts can cascade into noticeable variations in electrical output, given the high sensitivity of thermoelectric modules. Despite this localised deviation, the general TEG trend remains intact - increased cooling speed secures a larger TEG temperature difference, driving higher heat flow and generating superior electrical power.

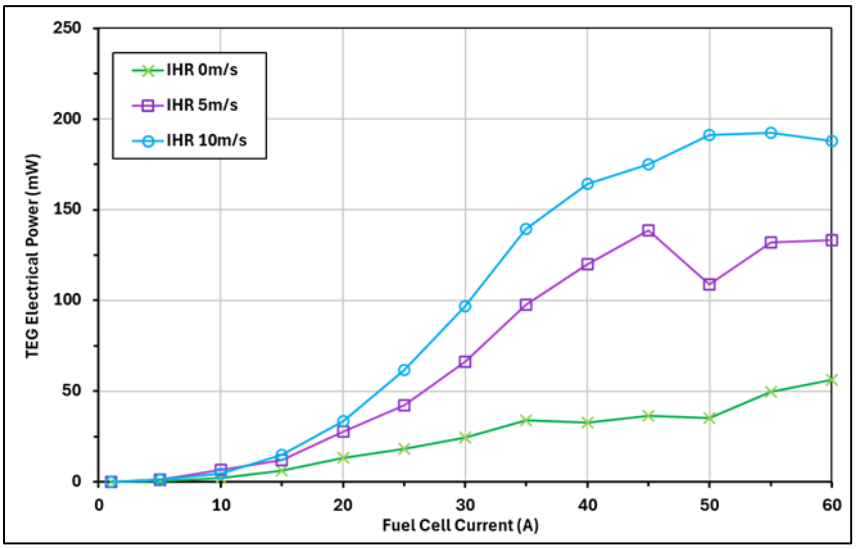

Figure 4.25 Electrical Power Generated by the TEG

4.3.6 Fuel Cell Efficiency

This subsection evaluates the overall fuel cell efficiency relative to the electrical demand. Figure 4.26 demonstrates that inversely tracks the current load. The baseline stack experiences a steady decay from 57.4% at 1 A down to 39.3% at 60 A. In contrast, the integrated configurations preserve a noticeably higher efficiency across the medium and high-demand regions. At the 60 A maximum, the fuel cell efficiency for the IHR cases stabilize at 43.4% (0 m/s), 43.5% (5 m/s), and 43.8% (10 m/s). Assessing this as a relative percentage improvement over the baseline, the gains expand progressively to 10.6%, 10.8%, and 11.6%, respectively. In absolute terms, this translates to efficiency increases of 4.2, 4.2, and 4.6 percentage points (pp) at 60 A, as shown in Figure 4.27.

At low currents, the efficiency curves cluster tightly and reflecting minimal benefit. However, as the load surpasses 25 A, the separation becomes persistent and mechanistically clear. The efficiency relative to hydrogen energy input is entirely dependent on the operating voltage. Because the integrated system successfully mitigates the voltage drop at high loads, it yields a greater electrical output for the exact same chemical input, thereby registering a higher efficiency. These substantial improvements at high loads correlate perfectly with the operating regime where polarization and mass transport losses heavily dominate, rendering the cell highly responsive to favourable changes in reactant temperature. The high sensitivity of fuel cell efficiency to voltage drop mitigation at elevated current densities is extensively documented in performance literature.

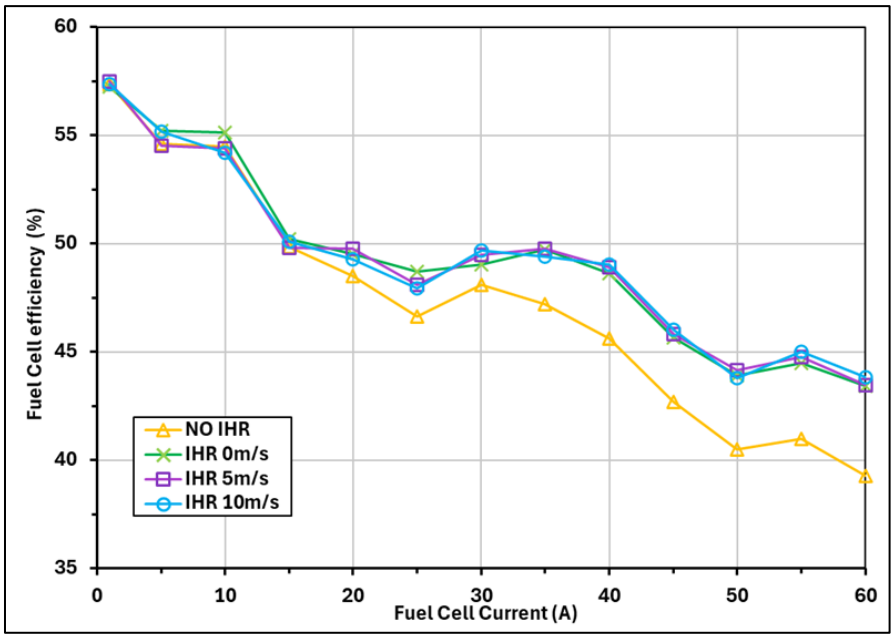

Figure 4.26 Fuel Cell Conversion Efficiency Profiles Across Load Current Polarization

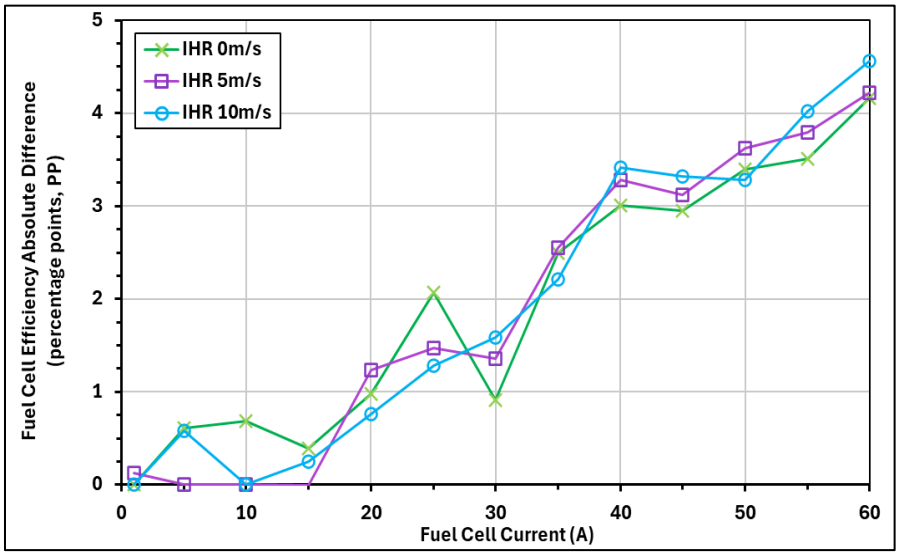

Figure 4.27 Absolute Difference of Fuel Cell Efficiency Under Stack Current Variation

Examining the correlation between the hydrogen temperature difference and the absolute efficiency percentage point gain (refer Figure 4.28) reveals a clear progressive dependence. Taking the 10 m/s case as a primary example, the efficiency increments scales from near-zero values at low temperature differentials up to a 4.56 pp gain when hydrogen temperature difference reaches 17.3 °C. A similar relationship governs the 5 m/s case, culminating in a 4.22 pp gain at a hydrogen temperature difference of 17.6 °C. The 0 m/s profile follows suit, climbing from 0 pp at 1.7 °C to approximately 4.16

pp at 17.3 °C. When the temperature differential is small (below 5 °C), the efficiency increments remain marginal and susceptible to slight experimental discrepancies. However, as the waste-heat source intensifies at higher loads and yielding hydrogen temperature difference values above 12 °C, the efficiency improvements lock into a stable and upward trajectory. This data correlation indicates that the degree of active hydrogen preheating acts as a direct driver for the observed enhancements in overall fuel cell efficiency.

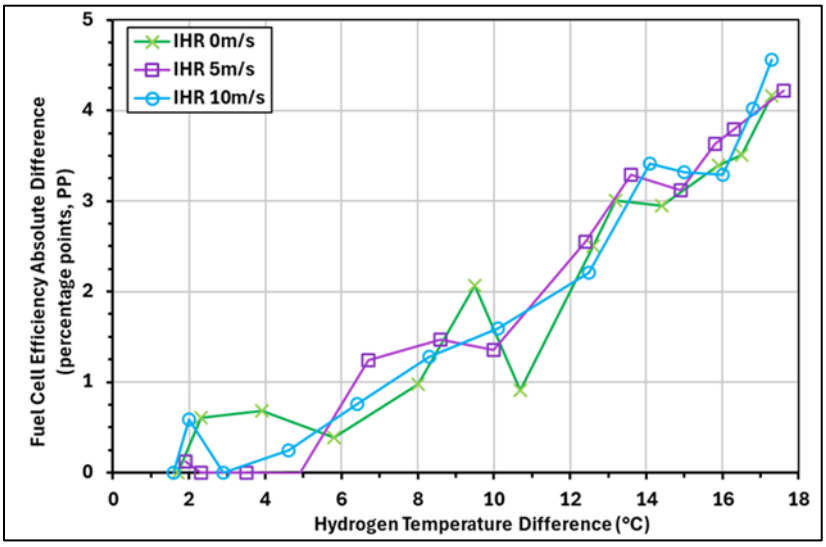

Figure 4.28 Absolute Difference of Fuel Cell Efficiency Across Hydrogen Temperature Difference Variations

4.3.7 Waste Heat Utilization

This subsection investigates the waste heat utilization (WHU), a metric reflecting the system's effectiveness in capturing available stack waste heat and converting it into useful thermal energy and secondary TEG power. The objective of the analysis is on mapping the fractional utilization scales with load and its responses to external convection.

Figure 4.29 indicates a distinct parabolic trend for the waste heat utilization across all three speed configurations. At the low-load boundary (5 A), the WHU registers at 0.69% (0 m/s), 1.2% (5 m/s), and 1.1% (10 m/s). Progressing toward the mid-load region, the utilization factor climbs steadily to a maximum at 35 A. At this optimal operating point, the factors maximize at 1.0%, 1.4%, and 1.6%, respectively. This initial ascent indicates that as the fuel cell begins generating substantial waste heat,

the thermal driving potential through the IHR assembly improves and allowing the mechanisms to operate more efficiently relative to the available energy.

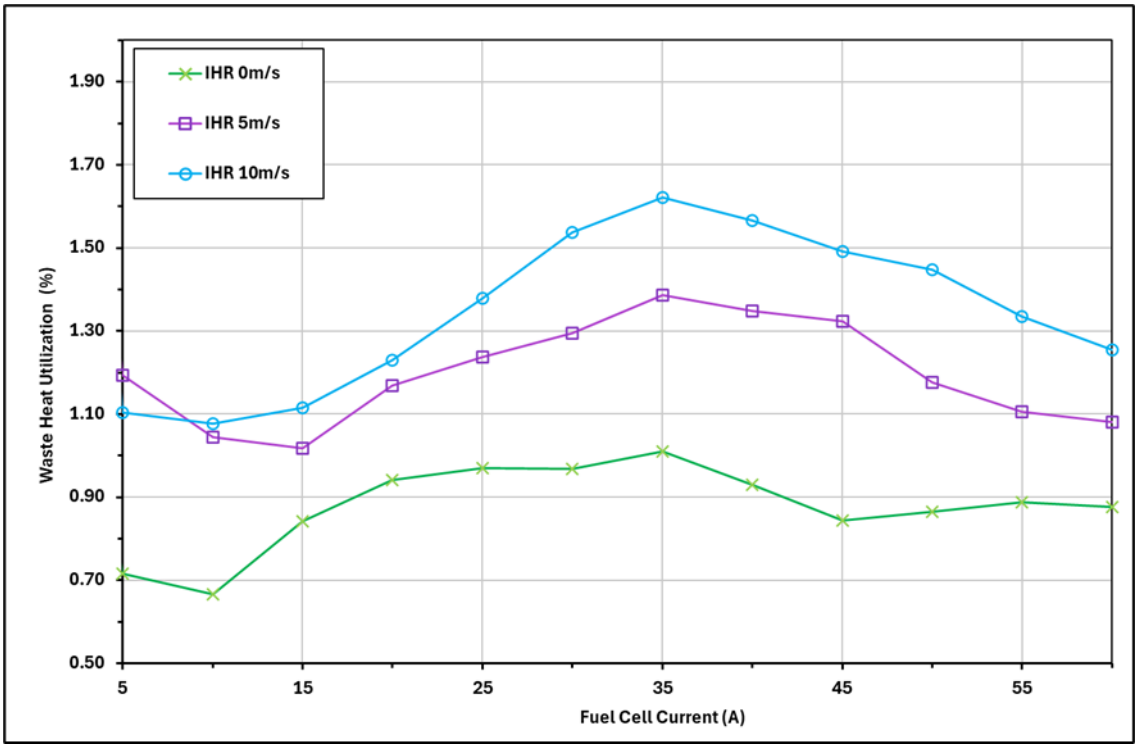

Figure 4.29 Waste heat utilization for the IHR cases

As the current pushes beyond 35 A into the high-load territory (40–60 A), the WHU undergoes a gradual, continuous decline. By 60 A, the metrics recede to 0.9% (0 m/s), 1.1% (5 m/s), and 1.3% (10 m/s). This downturn highlights the physical thermal limitations inherent in the recovery architecture. While absolute recovered energy TEG total heat flux and hydrogen absorption continues to rise at high loads, the gross waste heat generated by the stack accelerates much more aggressively due to escalating polarization and ohmic losses. Consequently, the fixed physical footprint of the TEG modules and the strictly limited thermal mass flow rate of the hydrogen act as rigid bottlenecks. Because the recovery pathways cannot absorb the exponentially surging waste heat at the same proportional rate, the fractional utilization mathematically drops.

Furthermore, the external cooling speed exerts a major influence on the magnitude of recovery. The 10 m/s condition consistently achieves the highest waste heat utilization across almost the entire spectrum. At the 35 A peak, shifting from 0 m/s to 10 m/s convection improves the WHU from 1.0% up to 1.6%. This behaviour suggests that applying a robust cold-side sink not only maximizes localised TEG

conversion but also encourages a more effective thermal draw through the entire heat-exchanger assembly, thereby actively utilising a larger slice of the waste heat before it is passively lost to the environment. In summary, the IHR system hits its peak WHU in the 30 to 40 A mid-load range, whereas high-load operation limits the thermal capacitance of the individual IHR components.

4.3.8 CFD Validation against Test Bench Results

Previous mathematical model in Section 4.2 verified the initial computational fluid dynamics models. The experimental data gathered throughout Section 4.3 now serves as the empirical baseline to validate these 3D numerical simulations. The primary critical outputs extracted for this validation were:

i) the hydrogen preheated temperature,
ii) the TEG hot surface temperature, and
iii) the TEG cold surface temperature.

The validation is specifically based on the selected and developed IHR design at the highest experimental current load of 60 A. To replicate the exact physical testing environment, the boundary conditions were based on empirical values from the lab test performance. The measured waste heat stream at point 2 and the cold chamber outlet at point 7, which were previously defined in the dimensionless temperature profile figure 4.19, are applied as the boundary conditions.

Figure 4.30 presents the resulting computational temperature profiles across the three convection cooling cases. These visual profiles demonstrate sequentially higher thermal distributions as the external cruising speed increases. Table 4.2 extracts the average temperature parameters from these spatial profiles to enable a direct numerical comparison. For the stagnant 0 m/s condition, the simulation predicts a hydrogen outlet temperature of 43 °C with a hydrogen temperature difference of 20.4 °C. The TEG hot and cold surfaces record 42.8 °C and 41.6 °C respectively, producing a narrow TEG temperature difference of 1.1 °C. When evaluating the 5 m/s case, the hydrogen outlet reads 41.6 °C with a 19.8 °C hydrogen temperature difference. The module surfaces reach 41.1 °C and 37.9 °C, increasing the TEG temperature difference to 3.1 °C. Finally, the 10 m/s boundary yields a 42 °C hydrogen outlet, a 20.5 °C hydrogen temperature

difference, module temperatures of 41.3 °C and 37.5 °C, and maximizing the TEG temperature difference at 3.8 °C.

Figure 4.31 illustrates the percentage deviation between these computational predictions and the established experimental baseline. The analysis extracts the average TEG hot and cold surface temperatures from the test bench data to ensure a direct comparison with the computational spatial averages. Across all three speed conditions, every evaluated parameter remains below the 10% acceptable error threshold. The hydrogen outlet temperature deviates by only 3.6% for both the 0 and 5 m/s cases, and 4.6% for the 10 m/s case. The hydrogen temperature difference exhibits slightly higher variances of 7.9%, 8.4%, and 9.4% across the ascending speed conditions. The TEG surface temperatures show very close agreement. The hot surface errors are minimal at 0.6%, 1.2%, and 2.5%, while the cold surface deviates by just 0.4%, 0.6%, and 2.5%. Consequently, the resulting TEG temperature difference predictions deviate by 5.2%, 2.5%, and 2.7%.

These minor discrepancies are expected within complex geometry simulations. The computational domain features a highly intricate geometry encompassing two distinct fluid domains separated by solid boundaries. Furthermore, resolving the thermal transport across the 0.6 mm thickness cooling fins necessitates a mesh with a large aspect ratio. This mesh structure inherently introduces minor numerical diffusion and calculation approximations. Coupled with the natural dynamic fluctuations and measurement uncertainties present in physical bench testing, achieving absolute parity between a simulation and physical reality is highly improbable. However, maintaining all validation parameters within a 10% deviation band confirms that the 3D CFD model operates with an approximate 90% accuracy. This strong correlation validates the numerical approach, rendering it a reliable tool for predicting thermal recovery behaviours under varying operational loads and boundary conditions.

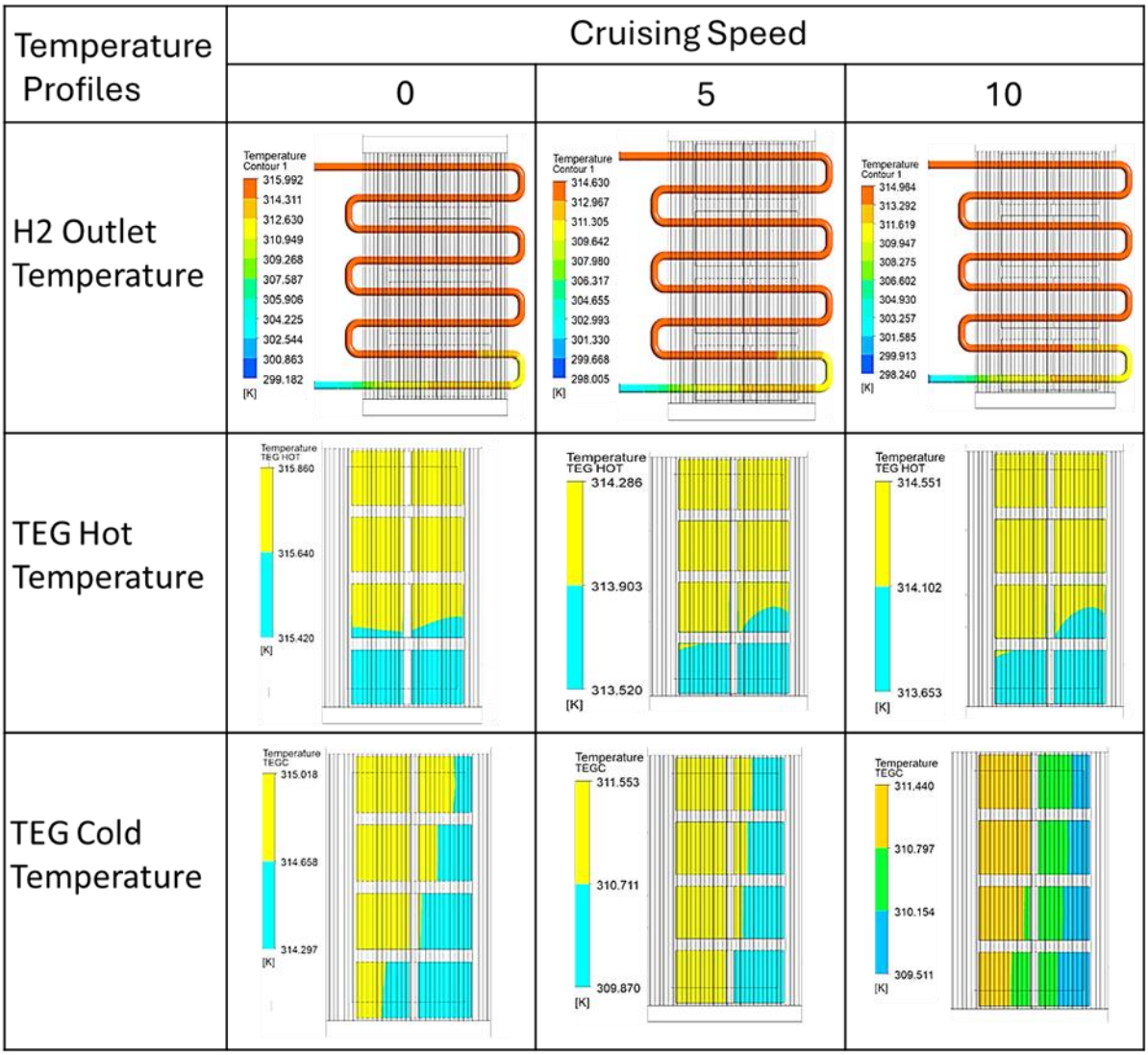

Figure 4.30 Temperature Distribution Profiles for the Hydrogen Stream And TEG Surface Temperatures Based on Experimental Boundary Conditions At 60 A

Table 4.2
Predicted Temperature Profiles for the IHR System Domain from CFD

CFD Temperature Validation Parameters (°C)	**Cruising Speed (m/s)**		
	0	**5**	**10**
H2 Outlet Temperature	42.99	41.63	41.96
H2 Temperature Difference	20.39	19.83	20.46
TEG Hot Temperature	42.75	41.05	41.27
TEG Cold Temperature	41.61	37.92	37.48
TEG Temperature Difference	1.14	3.12	3.79

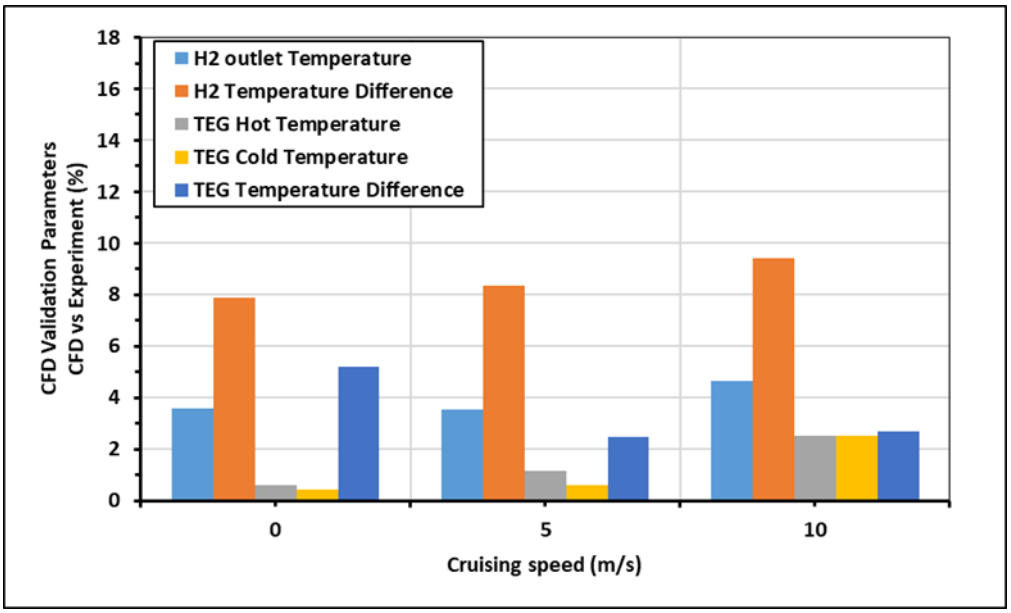

Figure 4.31 Validation of CFD Results Against Test Bench Experiment Results

4.3.9 Summary of Experimental Test Bench Validation

The laboratory test bench validation successfully demonstrated that integrating the passive heat recovery architecture provides measurable electrochemical benefits under controlled steady state boundaries. By repurposing exhaust waste heat to elevate the incoming hydrogen temperature by up to 17 °C, the system effectively mitigated internal polarization losses. This active thermal conditioning yielded a maximum electrical power increment of 196.7 W, representing an 11.1% improvement at the 60 A peak load under 10 m/s convective cooling. Consequently, the total fuel cell efficiency increased by an absolute 4.6 percentage points. Furthermore, the solid state thermoelectric modules generated a maximum secondary output of 192.5 mW, proving the fundamental viability of the dual recovery concept.

Despite these primary power enhancements, the physical testing explicitly exposed the severe thermodynamic limitations inherent to the physical recovery architecture. The overall waste heat utilization remained strictly bounded, peaking at merely 1.6% during mid load operation before decaying under high load demands. As observed in the empirical data, this low utilization originates from two fundamental physical bottlenecks. First, the extremely low hydrogen mass flow rate of 2.80107 mg/s strictly caps the absolute thermal absorption capacity to less than 8 W, regardless of the driving temperature difference. Second, the spatial thermal mapping revealed a severe 24% temperature degradation occurring immediately upstream of the recovery

chamber. This steep gradient highlights significant conductive heat losses and imperfect physical insulation across the connection manifolds.

Finally, utilising this empirical data to validate the three dimensional computational fluid dynamics models confirmed a strong numerical agreement. All evaluated spatial temperatures remained within a 10% deviation threshold, establishing an approximate 90% reliability for the numerical simulations. However, it is cautiously acknowledged that minor discrepancies inherently persist due to unavoidable experimental measurement noise, physical contact resistances, and numerical mesh approximations. Ultimately, these steady state laboratory findings establish a highly reliable empirical baseline. This confirms the absolute necessity to transition the physical prototype into dynamic on road vehicular environments to evaluate its thermodynamic response against chaotic external convection, transient thermal lag, and continuous operational loads.

4.4 On-Road Test Introduction

This subsection discusses the findings for light weight FCeV buggy with IHR system findings. Since the test has 2 driving cycle, 1km constant and dynamic, the section is segregated into to subsection respectively.

4.4.1 Constant Speed On-Road Test

This subsection presents the on-road results for the 1 km constant-speed test, which had been conducted under combinations of targeted speed (1S, 2S, and 3S) and weight loading (1P, 2P, and 3P). The constant-speed route had been treated as the closest on-road condition to a controlled test, where the traction demand had been intended to remain steady. This configuration had made it suitable for observing how the IHR operation influences the fuel cell behaviour before moving to the more complex dynamic cycle. In practice, the route still introduces repeatable disturbances from cornering and local road resistance, and these had appeared as short fluctuations in the electrical signals. The results have been presented in the same sequence that the system response can be interpreted.

The section starts with the raw electrical response of the fuel cell to confirm that the baseline and IHR system runs had remained comparable within each matched speed and loading case. The fuel cell power is then normalized to allow for a clearer

comparison across cases and to quantify any consistent changes relative to the baseline. The discussion then progresses to the supporting mechanisms through the stack and system thermal behaviour, followed by the hydrogen-side temperature rise, temperature flow behaviour, and the associated heat absorption. Finally, the TEG thermal and electrical responses are presented and consolidated into waste heat utilization to summarize the overall recovery outcome under constant-speed on-road operation.

4.4.1.1 Fuel Cell Raw Electrical Analysis

Figures 4.32 a and b provides the raw fuel cell electrical power profiles for the 1 km constant-speed test, for 3P weight loading day and night time conditions. While Figures 4.33 a and b are the electrical motor power profiles. The other conditions figures are placed at the APPENDIX X. For all cases, the fuel cell power had remained largely quasi-steady across the drive duration, with small but distinct fluctuations superimposed on the main operating level. These fluctuations had been expected during on-road testing even under a constant-speed target because the 1 km track includes cornering and local resistance variations. Therefore, the driver had to apply small throttle corrections to maintain the targeted speed, especially during corner entry and exit.

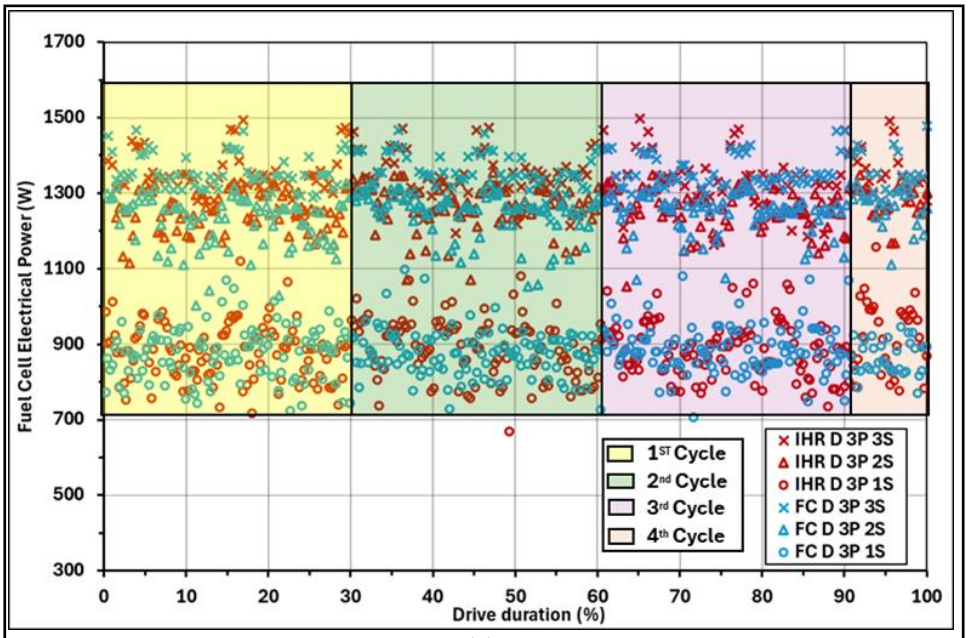

(a)

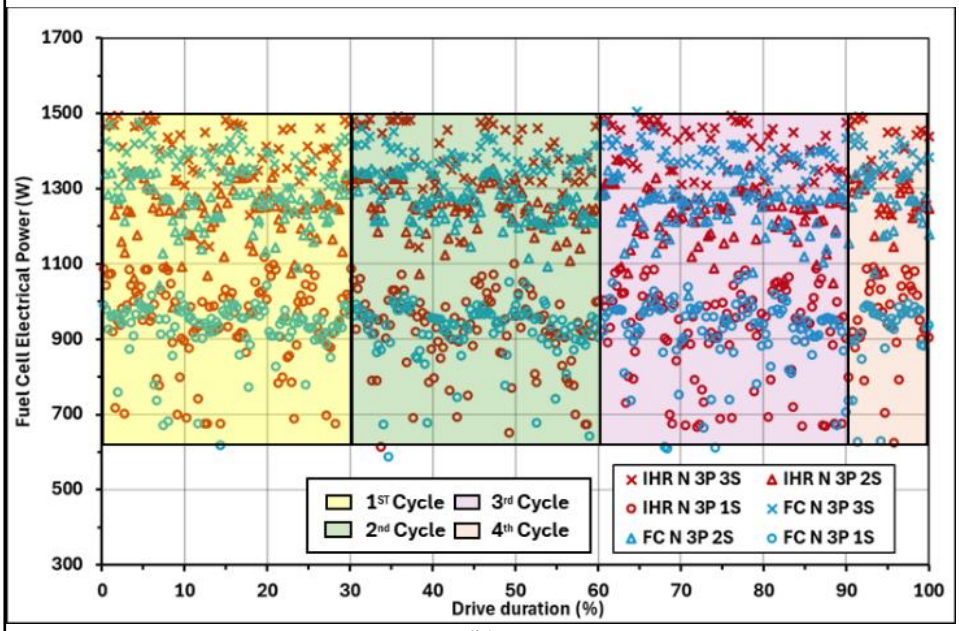

(b)

Figure 4.32 Fuel Cell Electrical Power Profile for 3P Cases (a) Day (b) Night

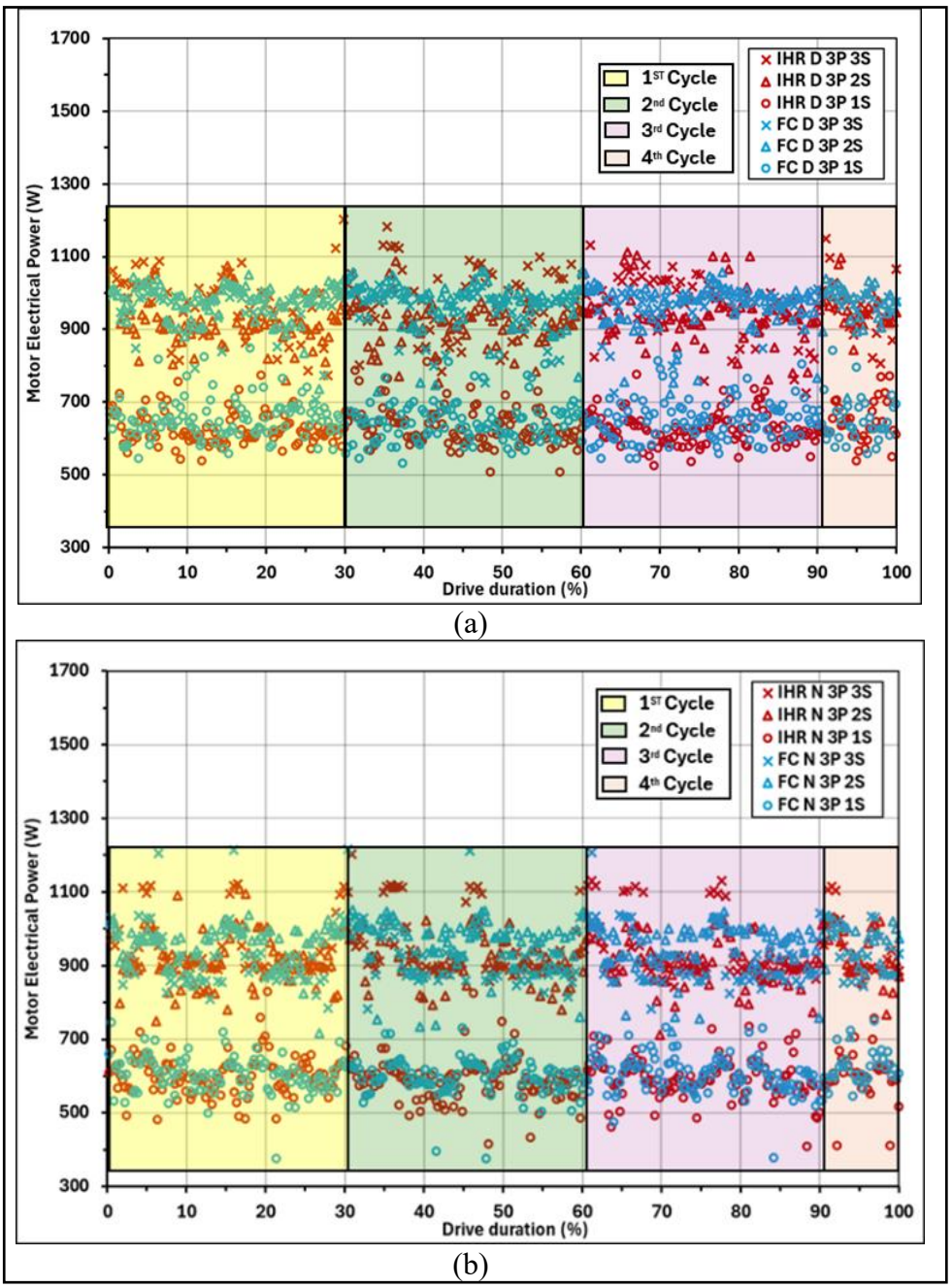

Figure 4.33 Electrical Motor Power Profile for 3P cases (a) Day (b) Night

As a result, short transient changes in traction demand had appeared as corresponding perturbations in both the motor and fuel cell electrical power. The repeated appearance of similar perturbations across the laps had indicated that the behaviour was track-related rather than random scatter. The electrical demand also follows a consistent ranking with speed and loading. For a fixed loading, a higher targeted speed requires higher traction power, yielding the expected order of 3S > 2S > 1S. For a fixed speed setting, increasing the weight loading increases the required power level, where 3P generally exceeds 2P, and 2P exceeds 1P.

Within this subsection, the electrical response has been interpreted mainly in terms of this speed and loading effects alongside the route-induced fluctuations. The day and night conditions had not been treated as a distinguishing factor for electrical demand here because comparisons had only been made within matched speed and loading cases. Its influence was expected to appear more clearly through the thermal boundary conditions that later affect the fuel cell behaviour and TEG response, which has been addressed in the subsequent thermal-related subsections.

To verify that the baseline and IHR comparisons had been conducted under comparable traction demand within each matched case, the total motor electrical energy on figure 4.34 is chosen as the verification metric. The motor energy is obtained directly from the logged data. As depicted in the electrical motor demand difference figure 4.35, the relative motor energy deviation between the IHR and baseline runs had fallen within the range of 0.99% to 4.82% across all matched cases, successfully satisfying the ±5% acceptance criterion adopted for this on-road study. The ±5% tolerance had been considered reasonable because on-road tests inevitably include external factors that are difficult to control tightly, such as minor throttle correction differences, uneven road surfaces, turning losses, wind disturbances, and small variations in the vehicle path during cornering. Within this practical limit, the matched comparisons had been considered sufficiently fair, ensuring that subsequent differences observed in fuel cell and IHR performance could be interpreted without being dominated by unequal traction demand.

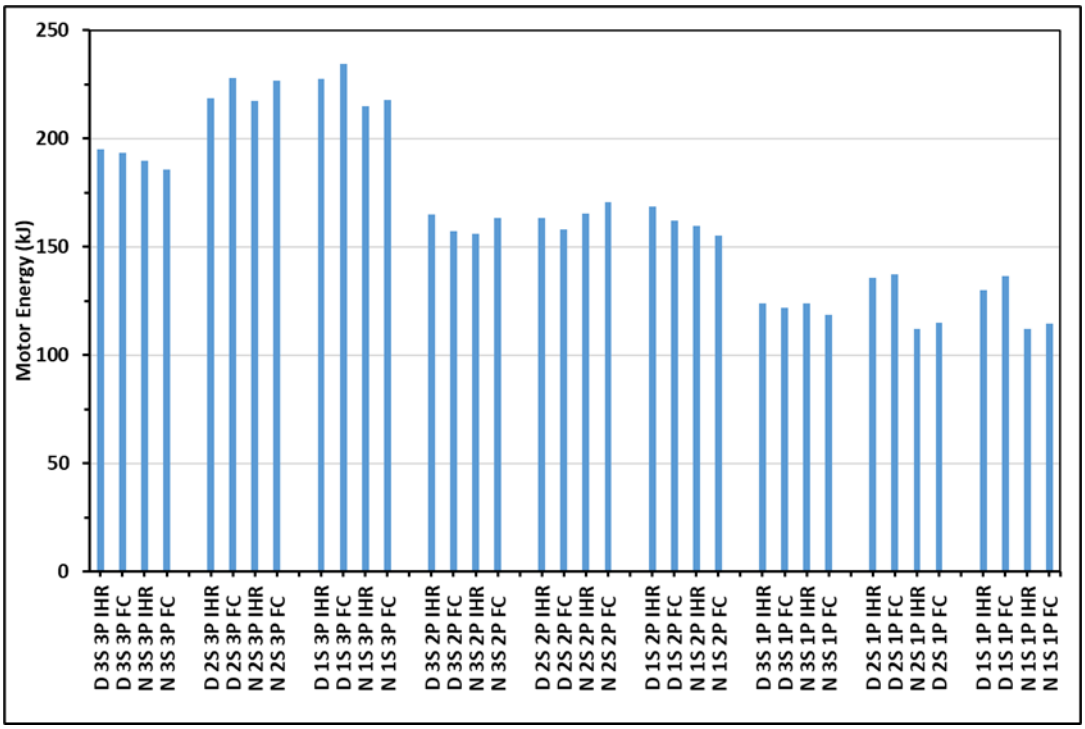

Figure 4.34 Electrical Motor Demand Energy For All Cases

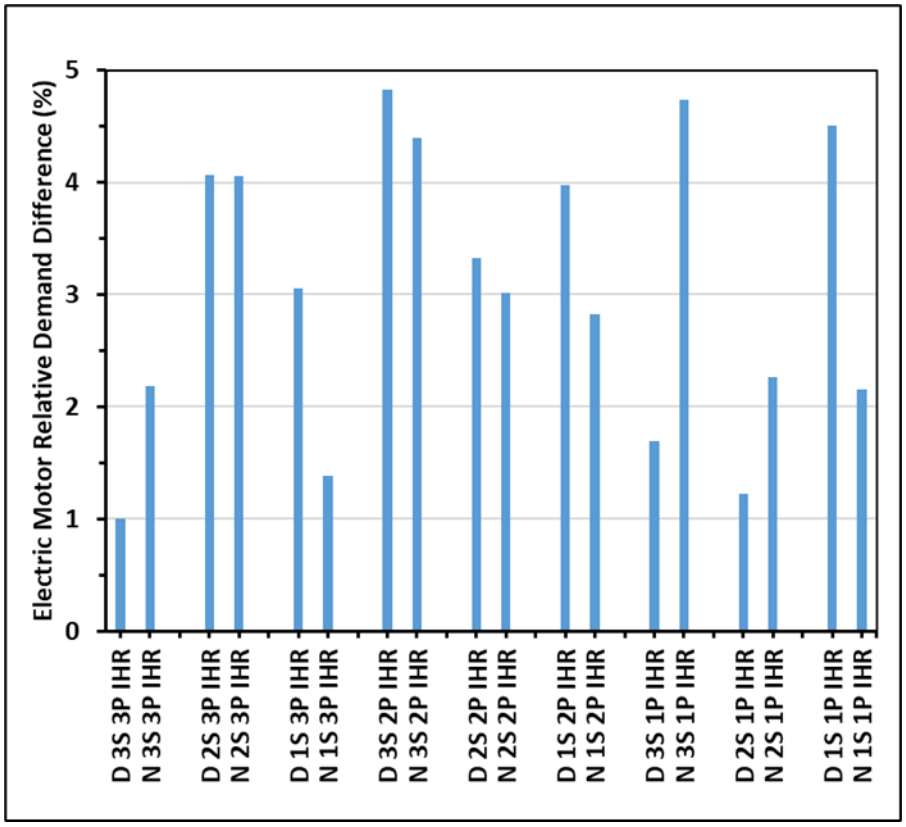

Figure 4.35 Electrical Motor Demand Difference (Between IHR Against Baseline) For All Cases

Fuel cell power is treated as the primary electrical indicator in this subsection because any benefit derived from the IHR must ultimately reflect on the fuel cell's operating output. Therefore, the power traces had been presented not only as profiles but also reduced into descriptive statistics so the comparison between baseline and IHR operation could be discussed without relying solely on visual judgment. Each case had been summarized using the mean power level, the standard deviation to reflect short-term on-road fluctuations, and the relative standard error (RSE) to indicate the reliability of the estimated mean over the drive duration. Where figure 4.36 plots for the mean electrical power and figure 4.37 for the relative power difference. Across the matched cases, the mean fuel cell power deviation between the baseline and IHR had remained below 5%, indicating comparable operating demand. However, the pointwise fluctuation around the mean had been occasionally larger, where the coefficient of variation had reached up to 12% but only for 1S3P with IHR Night driving condition while the other cases fall between the range of 3.5 to 10.6%. This aligns with the previously described route-driven disturbances, except that the fuel cell signal tends to appear more active as it sits upstream in the vehicle's energy chain. The fuel cell responds earlier to the required electrical load, while the motor response acts as the end output that is damped by drivetrain inertia and vehicle dynamics.

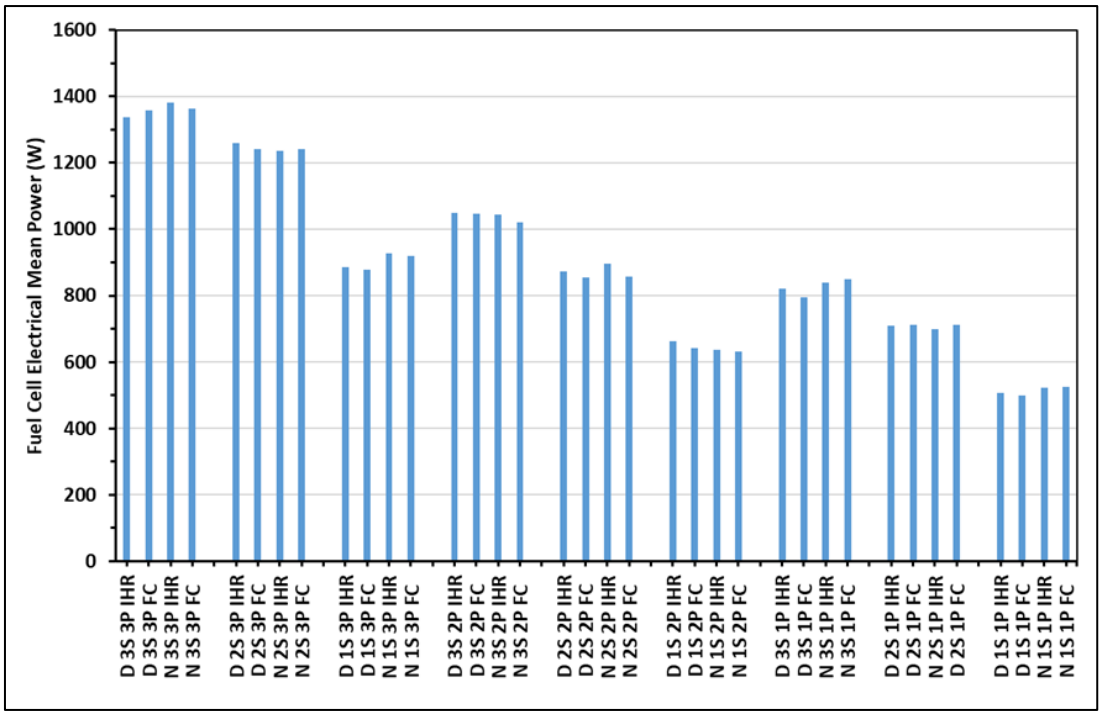

Figure 4.36 Fuel cell electrical mean power for all cases

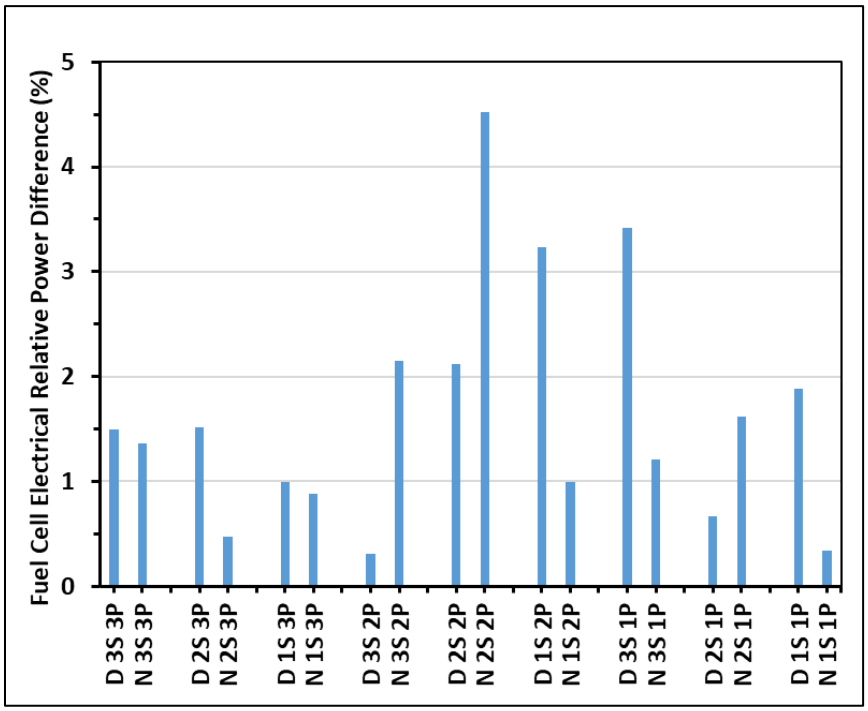

Figure 4.37 Fuel Cell Electrical Relative Power For All Cases

Even with this higher short-term variation, the overall uncertainty of the mean had remained low, with the RSE staying below 1% due to the 1-second logging intervals over the 200 to 360-second duration, providing sufficient data density. In terms of operating bounds, the fuel cell power range remains clearly separated. For the 3P condition, the fuel cell had operated approximately within 1144 to1504 W at 3S3P, 977 to 1376 W at 2S3P, and 586 to 1156 W at 1S3P. For the 2P condition, the ranges had been approximately 794 to 1277 W (3S2P), 688 to 1036 W (2S2P), and 506 to 846 W (1S2P). For the 1P condition, the ranges had reduced further to approximately 648 to 1000 W (3S1P), 546 to 896 W (2S1P), and 372 to 657 W (1S1P). The overall statistics (Max, min, mean, SD, CV, SE, RSE) of fuel cell electrical power data are tabulated on table 4.3 (a), (b) and (c).

Table 4.3
Overall Statistics for the Fuel Cell Electrical Power (a) 3P (b) 2P (c) 1P
(a)

	3P						
Cases	Mean (W)	Max (W)	Min (W)	SD (W)	CV (%)	SE (W)	RSE (%)

D 3S 3P IHR	1342.8	1497.8	1164	66.9	5	4.7	0.4
D 3S 3P FC	1356.9	1477.5	1190.8	47.7	3.5	3.4	0.2
N 3S 3P IHR	1389.1	1493.3	1144.2	81.2	5.8	5.7	0.4
N 3S 3P FC	1363.6	1503.7	1206.6	54.1	3.9	3.8	0.3
D 2S 3P IHR	1259.9	1355.4	1054.1	55.3	4.4	3.4	0.3
D 2S 3P FC	1241.2	1329.8	1003.2	61.6	5	3.8	0.3
N 2S 3P IHR	1239.6	1376.2	977.4	72.7	5.9	4.5	0.4
N 2S 3P FC	1245.1	1349.9	1016.2	62.1	5	3.9	0.3
D 1S 3P IHR	885.8	1155.9	668.9	77.6	8.8	4.1	0.5
D 1S 3P FC	877.1	1097.3	704.6	63.1	7.2	3.3	0.4
N 1S 3P IHR	930.7	1118.2	613.5	112.7	12.1	5.9	0.6
N 1S 3P FC	922.6	1067.8	586	84	9.1	4.4	0.5

(b)

	2P						
Case	Mean (W)	Max (W)	Min (W)	SD (W)	CV (%)	SE (W)	RSE (%)
D 3S 2P IHR	1048.9	1276.7	895.9	86.4	8.2	6.1	0.6
D 3S 2P FC	1045.7	1209.3	864.7	65.8	6.3	4.7	0.4
N 3S 2P IHR	1043.7	1246.1	806.9	86.5	8.3	6.1	0.6
N 3S 2P FC	1021.7	1244.6	793.8	92.3	9	6.5	0.6
D 2S 2P IHR	877.1	1003.6	708.5	59.8	6.8	3.7	0.4
D 2S 2P FC	858.5	1017.4	711.7	53.9	6.3	3.4	0.4
N 2S 2P IHR	895.4	1029.9	707.4	74.4	8.3	4.6	0.5
N 2S 2P FC	859.3	1036.1	688.3	68	7.9	4.2	0.5
D 1S 2P IHR	662.2	846.1	505.5	52.6	7.9	2.8	0.4
D 1S 2P FC	641.4	815.4	530.6	48.8	7.6	2.6	0.4
N 1S 2P IHR	637.5	788.6	509.4	64.2	10	3.4	0.5
N 1S 2P FC	631.2	799.8	521.3	49.6	7.9	2.6	0.4

(c)

	1P						
Case	Mean (W)	Max (W)	Min (W)	SD (W)	CV (%)	SE (W)	RSE (%)
D 3S 1P IHR	824.3	989.5	675.5	66.1	8	4.7	0.6
D 3S 1P FC	793.9	918.7	681.1	44.6	5.6	3.2	0.4
N 3S 1P IHR	837.9	998.8	709.7	65.4	7.8	4.6	0.6
N 3S 1P FC	848.2	999.8	648.4	83	9.8	5.9	0.7
D 2S 1P IHR	708	895.7	546.2	67.1	9.5	4.2	0.6
D 2S 1P FC	712.8	894.6	585	53.3	7.5	3.3	0.5
N 2S 1P IHR	700.2	876.6	582.3	59.2	8.5	3.7	0.5
D 2S 1P FC	714.6	866.4	547.6	58.2	8.1	3.6	0.5
D 1S 1P IHR	507.9	656.6	371.7	46.9	9.2	2.5	0.5
D 1S 1P FC	498.5	627.2	380.5	52.7	10.6	2.8	0.6
N 1S 1P IHR	522.8	635.8	399.6	42.6	8.1	2.2	0.4
N 1S 1P FC	524.6	612.3	426.8	37.3	7.1	2	0.4

4.4.1.2 Fuel Cell Electrical Power Analysis

The constant-speed test maps the fuel cell operational power load demand relative to the different loading conditions. The raw power traces and the motor-energy verification indicate the practical limits of the on-road testing where the experiments had been conducted under sufficiently controlled conditions. This provides clarity on the reliability of the dataset, suggesting that the overall operating level and total demand had remained consistent enough to support meaningful case-to-case evaluations.

This subsection has been intentionally oriented toward exploring how the IHR affects fuel cell performance under on-road operation by quantifying the change in electrical output through fuel cell power increments. Figure 4.38; (a), (b) and (c) present the normalized fuel cell electrical power against fuel cell current for both the baseline FC and the FC-IHR during day and figure 4.39 (a), (b) and (c) for night operations. The FC legend on the plots is now called as the baseline as it will be used for comparison against the IHR cases respective to the matching loading conditions. To standardize the

fitted comparisons across cases with limited operating windows, the power traces had been anchored using the open-circuit reference point of 45 V at 1 A, which serves as the anchor point for trendline generation. This anchoring is necessary because each case had spanned a relatively small current range 33 A for 1P, 42 A for 2P, and 55 A for 3P, which would have otherwise limited the trendline-based predictions. The normalized plots had included trendlines selected to satisfy an R^2 of not less than 92%, using linear and non-linear polynomial forms depending on the individual case. These fits had provided a minimum 92% prediction reliability for fuel cell power, supporting a more consistent comparison between the configurations at matched currents.

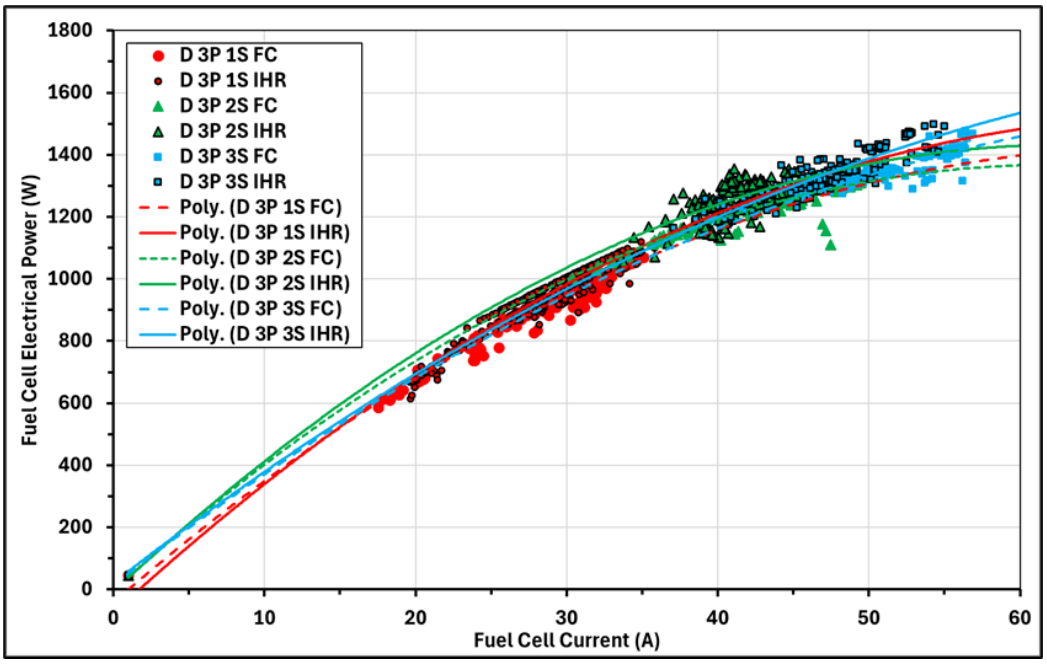

(a)

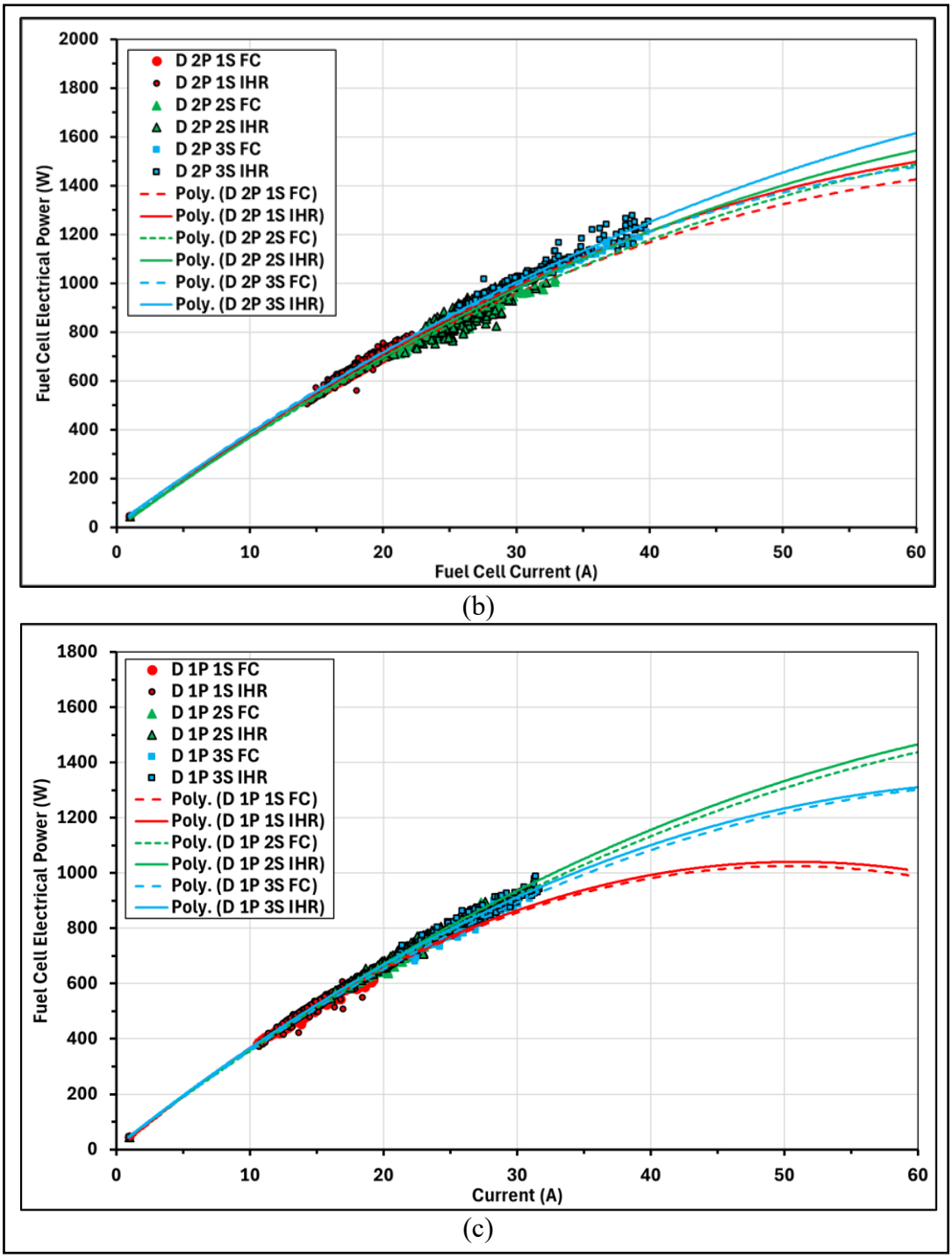

Figure 4.38 Fuel Cell Electrical Power Against Current With the Normalize Trendline for Day Time Cases (a) 3P (b) 2P (c) 1P

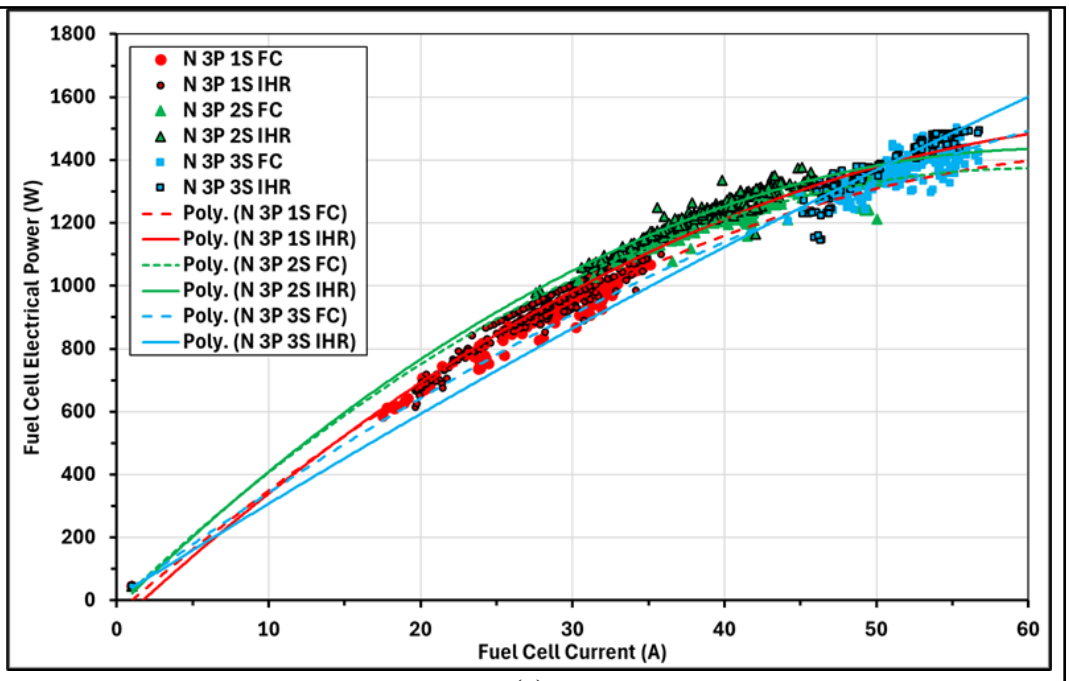
N 3P 1S FC
N 3P 1S IHR
N 3P 2S FC
N 3P 2S IHR
N 3P 3S FC
N 3P 3S IHR
Poly. (N 3P 1S FC)
Poly. (N 3P 1S IHR)
Poly. (N 3P 2S FC)
Poly. (N 3P 2S IHR)
Poly. (N 3P 3S FC)
Poly. (N 3P 3S IHR)
Fuel Cell Electrical Power (W)
Fuel Cell Current (A)
0
200
400
600
800
1000
1200
1400
1600
1800
0
10
20
30
40
50
60

(a)

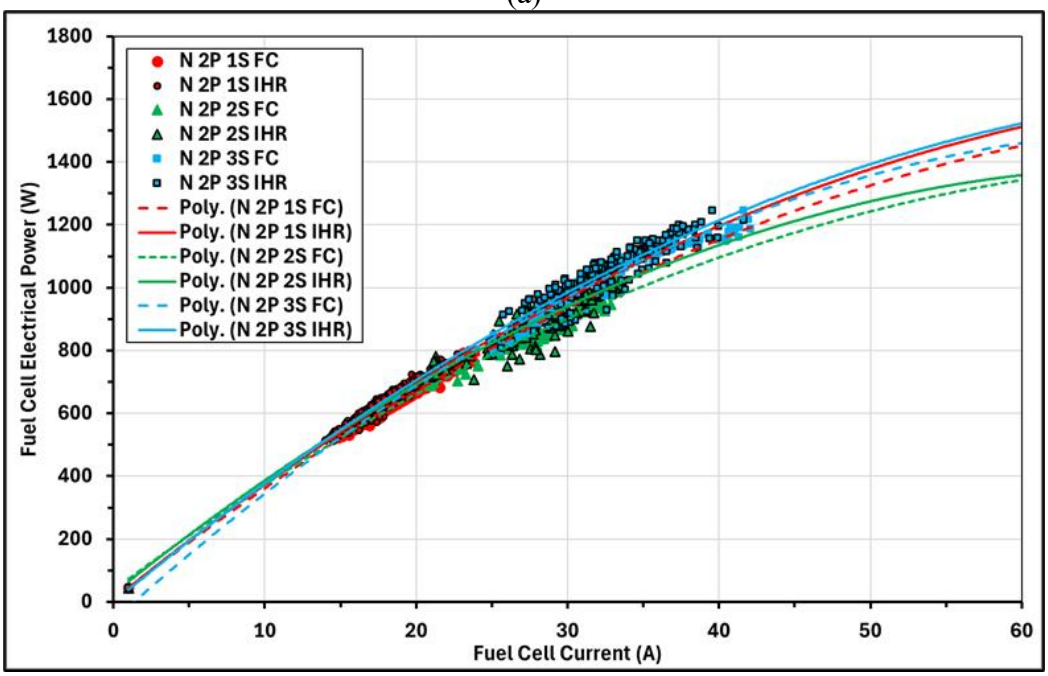
N 2P 1S FC
N 2P 1S IHR
N 2P 2S FC
N 2P 2S IHR
N 2P 3S FC
N 2P 3S IHR
Poly. (N 2P 1S FC)
Poly. (N 2P 1S IHR)
Poly. (N 2P 2S FC)
Poly. (N 2P 2S IHR)
Poly. (N 2P 3S FC)
Poly. (N 2P 3S IHR)
Fuel Cell Electrical Power (W)
Fuel Cell Current (A)
0
200
400
600
800
1000
1200
1400
1600
1800
0
10
20
30
40
50
60

(b)

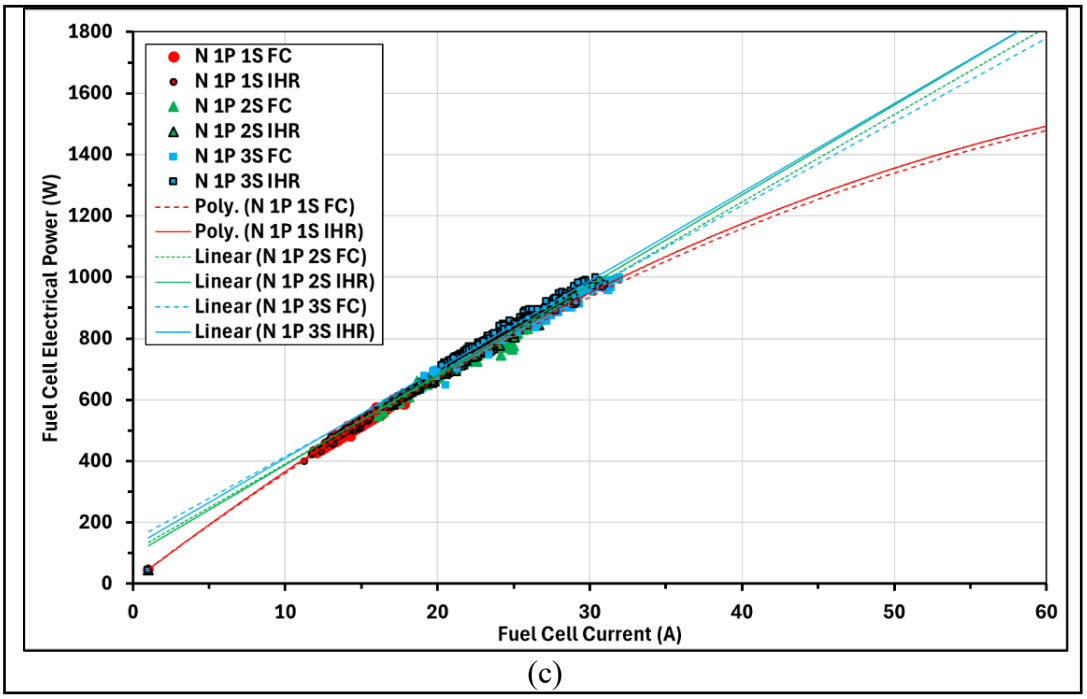

(c)

Figure 4.39 Fuel Cell Electrical Power Against Current With the Normalize Trendline for Night Time Cases (a) 3P (b) 2P (c) 1P

Figure 4.40 (a), (b) and (c) reports the fuel cell electrical power increment percentages against load current. Across all on-road cases, the observed increments had ranged from 0% to 6%. For the 1P configurations, the highest increment occurred at 3S for both day and night modes, reaching approximately 4% to 4.2% at 60 A. For 2P, the increments range from approximately 1% at low current to above 4% at higher current, with a maximum near 4.5% at selected operating points. Some of these conditions had exhibited a peak around 20 to 30 A before levelling or reducing at higher currents. For the 3P configurations, the increment rises with load current and reach approximately 6% to 6.3% at 60 A for the highest-speed case, while lower speeds are within approximately 4% to 5% at the same load current. Within the normalized power comparisons of Figure 4.38 and 4.37, the FC-IHR trendlines remain consistently above the baseline FC trendlines.

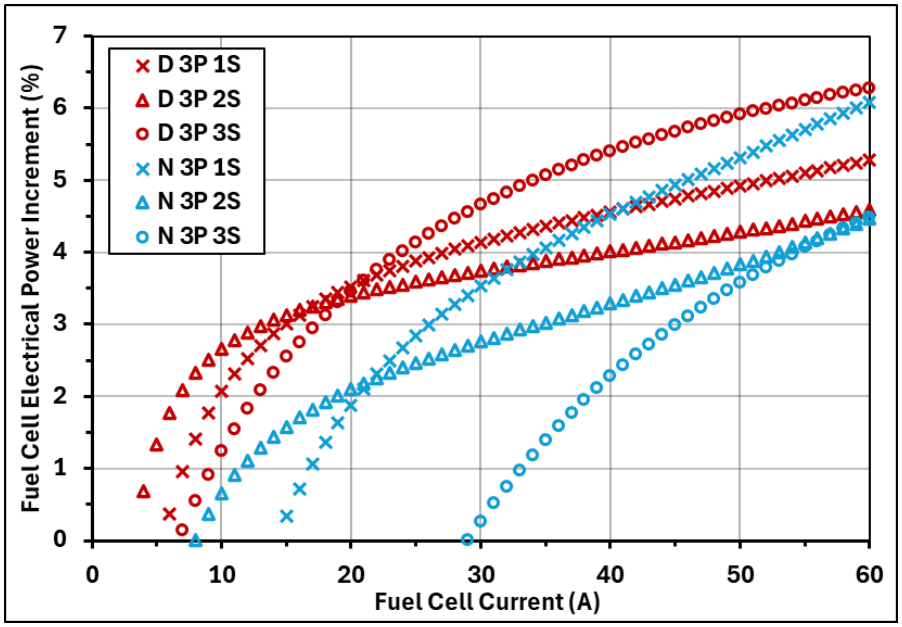
D 3P 1S
D 3P 2S
D 3P 3S
N 3P 1S
N 3P 2S
N 3P 3S
Fuel Cell Electrical Power Increment (%)
Fuel Cell Current (A)
0
1
2
3
4
5
6
7
0
10
20
30
40
50
60

(a)

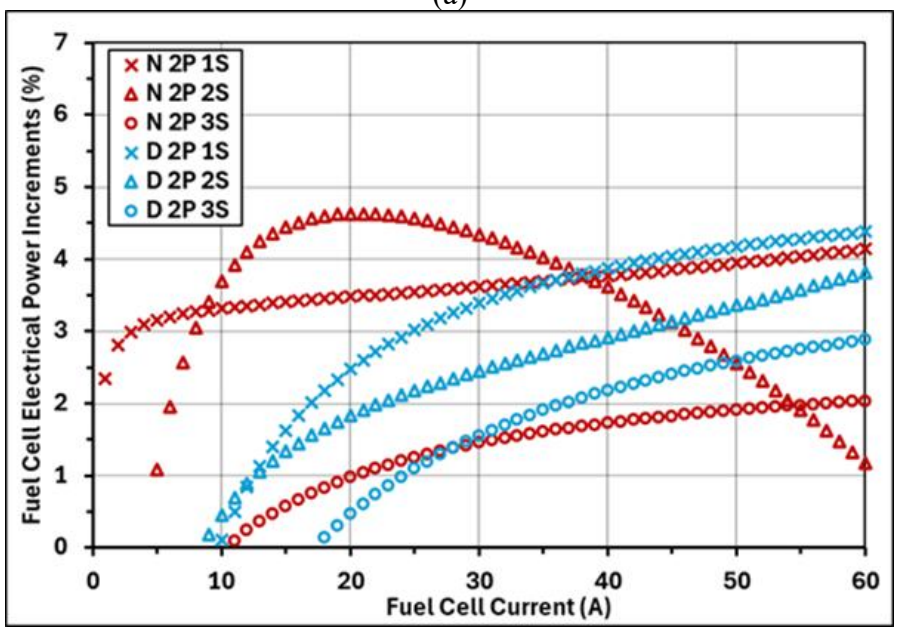
N 2P 1S
N 2P 2S
N 2P 3S
D 2P 1S
D 2P 2S
D 2P 3S
Fuel Cell Electrical Power Increments (%)
Fuel Cell Current (A)
0
1
2
3
4
5
6
7
0
10
20
30
40
50
60

(b)

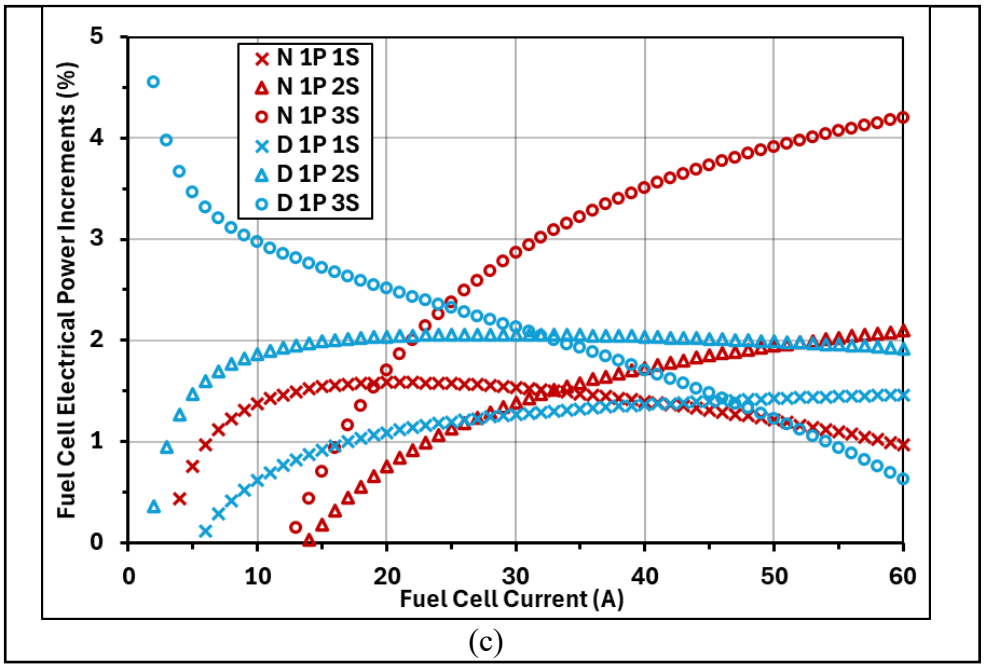

(c)

Figure 4.40 Fuel Cell Electrical Power Increments as Compared to Baseline Respective to the Load Conditions (a) 3P (b) 2P (c) 1P

The impact of IHR is limited at low currents and became pronounced only as the current rose, with the most visible divergence occurring beyond 30 A. However, the on-road data increment is not perfectly consistent with the theoretically expected results. Theoretically, a sequenced increment ranking is anticipated because higher speeds and weight load typically push the fuel cell towards higher power output, increases the waste heat availability and strengthening hydrogen temperature elevation. Yet, this exact ordering had not been reproduced in the on-road dataset. The highest increment under 3P had occurred during Day 3S, but under night conditions, the maximum had shifted to Night 1S. Under 2P, the intermediate speed (2S) had formed the minimum while 1S had formed the maximum. For the 1P Day 3S case, a further deviation had appeared where the increment curve had followed a decreasing polynomial trend with increasing current, contrasting with the generally increasing trends observed elsewhere. This non-sequenced pattern is in contrast with the behaviour previously reported during test bench operations, where a more strictly sequenced pattern of power increments had been observed.

The mismatch between the expected ordering and the observed on-road ordering appears consistent with the differing levels of control between a laboratory test bench and an on-road environment. Test bench conditions are inherently more controlled, allowing the IHR influence to manifest as an orderly progression. Conversely, on-road

operation is naturally subject to unavoidable variations in transient driver inputs, airflow changes, and environmental fluctuations. Those disturbances can shift the instantaneous thermal state and the recoverable fraction of waste heat even when nominal speeds and loads are targeted.

From an engineering perspective, the IHR benefit at a given current depends on both waste heat generation and waste heat utilization. A higher motor load demand leads to greater waste heat yet deliver a smaller electrical increment if the recoverable fraction is restricted by temperature-difference limits, heat-exchanger effectiveness ceilings, or operating-state stability. The decreasing polynomial increment trend for the 1P Day 3S case is an anomaly but it fits a system-limitation interpretation where counteracting effects, such as diminishing marginal hydrogen temperature rise due to thermal saturation, operating-dependent auxiliary loads, or increasing voltage-loss mechanisms at higher currents that might reduce the net incremental benefit as current increases. Prior work on PEMFC thermal integration has suggested that reactant conditioning and heat recovery can improve electrical output, but the magnitude and ordering across operating conditions depend strongly on recoverable temperature differences and component effectiveness rather than scaling exclusively with nominal demand. Studies comparing controlled bench operation to vehicular operation have also described how uncontrolled transients and environmental variability can disrupt orderly trends while still preserving a consistent direction of improvement attributable to thermal management interventions.

4.4.1.3 Fuel Cell and IHR System Thermal Analysis

The fuel cell thermal power generated was calculated using Equation (3.35) and plotted in Figure 4.41 a, and b. Only the 3P at day time condition was presented for simplicity and more focused on the total heat energy generated from fuel cell which is plotted on figure 4.42. As illustrated, the thermal power functions as a dependent variable of the electrical current and voltage production. Specifically, the heat generation profile exhibits a distinct exponential increase as the load current escalates. This nonlinear physical behaviour is driven directly by the compounding effect of internal electrochemical irreversibilities. At higher current demands, the PEM fuel cell experiences intensified ohmic resistance across the polymer membrane alongside

severe mass transport limitations within the porous media. Because these polarization phenomena increasingly restrict the operational voltage from reaching its theoretical reversible limit, the expended chemical energy fundamentally manifests as localised waste heat. Consequently, the rate of thermal dissipation scales exponentially with the corresponding decline in voltage efficiency.

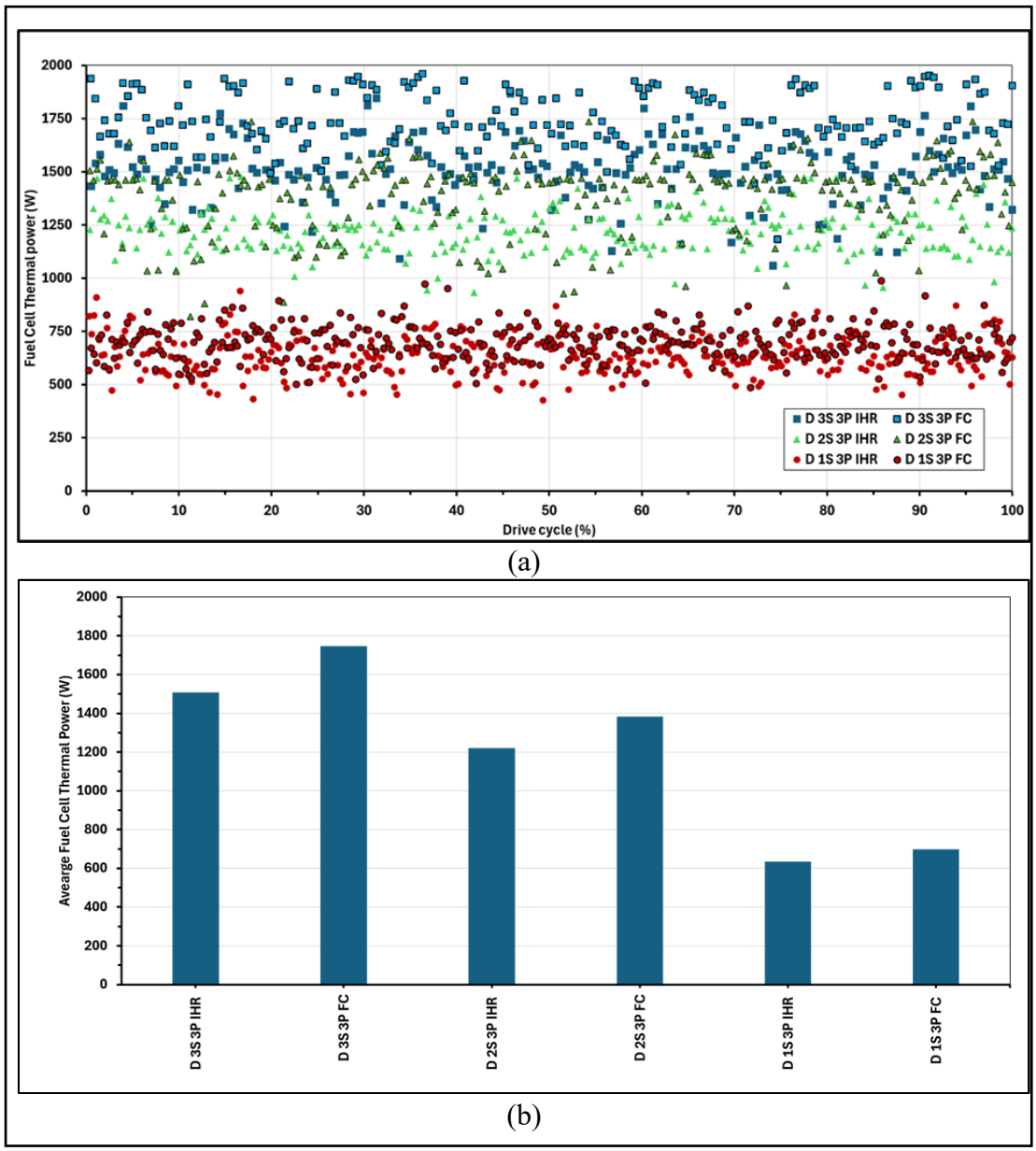

Figure 4.41 Fuel Cell Thermal Power Produced for Cases of 3P During the Day Time (a) Raw Data (b) Average

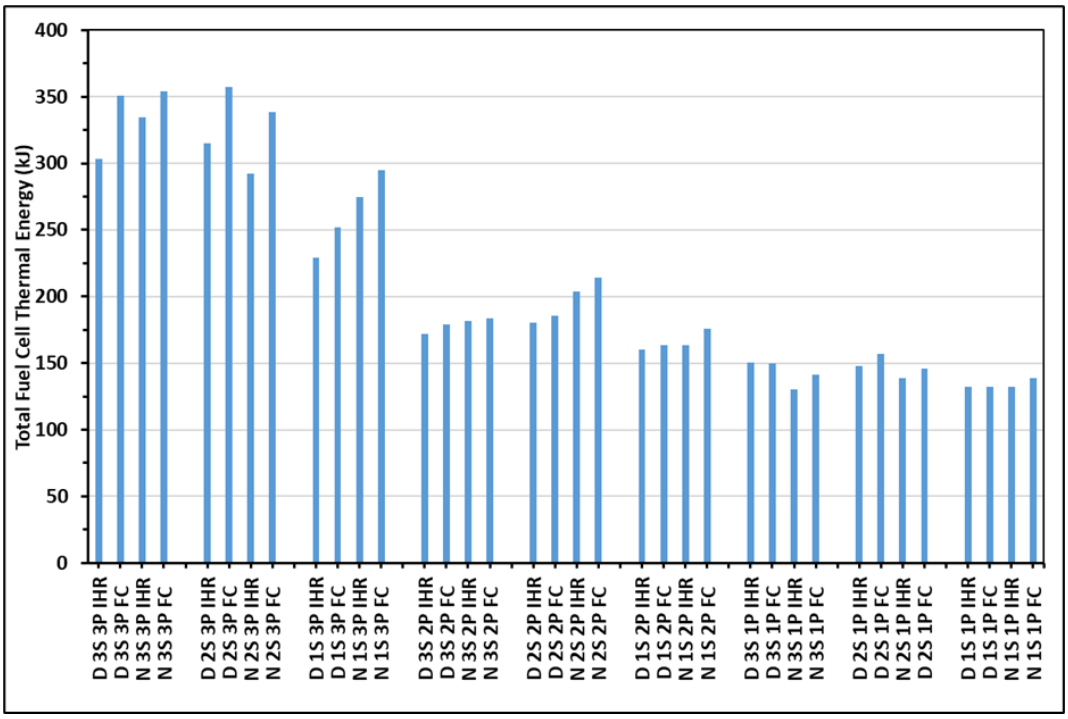

Figure 4.42 Total Fuel Cell Thermal Energy Produced for All Cases

Figure 4.43 (a) and (b) displays the dimensionless temperature profiles for the fuel cell without the IHR during the day and night driving cycles, respectively. For analytical consistency, the standalone fuel cell had been scaled to represent 0.33 of the entire system length, which considers the full spatial extent of the combined fuel cell and IHR system. This approach had ensured a comparable dimensionless temperature profile between the conditions with and without the IHR. Within this profile, Point 1 is the location of the inlet air for the fuel cell cathode, whereas Point 2 is the fuel cell exhaust.

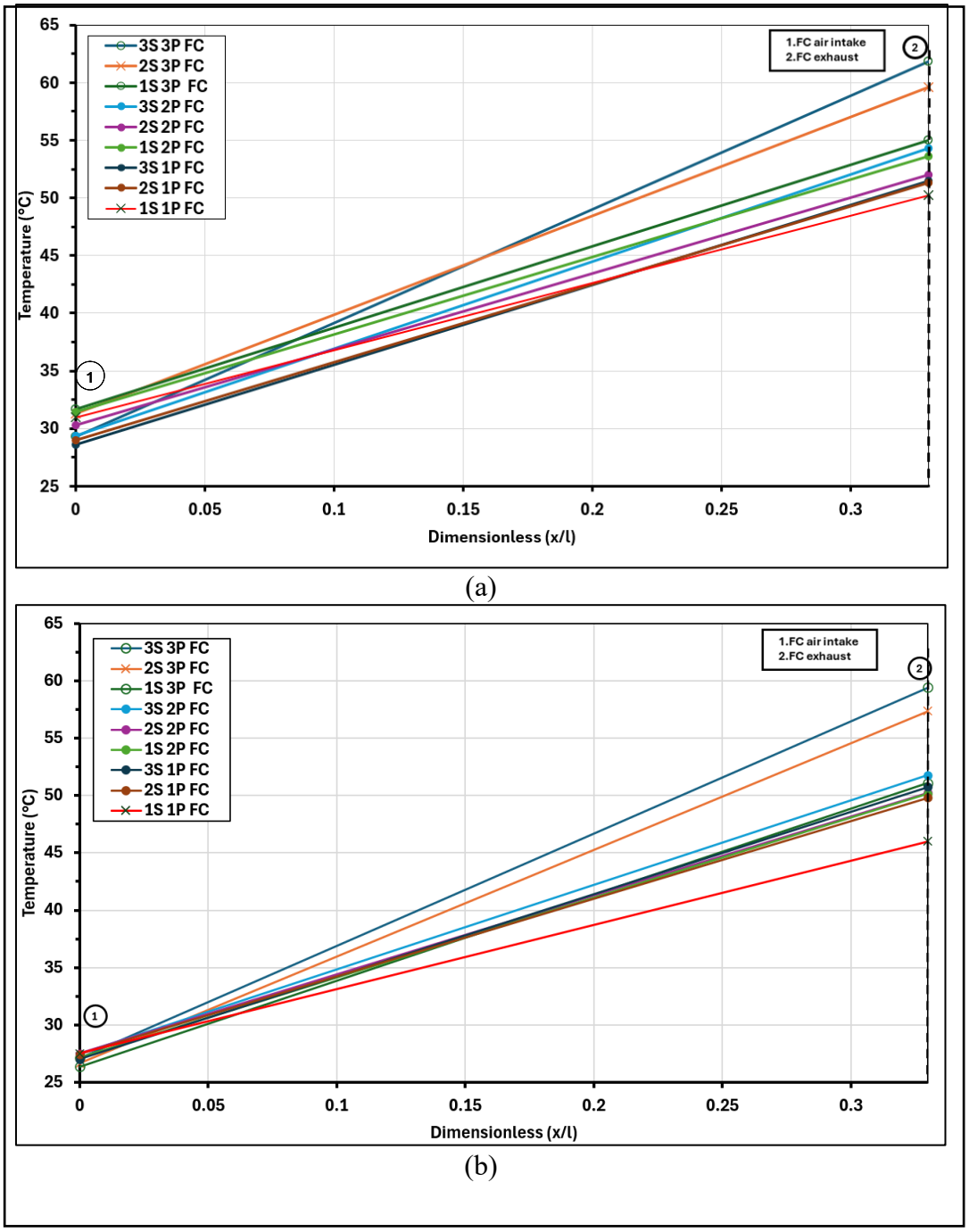

Figure 4.43 Baseline (FC Without IHR) Dimensionless Temperature Profile (a) Day (b) Night Conditions

Based on Point 1 data, the range of daytime inlet air temperatures is wider and higher (28.6 °C to 31.7 °C) compared to the nighttime temperatures (26.4 °C to 27.5 °C). This variation in ambient baseline conditions causes higher fuel cell exhaust temperature during the day compared to the night under the same relative speed and

weight loadings. For instance, without the IHR, the daytime fuel cell exhaust (Point 2) had reached a maximum of 61.9 °C for the 3s3p case, whereas the corresponding nighttime maximum had recorded 59.4 °C. An approximate fuel cell temperature difference of 0.7 °C to 4.2 °C is observed between the day and night drive time cases.

Figure 4.44 (a) and (b) presents the temperature profiles for the fuel cell integrated with the IHR system during the day and night drives. The segment from Point 1 to Point 2 represents the heat from the fuel cell. From the fuel cell stack exit at Point 2, the waste heat enters the heating zone designated for the TEG and hydrogen preheating, spanning up to Point 6. Point 3 is located within the hot chamber of the IHR system, monitoring the hot stream. Point 4 measures the temperature of the aluminium hot fins, Point 5 represents the hot base connecting the hot fins to the TEG hot side via conduction at Point 6. The hydrogen preheating interaction ceases at Point 4 and has been detailed extensively in Section 4.4.1.4. Following the hot side, the cold chamber facilitates the cooling of the TEG, starting from the TEG cold side at Point 6 and extending to Point 10. This cooling process occurs through a combination of conduction and convection. The thermal transfer progresses from Point 7 to Point 8 across the heat pipe, moves to the cold fins at Point 9, and concludes with convection cooling from the cruising air between Point 9 and Point 10.

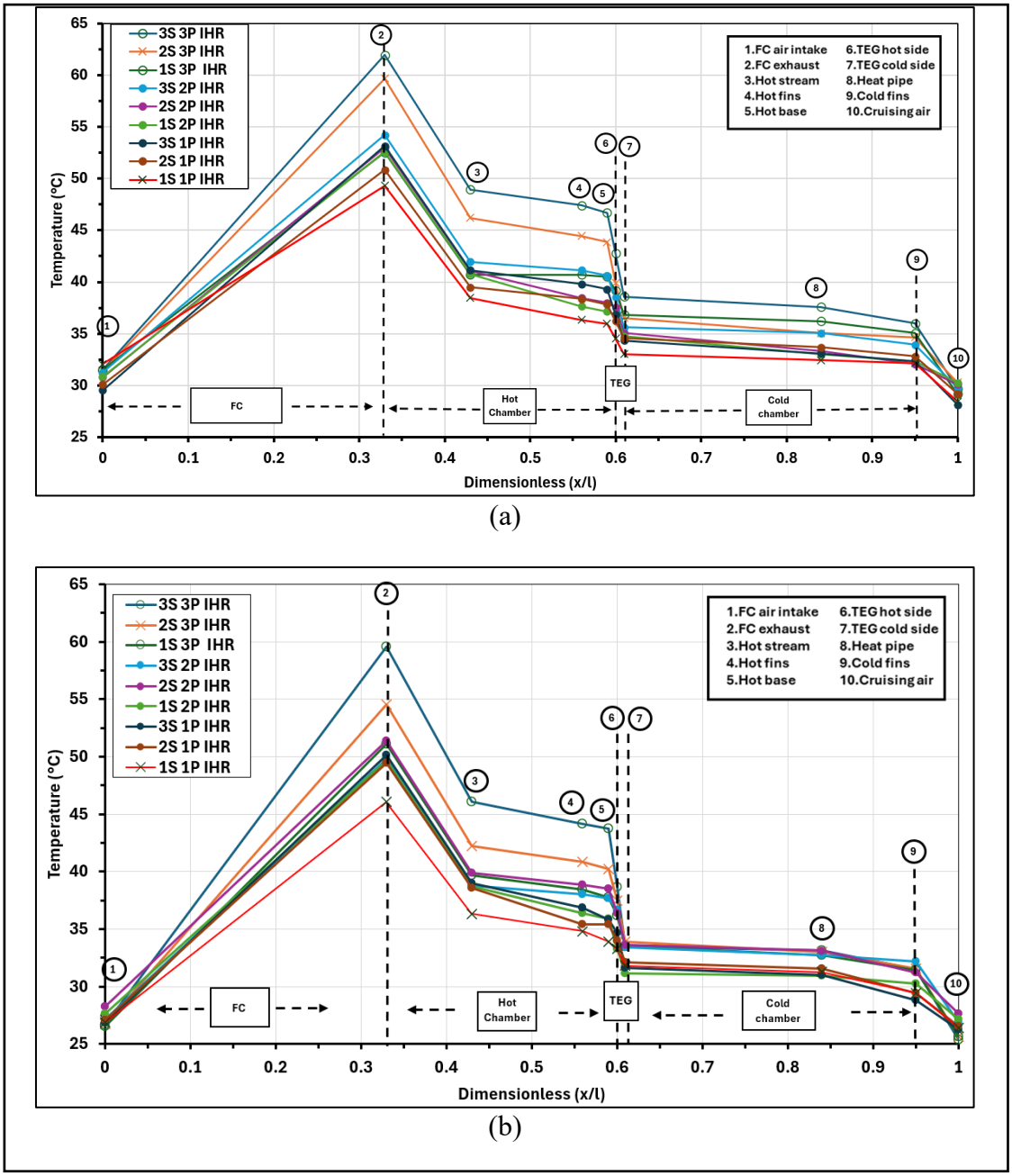

Figure 4.44 Fuel Cell with IHR Dimensionless Temperature Profile (a) Day (b) Night Time Conditions

An analysis of the thermal gradients reveals a very steep decrease between Point 2 and Point 3 (within hot chamber), where there is an approximately 50% of the fuel cell exhaust temperature drop. For instance, the daytime data for the 3s3p configuration had shown the fuel cell exhaust temperature at Point 2 is at 61.9 °C, which then dropped sharply to 48.9 °C at the hot stream (Point 3). The pronounced decrement across the broader Point 2 to Point 6 heating zone had indicated less effective heat transfer, as the TEG hot surface temperature had remained relatively low compared to the primary heat

source. In the same daytime 3s3p case, the temperature continues to decline to 47.4 °C at the hot fin (Point 4), 46.7 °C at the hot base (Point 5), and 42.78 °C at the TEG hot side (Point 6). This steep decline had also been evident in the nighttime profiles, such as the night 3s3p IHR case, where the temperature dropped from 59.54 °C at Point 2 down to 46.1 °C at the hot stream (Point 3), and further decreased to 38.63 °C at the TEG hot side (Point 6). Another steep gradient decline is observed moving from the hot base at Point 5 across the TEG module to the cold side at Point 7, which recorded 38.59 °C in the daytime 3s3p test and 33.48 °C in the nighttime equivalent.

Conversely, within the cooling chamber, the heat pipe functions as an excellent heat transfer medium, evidenced by the very small temperature difference between Point 7 and Point 8. Using the daytime 3s3p configuration as a reference, the temperatures are 38.6 °C at Point 7 and 37.6 °C at Point 8. Similarly, in the nighttime 3s3p configuration, the temperature had recorded 33.5 °C at Point 7 and 33.2 °C at Point 8. The temperature difference between Point 8 and Point 9 had also remained small (dropping from 37.6 °C to 36 °C during the day, and 33.15 °C to 31.45 °C during the night), indicating adequate heat rejection from the heat pipe to the cold fins before reaching the cruising air temperature of 29.7 °C (day) and 25.35 °C (night) at Point 10. Overall, the hot chamber had shown larger temperature differences between its localised measurement points compared to the more stable temperature differences observed within the cold chamber. As expected, the daytime driving cycle operates at higher overall temperatures because of hotter ambient compared to nighttime cycle.

4.4.1.4 Preheated Hydrogen Thermal Analysis

The IHR system has been designed to harness the exothermic waste heat from the PEM fuel cell to preheat the incoming hydrogen stream, thereby exploring potential improvements to the electrochemical reaction kinetics. The preheated hydrogen characteristics encompassing the initial hydrogen temperature before preheating, the final preheated hydrogen temperature, the resulting temperature difference, and the total preheated hydrogen energy obtained during the 1 km on-road experiments are analysed in this section.

Figure 4.45 (a), (b) and (c) shows the overall preheated hydrogen temperature profiles for all the test cases, spanning from the maximum operational demand condition (3s3p) down to the minimum condition (1s1p) during both day and night driving cycles.

Across the experimental matrix, the IHR has facilitated sensible heat transfer from the fuel cell exhaust to the incoming hydrogen gas. A baseline analysis reveals that the initial hydrogen temperature before preheating is inherently higher during the daytime drives, ranging from 28.75 °C to 30.95 °C, compared to the nighttime drives which ranged from 25.9 °C to 27.8 °C. Consequently, the maximum absolute preheated hydrogen temperature is recorded during the highest operational demand condition (3s3p) during the day, reaching 42.3 °C.

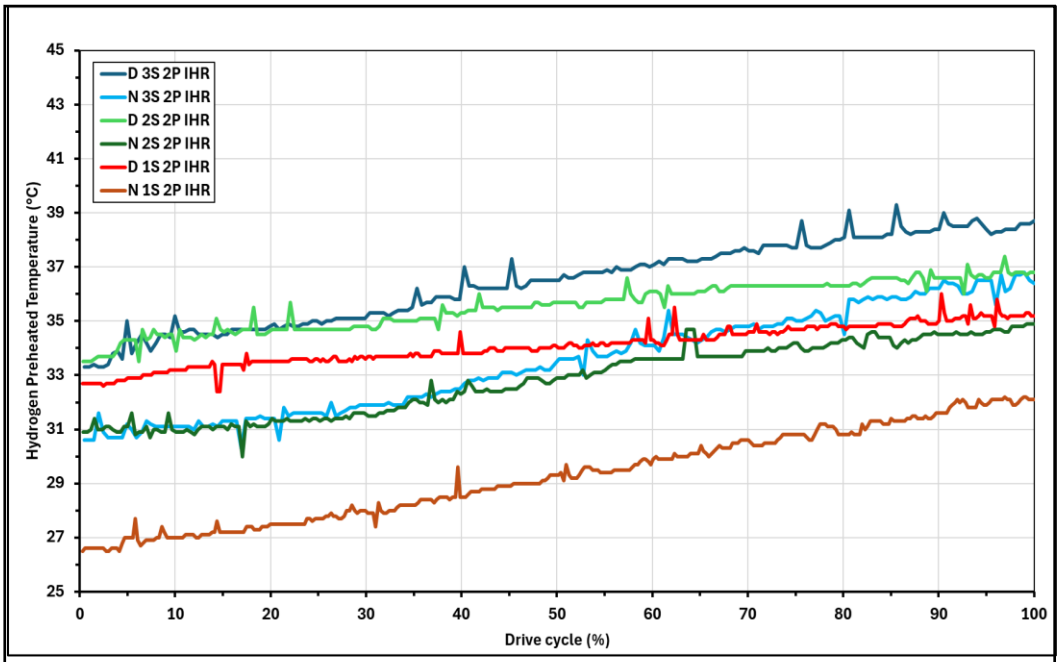
D 3S 2P IHR
N 3S 2P IHR
D 2S 2P IHR
N 2S 2P IHR
D 1S 2P IHR
N 1S 2P IHR
Hydrogen Preheated Temperature (°C)
Drive cycle (%)
45
43
41
39
37
35
33
31
29
27
25
0
10
20
30
40
50
60
70
80
90
100

(a)

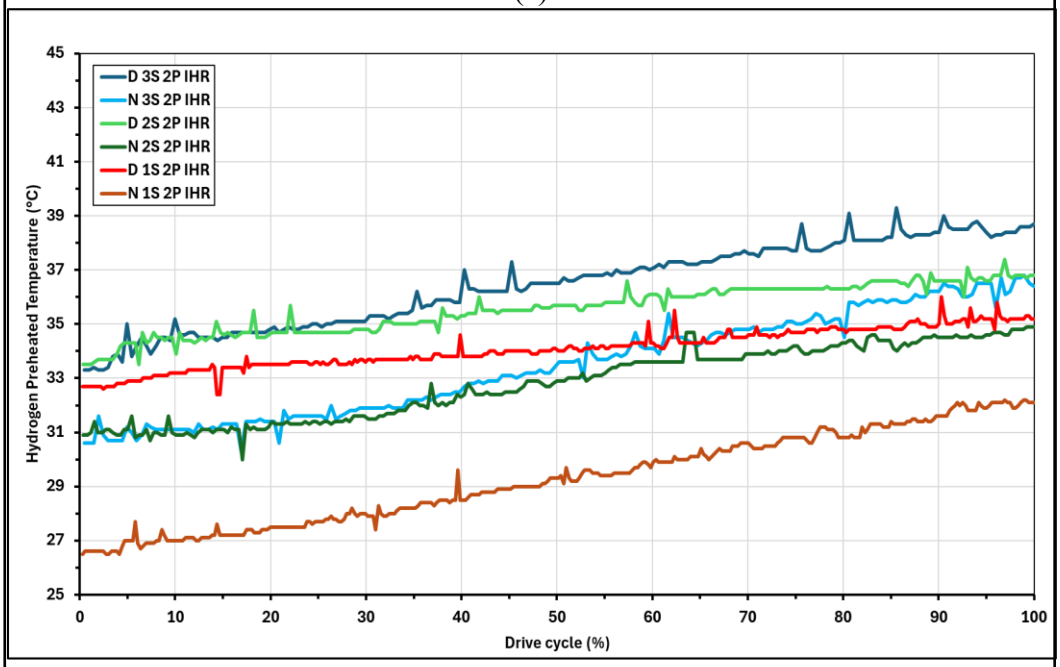
D 3S 2P IHR
N 3S 2P IHR
D 2S 2P IHR
N 2S 2P IHR
D 1S 2P IHR
N 1S 2P IHR
Hydrogen Preheated Temperature (°C)
Drive cycle (%)
45
43
41
39
37
35
33
31
29
27
25
0
10
20
30
40
50
60
70
80
90
100

(b)

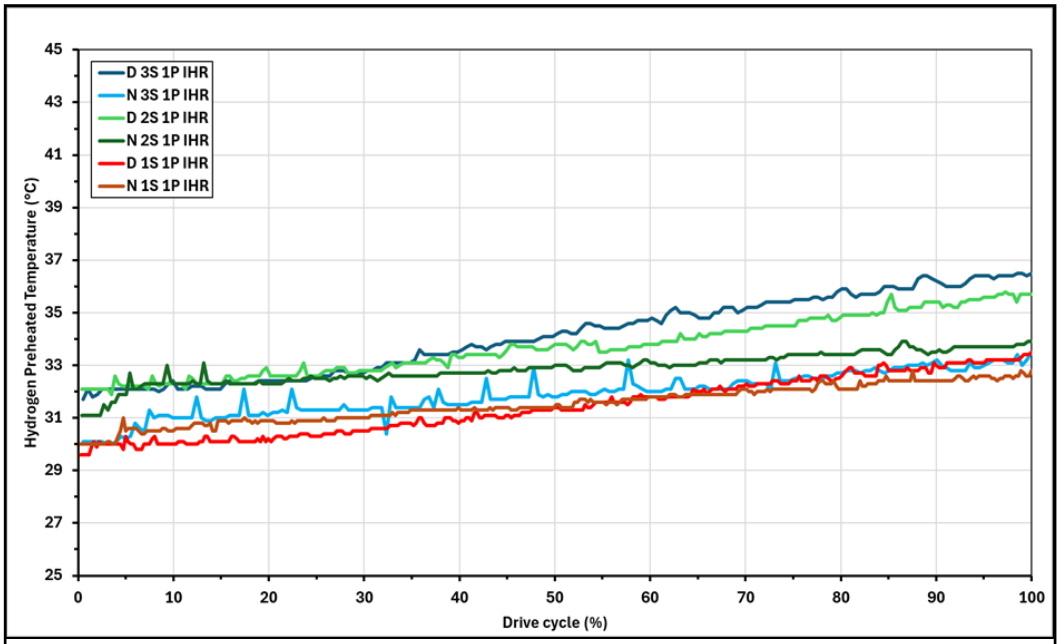

(c)

Figure 4.45 Hydrogen Preheated Temperature from IHR system for Cases (a) 3P (b) 2P (c) 1P

Notably, the nighttime driving cycles have frequently yielded a higher temperature difference and total preheated hydrogen energy than the daytime cycles. The maximum temperature difference is observed during the 3s3p condition at night, achieving an increase of 13 °C (from 25.9 °C to 38.9 °C) compared to 12 °C during the day. Correspondingly, the total preheated hydrogen energy for the night 3s3p case reaches 600 J, surpassing the daytime preheated hydrogen energy of 537 J. The effect of weight was first analysed. To isolate the influence of weight loading on the hydrogen temperature difference and hydrogen heat transfer profile, Figures 4.46, 4.47, and 4.48 presents the (a) temperature difference measurements and (b) calculated energy absorb energy at constant speeds (3s, 2s, and 1s, respectively) with varying weight conditions on each plot.

At the highest constant speed of 3s (figure 4.46), the preheated hydrogen temperature difference and total energy showed an upward trend as the weight loading increases. The 3p configuration recorded the highest energy transfer, achieving a temperature difference of 11.95 °C with 537 J of recovered energy during the day, and a temperature difference of 13 °C with 600 J during the night. This was followed by the 2p configuration (temperature difference Day: 8.2 °C, Night: 9.85 °C; Energy Day: 284 J, Night: 322 J) and the 1p configuration (temperature difference Day: 7.7 °C, Night:

7.25 °C; Energy Day: 208 J, Night: 155 J). It appears that the increased weight loading increases the operational demand for electrical power output from the fuel cell and proportionally increases the rate of exothermic electrochemical reactions, thereby generating a higher volume of waste heat directed into the IHR.

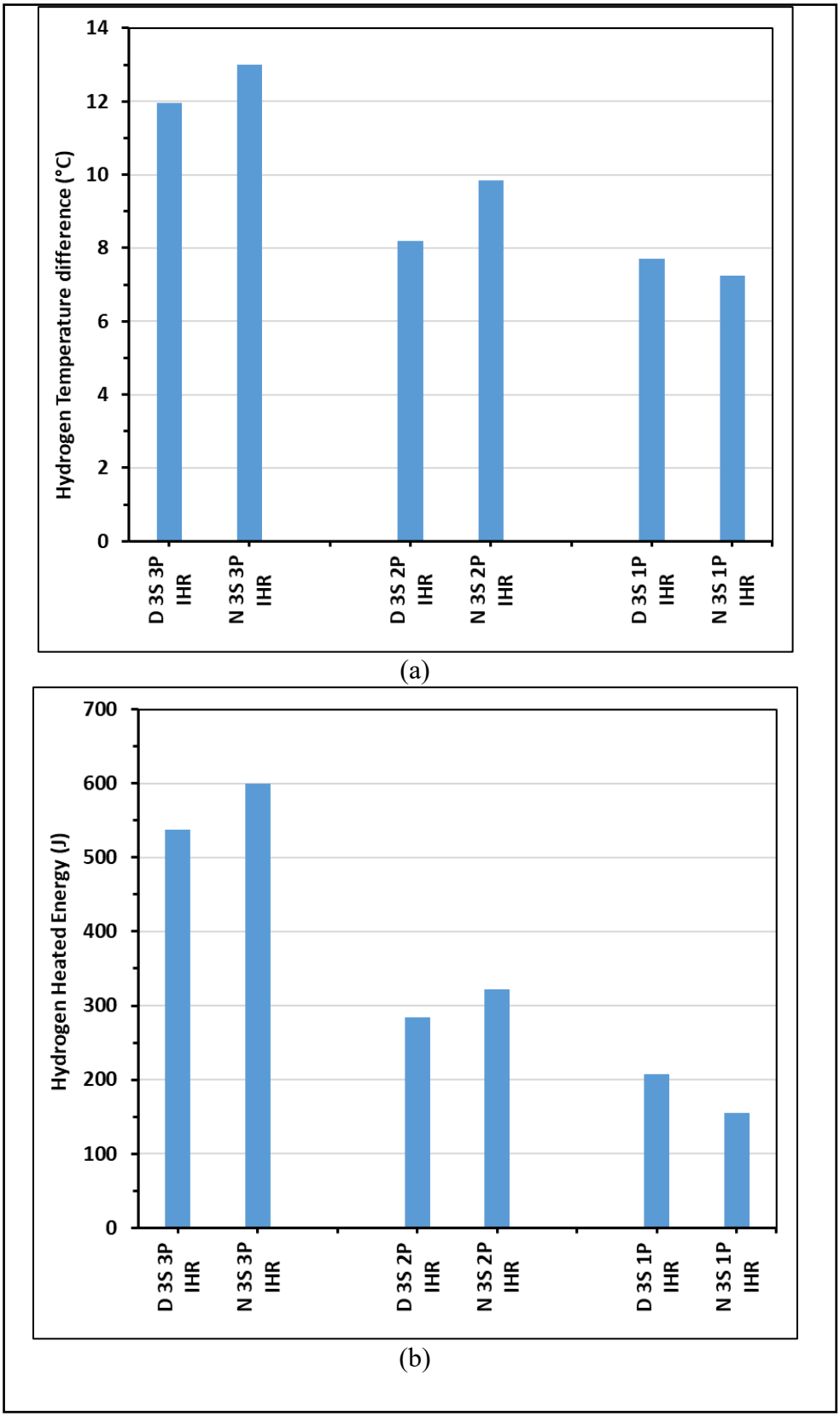

Figure 4.46 **3s** Cases for Hydrogen (a) Final Temperature Difference (b) Calculated Energy Absorb Energy

A similar relationship was observed at the intermediate speed of 2s (Figure 4.47). The performance for the 3p case (temperature difference Day: 9.85 °C, Night: 11.5 °C; Energy Day: 354 J, Night: 611 J) surpasses that of the 2p case (temperature difference Day: 6.75 °C, Night: 7.1 °C; Energy Day: 227 J, Night: 285 J) and the 1p case (temperature difference Day: 6.8 °C, Night: 7.4 °C; Energy Day: 195 J, Night: 207 J). The separation in energy recovery and temperature difference between the different weight loadings has remained distinct, suggesting that weight loading variations have influenced the magnitude of waste heat generated by the fuel cell.

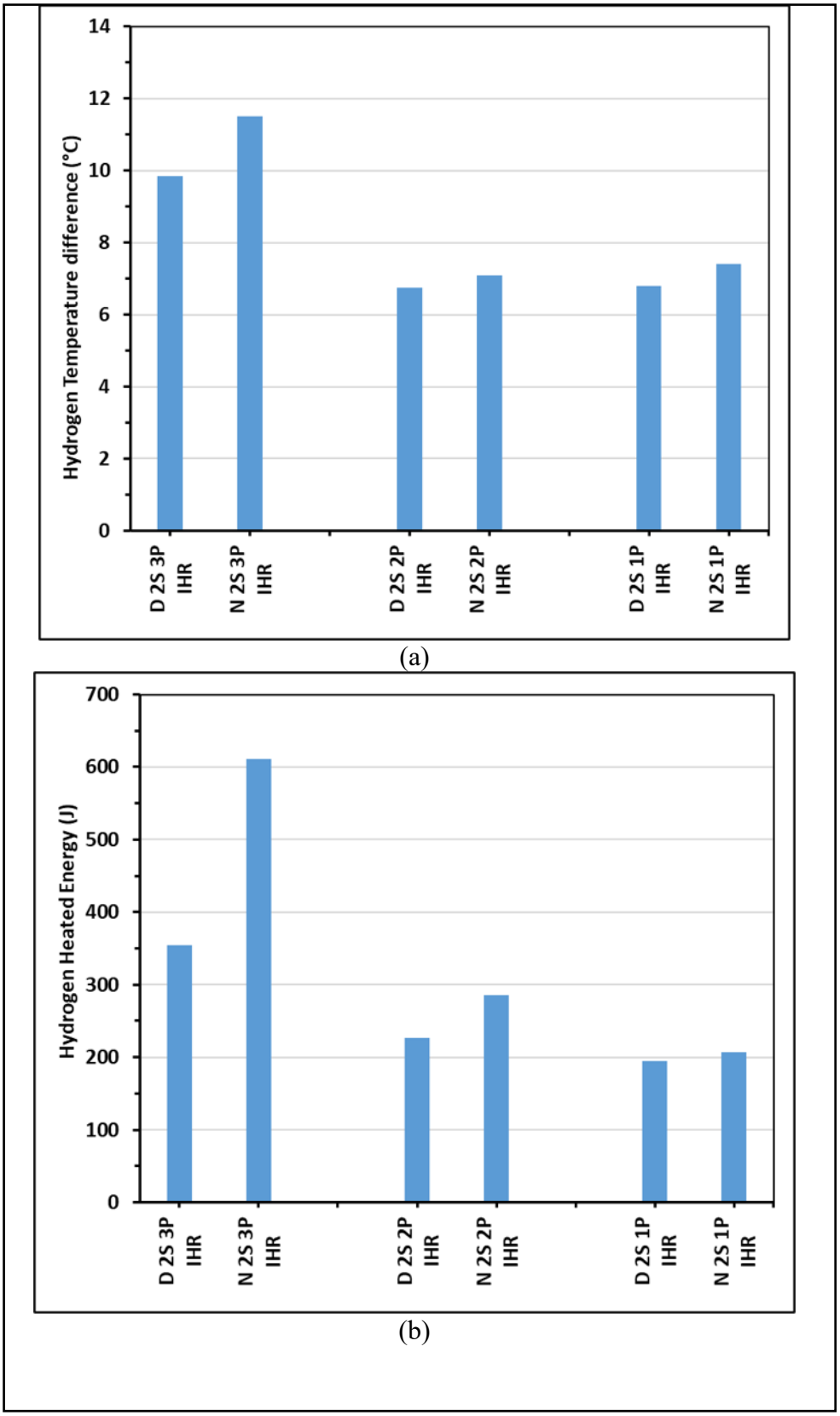

Figure 4.47 **2s** Cases for Hydrogen (a) Final Temperature Difference (b) Calculated Energy Absorb Energy

At the lowest speed of 1s (Figure 4.48), the system continues to demonstrate that higher weight loadings produced superior preheating performance. The 3p configuration achieves a temperature difference of 7.2 °C (Day) and 9.9 °C (Night), recovering 409 J and 483 J of energy, respectively. The absolute minimum energy transfer was observed in the lower loading categories, such as the 1s1p daytime case, with a temperature difference of only 4.8 °C and a total preheating energy recovery of just 101 J.

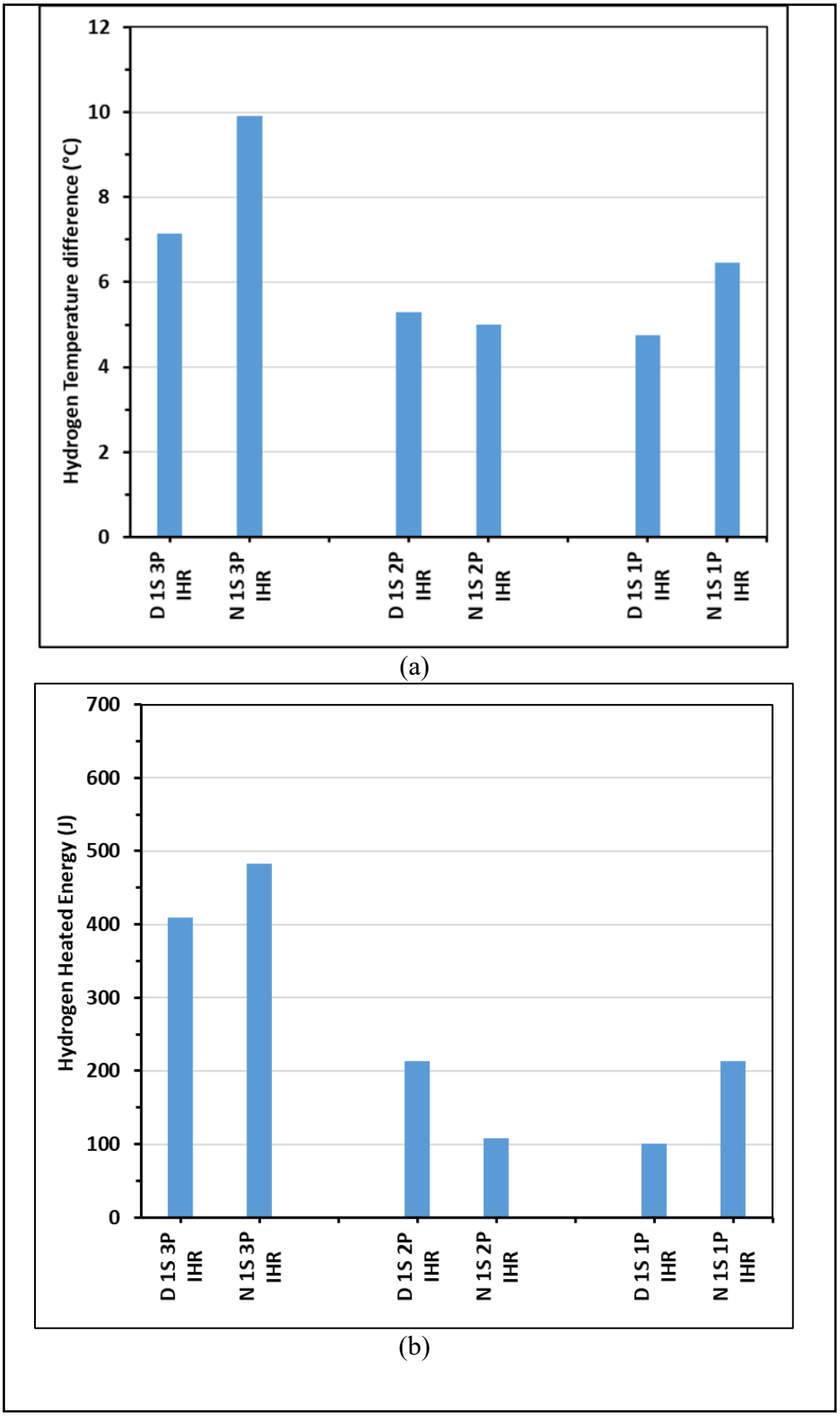

Figure 4.48 **1s** Cases for Hydrogen (a) Final Temperature Difference (b) Calculated Energy Absorb Energy

Cross-evaluating the data to analyse the impact of varying speeds under constant weight loading had indicated a relationship between vehicle speed, power demand, and waste heat generation. Comparing the maximum weight loading condition (3p) across the different speeds, the preheated hydrogen temperature difference increases sequentially with vehicle speed. The 3s3p case (temperature difference Day: 11.95 °C, Night: 13 °C; Energy Day: 537 J, Night: 600 J) has generated higher preheating profiles than the 1s3p case (temperature difference Day: 7.15 °C, Night: 9.9 °C; Energy Day: 409 J, Night: 483 J). While the 2s3p nighttime case has recorded a slight peak in total energy (611 J), the high-speed profiles have consistently maintained the upper boundaries of heat transfer. The increase in speed has increased the operational demand for higher electrical power production from both the fuel cell and the electric motor. As the fuel cell produces more electrical power to overcome the kinetic demands of higher speeds, the amount of waste heat generated increases proportionally, which resulted in the higher temperature differences observed in the 3s cases.

A quantitative evaluation of the percentage increments in temperature difference and total preheated energy has further elucidated the system's sensitivity to operational variables. Analysing the effect of variable weight loading at a constant high speed (3s), increasing the weight from 1p to 3p produces a substantial temperature difference increment of approximately 55.2% during the day (rising from 7.7 °C to 11.95 °C) and 79.3% during the night (rising from 7.25 °C to 13 °C). Correspondingly, there was a significant increase in total recovered energy of 158.2% during the daytime (from 208 J to 537 J) and further to 287.1% during the nighttime (from 155 J to 600 J).

Conversely, evaluating the effect of variable speed at a constant maximum weight loading (3p), accelerating from 1s to 3s has resulted in a temperature difference increment of 67.1% during the daytime (from 7.15 °C to 11.95 °C) and 31.3% during the nighttime (from 9.9 °C to 13 °C). The energy recovery has reflected this trend, showing an increment of 31.3% during the day (from 409 J to 537 J) and 24.2% during the night (from 483 J to 600 J). These percentage variances indicate that both vehicle speed and weight loading are significant operation variables, with weight loading exerting a noticeable and dominant influence on both the temperature difference and total energy transfer under cooler ambient conditions.

A qualitative assessment suggests that the IHR system functions as a highly responsive thermal buffer that adapts to dynamic external conditions. It has been observed that during the daytime driving cycles, the overall heat transfer process has

appeared to be constrained by a smaller thermal gradient between the ambient environment and the system components. This has led to a state where the system has retained a high absolute temperature but has transferred heat less aggressively to the hydrogen stream.

In contrast, the nighttime environment provides a cooler ambient heat sink. This cooler boundary condition facilitates a more rapid dissipation of thermal resistance within the heat exchanger fins, allowing the fuel cell exhaust heat to channel more efficiently into the cold hydrogen gas. The physical behaviour of the system under these varying conditions has implied that the IHR was not merely a passive conduit for exhaust gases, but rather a dynamic component whose thermodynamic exchange efficiency was dictated by the interplay between internal heat generation and external environmental boundary conditions.

In summary, while the daytime experimental cases have consistently recorded higher absolute preheated hydrogen outlet temperatures due to the elevated ambient baseline conditions, the nighttime cases have predominantly produced higher temperature differences and total preheated energy recovery. It has been observed that the lower initial hydrogen temperatures before preheating at night have provided a greater thermodynamic leverage for heat absorption. This amplified temperature gradient between the cold hydrogen gas, and the hot fuel cell exhaust appears to have enhanced the driving force within the integrated heat recovery mechanism, thereby optimizing the system's overall heat absorption capabilities during the cooler driving cycles.

4.4.1.5 Fuel Consumption and Efficiency

An important aspect in the integration of the IHR system as a novel thermal management strategy of a fuel cell vehicle was the evaluating the impact of hydrogen preheating on the fuel consumption and conversion efficiency. Figure 4.49, 4.50, 4.51 and 4.52 shows the hydrogen fuel flow rate, tank pressure dropped, absolute hydrogen consumption in grams, and the resulting fuel cell efficiency, respectively, for all tested configurations during the day and night driving cycles.

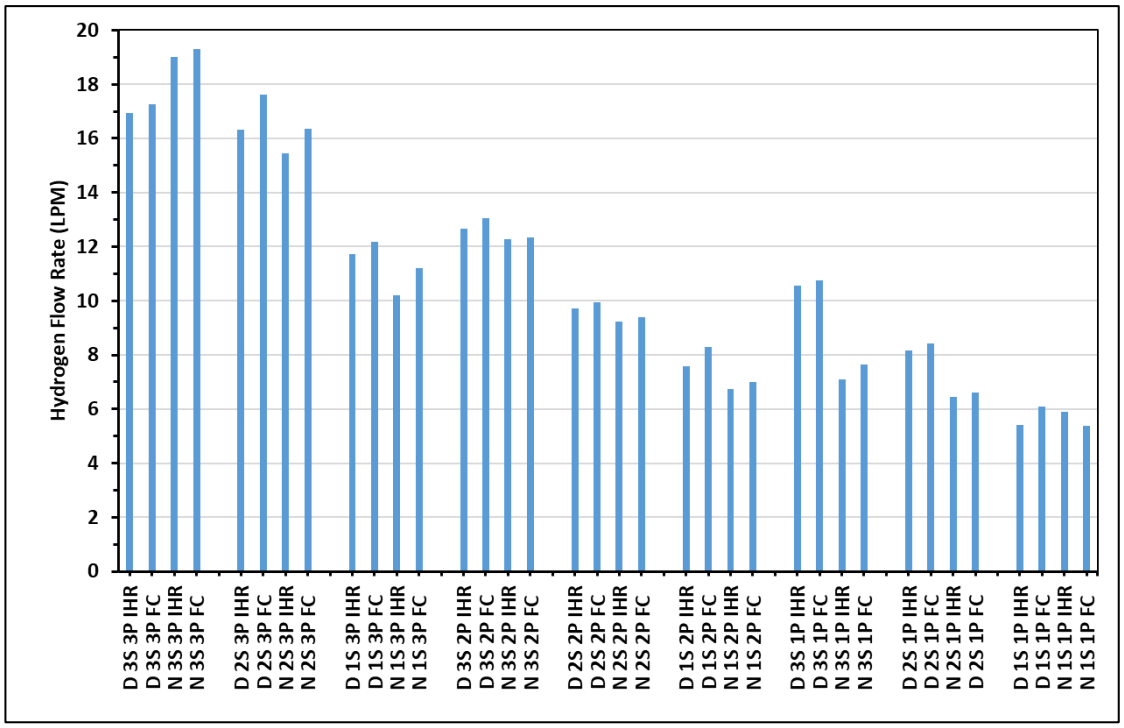

Figure 4.49 Hydrogen Flow Rate Through the Cases

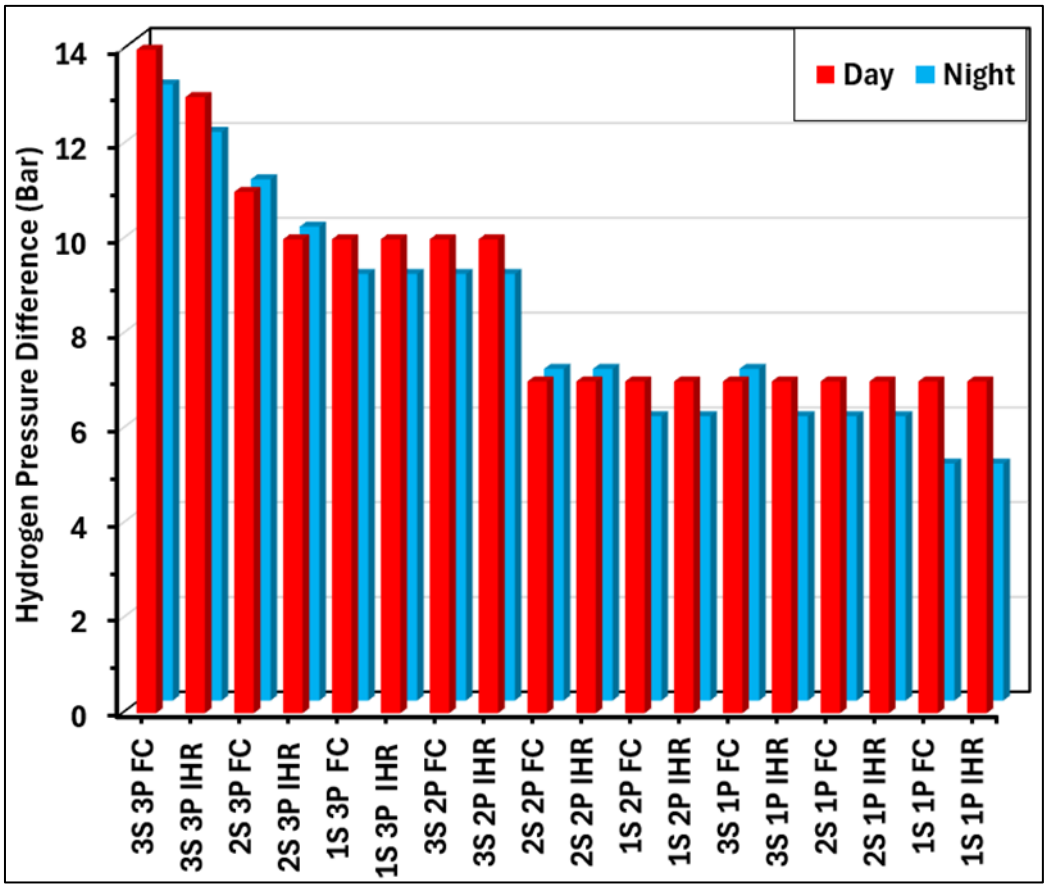

Figure 4.50 Hydrogen Tank Pressure Dropped Through the Cases

Figure 4.49 displays the hydrogen fuel flow rate in litres per minute (LPM), while Figure 4.50 profiles the corresponding hydrogen tank pressure drop across the various operations. As expected, both the flow rate and the pressure drop escalates proportionally when the vehicle speed and weight loading increases. When comparing the baseline standard fuel cell operation (without IHR) to the fuel cell with IHR, slight differences are observed. During the daytime 3s3p test, the baseline fuel cell recorded a flow rate of 17.27 LPM with a 14 bar pressure drop, whereas the fuel cell with IHR had recorded 16.94 LPM with a 13 bar drop. However, it must noted that these slight variances in flow rate and tank pressure readings between the standard fuel cell and the fuel cell with IHR might be attributed to uncontrollable measurement errors and transient environmental variables inherent to dynamic on-road testing, rather than acting as definitive proof of immediate consumption reduction.

Figure 4.51 details the absolute hydrogen consumption measured in grams. The data indicates a slight reduction in fuel mass consumed across several driving cycles when the IHR was installed and active. At the maximum operational demand of 3s3p during the day, the standard fuel cell had consumed 10.14 grams of hydrogen compared to 9.10 grams for the fuel cell with IHR. While these absolute consumption figures show minor differences that could also be influenced by the aforementioned on-road testing tolerances, it also provides the necessary quantitative baseline required for subsequent efficiency calculations.

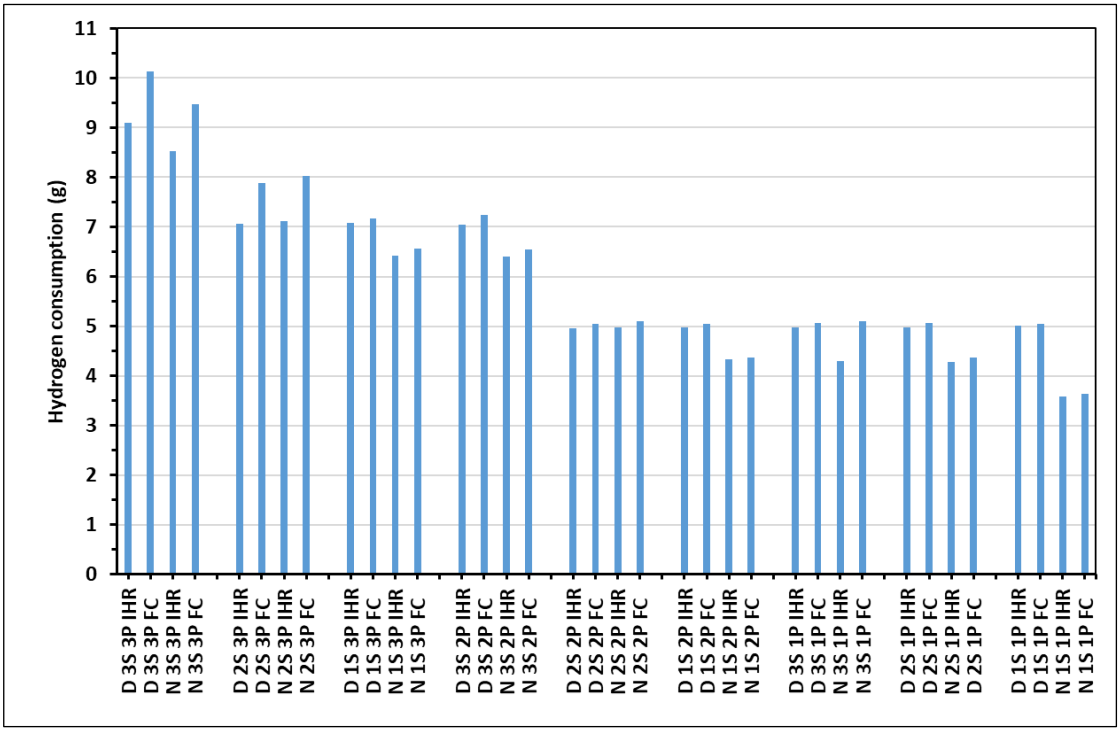

Figure 4.51 Hydrogen Consumption Measured in Grams for All Cases

The main focus of the evaluation was the overall fuel cell efficiency derived from the consumption data, as presented in Figure 4.52 (a), (b). Since all comparative cases had been conducted over a fixed 1 km distance at constant speeds and weight loadings, the mechanical work output required for each matched pair (standard fuel cell without IHR versus fuel cell with IHR) had remained theoretically constant. Consequently, evaluating the system based on calculated efficiency had provided a more robust metric than absolute consumption alone.

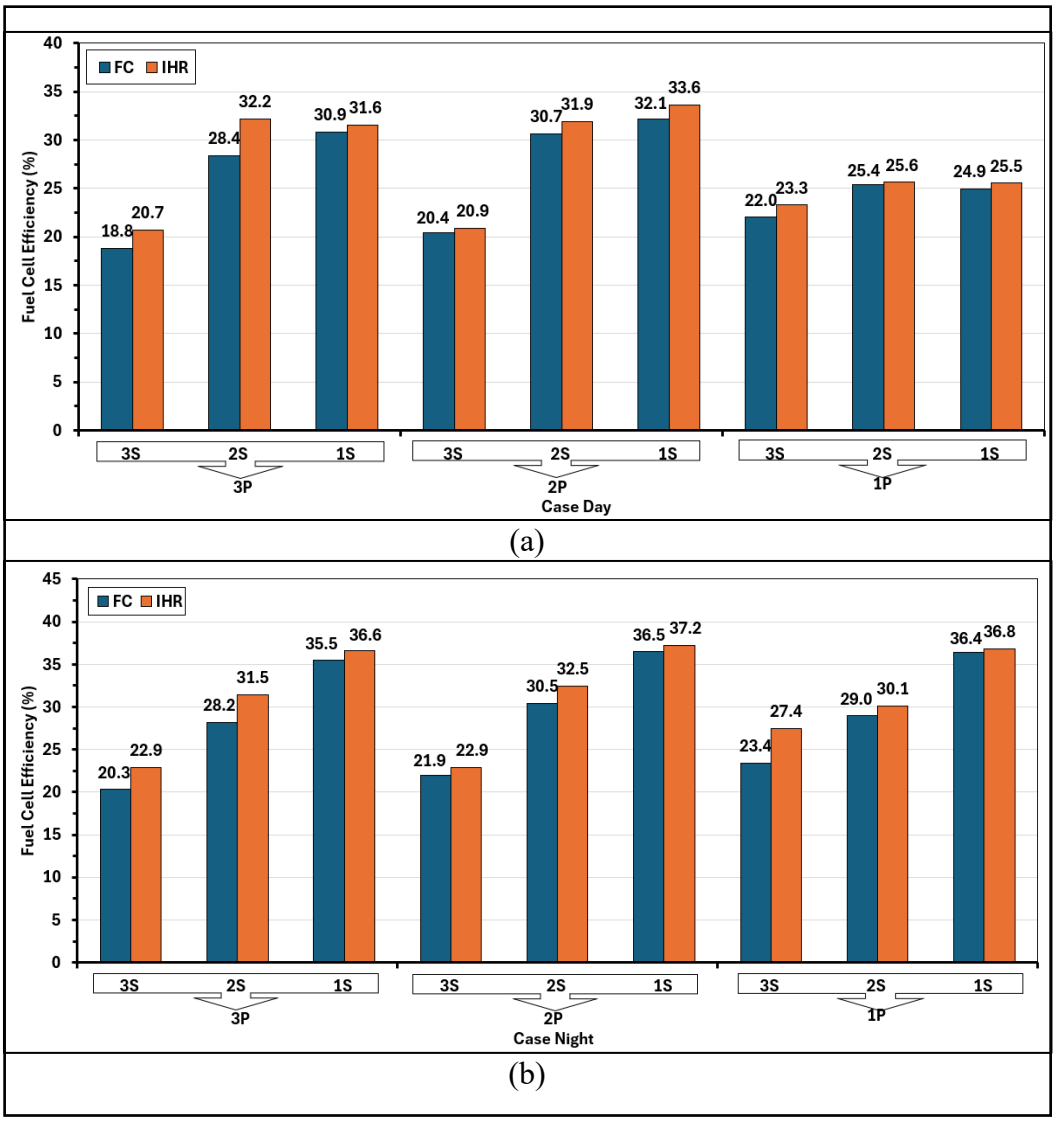

Figure 4.52 Fuel Cell Efficiency for (a) Day (b) Night for All Cases

The calculations reveal that the implementation of the IHR produces higher efficiency across the test matrix when utilising the preheated hydrogen. For instance, under the heavy operational demand of the daytime 3s3p configuration, the standard fuel cell recorded an efficiency of 18.8%, whereas the fuel cell with IHR elevated this to 20.7%. This enhancement was similarly observed during the daytime 2s3p case, where the efficiency had increased from 28.4% (standard fuel cell) to 32.2% (fuel cell with IHR). The nighttime driving cycles had also showed similar enhancements - the 3s3p nighttime configuration improves from 20.3% to 22.9%. The highest efficiency gain was recorded during the nighttime 3s1p case (speed 3s, weight 1p), increasing from 23.4% (standard fuel cell) to 27.4% (fuel cell with IHR). The ability of the IHR-equipped fuel cell to achieve these higher efficiency percentages while completing the

exact same fixed-distance mechanical work indicates that the preheated hydrogen successfully improves the electrochemical reaction kinetics within the fuel cell stack. Under these specific conditions, the elevated reactant temperature allowed for a more complete utilization of the hydrogen gas, minimizing waste and optimizing the electrical current generation necessary to overcome the physical loads.

The effect of weight loading on the fuel cell efficiency indicates a general trend where higher weight loadings resulted in reduced efficiency. For example, at a constant cruising speed of 3s during the daytime cycle, increasing the weight from 1p to 3p causes the efficiency of the fuel cell with IHR to decrease from 23.3% to 20.7%. A similar reduction was observed during the nighttime 3s cycle, where the efficiency of the fuel cell with IHR dropped from 27.4% at the 1p load down to 22.9% at the 3p load.

Similarly, when evaluating the effect of variable speeds under constant weight loadings, the data showed that higher speeds also contributed to lower efficiency outcomes. At the maximum weight condition of 3p during the night, as the speed increased from 1s to 2s and further to 3s, the efficiency of the fuel cell with IHR steadily declined from 36.6% to 31.5%, and finally to 22.9%. Consequently, the 3s3p case, representing the maximum combined operational load, recorded the lowest overall efficiency values across both the daytime (20.7%) and nighttime (22.9%) tests.

Despite this inverse relationship between operational load and efficiency, the trend exhibited specific fluctuations. Notably, the 2p weight loading configurations maintained higher efficiency levels compared to the maximum load, generally remaining above 30% during the lower and intermediate speed cycles. During the daytime, the 1s2p and 2s2p cases for the fuel cell with IHR recorded efficiencies of 33.6% and 31.9%, respectively. The corresponding night time tests similarly maintained this trend, yielding 37.2% and 32.5% for the 1s2p and 2s2p cases with IHR.

A further comparative analysis between the daytime and nighttime driving cycles reveals the influence of ambient conditions on the system's overall performance. When evaluating the two conditions, the nighttime cycles predominantly produced the highest overall efficiencies. For example, while the daytime tests reached a peak efficiency of 33.6% during the 1s2p IHR configuration, the nighttime tests exceeded this threshold. The highest efficiency across the entire experimental matrix recorded during the nighttime was the 1s2p configuration for the fuel cell with IHR, achieving 37.2%. Similar higher efficiency peaks was observed in the nighttime 1s1p IHR (36.8%) and nighttime 1s3p IHR (36.6%) configurations, which had outperformed their

respective daytime load conditions (25.5% and 31.6%). This consistent superiority in the nighttime data suggests that a cooler ambient provides a more optimal thermal gradient for the heat recovery process on heating the hydrogen fuel, thereby allowing the fuel cell to operate at a higher degree of efficiency.

In summary, while the direct measurements of flow rate, pressure drop, and absolute fuel consumed in grams had exhibited only slight differences that were highly susceptible to on-road measurement noise, the comparative efficiency analysis had yielded important thermodynamic insights. The calculated efficiency trends indicate that the recovery and transfer of waste heat into the hydrogen fuel stream does not significantly transform the flow rate but rather facilitates a more complete, efficient utilization of the reactant gases under specific, high-demand scenarios. Ultimately, embedding the IHR system into the fuel cell had demonstrated a range of positive effects on the fuel cell efficiency of a lightweight fuel cell vehicle during high-load driving cycles.

4.4.1.6 TEG Thermal and Electrical Analysis

This subsection focuses on the thermal and electrical performance of the TEG sub-system that was integrated as a secondary energy recovery platform within the IHR. Figures 4.53 to 4.57, presents the TEG temperature profiles, total heat transfer, maximum electrical power, and total electrical power generated, respectively.

Figure 4.53 (a), (b) and (c) displayed the instantaneous temperature difference, while figure 4.54 provides the final temperatures of the testing. The hot side and cold side temperature profiles in Figure 4.53 indicated that the absolute maximum hot side temperature was reached during the highest operational demand in the daytime, specifically the 3s3p configuration, which had recorded 42.8 °C. In contrast, the lowest cold side temperature was observed during the nighttime driving cycles, dropping to 31.1 °C during the 1s2p case. Despite the daytime cycles operating at higher absolute temperatures, the nighttime cycles generally exhibit a larger temperature difference across the TEG module. For example, the nighttime 3s3p configuration achieved a maximum temperature difference of 4.4 °C, compared to 4.2 °C for the corresponding daytime case. This had suggested that the cooler nighttime ambient air functions as a more effective heat sink, facilitating a slightly steeper thermal gradient across the TEG surfaces.

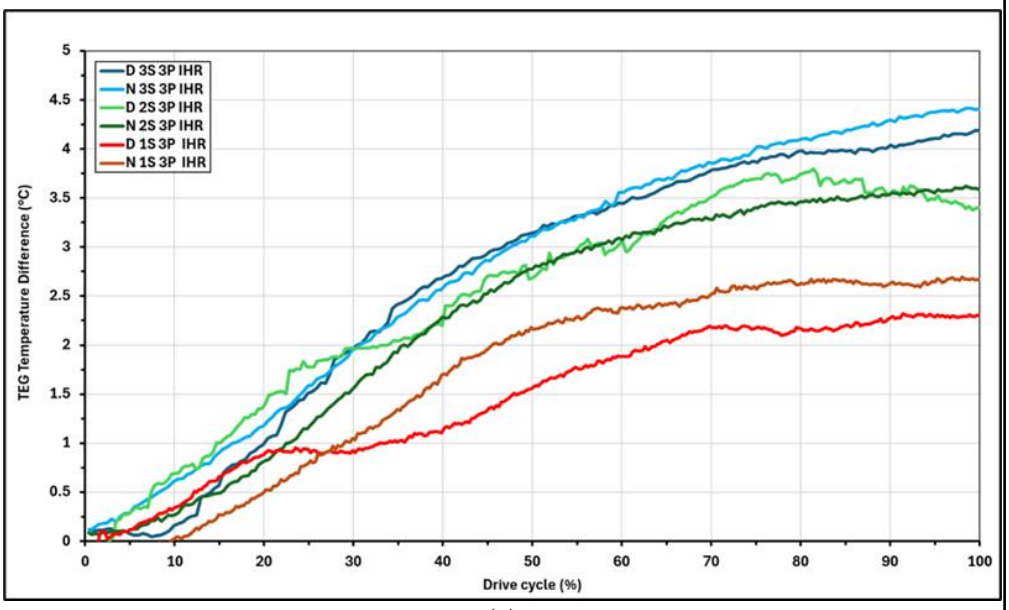
D 3S 3P IHR
N 3S 3P IHR
D 2S 3P IHR
N 2S 3P IHR
D 1S 3P IHR
N 1S 3P IHR
TEG Temperature Difference (°C)
Drive cycle (%)
0
0.5
1
1.5
2
2.5
3
3.5
4
4.5
5
0
10
20
30
40
50
60
70
80
90
100

(a)

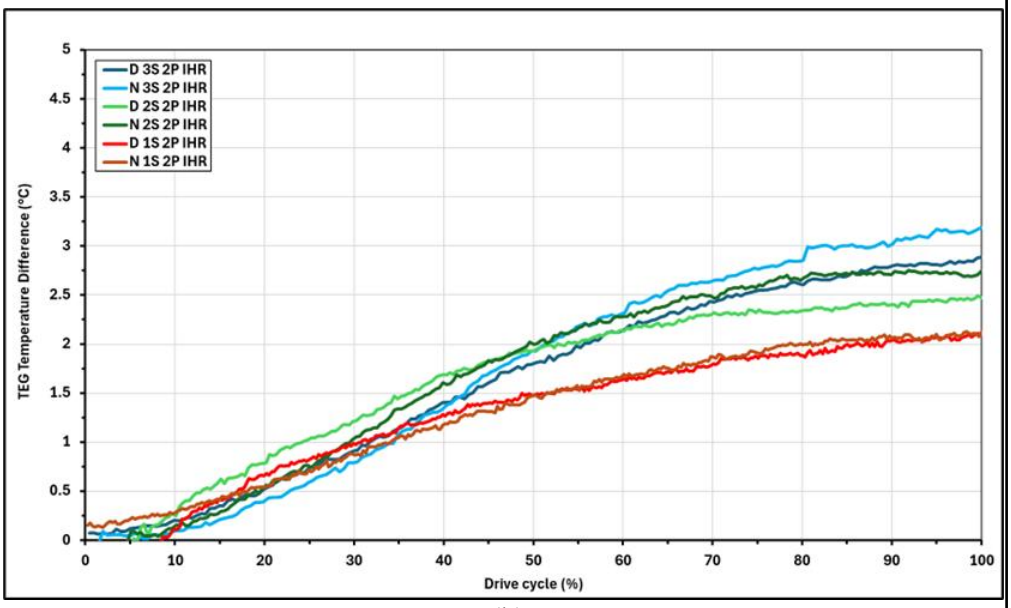
D 3S 2P IHR
N 3S 2P IHR
D 2S 2P IHR
N 2S 2P IHR
D 1S 2P IHR
N 1S 2P IHR
TEG Temperature Difference (°C)
Drive cycle (%)
0
0.5
1
1.5
2
2.5
3
3.5
4
4.5
5
0
10
20
30
40
50
60
70
80
90
100

(b)

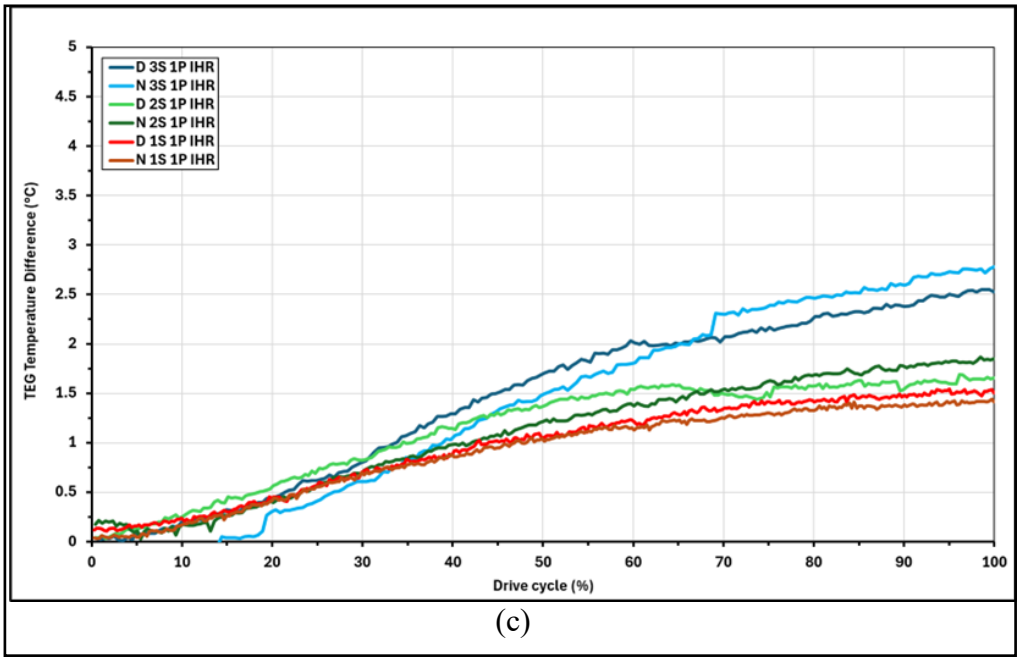

(c)

Figure 4.53 Instantaneous TEG Temperature Difference Throughout The Whole Testing for Cases (a) 3P (b) 2P (c) 1P

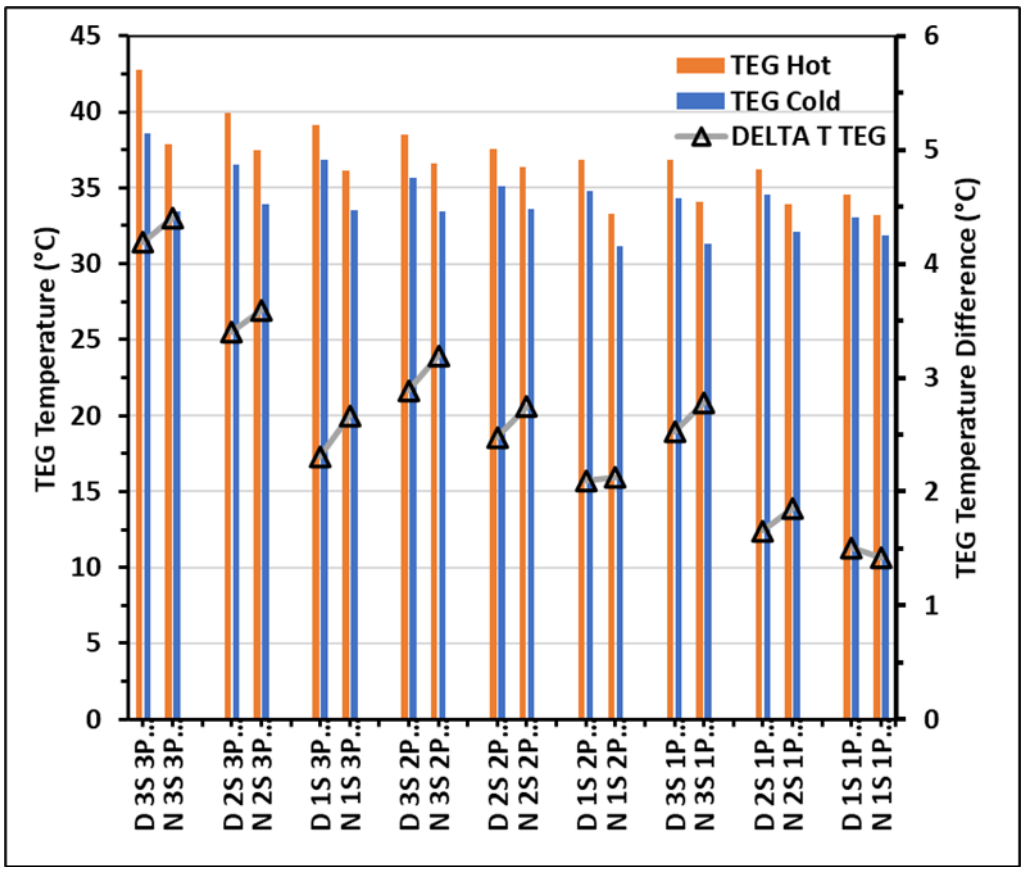

Figure 4.54 The Final TEG Surface Temperatures and Temperature Difference for All Conditions

The total heat transferred through the TEG over the 1 km test distance was depicted in Figure 4.55. The analysis reveals a relationship between driving speed, cycle duration, and thermal transfer. While the highest speeds generate the highest instantaneous temperatures, the intermediate and lower speeds frequently resulted in a greater total heat transfer in kilojoules (kJ). For instance, the daytime 2s3p configuration had recorded the maximum total heat transfer of 6.0 kJ, which exceeded the 4.9 kJ recorded for the faster daytime 3s3p case. This observation was likely due to the longer driving duration required to complete the 1 km distance at slower speeds, which allowed a prolonged period for thermal energy exchange to occur. Furthermore, evaluating the effect of weight loading shows a consistent trend where increased weight had resulted in higher thermal outputs. At a constant cruising speed of 3s during the night, increasing the weight from 1p to 3p increases the temperature difference from 2.8 °C to 4.4 °C, and the total heat transfer from 2.6 kJ to 5.0 kJ. This indicates that heavier vehicle loads demand greater electrical power from the fuel cell, thereby generating more continuous waste heat for the TEG to absorb and convert.

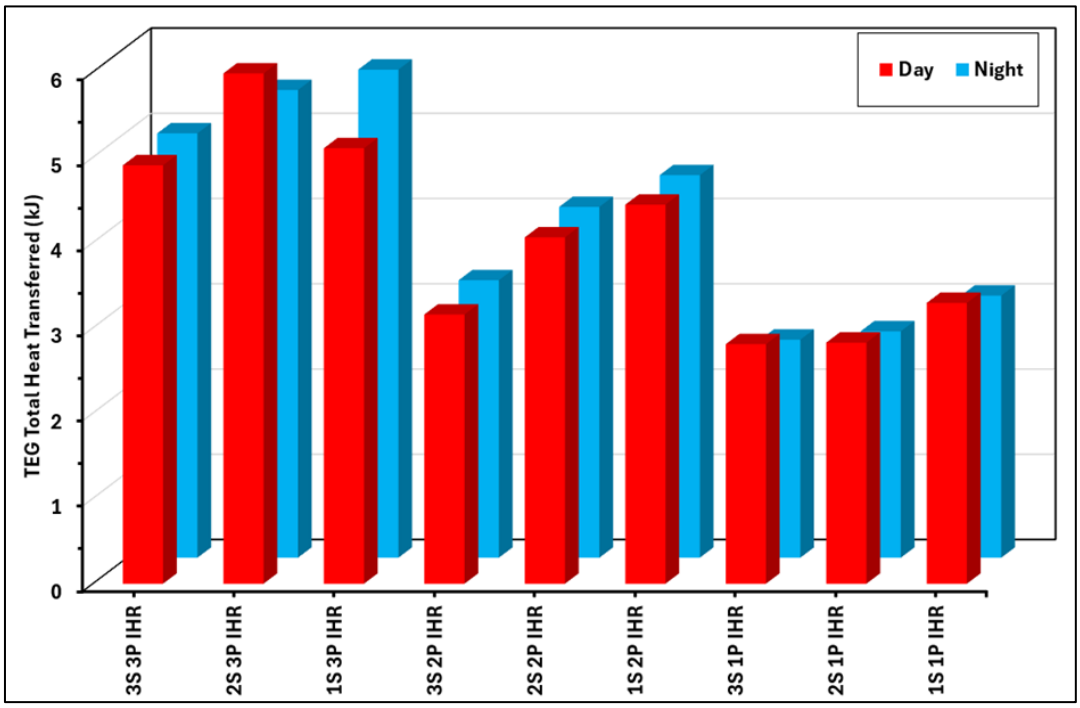

Figure 4.55 The Total TEG Heat Transfer for All Conditions

Figures 4.56 and 4.57 illustrates the maximum power produced in milliwatts (mW) and the total electrical power generated in watt-hours (Wh), respectively. The electrical generation closely mirrors the temperature difference trends as the nighttime

cases generally generate higher electrical values than daytime cases due to the enhanced thermal gradients. The maximum instantaneous power was recorded during the nighttime 3s3p configuration at 345.76 mW, which was higher than the daytime equivalent of 316.79 mW. Similarly, the highest total electrical energy generated over the driving cycle also occur during the nighttime 3s3p case, which generated 0.00975 Wh. The lowest electrical output was observed during the minimal load conditions, such as the nighttime 1s1p case, which had generated only 40.10 mW of peak power and 0.00201 Wh of total energy.

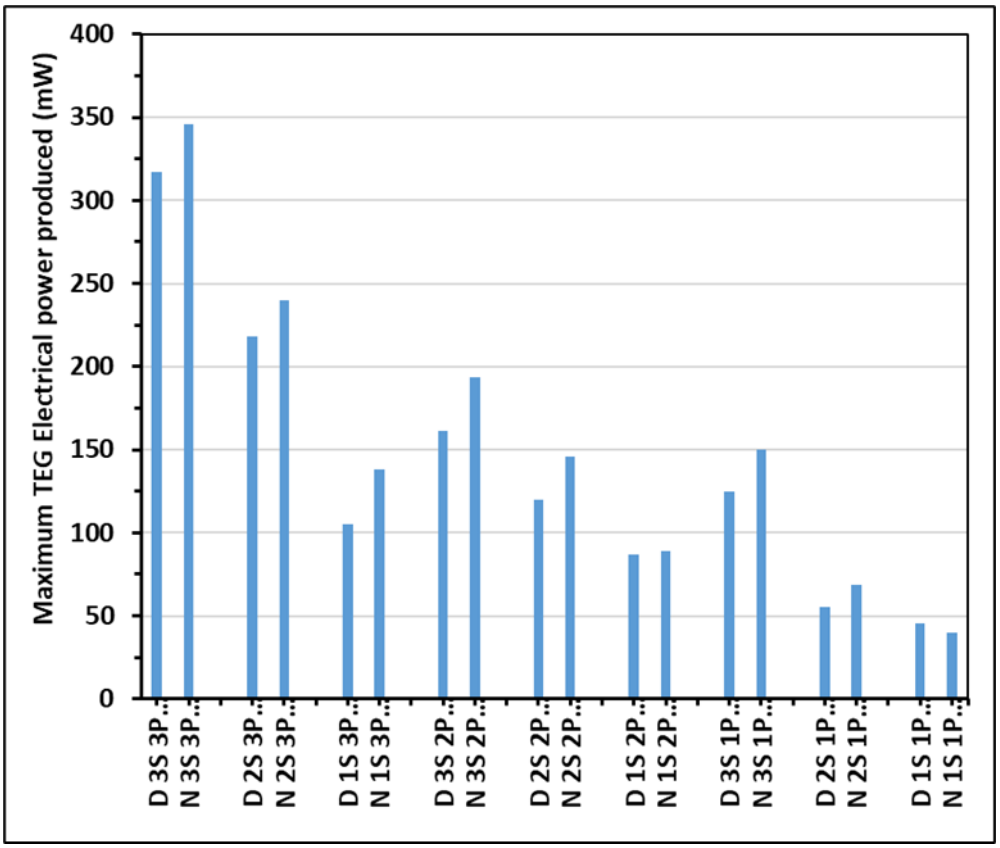

Figure 4.56 Maximum TEG Electrical Power Produced Through Out the Testing for All Conditions

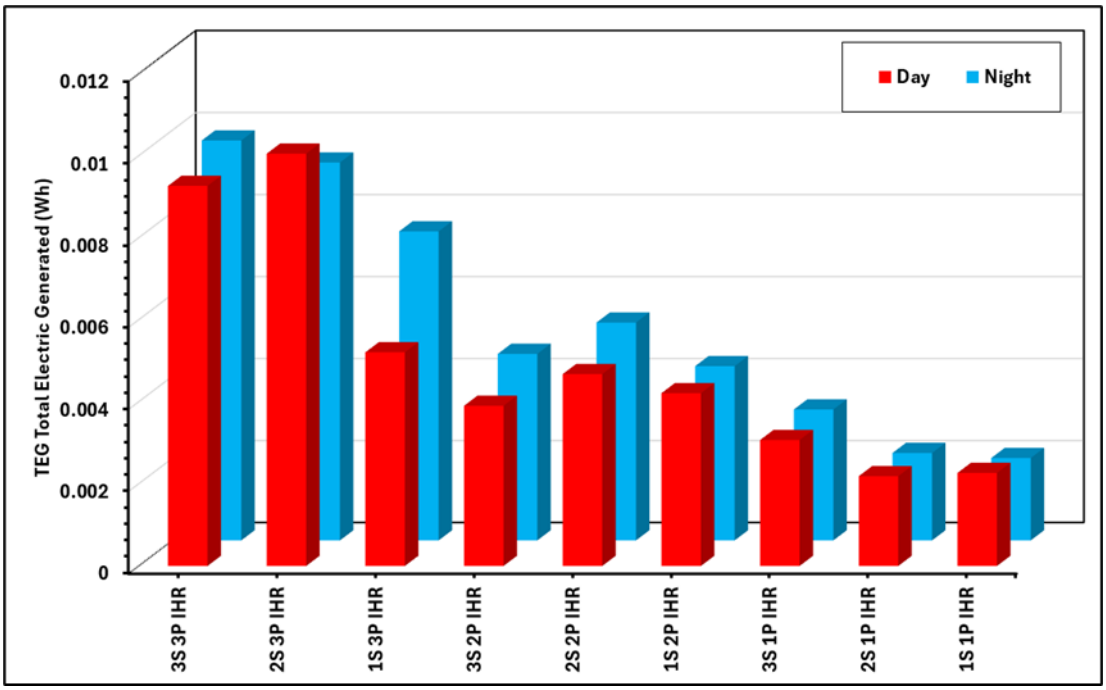

Figure 4.57 Total TEG Electrical Production for All Conditions

When analysing these electrical outputs, it must be acknowledged that the overall magnitude of TEG power generated was relatively small compared to fuel cell power outputs. The low output was constrained by the small thermal boundary conditions of the lightweight vehicle scenario. The maximum heat source from the fuel cell exhaust had remained below 65 °C (ultra-low waste heat grade), while the ambient cooling sink had often exceeded 32 °C during the day, coupled with a maximum convective cooling velocity limited to the vehicle's top cruising speed of 18 km/h (5 m/s). These restrictive thermal boundaries had naturally limited the achievable temperature difference across the TEG modules, peaking at only 4.4 °C. Therefore, while the data had demonstrated that the TEG could convert a portion of the waste heat into electrical energy, the results suggest that the TEG subsystem was subject to thermal limitations and design weaknesses and that further thermal insulation and redesign of heat sink would likely be necessary to obtain a larger scale energy recovery.

Although the electrical power generated by the TEG was well below 1 Watt of instantaneous power and less than 1 Wh of total energy, it should be noted that this energy had been recovered entirely passively. The TEG operation required no additional moving parts or active maintenance, functioning solely by scavenging the existing waste heat from the fuel cell and utilising the forced convection induced by the vehicle's

cruising motion. Consequently, the system had demonstrated the fundamental concept of recovering otherwise wasted energy without imposing additional parasitic electrical loads. Nevertheless, the small magnitude of electrical production must be acknowledged as a limitation for this initial phase development and experimental work. If this novel fuel cell with IHR system was implemented in a more favourable operational scenario, characterized by a higher-temperature exhaust source and a cooling system with greater thermal capacity, then the system would likely exhibit a higher energy recovery capability.

4.4.1.7 Waste Heat Utilization

The waste heat utilization (WHU) had been calculated using equation 3.42 to quantify the percentage of total fuel cell thermal energy successfully recovered by the IHR. The resulting data for all tested configurations during the day and night driving cycles was as plotted in Figure 4.58. Theoretically, it was expected that higher operational loading would directly correlate with a higher rate of utilization. A heavier vehicle load requires a higher electrical power demand from the motor, which subsequently forces the fuel cell to increase its power production. This elevated operational state amplifies the exothermic electrochemical reactions within the stack, thereby generating a larger volume of waste heat. Consequently, this excess thermal energy was anticipated to provide a more abundant source for the IHR system to harness for both hydrogen preheating and thermoelectric generation.

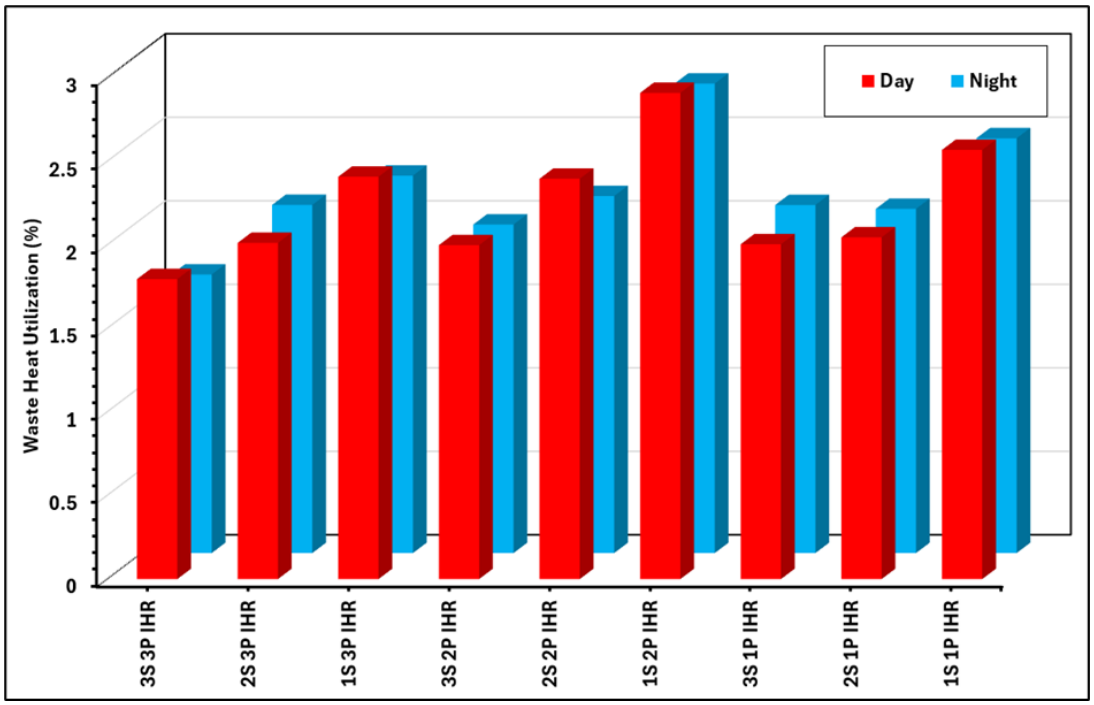

Figure 4.58 Total WHU for All Conditions

However, the WHU did not scale in a strictly linear, direct proportion to the operational loading. Instead, it exhibited specific fluctuations, revealing that the relationship between absolute heat generation and the percentage of heat utilised was more complex. When evaluating the effect of speed under a constant maximum weight loading (3p), the WHU actually increased as the speed decreased. During the daytime cycles, the WHU progressed from 1.8% at the fastest 3s speed, to 2.0% at the intermediate 2s speed, and up to 2.4% at the lowest 1s speed. A similar trend was observed during the nighttime 3p tests, increasing from 2.0% (3s) to 2.3% (1s). This inverse relationship with speed was attributed to the findings previously discussed in Section 4.3.1.6; slower cruising speeds require a longer temporal duration to complete the 1 km distance. This extended travel time likely provides a prolonged residency period for the thermal energy, facilitating a more thorough heat exchange process within the IHR modules compared to the rapid, transient nature of high-speed drives.

Furthermore, evaluating the effect of weight loading reveals that the maximum WHU did not occur at the heaviest configurations. The highest WHU was recorded during the intermediate 1s2p configuration that achieved 2.9% during daytime and 2.8% during nighttime driving cycles. When the weight was increased further to the 3p condition at the same 1s speed, the WHU reduces to 2.4% (day) and 2.3% (night). The fluctuation suggests that the IHR system possesses a specific optimal thermal

absorption capacity or operational "sweet spot." At the maximum 3s3p operational demand, the sheer volume and rapid flow rate of the waste heat generated by the fuel cell might have simply overwhelmed the physical heat transfer limitations of the heat exchanger fins and the TEG surfaces. Consequently, while the absolute amount of heat recovered might have been high, the actual percentage of the total available heat utilised had dropped (recording only 1.80% for the daytime 3s3p case).

Overall, the waste heat utilization trends indicate that maximizing the recovery efficiency of the integrated system depends on balancing the thermal generation rate with the system's physical absorption capacity and the duration of exposure. The highest WHU values are achieved under moderate loads and slower speeds, where the system had sufficient time and capacity to absorb the available thermal energy. These observations acknowledge the inherent limitations and uncertainties of the current IHR design under peak dynamic loads, suggesting that further geometric scaling of the heat sinks was required to capture a larger percentage of the available waste heat during extreme high-demand scenarios.

4.4.1.8 Summary of Constant Speed on Road Testing

The constant speed on road evaluation of the lightweight fuel cell buggy established a critical intermediate baseline between controlled laboratory testing and fully dynamic driving cycles. By subjecting the integrated heat recovery architecture to matched operational speeds and weight loadings over a 1 km distance, the empirical data confirmed that passive waste heat recovery successfully enhances primary fuel cell performance. Repurposing the exhaust heat elevated the incoming hydrogen temperature by a maximum of 13 °C under cooler nighttime conditions. This thermal conditioning actively mitigated internal activation polarization, yielding a fuel cell electrical power increment of up to 6.3% at peak current loads. Consequently, the system recorded measurable improvements in overall electrochemical efficiency, escalating from 18.8% to 20.7% under maximum daytime vehicular loads and reaching a peak system efficiency of 37.2% during intermediate nighttime operations.

Furthermore, the solid state TEG successfully harvested a fraction of the residual thermal energy to produce a maximum secondary electrical output of approximately 345 mW. However, this phase of physical testing explicitly exposed the severe thermodynamic limitations inherent to outdoor vehicular applications. The

empirical thermal mapping revealed a profound 50% temperature degradation occurring immediately upstream of the recovery chamber due to inadequate physical insulation and upstream conductive heat losses. Because the ultra low grade exhaust source struggled to maintain a robust thermal gradient against the fluctuating ambient cruising air, the maximum temperature difference across the thermoelectric modules remained strictly bounded at only 4.4 °C.

Ultimately, the overall waste heat utilization factor quantified the strict physical bottlenecks of the integrated architecture. The utilization peaked at a mathematically low 2.9% during slower cruising speeds, where the prolonged thermal residency time facilitated better heat exchange. Conversely, during maximum operational demands, the sheer volume of generated waste heat fundamentally overwhelmed the physical absorption capacity of the internal heat sink fins and the inherently low mass flow rate of the hydrogen reactant. These empirical observations acknowledge that while the integrated system provides undeniable electrochemical benefits, evaluating physical systems in open environments introduces unavoidable transient noise, structural thermal leakages, and aerodynamic disturbances. The quantitative data strongly suggests that future architectural iterations must focus on extreme geometrical optimization and rigorous thermal insulation to capture a more substantial fraction of the available waste heat under strict vehicular constraints.

4.4.2 Dynamic On-Road Testing

This subsection presents the experimental findings from the dynamic on-road evaluations. To assess the integrated system under realistic transient conditions, the driving profile incorporated testing principles adapted from the New European Driving Cycle. However, the physical constraints of the lightweight vehicle platform require a scaled approach to these standard protocols. The maximum cruising speed was restricted to 18 km/h. Consequently, the total driving distance for this dynamic evaluation spanned only 2.6 km, which was significantly shorter than the 11 km minimum typically required by full scale automotive cycles. Despite this reduced scale, the continuous acceleration and deceleration phases provided a highly dynamic operational load to evaluate the integrated heat recovery architecture under fluctuating environmental boundary conditions.

The subsequent analysis explores the system response across seven specific operational sections. Section 4.4.2.1 examines the raw electrical demands of the fuel cell and the traction motor during the drive cycle. Section 4.4.2.2 evaluates the corresponding fuel cell electrical performance under these transient loads. The internal thermal behaviour of the fuel cell stack and the integrated recovery system was discussed in Section 4.4.2.3. Following this, Section 4.4.2.4 and Section 4.4.2.5 analyses the hydrogen fuel consumption and the specific hydrogen preheating outcomes, respectively. Finally, Section 4.4.2.6 details the secondary electrical generation from the solid-state thermoelectric modules, culminating in Section 4.4.2.7, which quantifies the overall waste heat utilization achieved during the dynamic cycle.

4.4.2.1 Raw Fuel Cell and Motor Electrical Analysis

Figure 4.59 through Figure 4.62 displays the raw electrical power profiles for the fuel cell and the traction motor across the varied day and night test cases. Generally, within dynamic evaluations adapted from the NEDC the electrical power profile closely mirrors the instantaneous vehicle speed. During vehicle acceleration phases, the traction motor draws higher electrical power to overcome inertia, which subsequently forces the fuel cell stack to rapidly increase its power generation. Conversely, during steady cruising and deceleration phases, the power demand stabilizes or drops. The mapped profiles confirmed this fundamental behaviour, demonstrating continuous electrical power fluctuations dictated entirely by the specific speed phases of the 2.6 km driving route.

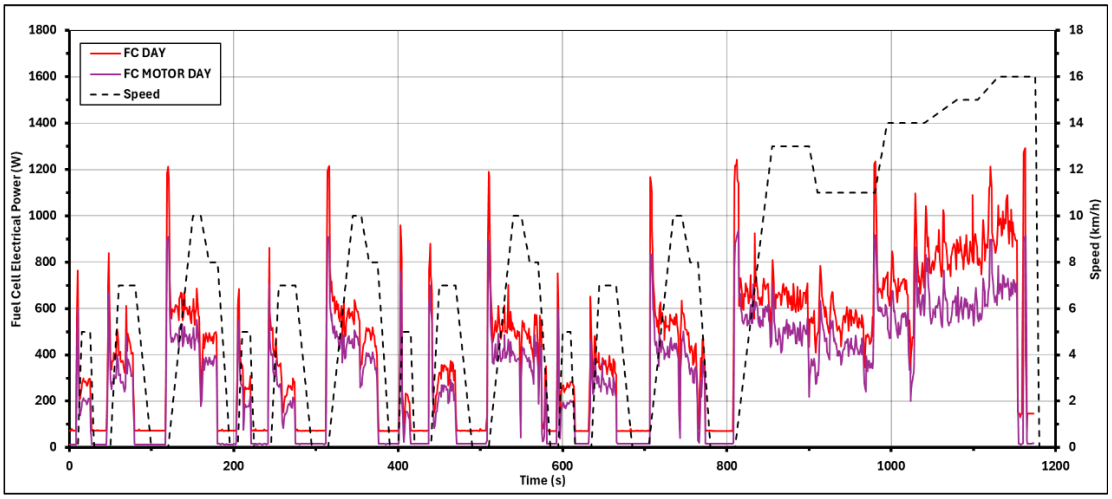

Figure 4.59 Power Profiles for the Fuel Cell Stack and the Traction Motor Corresponding to Scaled-Down NEDC – Daytime Operation Without IHR

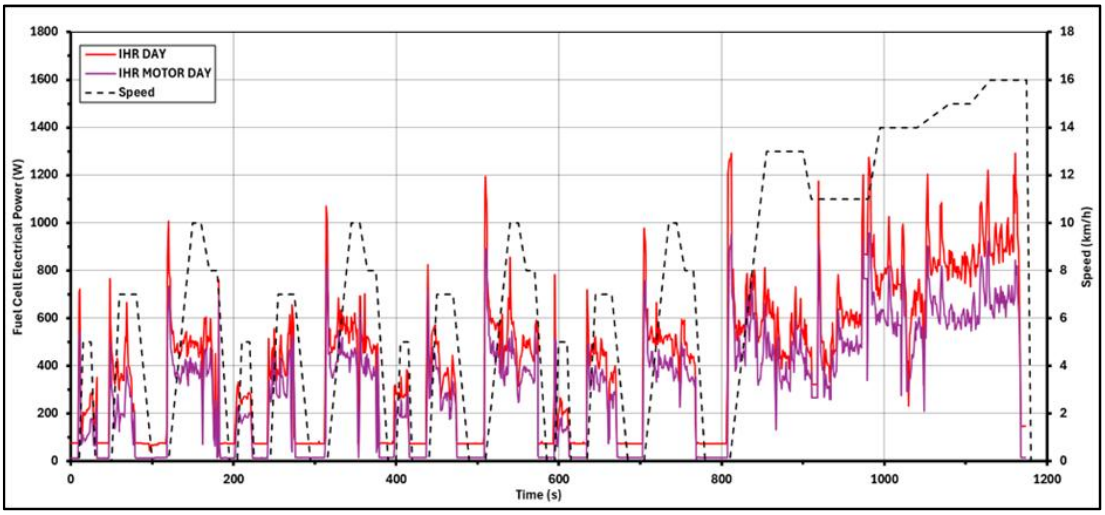

Figure 4.60 Power Profiles for the Fuel Cell Stack and the Traction Motor Corresponding to Scaled-Down NEDC – Daytime Operation Using IHR

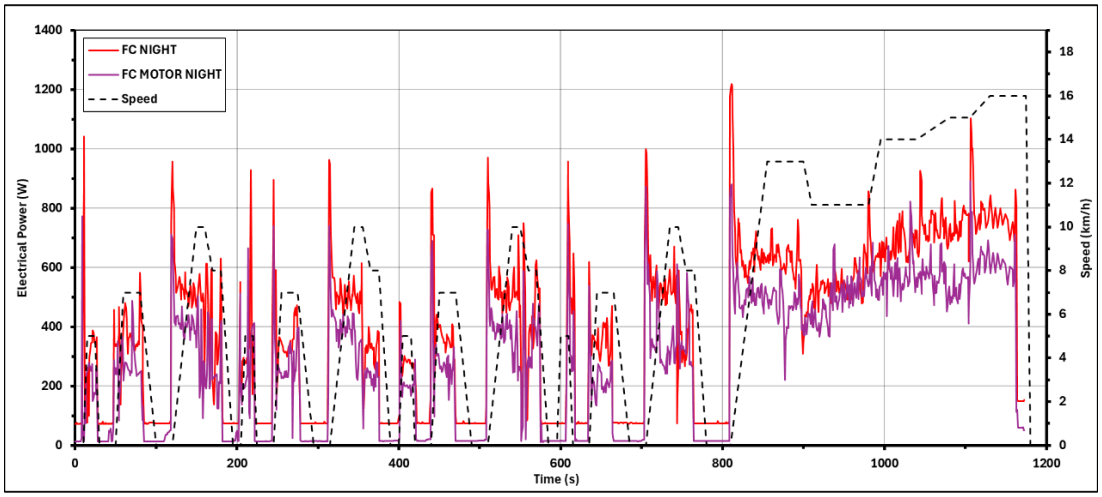

Figure 4.61 Power Profiles for the Fuel Cell Stack and the Traction Motor Corresponding to Scaled-Down NEDC – Nighttime Operation Without IHR

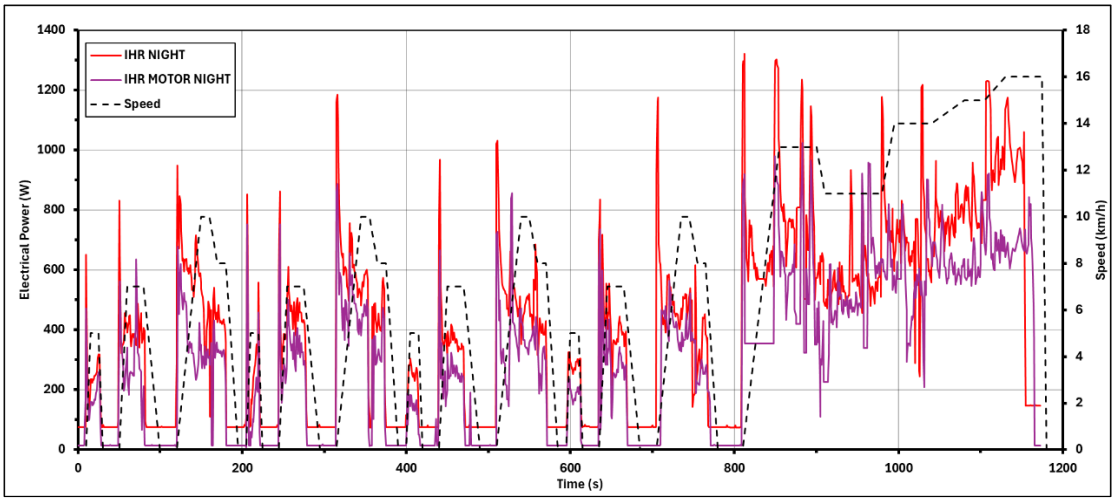

Figure 4.62 Power Profiles for the Fuel Cell Stack and the Traction Motor Corresponding to Scaled-Down NEDC – Nighttime Operation Using IHR

While the transient power traces provide a visual representation of the dynamic system response, evaluating the total accumulated energy provides a more reliable metric to ensure the test conditions remained consistent across the different evaluation days. Figure 4.63 and Table 4.4 present the total electrical energy generated by the fuel cell and utilised by the motor across all driving conditions. During the day evaluations, the baseline fuel cell generated 528.2 kJ, while the IHR configuration generated 533.7 kJ. The corresponding motor energy demands recorded 388.4 kJ and 390.9 kJ, respectively. Under the varying ambient night conditions, the baseline fuel cell produced 473.9 kJ and the integrated system produced 499.9 kJ, with the motor consuming 347.6 kJ and 360.0 kJ, respectively.

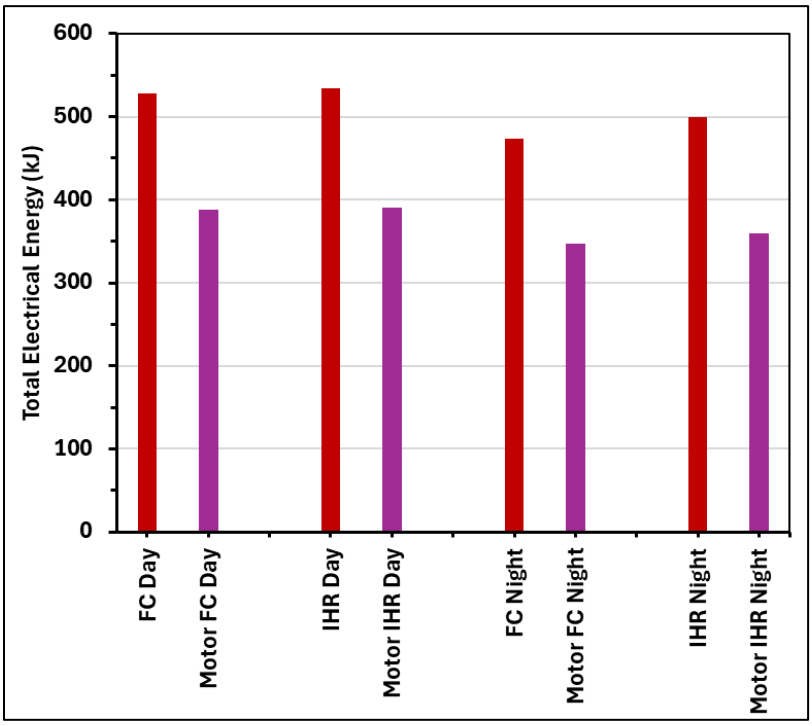

Figure 4.63 Total Fuel Cell Power Generation and Motor Power Consumption Across All Driving Conditions

Table 4.4
Statistical Verification Metrics Between Mean Fuel Cell and Motor Power Values Compared to Dynamic Profiles

Metric	Total Fuel Cell Energy	Total Motor Energy
Mean (kJ)	508.9	371.7
STD (kJ)	27.6	21.3
CV (%)	5.4	5.7
SE (kJ)	13.8	10.7
RSE (%)	2.7	2.9

To ensure these different on road test runs remain valid for direct comparison, statistical verification metrics were applied to the total energy dataset. Table 4.3 shows that the mean fuel cell energy across all evaluation cases recorded 508.9 kJ with a standard deviation (STD) of 27.6 kJ, yielding a small coefficient of variation (CV) of 5.4% and a relative standard error (RSE) of 2.7%. Similarly, the mean motor energy recorded 371.7 kJ with a standard deviation of 21.3 kJ, resulting in a coefficient of variation of 5.7% and a relative standard error of 2.9%.

These small statistical variances verify that the overall traction demand remained within a highly consistent and acceptable range across all testing iterations. The minor recorded deviations did not arise from systemic flaws but rather originated from unavoidable experimental uncertainties inherent to dynamic on-road testing. These dynamic variables include slight driver throttle variations to maintain the target speed, transient changes in ambient wind resistance, and minor road surface irregularities. Because the coefficient of variation and relative standard error confirm that the fundamental energy demand remained stable despite these environmental uncertainties, the dataset provides a reliable baseline for the subsequent detailed performance analyses.

4.4.2.2 Fuel Cell Electrical Performance

To effectively evaluate the electrical performance of the integrated architecture under highly transient on road conditions, the analysis was systematically partitioned into two distinct physical phenomena. The evaluation first examined the dynamic system response to the continuous vehicular load shifts, followed by an assessment of the fundamental thermodynamic capability of the fuel cell stack. The dynamic system response was quantified utilising discrete time average formulations based on the scaled NEDC speed profile time or duration (the speed and time duration presented on table 3.15 and figure 3.25), mapping exactly how the IHR system managed the electrical burden over the prolonged driving cycle. Subsequently, the fundamental thermodynamic capability was isolated by plotting the raw instantaneous electrical power against the drawn current, explicitly revealing the underlying electrochemical improvements independent of the vehicle momentum.

Figure 4.64 a and b presented the time average fuel cell electrical power across the scaled dynamic driving profile. An initial evaluation of this temporal data indicated that all four configurations successfully tracked the volatile traction demands. The electrical power dropped to approximately 75 W during the idling phases and spiked appropriately during the acceleration and highway cruising segments, confirming that the overarching control system remained stable. When comparing the specific architectures during the day time driving cycle, the data revealed that the IHR system generally required a lower peak fuel cell power to satisfy the vehicle traction demand

compared to the unconditioned baseline. For instance, during the final acceleration at 1130 seconds, the baseline fuel cell required 970 W, whereas the integrated system only demanded 868 W. This reduction likely occurred because the preheated hydrogen reactant successfully improved the internal electrochemical kinetics and mitigated activation polarisation. By operating at a higher internal efficiency, the integrated fuel cell satisfied the exact same vehicular kinetic demand while requiring a lower peak electrical power generation from the primary stack.

Conversely, the night time driving cycles exhibited a fascinating inverse behaviour. During the cold night time highway acceleration peaks at 1130 seconds, the integrated system generated a higher primary time average power of 897 W compared to the baseline output of 764 W. This specific phenomenon highlighted the severe impact of the environmental boundary on electrochemical kinetics. Cold ambient night air inherently suppresses internal reaction kinetics and exacerbates activation polarisation. The unconditioned baseline fuel cell struggled to produce sufficient power in this cold environment without suffering a severe voltage collapse. However, the integrated architecture successfully preheated the incoming hydrogen reactant, overcoming this cold weather penalty. This preheating rescue mechanism allowed the fuel cell to safely achieve higher power outputs to meet the kinetic demand, explicitly demonstrating that environmental weather conditions strictly dictate fuel cell dynamic performance. All the amendments are compiled in a separate file attached to this document.

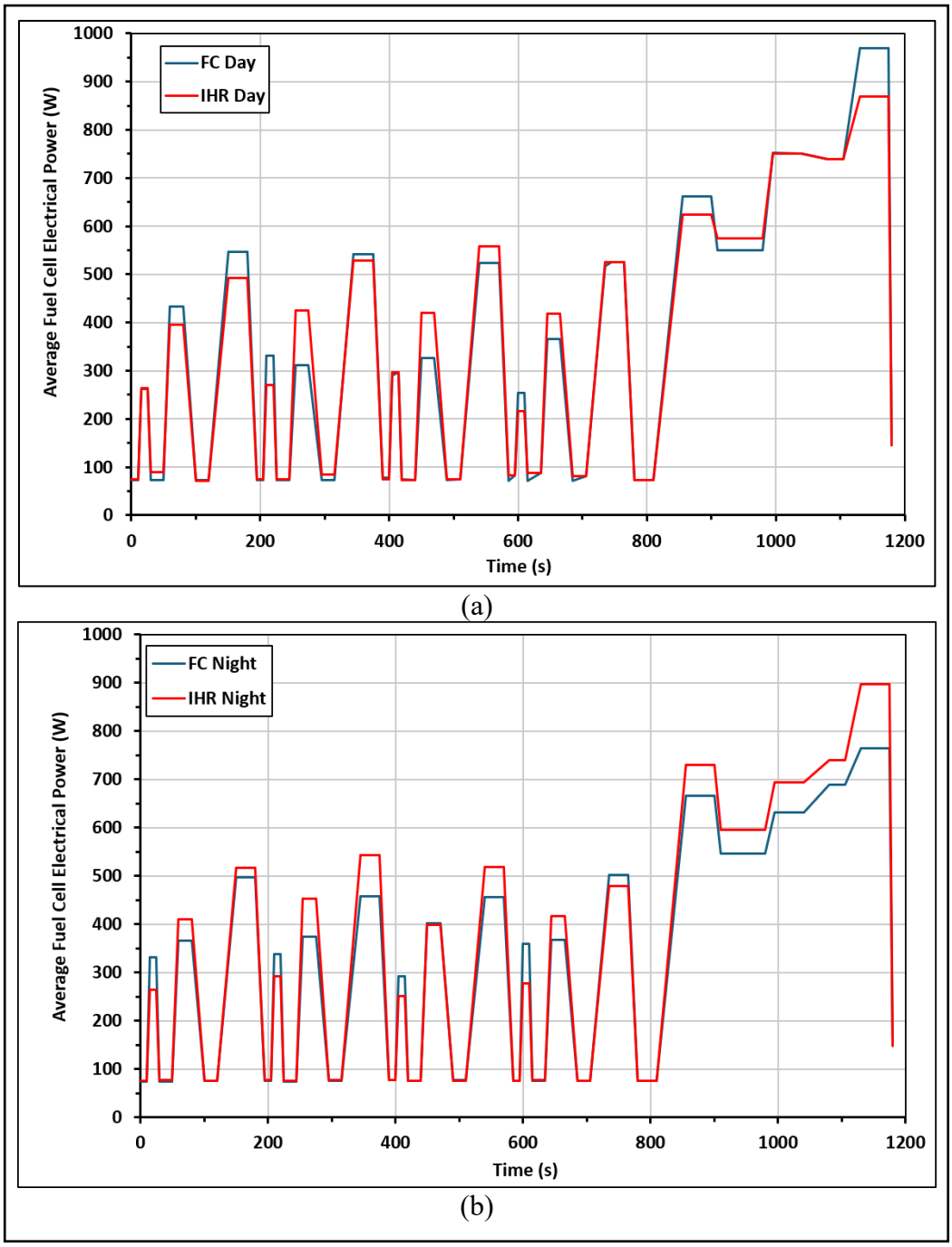

Figure 4.64 Average Fuel Cell Electrical Power for a) Day Driving Condition, b) Night Driving Condition

While the time average temporal data illustrated how the system dynamically shared the electrical burden, isolating the fundamental electrochemical efficiency required evaluating the raw power generation against the independent current draw. Figure 4.65 a and b displayed the fuel cell electrical power with respect to the drawn current for the day and night driving conditions. Although it might initially appear contradictory that the integrated system produced a lower time average power during

the day but consistently higher power on the performance curve, these two metrics measured completely different phenomena. The raw power versus current profiles isolated the intrinsic thermodynamic capability of the stack. Across all evaluated cases, the nonlinear trends demonstrated that the integrated system consistently produced higher electrical power capacity at any given high current load. Unlike the preliminary on-road analysis detailed in Section 4.4.1, which did not produce a sufficient dataset across the entire load spectrum, the dynamic speed driving cycle utilised here provided an extensive operational current span. This broad data collection established a highly mature pattern for direct evaluation. Consequently, the electrical analysis for this section did not require a normalized electrical profile to conduct a standardised fitted comparison. Across all evaluated cases, the raw data exhibited a distinct nonlinear profile. At low current demands, the power curves for the baseline fuel cell and the fuel cell integrated with the IHR system remained closely aligned. However, during high current operation, a clear performance gap emerges. The configurations utilising the integrated recovery system consistently generated higher electrical power than the baseline setups.

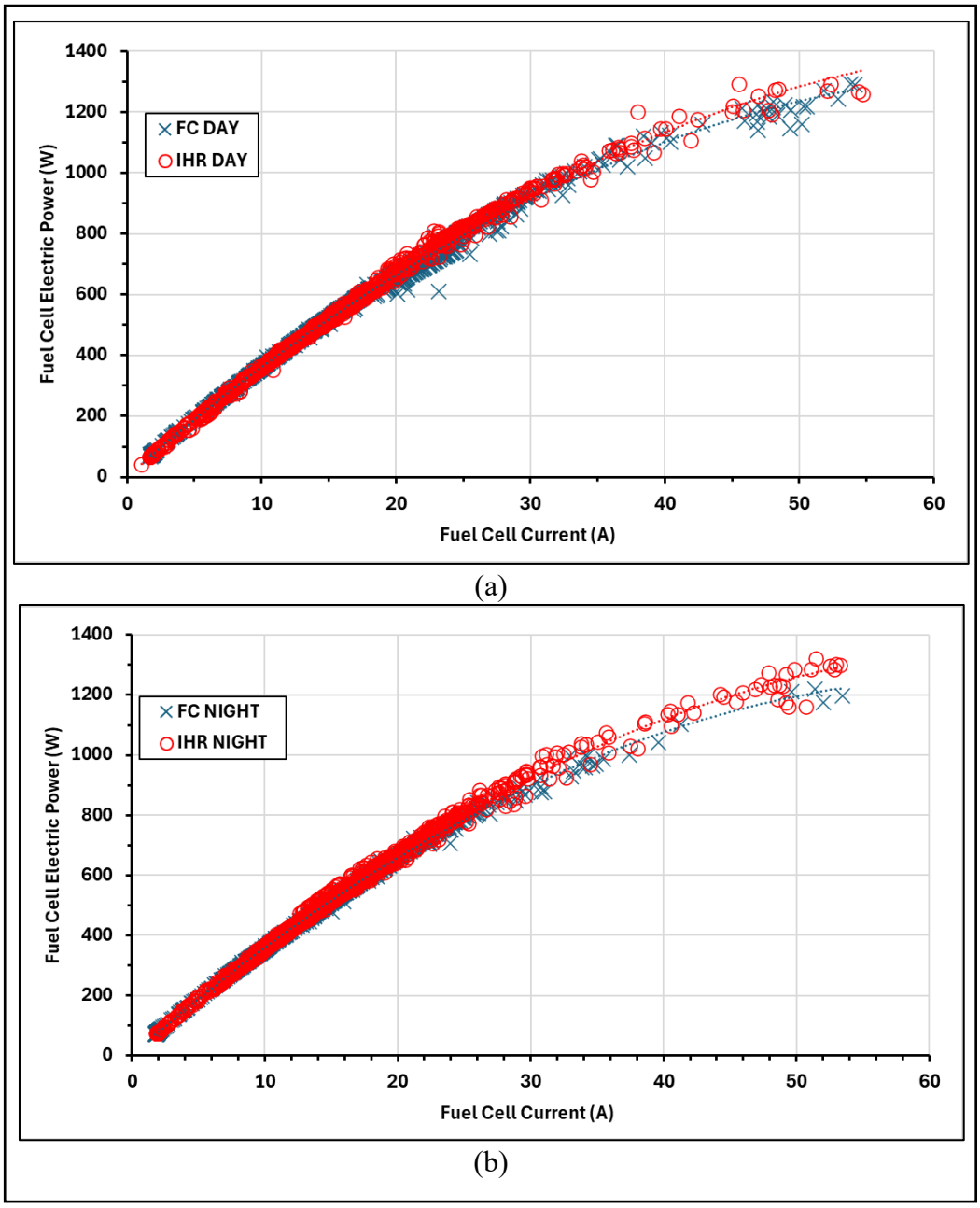

Figure 4.65 Fuel Cell Electrical Power Mapping Against Load Current for a) Day Driving Condition, b) Night Driving Condition

To further investigate this nonlinear relationship, Figure 4.66 and Figure 4.67 presents the corresponding polarization curves, which map the direct physical relationship between stack voltage, current, and total power output. The recorded data confirmed that the improved electrical power production originated from a measurable reduction in the internal voltage drop. As a fuel cell produces more electrical current, its voltage potential inevitably drops due to inherent activation and ohmic resistances. The polarization profiles demonstrated that the IHR cases successfully maintained a

higher operational voltage at equivalent current demands. For example, during the daytime evaluation at the peak 60 A load, the baseline fuel cell recorded 21.9 V and produced 1313.7 W, whereas the IHR configuration maintained 23.0 V to produce 1381.0 W. This behaviour became even more evident during the nighttime evaluations. At the same 60 A boundary, the nighttime baseline fuel cell dropped to 20.9 V delivering 1255.1 W, while the IHR system preserved 22.4 V to output 1343.0 W.

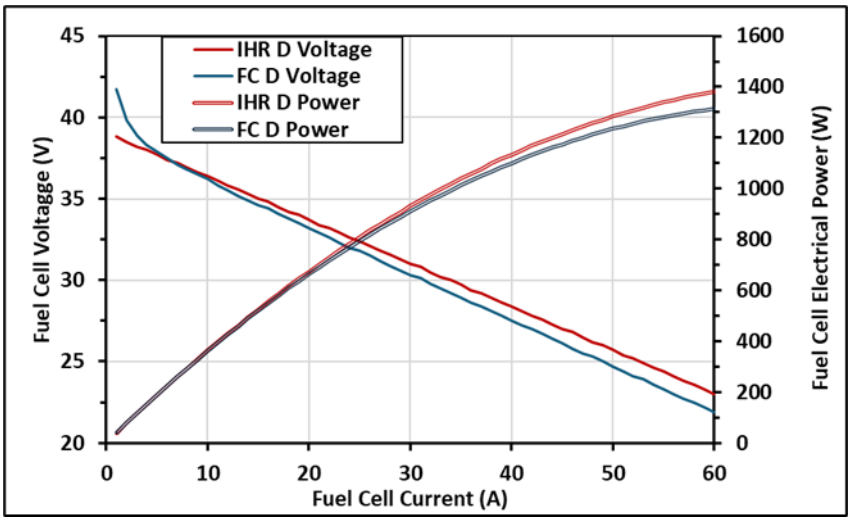

Figure 4.66 The Polarization Curves of the Fuel Cell Stack With and Without IHR During Daytime Operation

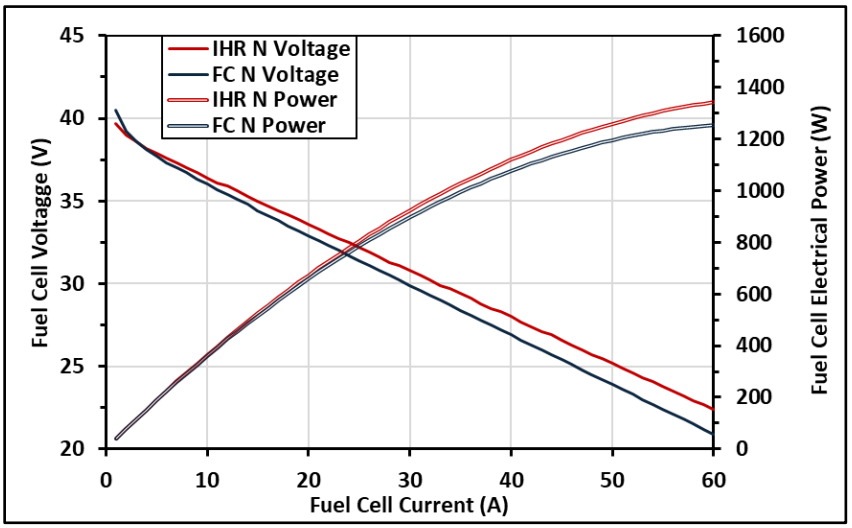

Figure 4.67 The Polarization Curves of the Fuel Cell Stack With and Without IHR During Nighttime Operation

Figure 4.68 quantifies this performance separation by plotting the electrical power improvement percentage. The data revealed a nonlinear increasing trend for the power increment as the current demand escalated. Furthermore, the magnitude of this

improvement varied between the environmental conditions. During the daytime evaluations, the power increment expanded continuously to achieve a maximum of 5.1% at 60 A. In contrast, the nighttime evaluations demonstrated a stronger response, reaching a maximum increment of 7.0% at 60 A.

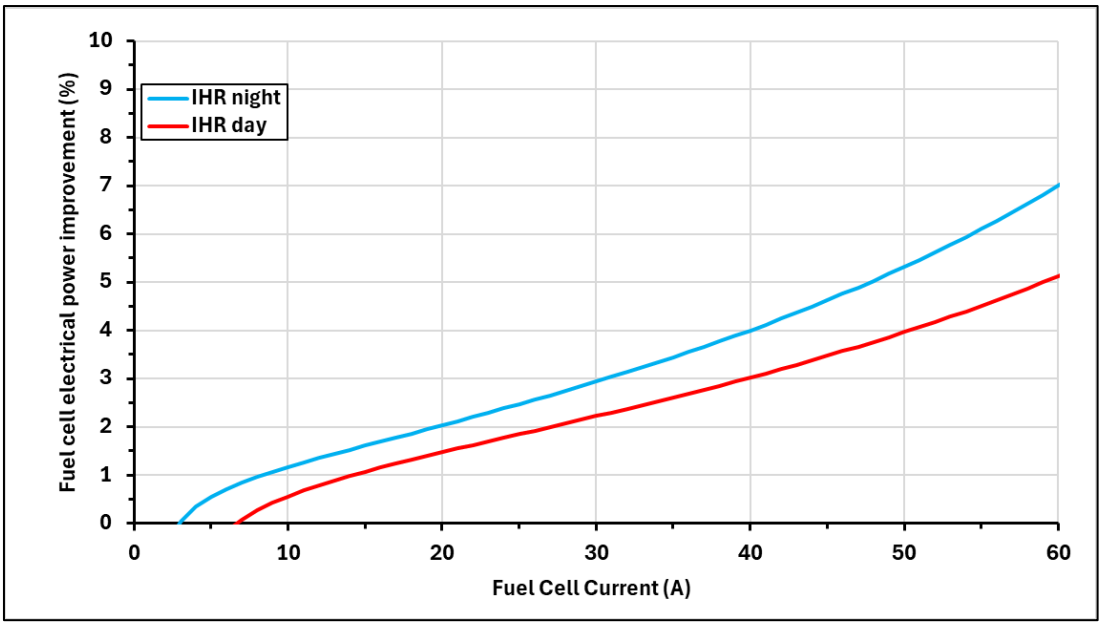

Figure 4.68 Electrical Power Improvement Percentage From the Application of IHR

The wider performance gap and higher power generation observed during the nighttime cycles indicate that cooler ambient conditions provide a more favourable thermal boundary for the recovery system. This cooler external environment likely established a steeper temperature gradient across the internal heat exchanger components. A stronger thermal driving force allows the system to absorb waste heat more aggressively from the exhaust stream and transfer it into the incoming hydrogen gas, which explains the higher magnitude of the power increments during the night evaluations.

From an electrochemical perspective, this performance improvement aligns with fundamental reaction kinetics. Elevating the temperature of the hydrogen reactant before it enters the anode lowers the internal activation energy required to initiate the electrochemical reaction. This physical mechanism directly mitigates activation polarization. Consequently, the fuel cell can sustain a higher operational voltage even as the current density increases. By preserving this voltage potential and supplying up to seven percent more electrical power at peak demand, the integrated system generates more usable energy from the exact same mass of hydrogen consumed. While these

physical interactions remain naturally susceptible to minor transient thermal lag and environmental noise inherent to dynamic on road testing, this sustained electrical enhancement provides the foundational evidence required to evaluate the subsequent fuel consumption and total system efficiency.

4.4.2.3 Fuel Cell with IHR Systems Thermal Analysis

This section provides a compact and exact evaluation of the physical thermal dynamics within the integrated architecture, progressing from the internal temperature distribution mapping to the transient fuel cell heat generation.

Figure 4.69 presents the dimensionless temperature profile across the fuel cell and the integrated heat recovery system. The measurement methodology mirrors the approach utilised in Section 4.4.1. The baseline fuel cell evaluations utilised only two primary measurement locations, whereas the configurations featuring the integrated system incorporated ten specific measurement points. The thermal mapping starts at point 1 which was located at the stack air intake. The fuel cell generated heat was transferred to the exiting air and was measured at point 2 at the fuel cell exhaust. This exhaust served as the primary heating source for the IHR system. The thermal energy enters the hot chamber and point 3 records the hot stream temperature immediately before it transferred its heat to the internal hot fins and the hydrogen tube passes. Points 4 and 5 provides the intermediate component temperatures leading to the solid-state thermoelectric generator surfaces. Point 6 measures the hot side surface of the TEG, while point 7 records the cold side surface. The remaining thermal energy was subsequently transferred to the cold chamber, where a series of heat pipes and cold fins conducted the heat toward the final rejection boundary, measured across points 8 and 9, before dissipating into the ambient cruising air at point 10.

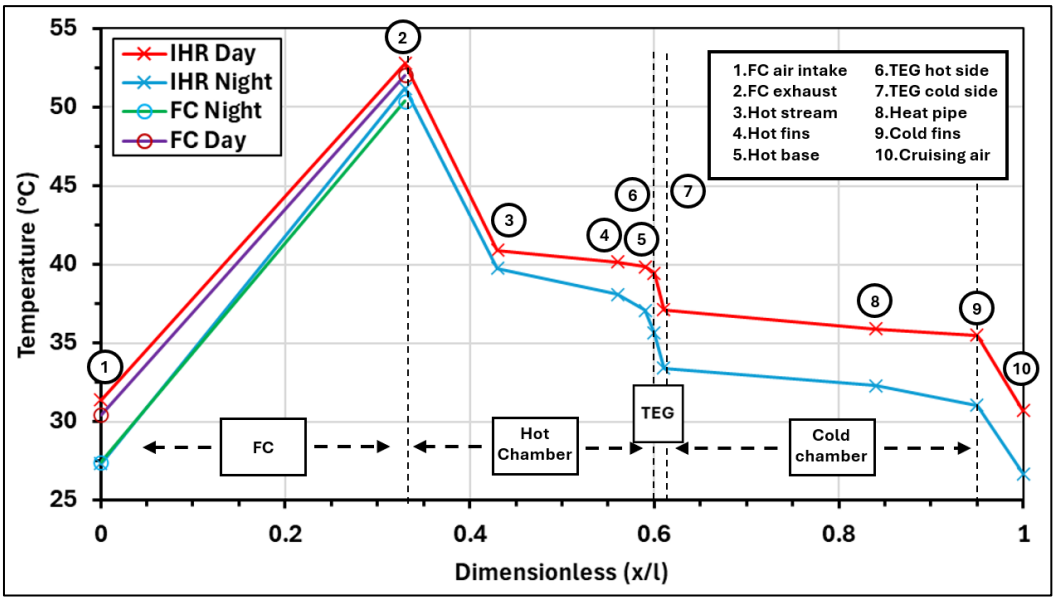

Figure 4.69 Fuel Cell and IHR System Dimensionless Temperature Profile for All Cases

The plotted profiles reveal a substantial thermal loss occurring immediately after the fuel cell exhaust. Consistent with the laboratory test bench observations, an approximate 50% temperature drop occurred between the heat source at point 2 and the hot chamber inlet at point 3. This severe temperature degradation indicates significant conductive thermal resistance and inadequate physical insulation along the connection boundary. Consequently, the maximum temperature generated from fuel cell did not reach the high load conditions observed during the constant load on-road test as discussed in section 4. 4. 2 but rather aligns closer to the lower load conditions which are 1p and 2s conditions. In contrast, the temperature gradient from point 3 to point 6 remained small, indicating efficient heat conduction through the internal hot fins. Within the cold chamber, the system demonstrated effective heat removal from point 7 to point 9 with a minimal temperature gradient, followed by a larger gradient between point 9 and point 10 as the heat rejected into the fluctuating ambient air. Comparing the environmental conditions, the nighttime evaluations displayed overall lower temperature profiles, directly reflecting the cooler boundary condition where the ambient temperature was approximately 4 °C lower than the daytime equivalent.

The calculated transient fuel cell thermal power generation was plotted in Figure 4.70 and Figure 4.71. The maximum heat generation consistently occurs during the extra urban driving cycle phase. During this phase, the higher vehicle speed demanded a greater electrical production from the fuel cell to power the traction motor. However,

distinct behavioural differences emerged during the urban driving phases. For the daytime conditions, the heat generation peaked during every initial third speed phase of the urban cycle, as the third speed represented the highest velocity demand. In contrast, during the nighttime evaluations, the thermal peaks primarily occurred on the second and fourth phases corresponding to the highest speed demands. The only exception was the nighttime baseline fuel cell, where the heat generation peaks remained almost constant across every initial speed increase. Crucially, these peak fluctuations were exclusively observed during the vehicle acceleration phases. This occurred because the electrical demand spiked momentarily to overcome vehicle inertia and rolling resistance to acquire the targeted speed.

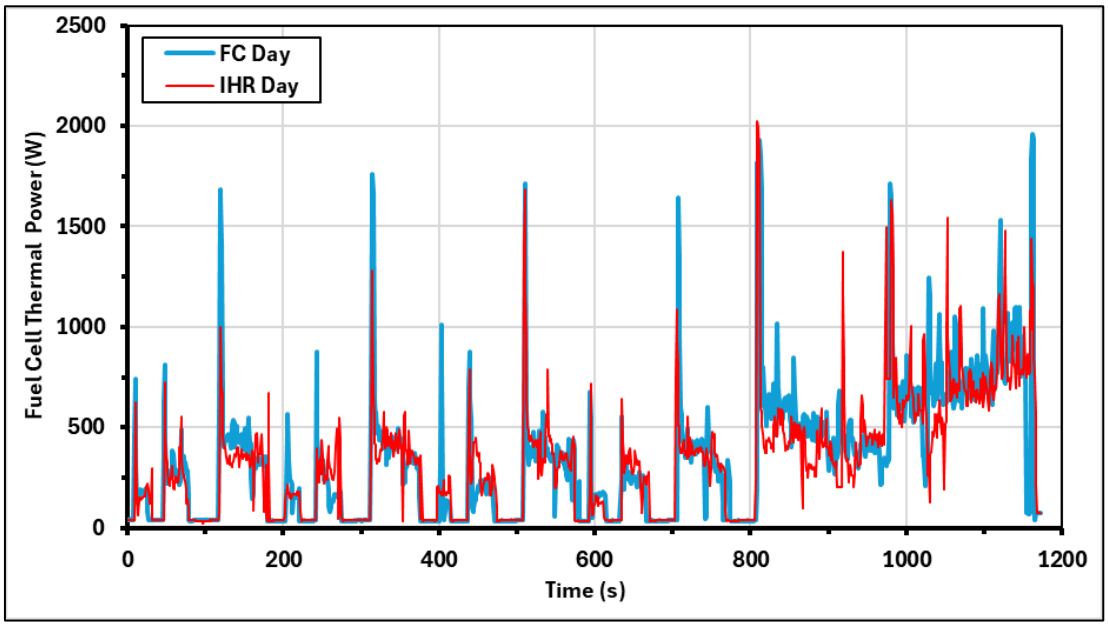

Figure 4.70 Fuel Cell Thermal Power for Night Cases

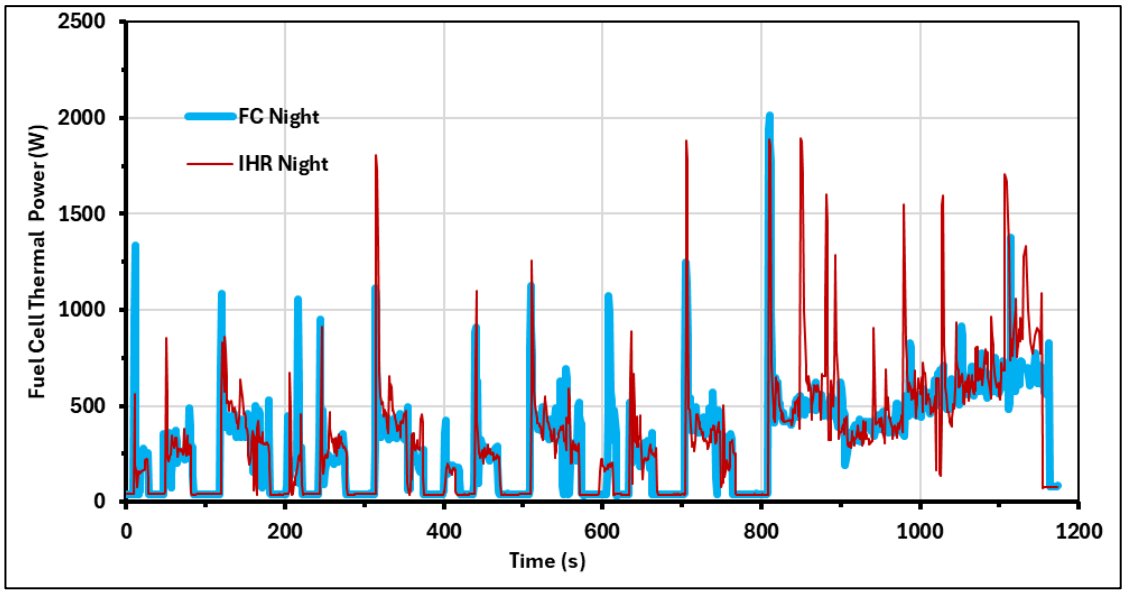

Figure 4.71 Fuel Cell Thermal Power for Day Cases

These dynamic fluctuations culminate in the total thermal energy variations presented in Figure 4.72. The daytime evaluations recorded the highest total generated heat, with the baseline fuel cell producing 432.7 kJ and the integrated system producing 418.4 kJ. During the cooler nighttime conditions, the total thermal energy dropped, recording 370.6 kJ for the baseline case and 397.7 kJ for the integrated case. The daytime baseline fuel cell registered the highest total thermal energy because it operates under warmer ambient conditions and experiences frequent and higher peaks during the transient acceleration phases.

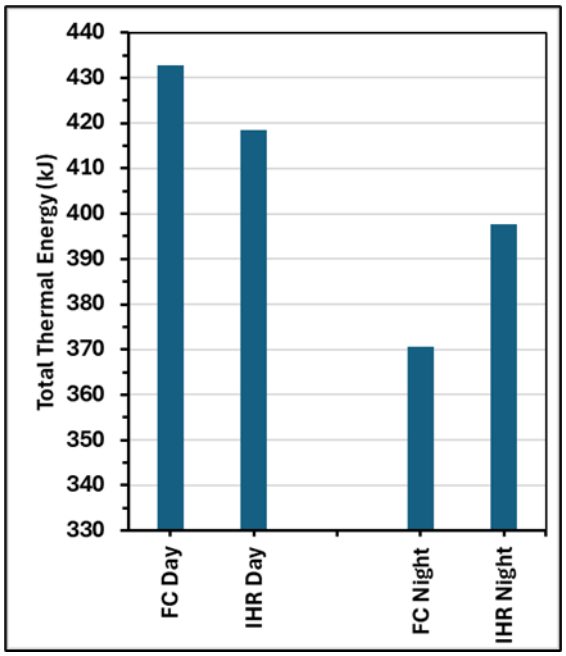

Figure 4.72 Total Thermal Energy Generated by the Fuel Cell for All Cases

4.4.2.4 Hydrogen Preheating Analysis

This subsection evaluates the thermal conditioning of the reactant gas, analysing the specific inlet temperatures, the elevated outlet temperatures, the resulting temperature difference, and the total heat energy absorbed by the hydrogen stream.

Figure 4.73 illustrates the transient temperature profiles for the reactant gas entering and exiting the IHR. The inlet temperatures remain relatively stable throughout the physical evaluations, dictated primarily by the external storage conditions. The daytime driving cycles recorded an approximate inlet temperature of 30 °C, whereas the cooler nighttime conditions provide a lower inlet baseline of approximately 27 °C. As the gas traversed the internal heating chamber, the outlet temperatures exhibit a distinct nonlinear ascending profile for both environmental cases. However, the initiation of this thermal elevation varied. During the nighttime evaluations, the outlet temperature began to rise early in the drive cycle, prior to 200 seconds during the first ECE-15 driving phase. Conversely, the daytime operation experiences a greater initial thermal lag and delaying any substantial outlet temperature increment until approximately 300 seconds during the second ECE-15 phase. Ultimately, the daytime outlet achieves a maximum temperature approaching 39 °C, while the nighttime equivalent was approximately 36 °C.

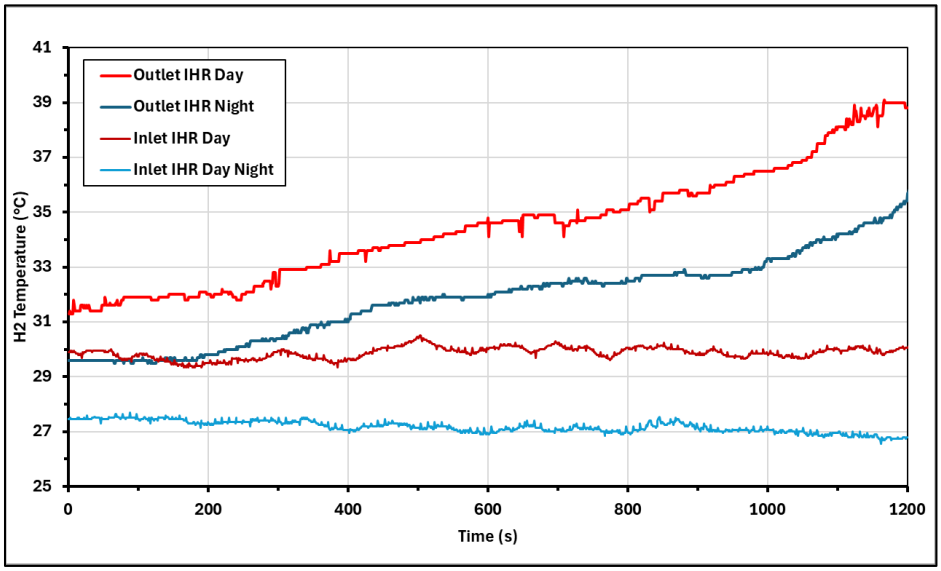

Figure 4.73 Hydrogen Temperature Profiles at the IHR Inlet and Outlet Across All Cases

To accurately quantify the effectiveness of the thermal conditioning, Figure 4.74 presents the preheated hydrogen temperature difference, representing the exact thermal elevation achieved between the inlet and the outlet. The transient progression of this thermal difference divides into three distinct temporal segments. The first segment, spanning from the start of the test to 200 seconds, displayed the lowest ascending gradient. During this initial period, both environmental conditions exhibited similar thermal resistance as the physical components required time to overcome their inherent thermal inertia. The second segment, spanning from 200 seconds to 800 seconds, revealed a clear divergence. The nighttime operation demonstrated a higher temperature difference during this intermediate phase, indicating that the cooler ambient boundary established a stronger initial thermal gradient, allowing the system to extract waste heat more efficiently.

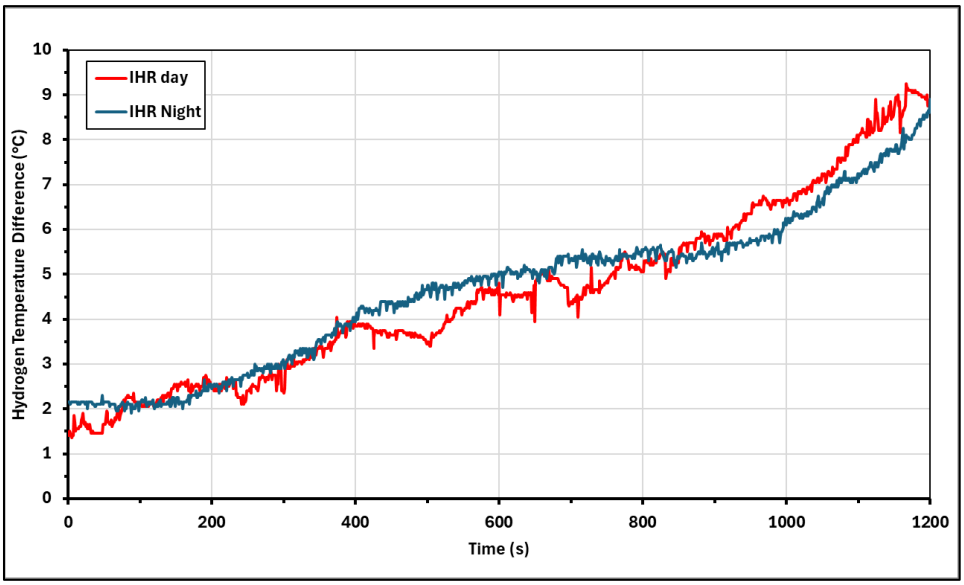

Figure 4.74 Hydrogen Temperature Difference For All Cases

The third segment, from 800 seconds to the conclusion of the test at 1200 seconds, corresponded with the EUDC phase. Because this phase demands higher vehicle speeds and generates substantial waste heat, the temperature difference profile exhibited its steepest increasing gradient. Interestingly, during this final high load segment, the daytime temperature difference surpassed the nighttime profile. The daytime evaluation achieved a peak hydrogen temperature difference of approximately 9 °C, slightly exceeding the 8.9 °C recorded at night. This specific crossover likely originates from the physical thermal mass of the recovery components. Over the extended 800 second preliminary driving period, the warmer daytime ambient environment allowed the external assembly to accumulate and retain more latent heat. In contrast, the cooler nighttime air continuously stripped residual heat away from the external casing. Consequently, when the massive surge of waste heat arrived during the EUDC phase, the daytime system possessed a warmer physical baseline, transferring slightly more energy into the gas stream.

Figure 4.75 tracks the transient thermal power absorbed by the hydrogen. The data shows a continuous increasing trend as the ECE-15 cycles progressed. Even though each ECE-15 cycle repeated the exact same speed pattern, the heat absorption climbed progressively, further confirming that the integrated system requires prolonged continuous operation to fully saturate its thermal mass. The absorption peaked

significantly during the EUDC phase due to the maximum availability of the high temperature exhaust source.

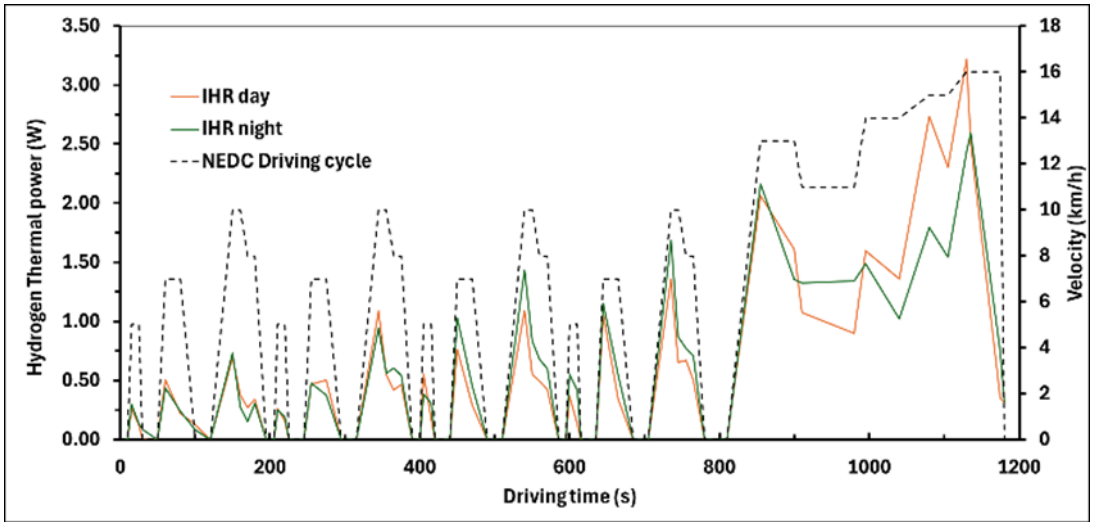

Figure 4.75 Hydrogen Preheating Power Responses Corresponding to Dynamic Drive Cycles

Despite these transient fluctuations where the daytime configuration showed slightly higher absorption peaks near the 1000 second mark, the cumulative performance remained remarkably consistent. Figure 4.76 details the total preheated energy transferred into the hydrogen stream. The absolute difference between the two environmental conditions was exceedingly small, recording less than a single Joule of variation. The nighttime evaluations transferred a total of 791.5 J into the reactant gas, while the daytime evaluations recorded 791.0 J. This minor deviation falls entirely within standard experimental error boundaries and sensor measurement noise. This ultimate parity indicates that while external ambient temperatures influence the transient thermal response and the initial heating delays, the total thermal capacity of the hydrogen stream was strictly constrained by its low physical mass flow rate. The system consistently maximizes the possible heat transfer regardless of minor environmental variations, confirming the reliability of the passive preheating architecture under dynamic on road conditions.

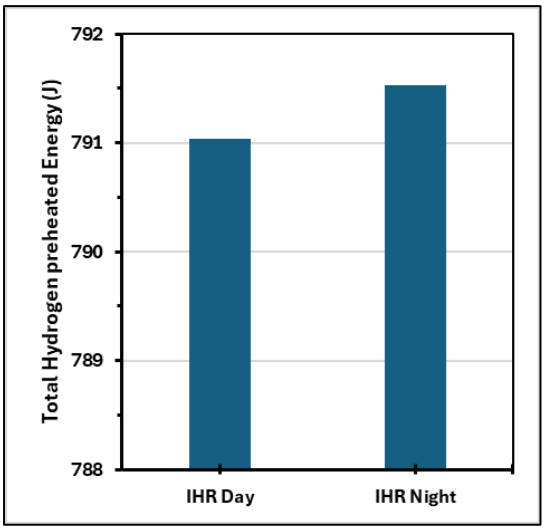

Figure 4.76 Total Thermal Energy Absorbed by the Hydrogen During Preheating

4.4.2.5 Hydrogen Fuel Consumption

This subsection investigates the reactant utilization characteristics during the dynamic driving cycles. The evaluation covers the transient volumetric flow rates, the resultant pressure differential within the storage tank, the absolute fuel mass consumed, and the normalized fuel economy per kilometre.

Figure 4.77 and Figure 4.78 presents the transient hydrogen volumetric flow rate profiles for the daytime and nighttime evaluations, respectively. Across all test configurations, the reactant flow consistently peaks during the initial acceleration phase to acquire a targeted speed. This behaviour occurs because accelerating from a stationary position demands maximum electrical power to overcome the vehicle static inertia and the mechanical rolling resistance of the lightweight buggy platform. Conversely, the dynamic data revealed that subsequent speed adjustments from a moving state did not provoke similar massive fuel surges. Because the moving vehicle retains physical momentum, dropping from a higher cruising speed to a lower speed, or accelerating slightly while already in motion, require substantially less traction power. For example, during the ECE-15 driving phase, accelerating from a standstill to 10 km/h generated a peak fuel demand exceeding 9 l/m. However, decelerating from 10 km/h to 8 km/h demanded less than 6 l/m, representing a lower fuel requirement than launching from a static position to merely 7 km/h. This physical momentum effect was equally evident during the EUDC phase. Decelerating from 13 km/h to 11 km/h require minimal reactant flow and subsequent continuous accelerations from 11 km/h to 14 km/h and

then to 15 km/h proved less demanding than a static launch, maintaining a flow rate below 8 l/m.

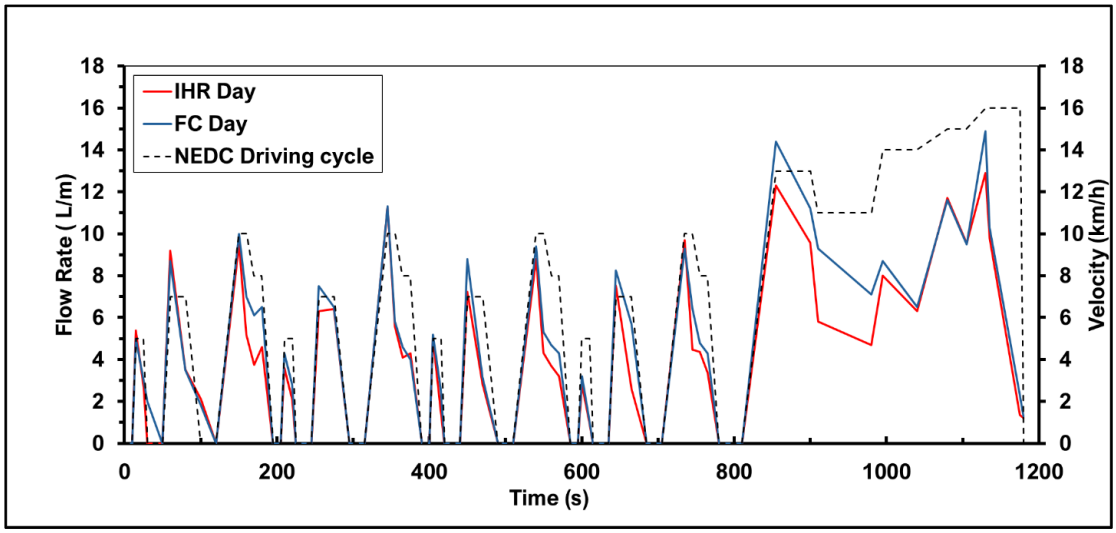

Figure 4.77 Transient Hydrogen Fuel Flow Rate for Daytime

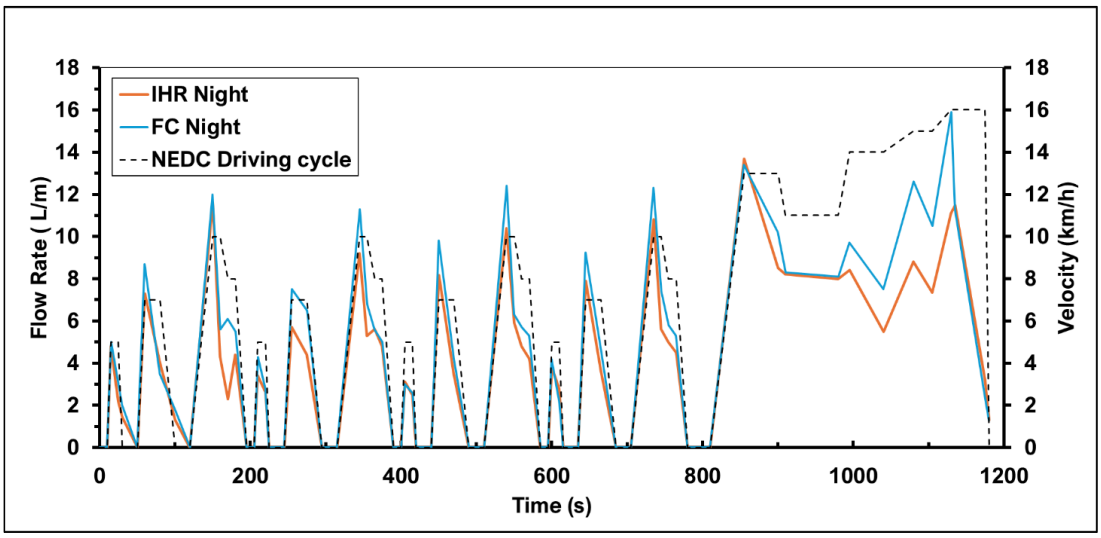

Figure 4.78 Transient Hydrogen Fuel Flow Rate for Nighttime

Comparing the environmental conditions, the nighttime driving cycles consistently elicited higher transient flow rates than the daytime equivalents. During the ECE-15 phase, the daytime flow peak reached 11 l/m, whereas the nighttime peak escalated to 12 l/m. This gap widened slightly during the high speed EUDC segment, where daytime maximums remained below 15 l/m while the nighttime demand touched 16 l/m. Crucially, across both environmental boundaries, the configurations equipped with the IHR system demonstrated a distinctly lower fuel demand than the baseline fuel cell. This performance separation became especially clear during the continuous high

loads of the EUDC phase, indicating that the preheated hydrogen successfully sustained the required electrical output while drawing less raw fuel.

This transient flow rate relates directly into hydrogen tank pressure change as in Figure 4.79 showing the total pressure drop within the tank. During the daytime evaluations, the baseline fuel cell caused a total pressure reduction of 19 bar, whereas the integrated recovery system restricted this drop to 16 bar. The nighttime evaluations mirrored this conservation trend, recording an 18 bar pressure drop for the baseline setup, and a 15 bar drop for the recovery configuration. In both scenarios, the thermal conditioning architecture successfully conserved approximately 3 bar of storage pressure over the brief 2.6 km driving distance.

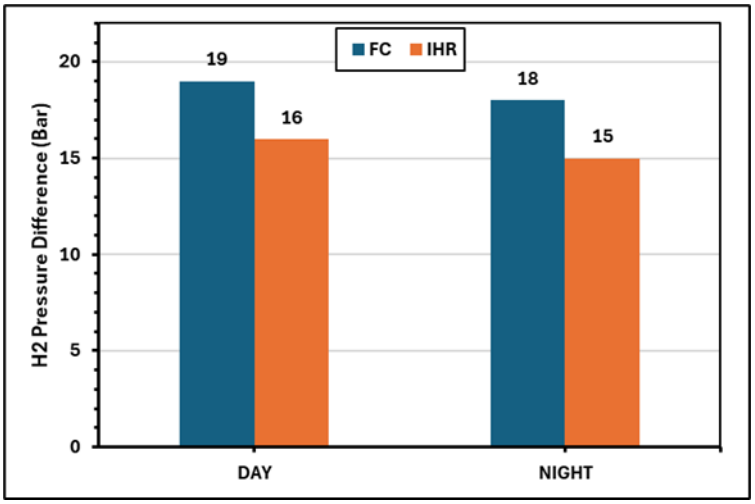

Figure 4.79 Hydrogen Tank Pressure Dropped Under Different Test Configurations

To provide a definitive quantitative metric, Figure 4.80 (a) and (b) displays the converted fuel consumption in absolute grams and normalized grams per kilometre. During the daytime tests, the baseline fuel cell consumed a total of 13.6 g of hydrogen, translating to an economy of 5.2 g/km. The integrated system improved these metrics to 11.5 g and 4.4 g/km, respectively. Under nighttime conditions, the baseline configuration utilised 13.0 g equating to 5.0 g/km, while the integrated system reduced the consumption to 10.9 g or 4.2 g/km.

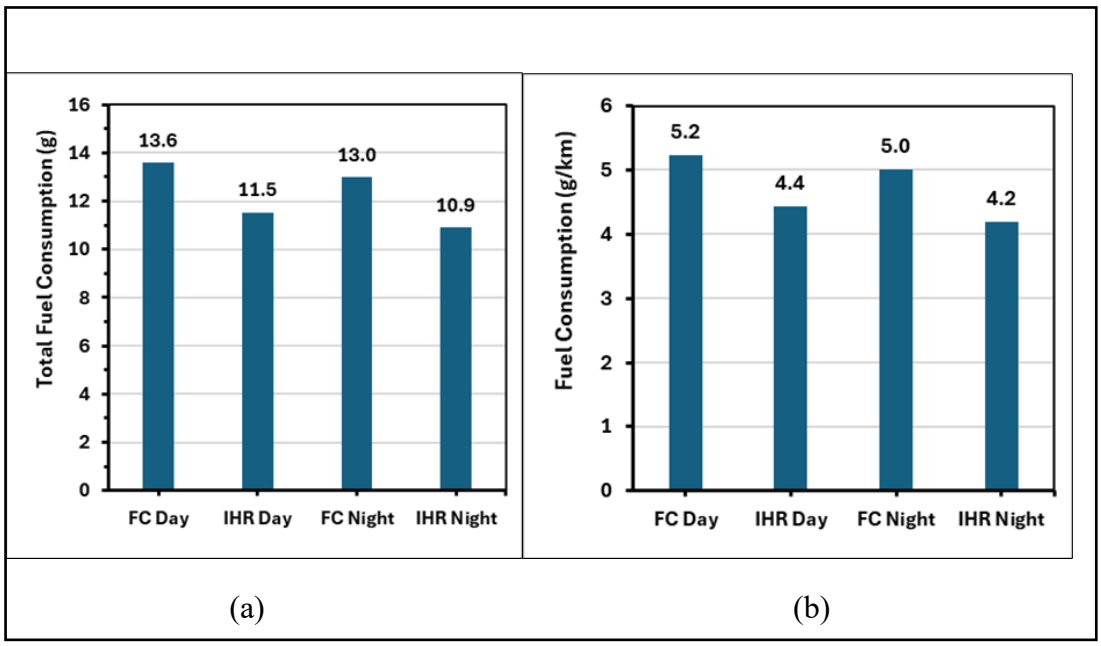

Figure 4.80 Fuel Cell Fuel Consumption, (a) Total Hydrogen Consumption, and (b) Fuel Economy Per km Distance

These quantitative reductions provide robust physical evidence that preheating the reactant gas fundamentally improves electrochemical fuel utilization. By lowering the internal activation energy barriers, the fuel cell extracts a higher magnitude of electrical power from every molecule of hydrogen supplied. While dynamic on road testing inherently includes minor measurement noise from mechanical vehicle vibrations and flow sensor sensitivity, the consistent reduction in both total mass and per kilometre consumption confirms the capability of the passive recovery architecture to enhance the overall fuel economy of lightweight vehicles.

4.4.2.6 TEG Performance Analysis

This subsection evaluates the secondary energy recovery mechanism, providing a systematic discussion that progresses from the transient TEG surface temperatures and their resulting temperature differences to the total heat transfer and ultimate electrical power generation.

Figure 4.81 presents the transient TEG surface temperatures alongside the calculated temperature difference between the hot and cold boundaries. The empirical data indicates that the environmental conditions produce two distinct operational domains. The daytime condition operates within an upper bound temperature profile, initiating from a stagnant ambient baseline of 32 °C. Conversely, the nighttime

condition operates within a lower bound profile, starting at an approximate 28 °C baseline.

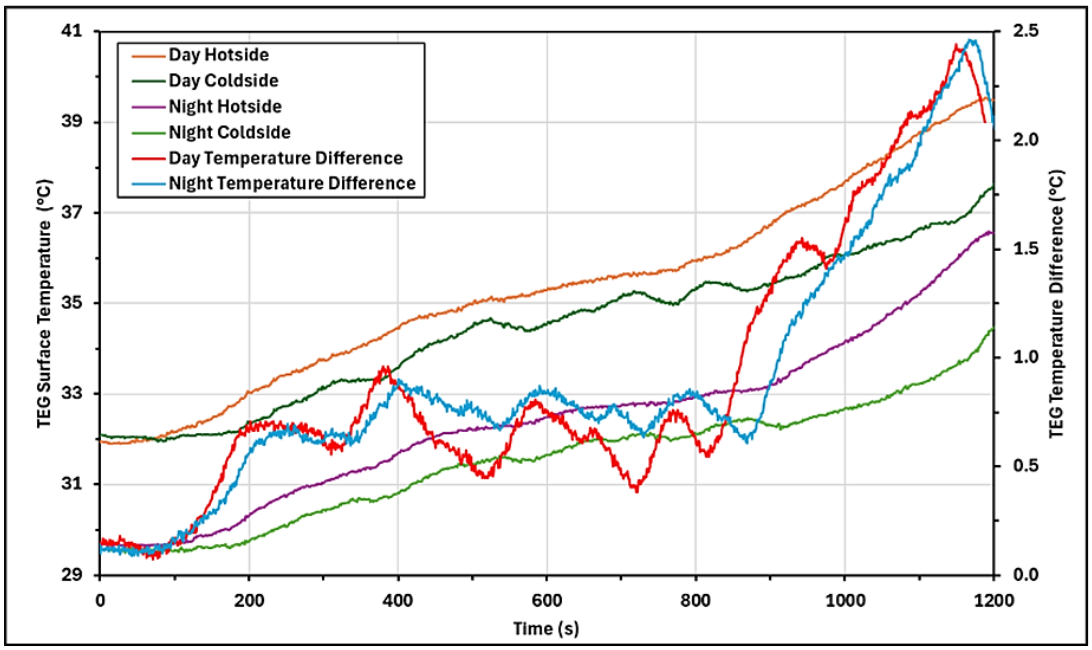

Figure 4.81 Transient TEG Surface Temperature and Difference

Despite these divergent starting points, the thermal difference for both cases exhibits a nearly similar nonlinear increasing trend. During the initial 50 seconds, the surface temperatures remain largely stagnant as the physical system absorbs the preliminary waste heat. From 50 seconds until 800 seconds, the temperature difference increased gradually during the ECE-15 driving phase, recording a narrow thermal gap of not more than 1 °C for both environmental cases. Following a short vehicle stop, a steeper inclination emerges as the higher load demands of the EUDC phase supplied a massive surge of high temperature exhaust. During this demanding phase, the temperature difference expanded considerably, spanning from 0.5 °C to a maximum of 2.4 °C. This high load phase generates maximum hot side temperatures of 39 °C for the day and 36 °C for the night, with corresponding cold side maximums reaching 37 °C and 34 °C. As the vehicle stops at 1180 seconds to complete the NEDC cycle, the overall temperature difference decreased rapidly. During this stall, the data captured a sudden temperature increment on the cold side, directly reflecting the immediate loss of forced ambient convection when the vehicle ceased its forward motion. The nonlinear upward trend observed in the temperature difference directly dictates the TEG heat transfer and electrical power production, as plotted in Figure 4.82 and Figure 4.83, respectively. The

system response was categorized into four distinct temporal stages. The initial stage, from 0 to 180 seconds, experiences stagnant heat transfer and generates almost zero electrical power due to the inherent thermal lag of the solid-state modules. The second stage, spanning from 180 to 850 seconds, corresponds with the dynamic ECE-15 cycle. During this phase, where the temperature difference remains constrained below 1 °C, the transient vehicle accelerations produced fluctuating heat transfer profiles that generated corresponding electrical power fluctuations.

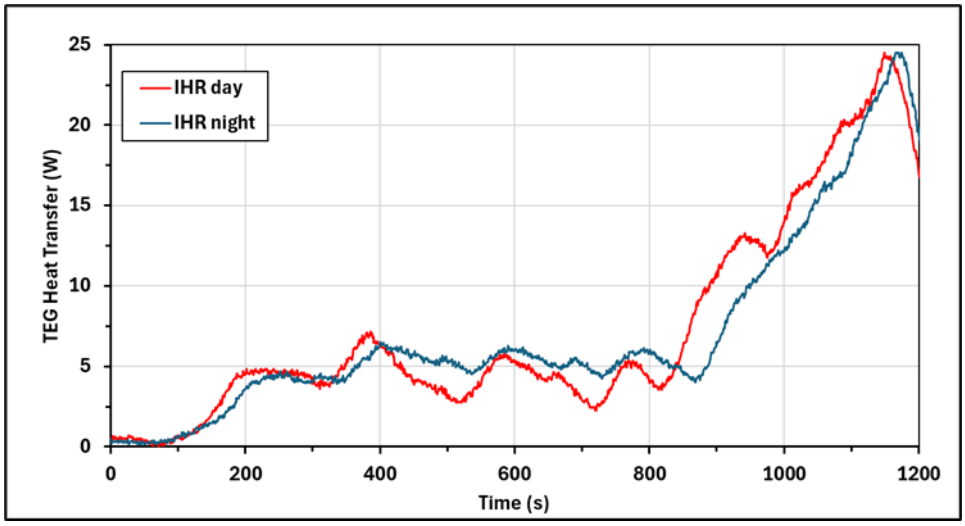

Figure 4.82 Transient TEG Heat Transfer

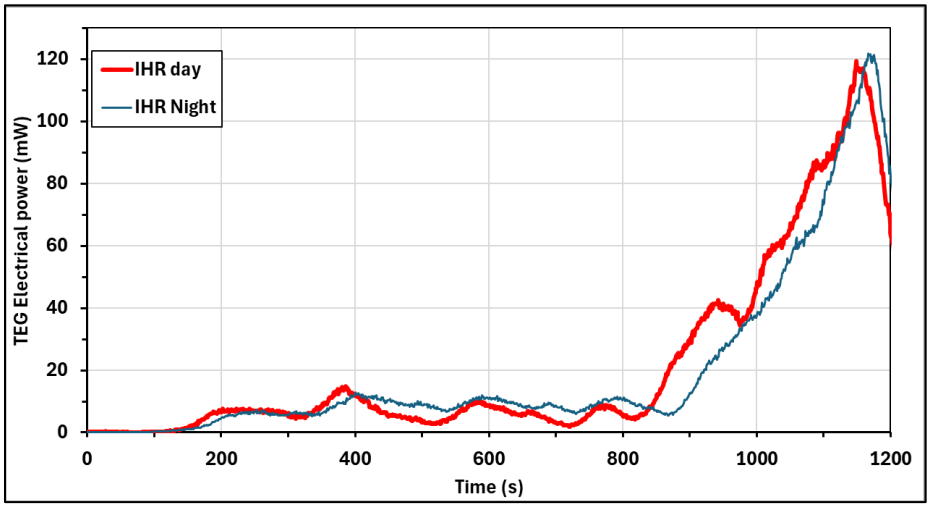

Figure 4.83 Transient TEG Electrical Power

These intermediate variations, maintained within a threshold of 2.5 W to 7.5 W for heat transfer, generates between 1 mW and 16 mW of electrical power. The third stage, occurring from 850 to 1180 seconds, aligned with the demanding EUDC phase.

Because the sustained high speeds and maximum waste heat availability drove the temperature difference up to 2.4 °C, this stage exhibits a sharp continuous increment. Within this 230 second window, the heat transfer escalated from 5 W to 24 W, while the electrical power generation surged from 5 mW to 120 mW. The final stage, from 1180 to 1200 seconds, recorded a steep decay in both metrics as the vehicle stalled and the thermal source diminished.

The cumulative energy metrics, detailed in Figure 4.84 and Figure 4.85, reveal that the TEG produce remarkably similar outputs across both environmental conditions. The total TEG heat transferred recorded 8.8 kJ for the daytime evaluation and 8.4 kJ for the nighttime evaluation. Consequently, the total electrical power production reached 8.8 Wh during the day and 8.1 Wh at night. This fundamental similarity indicates that absolute ambient temperature was not the primary determinant of TEG performance but rather, the specific temperature difference maintained across the module surfaces drives the power generation.

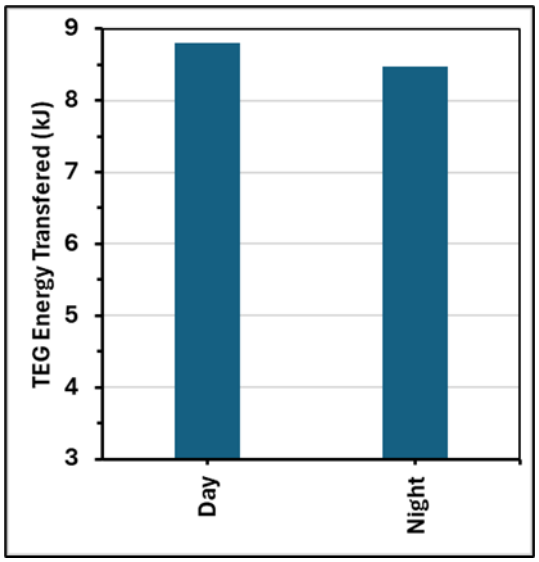

Figure 4.84 Total TEG Heat Transferred

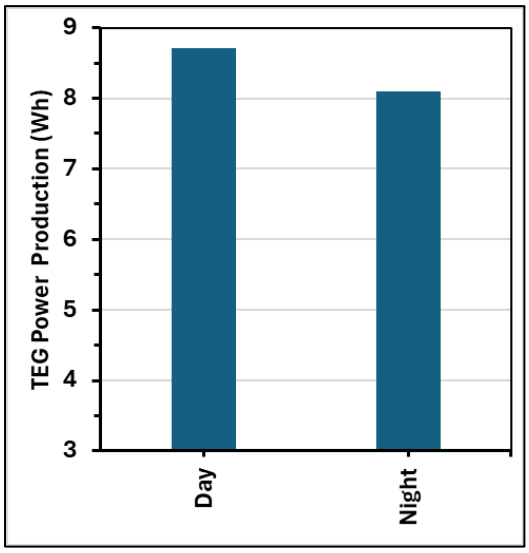

Figure 4.85 Total TEG Power Produced

While the lower ambient was expected to suggest that cooler nighttime air would provide a superior cold side heat sink and thus higher electrical generation, the empirical data demonstrated a minimum five percent power increment during the daytime operation. This physical anomaly likely originates from conductive heat losses occurring before the exhaust reaches the recovery chamber. During the cooler nighttime operation, the colder ambient air aggressively strips thermal energy from the external piping and the fuel cell manifold. By the time the exhaust stream physically reaches the TEG hot side, it has already lost a measurable fraction of its thermal potential. In contrast, the warmer daytime environment reduces this premature parasitic heat loss, allowing a slightly larger volume of thermal energy to reach the internal hot fins. While dynamic testing inherently involves minor sensor measurement uncertainties and unavoidable environmental noise, this consistent daytime advantage suggests that minimizing upstream heat loss was just as critical as maximizing downstream ambient cooling for successful solid state waste heat recovery.

4.4.2.7 Fuel Cell Efficiency and IHR System Waste Heat Utilization

This subsection evaluates the ultimate thermodynamic impact of the integrated architecture, analysing the primary fuel cell electrochemical efficiency alongside the overall WHU factor achieved during the dynamic driving cycles.

Figure 4.86 presents the total fuel cell efficiency across all evaluated cases. The empirical data demonstrates a clear and consistent efficiency improvement for the

configurations utilising the passive recovery architecture. The IHR improves the nighttime efficiency by 5.3% compared to 4.8% for daytime operation. During the night, the hydrogen temperature within the tank was lower; thus, the higher nighttime efficiency was contributed mainly by greater heat transfer to the hydrogen stream compared to daytime with higher hydrogen stream temperature. This substantial improvement aligns directly with the earlier findings regarding voltage retention and reduced fuel consumption. By repurposing the exhaust thermal energy to preheat the incoming hydrogen, the system successfully lowered the internal activation energy barriers. Consequently, the fuel cell extracts a greater magnitude of electrical power for every unit of reactant consumed, securing a higher net efficiency without introducing any additional parasitic electrical loads.

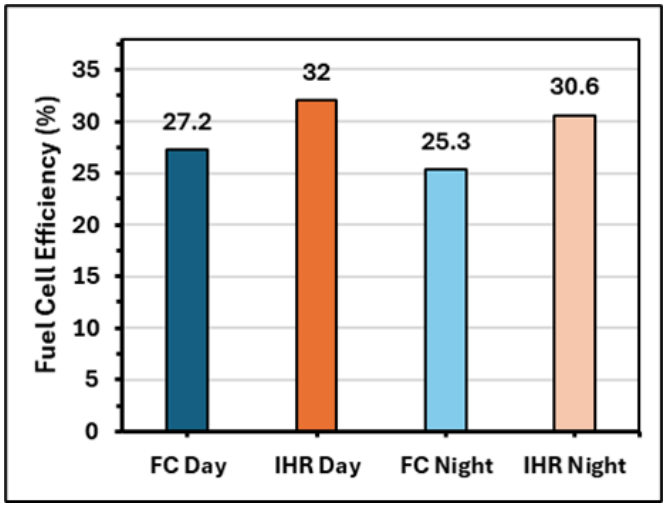

Figure 4.86 Fuel Cell Efficiency for All Cases

While the primary electrochemical efficiency shows distinct improvement, analysing the total fraction of recovered energy provides a necessary perspective on the physical system boundaries. Figure 4.87 plots the total WHU for the integrated configurations. The daytime dynamic cycles utilised only 2.29% of the total available waste heat, while the nighttime operation demonstrated a slightly higher utilization factor of 2.33%. Theoretically, it was anticipated that the highly dynamic NEDC profile, characterized by continuous accelerations and heavy traction loads, would provide a massive and abundant source of waste heat for the integrated recovery components. However, similar to the findings from the steady state evaluations, the relationship between absolute heat generation and the WHU was highly complex and nonlinear under dynamic conditions.

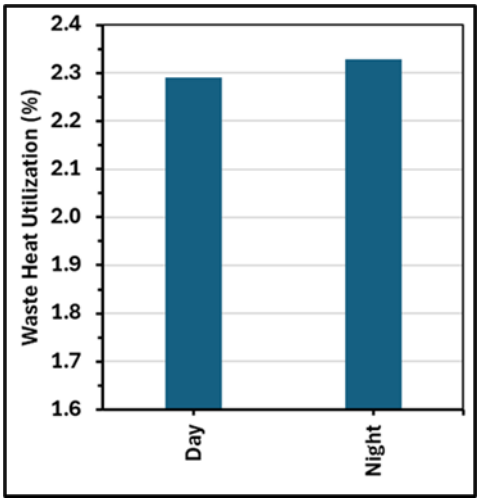

Figure 4.87 Fuel Cell With IHR Waste Heat Utilization

The transient nature of the NEDC testing cycle introduces specific operational fluctuations that dictate this low WHU. During the rapid accelerations and sustained high speeds of the EUDC phase, the fuel cell generates an enormous surge of exothermic heat. This sheer volume and rapid flow rate of waste heat likely overwhelms the physical heat transfer limitations of the internal heat exchanger fins and the TEG surfaces. While the absolute amount of heat recovered during these bursts remains high, the actual proportion of the total available heat utilised drops significantly because the system cannot absorb the energy as fast as it was produced. Conversely, during the slower cruising segments of the ECE-15 phase, the reduced exhaust velocities provide a prolonged residency period for the thermal energy. This extended exposure facilitates a more thorough heat exchange process, but the absolute heat available was much lower. This dynamic fluctuation suggests that the IHR architecture possesses a specific optimal thermal absorption capacity, or an operational sweet spot, that the extreme demands of the dynamic NEDC cycle frequently overshoot.

Furthermore, one of the major physical contributors to this low overall WHU factor originates from the hydrogen preheating mechanism itself. The total thermal energy absorbed by the reactant gas was fundamentally restricted by its exceptionally low mass flow rate. Even when the recovery system establishes a massive temperature gradient between the hot exhaust and the cold gas, the low physical mass of the hydrogen inherently caps the absolute thermal energy it can physically absorb. This fundamental bottleneck, or thermal saturation, severely limits the WHU regardless of how efficiently the heat exchanger operates. Additionally, this physical limitation was

compounded by the structural boundary flaws identified in the thermal analysis, where an approximate 50% temperature drop occurred before the recovery chamber due to inadequate physical insulation.

Therefore, while dynamic on road testing introduces unavoidable experimental uncertainties and transient thermal lag, the empirical data provides robust evidence supporting the functional concept. The integrated architecture successfully improves the operational efficiency of lightweight fuel cell vehicles by balancing the thermal generation rate with its available absorption capacity. However, the consistently low WHU clearly defines the future engineering trajectory. Hydrogen preheating was limited to the heat capacity of the hydrogen flow based on power demand. Main problem was low energy conversion via TEG. The heat capture and dissipation mechanics must be severely improved by geometrical optimization.

4.4.2.8 Summary of Dynamic On Road Testing

The dynamic on road evaluation of the 2 kW PEM fuel cell buggy under a scaled driving profile provided critical empirical data regarding the transient performance of the integrated heat recovery architecture. Unlike idealized steady state laboratory tests, the physical outdoor environment exposed the system to continuous electrical load fluctuations, varying ram air velocities, and unpredictable ambient temperature shifts. Despite these chaotic environmental variables and inherent sensor measurement noise, the physical prototype successfully demonstrated a measurable enhancement in overall system performance. By repurposing the exhaust thermal energy to preheat the incoming hydrogen, the system actively mitigated internal activation polarization. This mechanism allowed the fuel cell to sustain higher operational voltages during transient accelerations, yielding a maximum electrical power increment of 7.0% under nighttime conditions and 5.1% during the daytime.

This sustained electrical improvement translated directly into physical fuel conservation. The dynamic evaluations confirmed that the integrated architecture reduced the absolute hydrogen consumption from 5.2 g/km to 4.4 g/km during the day, and from 5.0 g/km to 4.2 g/km at night. Consequently, the total fuel cell electrochemical efficiency improved by 4.8% and 5.3% for the respective day and night operations. These quantitative reductions provide robust physical evidence that passive reactant

conditioning fundamentally improves fuel utilization, allowing the lightweight vehicle to extract more usable traction energy from the exact same mass of hydrogen consumed.

However, the dynamic on road testing also explicitly exposed the severe physical thermodynamic bottlenecks inherent to this recovery strategy. The total waste heat utilization remained strictly bounded at 2.29% for daytime and 2.33% for nighttime evaluations. As observed in the empirical data, this exceptionally low utilization originates from two primary physical constraints. First, the total thermal energy absorbed by the reactant gas was fundamentally restricted by its low physical mass flow rate, which inherently caps its thermal absorption capacity regardless of the available exhaust heat. Second, the secondary electrical conversion via the solid state thermoelectric generators remained mathematically marginal, peaking at only 120 mW. Furthermore, the thermal mapping revealed a severe 50% temperature degradation occurring upstream of the recovery chamber due to inadequate physical insulation. Therefore, while the physical testing successfully validates the primary power enhancement concept, it rigorously confirms that future engineering trajectories must focus on severe geometrical optimization of the thermoelectric heat capture and dissipation mechanics to overcome these fundamental low temperature conversion limits.

CHAPTER 5
CONCLUSION

5.1 Objective 1: Mathematical and Numerical Design Investigation

Numerical and one dimensional mathematical models successfully predicted the conjugate heat transfer and spatial temperature distribution across the evaluated geometries. The computational fluid dynamics simulations achieved a high degree of reliability, with all critical spatial temperature deviations remaining strictly below the 10% error threshold when validated against the experimental baselines, confirming at least 90% predictive accuracy for the CFD modelling.

Design 2 emerged as the optimal architecture because its expanded external cooling fins and heat pipes successfully balanced internal reactant heat absorption with effective external heat rejection to maintain a distinct thermal gradient. o However, the mathematical conversion from surface temperatures to secondary TEG electrical power yielded overpredictions when compared to the actual physical lab and on road generation. This discrepancy originates from the predictive methodology adopted from previous literature utilised during the preliminary numerical phase. The mathematical equations calculated electrical power as a product of the short circuit current, and the open circuit voltage derived directly from the simulated surface temperatures. Because open circuit voltage inherently represents a no load condition, it mathematically assumes the absolute maximum voltage potential. Consequently, this analytical approach vastly overpredicts the actual operational voltage achieved when the solid state modules are subjected to a physical electrical load, confirming the absolute necessity of advancing beyond preliminary equations to physical experimental validation.

5.2 Objective 2: Experimental Test Bench Validation

Controlled steady state laboratory test bench evaluations confirmed that the physical prototype successfully elevated the incoming hydrogen temperature, which actively mitigated internal activation polarization within the primary stack.

This reactant thermal conditioning yielded a maximum primary electrical power increment of 196.7 W, representing an 11.1% improvement at the peak 60 A load under a 10 m/s convective cooling boundary. Consequently, the overall steady state efficiency of the fuel cell improved by an absolute 4.6 percentage points.

The secondary solid state thermoelectric modules generated a maximum of 192.5 mW of auxiliary power. While proving the dual recovery concept, spatial thermal mapping exposed a severe 24% temperature degradation occurring immediately upstream of the recovery chamber, highlighting significant conductive heat losses and imperfect physical insulation across the test bench connection manifolds

5.3 Objective 3: Dynamic On Road Evaluation

Dynamic evaluations utilising a lightweight vehicular buggy across scaled driving cycles validated the recovery system under continuous transient traction loads. The integrated architecture successfully reduced absolute hydrogen fuel consumption from 5.2 g/km down to 4.4 g/km during daytime operations, and from 5.0 g/km down to 4.2 g/km under cooler nighttime conditions.

The dynamic electrical efficiency improved by 4.8% and 5.3% for the respective day and night operations. Furthermore, the cooler nocturnal ambient environment provided a superior convective heat sink, allowing the system to achieve a 7.0% primary power increment at night compared to a 5.1% increment during the day.

Despite these electrochemical improvements, the absolute waste heat utilization factor remained mathematically low, peaking at 2.9% during constant speed evaluations and 2.33% during the highly transient dynamic cycles. The outdoor evaluations recorded a profound 50% temperature drop occurring immediately upstream of the recovery chamber. These findings strongly indicate that severe aerodynamic disturbances, physical thermal inertia, and uncontrolled ambient boundaries strictly limit total energy recovery, confirming that dynamic on road validation remains an absolutely indispensable methodology for assessing true physical thermodynamic limits

Ultimately, the comprehensive evaluation confirms that the integrated heat recovery concept for PEM fuel cell electric vehicles was successfully validated across analytical, numerical, experimental, and dynamic on road environments to produce distinct passive performance gains. First, capturing exhaust thermal energy to elevate

the incoming hydrogen reactant temperature successfully mitigated internal activation polarization, yielding a measurable improvement in overall fuel cell efficiency without introducing any active parasitic heating loads. Second, the architecture successfully facilitated secondary electrical generation through the solid state thermoelectric modules. Although the absolute magnitude of this secondary electrical power remained exceptionally small due to strict physical thermodynamic boundaries and upstream conductive heat losses, the energy was recovered entirely passively. Therefore, this research establishes the foundational viability of dual passive thermal management from initial mathematical equations to actual physical on road applications, proving that low grade waste heat can be repurposed to enhance vehicular powertrain performance, provided that future iterations strictly address the insulation flaws and geometric bottlenecks exposed during these outdoor evaluations.

5.4 Recommendations

While this research successfully demonstrated the critical necessity of physical dynamic testing, the inherent complexities of vehicular powertrain integration suggest several distinct pathways for future exploration. The observations recorded during these outdoor trials highlight specific areas where advanced thermal architectures, empirical measurement techniques, and predictive modeling might benefit from further refinement.

First, to address the severe upstream temperature degradation observed during both the test bench and on road evaluations, future physical iterations must prioritize rigorous thermal insulation and geometrical optimization of the exhaust manifold interfaces. Minimizing these premature conductive heat losses was absolutely critical to preserve the ultra low-grade thermal driving potential before it reaches the thermoelectric modules.

Second, the empirical data revealed that rapid surges of waste heat during vehicle acceleration frequently overwhelmed the physical absorption capacity of the heat sinks. Future physical designs might benefit from integrating phase change materials into the secondary cooling chamber. These materials could potentially serve as a thermal buffer, absorbing excess latent heat during sudden acceleration spikes and releasing it slowly during deceleration phases, thereby stabilizing the temperature difference across the solid state modules.

Third, the physical methodologies and empirical performance limits established in this thesis serve as a critical benchmark for future integrated heat recovery designs tailored to different primary power plants. Subsequent studies might explore adapting this passive architecture for closed cathode polymer electrolyte membrane fuel cells. Because closed cathode systems and high temperature fuel cells operate at significantly elevated thermal boundaries, they generate a much more abundant waste heat source. This elevated thermal source could theoretically drive vastly superior thermoelectric operations. While transitioning to these higher temperature platforms would require a complete geometric redesign of the integrated heat recovery architecture to handle the increased thermal stress, the current study provides the necessary empirical benchmark to safely guide that future scaling process.

Fourth, future investigations might explore expanding this dynamic on road testing methodology to larger higher power liquid cooled automotive stacks exceeding 50 kW. Scaling the physical prototype would allow researchers to empirically observe how the massive thermal inertia of dielectric liquid coolant loops and heavy duty radiators respond to the aggressive load shifting of full scale automotive drive cycles.

Fifth, because the mathematical models utilising open circuit voltage vastly overpredicted the secondary electrical generation, future numerical investigations should incorporate fully coupled electrical load simulations. Exploring exactly how physical circuit resistance and dynamic traction loads alter the closed circuit voltage will provide a much more realistic baseline for projecting solid state recovery potential.

Sixth, the comprehensive empirical relationships established across the steady state test bench, constant speed evaluations, and highly transient dynamic on road driving cycles provide a highly valuable practical dataset. Future research could utilise this foundation to develop advanced core mathematical prediction models. By explicitly incorporating the actual transient thermal lag and physical contact resistances documented in this physical study, these new core models could predict integrated fuel cell and thermoelectric generator performance with far greater accuracy than currently available idealized mathematical equations.

Finally, fully acknowledging the experimental uncertainties and data noise inherent to outdoor testing, future studies might seek to develop hybrid digitally assisted surrogate models. Researchers could utilise the highly volatile empirical data arrays captured during real world buggy testing to continuously calibrate, correct, and refine idealized three dimensional CFD simulations. Furthermore, integrating machine

learning algorithms to preemptively adjust active cooling controls based on real time environmental sensor data might help mitigate the localised thermal lag observed during physical transient acceleration.

REFERENCES

[1] I. E. Agency, “Global Hydrogen Review 2024, Glob. Hydrog. Rev. 2024 (2024). https://doi.org/10.1787/cb2635f6-en. - Google Search,” 2024, [Online]. Available: https://www.google.com/search?q=Global+Hydrogen+Review+2024%2C+Glob.+Hydrog.+Rev.+2024+(2024).+https%3A%2F%2Fdoi.org%2F10.1787%2Fcb2635f6-en.&oq=GLObal+hydrogen+review+2024&gs_lcrp=EgZjaHJvbWUqCAgAEEUYJxg7MggIABBFGCcYOzIJCAEQRRg5GIAEMgYIAhBFGEAyDAgDEAAYQx

[2] P. M. D. Malaysia. Economic Planning Unit and C. System, “Malaysia National Energy Policy 2022-2040,” Sep. 2022.

[3] MGTC, “National Energy Transition Roadmap (NETR) 1,” Ministry of Economy Malaysia, pp. 1–70, 2023.

[4] T. dan I. (MOSTI) Kementerian Sains, Malaysia Hydrogen Economy and Technology Roadmap, 1st ed., vol. 1. PUTRAJAYA, 2023.

[5] Y. Yao, Z. Chen, F. Wang, H. Huo, F. Chen, and H. Han, “Thermal management of PEMFC system based on improved cascade internal model control,” Journal of Renewable and Sustainable Energy, vol. 18, no. 1, Jan. 2026, doi: 10.1063/5.0301925.

[6] S. Mitincik and M. Y. Yazici, “A comprehensive review of thermal management strategies in PEM fuel cells: From conventional cooling methods to advanced passive and hybrid solutions for sustainable energy application,” Apr. 01, 2026, Elsevier Ltd. doi: 10.1016/j.rser.2025.116684.

[7] W. A. N. W. Mohamed and R. Atan, “Experimental thermal analysis on air cooling for closed-cathode Polymer Electrolyte Membrane fuel cells,” Int. J. Hydrogen Energy, vol. 40, no. 33, pp. 10605–10626, 2015, doi: 10.1016/j.ijhydene.2015.06.095.

[8] M. M. R. Fairuz, W. a W. M. Najmi, and a Rahim, “Cooling Mechanisms and Contribution Analysis of an Experimental Polymer Electrolyte Membrane Fuel Cell System,” 3rd Engineering Conference on Advancement in Mechanical and Manufacturing for Sustainable Environment, pp. 1–4, 2010.

[9] M. Saufi Sulaiman, B. Singh, and W. A. N. W. Mohamed, “Experimental and theoretical study of thermoelectric generator waste heat recovery model for an ultra-low temperature PEM fuel cell powered vehicle,” Energy, vol. 179, pp. 628–646, 2019, doi: 10.1016/j.energy.2019.05.022.

[10] T. Ralph, “‘Principles of Fuel Cells’: BY XIANGUO LI, Taylor & Francis, New York, 2005, 572 pages, ISBN 978-1-59169-022-1, £50.00, U.S.$125.00,” Platin. Met. Rev., vol. 50, pp. 200–201, 2006, doi: 10.1595/147106706X158789.

[11] M. M. El Idi, M. Ankouni, R. Ben Haj Slama, P. Affonso Nobrega, A. Hajjar, and A. Atli, “Critical review of the latest advances in thermal management techniques for PEM fuel cells,” Renewable and Sustainable Energy Reviews, vol. 226, no. PA, p. 116199, 2026, doi: 10.1016/j.rser.2025.116199.

[12] R. A. O’Hayre, S.-W. A. Cha, W. A. Colella, and F. P. Prinz, Fuel Cell Fundamentals, 3rd ed. John Wiley & Sons., 2016. doi: 10.1002/9781119191766.

[13] Dicks and Andrew AU, Fuel Cell Systems Explained. John Wiley & Sons, 2018. doi: 10.1002/9781118706992.

[14] I. A. Zakaria, W. A. N. W. Mohamed, N. H. A. Azid, M. A. Suhaimi, and W. H. Azmi, “Heat transfer and electrical discharge of hybrid nanofluid coolants in a fuel cell cooling channel application,” Appl. Therm. Eng., vol. 210, no. February, p. 118369, 2022, doi: 10.1016/j.applthermaleng.2022.118369.

[15] A. Baroutaji et al., “Advancements and prospects of thermal management and waste heat recovery of PEMFC,” International Journal of Thermofluids, vol. 9, Feb. 2021, doi: 10.1016/j.ijft.2021.100064.

[16] D. H. Trinh, Y. Kim, and S. Yu, “One-dimensional dynamic model of a PEM fuel cell for analyzing through-plane species distribution and irreversible losses under various operating conditions,” Case Studies in Thermal Engineering, vol. 60, Aug. 2024, doi: 10.1016/j.csite.2024.104815.

[17] W. Mohamed and M. Kamil, “Hydrogen preheating through waste heat recovery of an open-cathode PEM fuel cell leading to power output improvement,” Energy Convers. Manag., vol. 124, pp. 543–555, 2016, doi: 10.1016/j.enconman.2016.07.046.

[18] L. Barelli, G. Bidini, F. Gallorini, and A. Ottaviano, “An energetic-exergetic comparison between PEMFC and SOFC-based micro-CHP systems,” Int. J.

Hydrogen Energy, vol. 36, no. 4, pp. 3206–3214, 2011, doi: 10.1016/j.ijhydene.2010.11.079.

[19] I. Aleknaviciute, T. G. Karayiannis, M. W. Collins, and C. Xanthos, “Towards clean and sustainable distributed energy system: The potential of integrated PEMFC-CHP,” International Journal of Low-Carbon Technologies, vol. 11, no. 3, pp. 296–304, 2016, doi: 10.1093/ijlct/ctv004.

[20] S. T. OH, B. B. SAHA, K. KARIYA, Y. HAMAMOTO, and H. MORI, “FUEL CELL WASTE HEAT POWERED ADSORPTION COOLING SYSTEMS,” International Journal of Air-Conditioning and Refrigeration, vol. 21, no. 02, p. 1350010, 2013, doi: 10.1142/S2010132513500107.

[21] W. Y. Lee, M. Kim, Y. J. Sohn, and S. G. Kim, “Power optimization of a combined power system consisting of a high-temperature polymer electrolyte fuel cell and an organic Rankine cycle system,” Energy, vol. 113, pp. 1062–1070, 2016, doi: 10.1016/j.energy.2016.07.093.

[22] A. A. Sinha, S. S. Bhogilla, and J. K. Kuo, “Waste heat recovery and performance assessment of low temperature fuel cell integrated with thermoelectric generator,” Int. J. Hydrogen Energy, vol. 175, Oct. 2025, doi: 10.1016/j.ijhydene.2025.151216.

[23] S. Khanmohammadi and R. Soleimani, “Advanced hybrid gas turbine configuration with PEM fuel cell and intercoolers: Towards cleaner and cost-efficient power generation,” Int. J. Hydrogen Energy, vol. 171, Sep. 2025, doi: 10.1016/j.ijhydene.2025.151239.

[24] X. Zhang and J. Chen, “Performance evaluation and parametric optimization of a proton exchange membrane fuel cell/heat-driven heat pump hybrid system,” Fuel Cells, vol. 12, no. 3, pp. 313–319, 2012, doi: 10.1002/fuce.201100115.

[25] X. Zhang, X. Chen, B. Lin, and J. Chen, “Maximum equivalent efficiency and power output of a PEM fuel cell/refrigeration cycle hybrid system,” Int. J. Hydrogen Energy, vol. 36, no. 3, pp. 2190–2196, 2011, doi: 10.1016/j.ijhydene.2010.11.088.

[26] P. Zhao, J. Wang, L. Gao, and Y. Dai, “Parametric analysis of a hybrid power system using organic Rankine cycle to recover waste heat from proton exchange membrane fuel cell,” Int. J. Hydrogen Energy, vol. 37, no. 4, pp. 3382–3391, 2012, doi: 10.1016/j.ijhydene.2011.11.081.

[27] P. Yang and H. Zhang, “Parametric analysis of an irreversible proton exchange membrane fuel cell/absorption refrigerator hybrid system,” Energy, vol. 85, pp. 458–467, Jun. 2015, doi: 10.1016/j.energy.2015.03.104.

[28] X. Zhang, Y. Pan, L. Cai, Y. Zhao, and J. Chen, “Using electrochemical cycles to efficiently exploit the waste heat from a proton exchange membrane fuel cell,” Energy Convers. Manag., vol. 144, pp. 217–223, 2017, doi: 10.1016/j.enconman.2017.04.058.

[29] A. P. Tetuko, B. Shabani, and J. Andrews, “Thermal coupling of PEM fuel cell and metal hydride hydrogen storage using heat pipes,” Int. J. Hydrogen Energy, vol. 41, no. 7, pp. 4264–4277, 2016, doi: 10.1016/j.ijhydene.2015.12.194.

[30] M. Nasri, I. Burger, S. Michael, and H. E. Friedrich, “Waste heat recovery for fuel cell electric vehicle with thermochemical energy storage,” 2016 11th International Conference on Ecological Vehicles and Renewable Energies, EVER 2016, May 2016, doi: 10.1109/EVER.2016.7476439.

[31] A. I. Dawahdeh, M. M. Alqeyam, and M. A. Al-Nimr, “Assessment of LaNi5 Metal Hydride Storage augmented by waste heat recovery for Proton Exchange Membrane Fuel Cell vehicles,” J. Energy Storage, vol. 153, Apr. 2026, doi: 10.1016/j.est.2026.120864.

[32] H. Q. Nguyen, A. M. Aris, and B. Shabani, “PEM fuel cell heat recovery for preheating inlet air in standalone solar-hydrogen systems for telecommunication applications: An exergy analysis,” Int. J. Hydrogen Energy, vol. 41, no. 4, pp. 2987–3003, 2016, doi: 10.1016/j.ijhydene.2015.12.108.

[33] M. Tran and A. Demuren, “Thermal management for optimal performance of polymer electrolyte membrane unitized regenerative fuel cells,” Next Energy, vol. 8, Jul. 2025, doi: 10.1016/j.nxener.2025.100271.

[34] M. Haghighi and F. Sharifhassan, “Exergy analysis and optimization of a high temperature proton exchange membrane fuel cell using genetic algorithm,” Case Studies in Thermal Engineering, vol. 8, pp. 207–217, 2016, doi: 10.1016/j.csite.2016.07.005.

[35] A. Uzun, B. Bokor, and D. Eryener, “PEM fuel cell performance with solar air preheating,” Int. J. Hydrogen Energy, vol. 45, no. 60, pp. 34654–34665, 2020, doi: 10.1016/j.ijhydene.2020.01.129.

[36] Iea, “Global Hydrogen Review 2025,” 2025. [Online]. Available: www.iea.org

[37] A. Amirfazli, S. Asghari, and M. Koosha, “Mathematical modeling and simulation of thermal management in polymer electrolyte membrane fuel cell stacks,” J. Power Sources, vol. 268, pp. 533–545, 2014, doi: 10.1016/j.jpowsour.2014.06.073.

[38] Y. Cai, W. W. Wang, L. Wang, D. Liu, and F. Y. Zhao, “A proton exchange membrane fuel cell-compound thermoelectric system: Bidirectional modeling and energy conversion potentials,” Energy Convers. Manag., vol. 207, no. January, p. 112517, 2020, doi: 10.1016/j.enconman.2020.112517.

[39] M. S. Sulaiman, W. A. N. W. Mohamed, B. Singh, and M. F. Ghazali, “Validation of a Waste Heat Recovery Model for a 1kW PEM Fuel Cell using Thermoelectric Generator,” IOP Conf. Ser. Mater. Sci. Eng., vol. 226, no. 1, 2017, doi: 10.1088/1757-899X/226/1/012148.

[40] W. Sun, F. Yi, D. Hu, and J. Zhou, “Research on matching design method of waste heat reuse system of fuel cell vehicle considering system energy consumption and waste heat exchange rate,” Wiley Online LibraryW Sun, F Yi, D Hu, J ZhouInternational Journal of Energy Research, 2021•Wiley Online Library, vol. 45, no. 4, pp. 5470–5485, Mar. 2021, doi: 10.1002/er.6175.

[41] X. Gao, S. J. Andreasen, S. K. Kær, and L. A. Rosendahl, “Optimization of a thermoelectric generator subsystem for high temperature PEM fuel cell exhaust heat recovery,” Int. J. Hydrogen Energy, vol. 39, no. 12, pp. 6637–6645, 2014, doi: 10.1016/j.ijhydene.2014.01.193.

[42] M. Ebrahimi and E. Derakhshan, “Design and evaluation of a micro combined cooling, heating, and power system based on polymer exchange membrane fuel cell and thermoelectric cooler,” Energy Convers. Manag., vol. 171, no. May, pp. 507–517, 2018, doi: 10.1016/j.enconman.2018.06.007.

[43] R. J. Parise and G. F. Jones, “Fuel cell thermal management with thermoelectric coolers,” Proceedings of the Intersociety Energy Conversion Engineering Conference, pp. 607–614, 2002, doi: 10.1109/iecec.2002.1392115.

[44] A. Behzadi, A. Arabkoohsar, and E. Gholamian, “Multi-criteria optimization of a biomass-fired proton exchange membrane fuel cell integrated with organic rankine cycle/thermoelectric generator using different gasification agents,” Energy, vol. 201, p. 117640, 2020, doi: 10.1016/j.energy.2020.117640.

[45] N. F. Zamri, M. H. Hamdan, S. N. A. Anuar, W. A. N. W. Mohamed, and M. F. Remeli, “Performance of A Plate-Finned Thermoelectric Generator (TEG)

Module for Industrial Waste Heat Recovery," Journal of Mechanical Engineering, vol. 19, no. 3, pp. 257–272, 2022, doi: 10.24191/jmeche.v19i3.19817.

[46] M. Hasani and N. Rahbar, "Application of thermoelectric cooler as a power generator in waste heat recovery from a PEM fuel cell - An experimental study," Int. J. Hydrogen Energy, vol. 40, no. 43, pp. 15040–15051, 2015, doi: 10.1016/j.ijhydene.2015.09.023.

[47] X. Gao, M. Chen, S. J. Andreasen, and S. K. Kær, "Potential usage of thermoelectric devices in a high-temperature polymer electrolyte membrane (PEM) fuel cell system: two case studies," SpringerX Gao, M Chen, SJ Andreasen, SK KærJournal of electronic materials, 2012•Springer, vol. 41, no. 6, pp. 1838–1844, Jun. 2012, doi: 10.1007/s11664-012-2098-2.

[48] S. Katayama, M. Matsumoto, H. Imai, T. Asaoka, and K. Amemiya, "Comparison of MEA degradation through FCV actual driving test and load-cycle durability test," iopscience.iop.orgS Katayama, M Matsumoto, H Imai, T Asaoka, K AmemiyaElectrochemical Society Transactions 244, 2023•iopscience.iop.org, vol. 112, no. 4, pp. 157–165, Sep. 2023, doi: 10.1149/11204.0157ecst.

[49] D. Manzo, R. Thai, H. T. Le, and G. K. Venayagamoorthy, "Fuel cell technology review: Types, economy, applications, and vehicle-to-grid scheme," Mar. 01, 2025, Elsevier Ltd. doi: 10.1016/j.seta.2025.104229.

[50] R. van den Hoed and P. J. Vergragt, "Institutional Change in the Automotive Industry," Greener Management International, vol. 2004, no. 47, pp. 44–61, 2014, doi: 10.9774/gleaf.3062.2004.au.00006.

[51] T. F. Tamimuddin, W. Mohamed, and M. F. A. Y. Mohamad, "An Overview on The Design , Operation and Levelized Costs of Hydrogen Refuelling Stations for Fuel Cell Electric Vehicles," Journal of Applied Engineering Design and Simulation, vol. 4, no. 1, pp. 21–34, 2024, doi: 10.24191/jaeds.v4i1.76.

[52] G. Paul, Hans-Werner K., Detlev M., and Dominik W., "Automotive revolution – perspective towards 2030 | McKinsey," advanced industries. Accessed: Mar. 13, 2026. [Online]. Available: https://www.mckinsey.com/industries/automotive-and-assembly/our-insights/disruptive-trends-that-will-transform-the-auto-industry/de-DE

[53] R. C. Samsun, M. Rex, L. Antoni, and D. Stolten, “Deployment of Fuel Cell Vehicles and Hydrogen Refueling Station Infrastructure: A Global Overview and Perspectives,” Energies (Basel)., vol. 15, no. 14, 2022, doi: 10.3390/en15144975.

[54] Sunita Satyapal, “U . S . Department of Energy Hydrogen and Fuel Cell Overview,” U.S. Department of Energy EERE, p. 46, 2016.

[55] J. Wang, H. Wang, and Y. Fan, “Techno-Economic Challenges of Fuel Cell Commercialization,” Engineering, vol. 4, no. 3, pp. 352–360, 2018, doi: 10.1016/j.eng.2018.05.007.

[56] D. Papageorgopoulos, “Fuel Cell R & D Overview,” 2019 Annual Merit Review and Peer Evaluation Meeting (Hydrogen and Fuel Cell Technologies Office, Office of Energy Efficiency and Renewable Energy, US Department of Energy, 2019), pp. 1–5, 2019, [Online]. Available: https://www.hydrogen.energy.gov/pdfs/review19/plenary_fuel_cell_papageorgopoulos_2019.pdf

[57] R. L. Borup et al., “(Invited) PEM Fuel Cell Catalyst Layer Architectures,” ECS Meeting Abstracts, vol. MA2018-01, no. 27, pp. 1591–1591, 2018, doi: 10.1149/ma2018-01/27/1591.

[58] L. Eudy, “Technology Validation: Fuel Cell Bus Evaluations,” Conference: Presented at the U.S. Department of Energy Hydrogen and Fuel Cells Program 2016 Annual Merit Review and Peer Evaluation Meeting, 6-10 June 2016, Washington, D. C., no. NREL/PR-5400-66177, p. Medium: ED; Size: 1.9 MB, 2018, [Online]. Available: https://www.osti.gov/biblio/1416134%0Ahttps://www.osti.gov/servlets/purl/1416134

[59] D. Papageorgopoulos, D. Peterson, 2019, “(Invited) US DOE Early-Stage Alkaline Membrane Fuel Cell R&D,” iopscience.iop.orgDC Papageorgopoulos, D Peterson, D Ho, G Kleen, NL Garland, ST ThompsonElectrochemical Society Meeting Abstracts 235, 2019•iopscience.iop.org, doi: 10.1149/MA2019-01/34/1820/META.

[60] C. Wang, S. Tang, X. Liu, G. H. Su, W. Tian, and S. Qiu, “Experimental study on heat pipe thermoelectric generator for industrial high temperature waste heat recovery,” Appl. Therm. Eng., vol. 175, no. February, 2020, doi: 10.1016/j.applthermaleng.2020.115299.

[61] T. Wilberforce et al., “Recovery of waste heat from proton exchange membrane fuel cells – A review,” Int. J. Hydrogen Energy, vol. 52, pp. 933–972, Jan. 2024, doi: 10.1016/j.ijhydene.2022.08.069.

[62] P. Ragupathi, D. Barik, G. Vignesh, and S. Aravind, “Electricity generation from exhaust waste heat of internal combustion engine using Al2O3 thermoelectric generators,” Journal of Applied Science and Engineering, vol. 23, no. 1, pp. 55–60, 2020, doi: 10.6180/JASE.202003_23(1).0007.

[63] Z. Su et al., “Opportunities and strategies for multigrade waste heat utilization in various industries: A recent review,” Energy Convers. Manag., vol. 229, no. January, p. 113769, 2021, doi: 10.1016/j.enconman.2020.113769.

[64] J. A. J. Gilbert, “A Waste Heat Recovery System Using Thermoelectric Generator for A Hydrogen Fuel Cell Mini Vehicle,” 2020.

[65] S. S. Niknezhad, F. Moghaddamali, and E. Pistikopoulos, “Toward More Efficient Large-Scale Green Hydrogen Systems via Waste Heat Recovery and ORC,” Applied Sciences (Switzerland), vol. 15, no. 10, 2025, doi: 10.3390/app15105224.

[66] Z. Zhan et al., “Experimental study on different preheating methods for the cold-start of PEMFC stacks,” Energy, vol. 162, pp. 1029–1040, 2018, doi: 10.1016/j.energy.2018.08.003.

[67] Q. Zhang, Z. Tong, S. Tong, and Z. Cheng, “Research on low-temperature heat exchange performance of hydrogen preheating system for PEMFC engine,” Int. J. Hydrogen Energy, vol. 45, no. 55, pp. 30966–30979, 2020, doi: 10.1016/j.ijhydene.2020.08.076.

[68] E. S. Mohamed, “Development and performance analysis of a TEG system using exhaust recovery for a light diesel vehicle with assessment of fuel economy and emissions,” Appl. Therm. Eng., vol. 147, pp. 661–674, Jan. 2019, doi: 10.1016/J.APPLTHERMALENG.2018.10.100.

[69] S. U. Org, “TRANSFORMING OUR WORLD: THE 2030 AGENDA FOR SUSTAINABLE DEVELOPMENT UNITED NATIONS”, https://sdgs.un.org/2030agenda.

[70] Q. Wu, Z. Dong, X. Zhang, C. Zhang, and A. Iqbal, “Towards More Efficient PEM Fuel Cells Through Advanced Thermal Management : From Mechanisms to Applications,” Sustainability 2025, 17, 94, doi.org/10.3390/su17030943.

[71] D. Kumar, H. Kumar, and A. S. Oberoi, “Thermal management system and its impact on PEMFC performance: Review,” Environ. Prog. Sustain. Energy, vol. 45, no. 1, p. e70131, Jan. 2025, doi: 10.1002/ep.70131.

[72] S. Zhang, L. Luo, X. Zhang, and H. Zhang, “Demonstration of a thermoelectric generator system for low-temperature heat harvesting in fuel cell,” iScience, vol. 27, no. 7, Jul. 2024, doi: 10.1016/j.isci.2024.110022.

[73] H. Tao, K. Al Mamun, A. Ali, E. Solomin, J. Zhou, and N. Sinaga, “Performance enhancement of integrated energy system using a PEM fuel cell and thermoelectric generator,” Int. J. Hydrogen Energy, vol. 51, pp. 1280–1292, Jan. 2024, doi: 10.1016/j.ijhydene.2023.03.442.

[74] H. S. Lim, B. Kang, M. Ahn, and M. S. Kim, “Optimizing hydrogen utilization in Fuel Cell Hybrid Vehicles: Modeling fuel cell systems and managing energy between batteries and fuel cells,” Int. J. Hydrogen Energy, vol. 99, pp. 819–835, Jan. 2025, doi: 10.1016/j.ijhydene.2024.12.150.

[75] W. Abdullah, R. Mohamed, I. Alrashdi, M. Abdel-basset, and M. Mahdi, “AI-Driven Prognostics for PEM Fuel Cells Using Optimized Machine Learning and Deep Learning Models for Accurate Lifetime Prediction,” 2014.

[76] F. Wang, A. Liu, C. Qu, R. Xiong, and L. Chen, “A Deep-Learning Method for Remaining Useful Life Prediction of Power Machinery via Dual-Attention Mechanism,” Sensors 2025, 25, 497. doi.org/10.3390/s25020497.

[77] Z. Ge, S. Xu, X. Fu, and Z. Zhao, “Improving the Cold-Start Performance of Proton Exchange Membrane Fuel Cells via Precision Engineering of Key Materials,” 2025, doi: 10.1021/prechem.4c00079.

[78] Z. Luo et al., “Dynamic response characteristics and water-gas-heat synergistic transport mechanism of proton exchange membrane fuel cell during transient loading,” Energy, vol. 302, no. March, p. 131852, 2024, doi: 10.1016/j.energy.2024.131852.

[79] Y. Wang, H. Yuan, A. Martinez, P. Hong, H. Xu, and F. R. Bockmiller, “Advances in Applied Energy Polymer electrolyte membrane fuel cell and hydrogen station networks for automobiles : Status , technology , and perspectives,” Advances in Applied Energy, vol. 2, no. December 2020, p. 100011, 2021, doi: 10.1016/j.adapen.2021.100011.

[80] S. G. Kandlikar and Z. Lu, “Thermal management issues in a PEMFC stack – A brief review of current status,” Appl. Therm. Eng., vol. 29, no. 7, pp. 1276–1280, 2009, doi: 10.1016/j.applthermaleng.2008.05.009.

[81] X. Li, C. Du, J. Zhao, and Y. Hu, “Dynamic load effects on performance stability and cell consistency in automotive PEM fuel cell systems,” Appl. Therm. Eng., vol. 289, no. P1, p. 129707, 2026, doi: 10.1016/j.applthermaleng.2026.129707.

[82] Q. Wu, Z. Dong, X. Zhang, C. Zhang, and A. Iqbal, “Towards More Efficient PEM Fuel Cells Through Advanced Thermal Management : From Mechanisms to Applications,” Sustainability 2025, 17, 94, doi.org/10.3390/su17030943..

[83] T. Wilberforce et al., “Optimization of Fuel Cell Performance Using Computational Fluid Dynamics,” Membranes 2021, 11, 146, doi:10.3390/membranes11020146.

[84] S. Seo, S. Oh, H. Oh, and M. Kim, “ScienceDirect Thermal management for a hydrogen-fueled 1-kW PEMFC based on thermoeconomic analysis,” Int. J. Hydrogen Energy, vol. 44, no. 45, pp. 24934–24946, 2019, doi: 10.1016/j.ijhydene.2019.07.171.

[85] Z. Yang, Q. Du, Z. Jia, C. Yang, and K. Jiao, “Effects of operating conditions on water and heat management by a transient multi-dimensional PEMFC system model,” Energy, vol. 183, pp. 462–476, 2019, doi: 10.1016/j.energy.2019.06.148.

[86] A. Merdjani and N. Kizilova, “Advancements and challenges in design of flow field plates in proton exchange membrane fuel cells : a comprehensive review,” vol. 2025, no. May, pp. 1–27, 2025, doi: 10.3389/fenrg.2025.1506011.

[87] D. Kumar, H. Kumar, and A. Singh Oberoi, “Investigation on the performance of reversible polymer electrolyte membrane fuel cell during the electrolysis phase,” EPJ Web Conf., vol. 345, p. 01016, 2026, doi: 10.1051/epjconf/202634501016.

[88] I. Veza, “Fuel-Cell Thermal Management Strategies for Enhanced Performance: Review of Fuel-Cell Thermal Management in Proton-Exchange Membrane Fuel Cells (PEMFCs) and Solid-Oxide Fuel Cells (SOFCs),” Hydrogen (Switzerland), vol. 6, no. 3, pp. 1–33, 2025, doi: 10.3390/hydrogen6030065.

[89] T. He, R. Shi, J. Peng, W. Zhuge, and Y. Zhang, “Waste heat recovery of a PEMFC system by using organic Rankine cycle,” Energies (Basel)., vol. 9, no. 4, 2016, doi: 10.3390/en9040267.

[90] D. Kumar, H. Kumar, and A. S. Oberoi, “Thermal management system and its impact on PEMFC performance: Review,” Environ. Prog. Sustain. Energy, vol. 45, no. 1, p. e70131, Jan. 2025, doi: 10.1002/ep.70131.

[91] M. T. Tran, “THERMAL MANAGEMENT FOR OPTIMAL PERFORMANCE OF UNITIZED REGENERATIVE FUEL CELLS,” 2024.

[92] V. Ionescu, “Thermal-hydraulic analysis of a louver fin-and-tube radiator for a liquid–cooled PEMFC stack system,” Ovidius University Annals of Chemistry, vol. 35, no. 2, pp. 111–117, 2024, doi: 10.2478/auoc-2024-0015.

[93] M. Ahmed and X. Shusheng, “Comprehensive review of serpentine flow fields for effective thermal management of proton exchange membrane fuel cell,” Heliyon, vol. 10, no. 21, p. e39793, 2024, doi: 10.1016/j.heliyon.2024.e39793.

[94] M. M. El Idi, M. Ankouni, R. Ben Haj Slama, P. Affonso Nobrega, A. Hajjar, and A. Atli, “Critical review of the latest advances in thermal management techniques for PEM fuel cells,” Renewable and Sustainable Energy Reviews, vol. 226, no. PA, p. 116199, 2026, doi: 10.1016/j.rser.2025.116199.

[95] D. Hyun, J. Han, and S. Hong, “Power Management Strategy of Hybrid Fuel Cell Drones for Flight Performance Improvement Based on Various Algorithms,” Energies (Basel)., vol. 16, no. 24, 2023, doi: 10.3390/en16248001.

[96] G. Etienne et al., “On the main factors limiting the performance of state-of-the-art polymer electrolyte membrane fuel cells in the 90–100 °C temperature range,” Electrochim. Acta, vol. 541, Nov. 2025, doi: 10.1016/j.electacta.2025.147320.

[97] J. Breitinger, M. Hellmann, H. Kemmer, and S. Kabelac, “Automotive Fuel Cell Systems: Testing Highly Dynamic Scenarios,” Energies (Basel)., vol. 16, no. 2, pp. 1–15, 2023, doi: 10.3390/en16020664.

[98] I. El-Khalil Bouziane and B. Abderezzak, “Thermal Optimization Model for Fuel Cell Vehicles under Dynamic Driving Conditions,” 2025 9th International Conference on Environment Friendly Energies and Applications (EFEA), pp. 1–6, Dec. 2025, doi: 10.1109/EFEA67685.2025.11386018.

[99] A. U. H. Najmi, A. Wahab, R. Prakash, O. Schopen, T. Esch, and B. Shabani, “Thermal management of fuel cell-battery electric vehicles: Challenges and

solutions," Appl. Energy, vol. 387, no. March, p. 125635, 2025, doi: 10.1016/j.apenergy.2025.125635.

[100] Q. Zhang, Z. Tong, S. Tong, and Z. Cheng, "Research on low-temperature performance of plate-fin hydrogen preheater for a proton-exchange membrane fuel cell," Int. J. Green Energy, vol. 18, no. 5, pp. 457–473, 2021, doi: 10.1080/15435075.2020.1865368.

[101] H. Q. Nguyen and B. Shabani, "Proton exchange membrane fuel cells heat recovery opportunities for combined heating/cooling and power applications," Jan. 15, 2020, Elsevier Ltd. doi: 10.1016/j.enconman.2019.112328.

[102] W. A. N. W. Mohamed, B. Singh, M. F. Mohamed, A. M. Aizuwan, and A. B. M. Zubair, "Effects of fuel cell vehicle waste heat temperatures and cruising speeds on the outputs of a thermoelectric generator energy recovery module," Int. J. Hydrogen Energy, Jul. 2021, doi: 10.1016/j.ijhydene.2021.05.084.

[103] B. Singh, W. A. N. W. Mohamed, M. N. F. Hamani, and K. Z. N. A. So, "Enhancement of low grade waste heat recovery from a fuel cell using a thermoelectric generator module with swirl fl ows," Energy 236, 2021, doi: 10.1016/j.energy.2021.121521.

[104] M. H. Hamdan, N. A. Mat Som, A. Abdul Rashid, and G. J. Jimmy, "Performance analysis on series and parallel circuit configurations of a four-cell thermoelectric generator module design," Journal of Applied Engineering Design and Simulation, vol. 1, no. 1, pp. 32–42, 2021, doi: 10.24191/jaeds.v1i1.18.

[105] W. Mohamed, M. H. Hamdan, N. F. Zamri, I. A. Zakaria, M. F. Mohamad, and M. I. Rosli, "Integrated Heat Regenerator (IHR) Designs with Hydrogen Preheater and Thermoelectric Generator for Power Enhancement of a 2 kW Fuel Cell Vehicle," International Journal of Integrated Engineering, vol. 14, no. 2, pp. 164–185, 2022, doi: 10.30880/ijie.2022.14.02.021.

[106] S. S. Niknezhad, F. Moghaddamali, and E. Pistikopoulos, "Toward More Efficient Large-Scale Green Hydrogen Systems via Waste Heat Recovery and ORC," Applied Sciences (Switzerland), vol. 15, no. 10, 2025, doi: 10.3390/app15105224.

[107] Q. Cao et al., "A novel thermal management for PEM fuel cell stack combining phase change materials with liquid cooling under low temperature condition,"

Appl. Therm. Eng., vol. 238, no. August 2023, p. 121949, 2024, doi: 10.1016/j.applthermaleng.2023.121949.

[108] H. Lambert, D. Hernàndez-Torres, C. Retière, L. Garnier, and J. P. Poirot-Crouvezier, "X-in-the-Loop Methodology for Proton Exchange Membrane Fuel Cell Systems Design: Review of Advances and Challenges," Energies (Basel)., vol. 18, no. 14, pp. 1–28, 2025, doi: 10.3390/en18143774.

[109] X. Yang and W. He, "Simulation study based on experimental flexible composite phase change material for battery thermal management," Taylor & FrancisX Yang, W HeHeat Transfer Engineering, 2025•Taylor & Francis, 2025, doi: 10.1080/01457632.2025.2459983.

[110] A. D'Adamo, M. Haslinger, G. Corda, J. Höflinger, S. Fontanesi, and T. Lauer, "Modelling methods and validation techniques for CFD simulations of PEM fuel cells," Processes, vol. 9, no. 4, pp. 1–48, 2021, doi: 10.3390/pr9040688.

[111] D. Arun, A. N.-J. of Metals, M. and, and undefined 2023, "Review of materials, functional components, fabrication technologies and assembling characteristics for polymer electrolyte membrane fuel cells (PEMFCs)–An," jmmm.material.chula.ac.thD Arun, AS NESARAJJournal of Metals, Materials and Minerals, 2023•jmmm.material.chula.ac.th, vol. 33, no. 4, p. 2023, doi: 10.55713/jmmm.v33i4.1775.

[112] A. U. Yakubu et al., "A comprehensive review of primary cooling techniques and thermal management strategies for polymer electrolyte membrane fuel cells PEMFC," Heliyon, vol. 10, no. 19, p. e38556, 2024, doi: 10.1016/j.heliyon.2024.e38556.

[113] Z. Zhan et al., "Experimental study on different preheating methods for the cold-start of PEMFC stacks," Energy, vol. 162, pp. 1029–1040, 2018, doi: 10.1016/j.energy.2018.08.003.

[114] A. P. Tetuko, B. Shabani, and J. Andrews, "Passive fuel cell heat recovery using heat pipes to enhance metal hydride canisters hydrogen discharge rate: An experimental simulation," Energies (Basel)., vol. 11, no. 4, 2018, doi: 10.3390/en11040915.

[115] X. Yang, J. Sun, S. Sun, and Z. Shao, "An efficient cold start strategy for proton exchange membrane fuel cell stacks," J. Power Sources, vol. 542, no. March, p. 231492, 2022, doi: 10.1016/j.jpowsour.2022.231492.

[116] A. P. Tetuko, B. Shabani, R. Omrani, B. Paul, and J. Andrews, “Study of a thermal bridging approach using heat pipes for simultaneous fuel cell cooling and metal hydride hydrogen discharge rate enhancement,” J. Power Sources, vol. 397, no. May, pp. 177–188, 2018, doi: 10.1016/j.jpowsour.2018.07.030.

[117] Y. Lan, J. Lu, L. Mu, S. Wang, and H. Zhai, “Waste heat recovery from exhausted gas of a proton exchange membrane fuel cell to produce hydrogen using thermoelectric generator,” Appl. Energy, vol. 334, no. October 2022, p. 120687, 2023, doi: 10.1016/j.apenergy.2023.120687.

[118] J. Fornaciari, S. Garg, X. Peng, … Y. R.-J. of the, and undefined 2022, “Performance and durability of proton exchange membrane vapor-fed unitized regenerative fuel cells,” iopscience.iop.orgJC Fornaciari, S Garg, X Peng, YN Regmi, AZ Weber, N DanilovicJournal of the Electrochemical Society, 2022•iopscience.iop.org, 2022, doi: 10.1149/1945-7111/ac6c51.

[119] X. Gao, S. Andreasen, M. Chen, S. K.-I. J. of hydrogen, and undefined 2012, “Numerical model of a thermoelectric generator with compact plate-fin heat exchanger for high temperature PEM fuel cell exhaust heat recovery,” ElsevierX Gao, SJ Andreasen, M Chen, SK KærInternational Journal of hydrogen energy, 2012•Elsevier.

[120] W. Huo et al., “High precision and efficient simulation of large-size proton exchange membrane fuel cells incorporated with a novel alternative cooling method,” Int. J. Heat Mass Transf., vol. 230, no. May, p. 125780, 2024, doi: 10.1016/j.ijheatmasstransfer.2024.125780.

[121] M. Seddiq, M. Alnajideen, and R. Navaratne, “Thermal Transient Performance of PEM Fuel Cells in Aerospace Applications: A Numerical Study,” Energy and Fuels, vol. 39, no. 16, pp. 7876–7889, 2025, doi: 10.1021/acs.energyfuels.4c04834.

[122] B. Xie et al., “Validation methodology for PEM fuel cell three-dimensional simulation,” Int. J. Heat Mass Transf., vol. 189, p. 122705, 2022, doi: 10.1016/j.ijheatmasstransfer.2022.122705.

[123] P. Thiele et al., “Realistic accelerated stress tests for PEM fuel cells: Operation condition dependent load profile optimization,” J. Power Sources, vol. 617, no. June, p. 234959, 2024, doi: 10.1016/j.jpowsour.2024.234959.

[124] L. Birkner, M. Foreta, A. Rinaldi, A. Orekhov, M. G. Willinger, and M. Eichelbaum, “Dynamic accelerated stress test and coupled on-line analysis

program to elucidate aging processes in proton exchange membrane fuel cells," Sci. Rep., vol. 14, no. 1, pp. 1–22, 2024, doi: 10.1038/s41598-024-54258-8.

[125] I. Bloom et al., "A comparison of Fuel Cell Testing protocols - A case study: Protocols used by the U.S. Department of Energy, European Union, International Electrotechnical Commission/Fuel Cell Testing and Standardization Network, and Fuel Cell Technical Team," J. Power Sources, vol. 243, pp. 451–457, 2013, doi: 10.1016/j.jpowsour.2013.06.026.

[126] R. M. A. Raja Arif, "Water and Thermal Management of PEM Fuel Cells," Mar. 2018.

[127] Q. Meyer et al., "Combined current and temperature mapping in an air-cooled, open-cathode polymer electrolyte fuel cell under steady-state and dynamic conditions," J. Power Sources, vol. 297, pp. 315–322, 2015, doi: 10.1016/j.jpowsour.2015.07.069.

[128] J. Zuo et al., "Long-term dynamic durability test datasets for single proton exchange membrane fuel cell," Data Brief, vol. 35, p. 106775, 2021, doi: 10.1016/j.dib.2021.106775.

[129] J. Han and S. Yu, "Ram air compensation analysis of fuel cell vehicle cooling system under driving modes," Appl. Therm. Eng., vol. 142, no. July, pp. 530–542, 2018, doi: 10.1016/j.applthermaleng.2018.07.038.

[130] V. Ionescu, "Thermal-hydraulic analysis of a louver fin-and-tube radiator for a liquid–cooled PEMFC stack system," Ovidius University Annals of Chemistry, vol. 35, no. 2, pp. 111–117, 2024, doi: 10.2478/auoc-2024-0015.

[131] H. John E., L. Richard, And R. David A., Compact Heat Exchangers Selection, Design and Operation, Second Edition. Elsevier Ltd, Joe Hayton, 2017.

[132] W. H. Chen, Y. X. Lin, Y. Bin Chiou, Y. L. Lin, and X. D. Wang, "A computational fluid dynamics (CFD) approach of thermoelectric generator (TEG) for power generation," Appl. Therm. Eng., vol. 173, no. February, p. 115203, 2020, doi: 10.1016/j.applthermaleng.2020.115203.

[133] R. C. and S. K.N., Compact Heat Exchanger, Analysis, Design and Optimization using FEM and CFD approach, First. The Atrium, Southern Gate, Chichester, West Sussex, PO19 8SQ, UK: John Wiley & Sons Ltd, 2018.

[134] N. M. and G. R.O., HEAT EXCHANGER DESIGN GUIDE A Practical Guide for Planning, Selecting and Designing of Shell and Tube Exchangers. Waltham, MA 02451, USA: Elsevier Inc., 2016.

[135] H. Jouhara et al., “Thermoelectric generator (TEG) technologies and applications,” Feb. 01, 2021, Elsevier B.V. doi: 10.1016/j.ijft.2021.100063.

[136] A. G. Rösch, L. Franke, M. M. Mallick, and U. Lemmer, “Optimizing printed thermoelectric generators with geometry and processibility limitations,” Energy Convers. Manag., vol. 279, Mar. 2023, doi: 10.1016/j.enconman.2023.116776.

[137] O. Högblom and R. Andersson, “Multiphysics CFD Simulation for Design and Analysis of Thermoelectric Power Generation,” Energies (Basel)., vol. 13, no. 17, Sep. 2020, doi: 10.3390/EN13174344.

[138] X. W. Chen, C. A. Vaithilingam, S. Ponnan, and A. Sharma, “Resolving the thermal incompatibility of CPV–TEG hybrids through asymmetric heat-pipe design,” Appl. Therm. Eng., p. 129860, Mar. 2026, doi: 10.1016/j.applthermaleng.2026.129860.

[139] T. Bin Nadeem, M. Imran, A. Arshad, and E. Tandis, “Numerical investigation and optimization of finned tube heat exchanger for enhanced thermal-hydraulic performance in IEC application,” Thermal Science and Engineering Progress, vol. 76, Aug. 2026, doi: 10.1016/j.tsep.2026.104805.

[140] H. Pourrahmani, H. Shakeri, and J. Van herle, “Thermoelectric Generator as the Waste Heat Recovery Unit of Proton Exchange Membrane Fuel Cell: A Numerical Study,” Energies (Basel)., vol. 15, no. 9, p. 3018, Apr. 2022, doi: 10.3390/en15093018.

[141] T. Taner, “The novel and innovative design with using H2 fuel of PEM fuel cell: Efficiency of thermodynamic analyze,” Fuel, vol. 302, p. 121109, Oct. 2021.

APPENDICES

APPENDIX A

IHR Design Specifications

Components	IHR specification (Design 1)	Units	Parameters
Overall IHR system size	Size (width x length x thickness)	mm	530 X 265 X 82
Heat sink	Size (width x height x length)	mm	226 x 66 x 265
	No. fins	Nos.	29
	Fin size (height x thickness x length)	mm	68.5 x 2 x 300 (fin gap 6 mm)
	Base thickness	mm	6
	Material		Aluminium
	Quantity	Nos.	1
	Heating surface area	m^2	0.968
Hydrogen preheat tube	Size (outer diameter x inner diameter x thickness x length)	mm	19.05 x 17.05 x 1 x 1416
	No. tube pass	Nos.	6
	Material		Copper
	Quantity	Nos.	1
	Heating surface area	m^2	0.076
TEG	Size (width x height x thickness)	mm	60 x 60 x 6
	Material		Bismuth telluride
	Quantity	Nos.	12
	Cooling surface area	m^2	0.0036 per 1 TEG
	Heating surface area	m^2	0.0036 per 1 TEG
Copper block	Size (width x length x thickness)	mm	226 x 264 x 10
	Material		Copper
	Quantity	Nos.	1
	Cooling surface area	m^2	0.0596
Heat pipe	Size (diameter x length)	mm	6 x 500
	Material		Copper
	Quantity	Nos.	8
Cooling fin sets	Size (width x height x length)	mm	48 x 40 x 98 (per set)
	Fin size (height x length x thickness)	mm	34 x 25 x 0.6
	Fins	Nos.	50 (per set)
	Material		Aluminium
	Quantity	Nos.	4 Set, 1 set for 2 heat pipes
	Cooling surface area	m^2	0.192 per set

Components	IHR specification (Design 2)	Units	Parameters
Overall IHR system size	Size (width x length x thickness)	mm	300 X 300 X 96
Heat sink	Size (width x height x length)	mm	186 x 80.5 x 300
	No. fins	Nos.	34
	Fin size (height x thickness x length)	mm	68.5 x 1.57 x 300 (fin gap 4mm)
	Base thickness	mm	12
	Material		Aluminium
	Quantity	Nos.	1
	Heating surface area	m^2	1.3242
Hydrogen preheat tube	Size (outer diameter x inner diameter x thickness x length)	mm	19.05 x 17.05 x 1 x 2826
	No. tube pass	Nos.	8
	Material		Copper
	Quantity	Nos.	1
	Heating surface area	m^2	0.0577
TEG	Size (width x height x thickness)	mm	60 x 60 x 6
	Material		Bismuth telluride
	Quantity	Nos.	8
	Cooling surface area	m^2	0.0036
	Heating surface area	m^2	0.0036
Copper block	Size (width x length x thickness)	mm	60 x 120 x 8
	Material		Copper
	Quantity	Nos.	4
	Cooling surface area	m^2	0.0072 for 1 pieces
Heat pipe	Size (diameter x length)	mm	6 x 300
	Material		Copper
	Quantity	Nos.	24
Cooling fin sets	Size (width x height x length)	mm	34 x 25 x 74 (per set)
	Fin size (height x length x thickness)	mm	34 x 25 x 0.6
	Fins	Nos.	47 (per set)
	Material		Aluminium
	Quantity	Nos.	8 Set, 1 set for 3 heat pipes
	Cooling surface area	m^2	0.0799 per set

Components	IHR specification (Design 3)	Units	Parameters
Overall IHR system size	Size (width x length x thickness)	mm	250 X 171 X 154
Heat sink	Size (width x height x length)	mm	226 x 64 x 171
	No. fins	Nos.	29
	Fin size (height x thickness x length)	mm	60 x 2 x 171 (fin gap 6mm)
	Base thickness	mm	4
	Material		Aluminium
	Quantity	Nos.	1
	Heating surface area	m^2	0.595
Hydrogen preheat tube	Size (outer diameter x inner diameter x thickness x length)	mm	19.05 x 17.05 x 1 x 1079
	No. tube pass	Nos.	4
	Material		Copper
	Quantity	Nos.	1
	Heating surface area	m^2	0.0577
TEG	Size (width x height x thickness)	mm	60 x 60 x 6
	Material		Bismuth telluride
	Quantity	Nos.	6
	Cooling surface area	m^2	0.0036
	Heating surface area	m^2	0.0036
Copper block	Size (width x length x thickness)	mm	226 x 150 x 10
	Material		Copper
	Quantity	Nos.	1
	Cooling surface area / m^2	m^2	0.0339
Heat pipe	Size (diameter x length)	mm	6 x 227 (max length), min 171 Length increment of 4mm for each.
	Material		Copper
	Quantity	Nos.	15
Cooling fins	Size (width x height x length)	mm	226 x 69 x 146
	Fin size (height x length x thickness)	mm	226 x 69 x 1
	Fins	Nos.	50
	Material		Aluminium
	Quantity	Nos.	1 for 15 heat pipes
	Cooling surface area	m^2	1.559

Components	IHR specification (Design 4)	Units	Parameters
Overall IHR system size	Size (width x length x thickness)	mm	250 X 171 X 154
Heat sink	Size (width x height x length)	mm	226 x 64 x 171
	No. fins	Nos.	29
	Fin size (height x thickness x length)	mm	60 x 2 x 171 (fin gap 6mm)
	Base thickness	mm	4
	Material		Aluminium
	Quantity	Nos.	1
	Heating surface area	m^2	0.595
Hydrogen preheat tube	Size (outer diameter x inner diameter x thickness x length)	mm	19.05 x 17.05 x 1 x 1079
	No. tube pass	Nos.	4
	Material		Copper
	Quantity	Nos.	1
	Heating surface area	m^2	0.0577
TEG	Size (width x height x thickness)	mm	60 x 60 x 6
	Material		Bismuth telluride
	Quantity	Nos.	6
	Cooling surface area	m^2	0.0036
	Heating surface area	m^2	0.0036
Copper block	Size (width x length x thickness)	mm	226 x 150 x 10
	Material		Copper
	Quantity	Nos.	1
	Cooling surface area / m^2	m^2	0.0339
Heat pipe	Size (diameter x length)	mm	6 x 227 (max length), min 171 Length increment of 4mm for each.
	Material		Copper
	Quantity	Nos.	15
Cooling fins	Size (width x height x length)	mm	92 x 31.5 x 159
	Fin size (height x length x thickness)	mm	226 x 69 x 1
	Fins	Nos.	2 sets of 20 fin, 1 set of 10fins
	Material		Aluminium
	Quantity	Nos.	3sets, 2 set for 6 heat pipes, 1set for 3 heat pipes
	Cooling surface area	m^2	0.892

APPENDIX B

Thermal Resistance Circuit For IHR

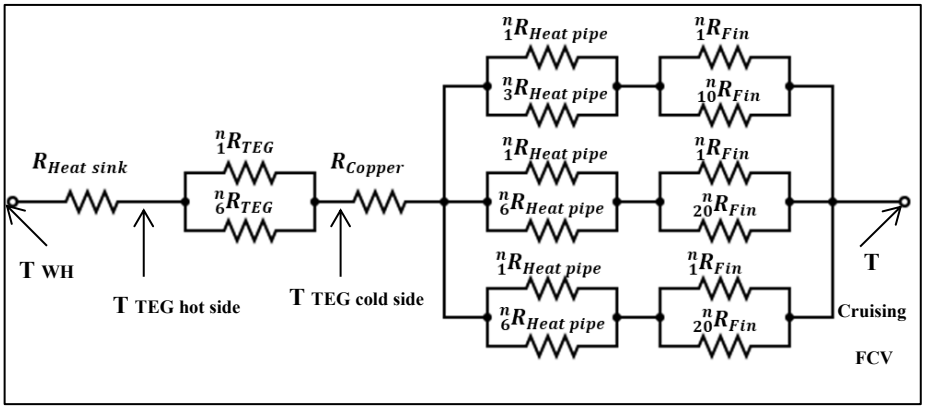

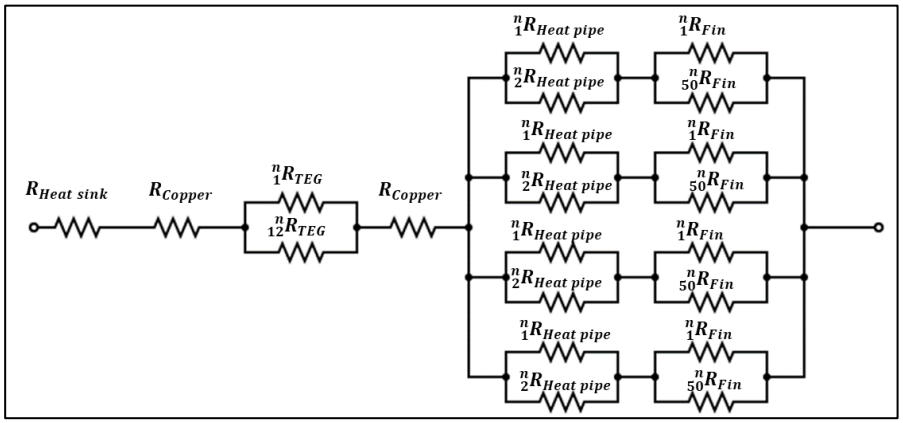

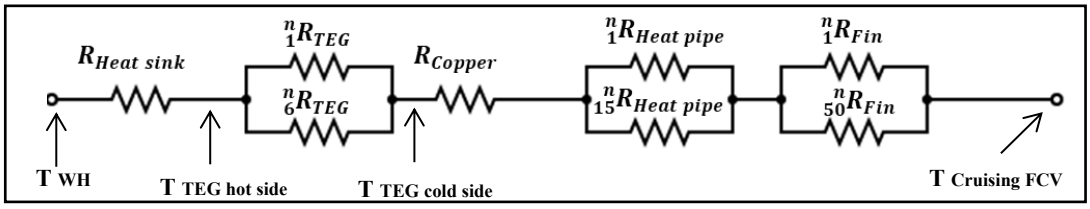

APPENDIX C

IHR Components Drawing

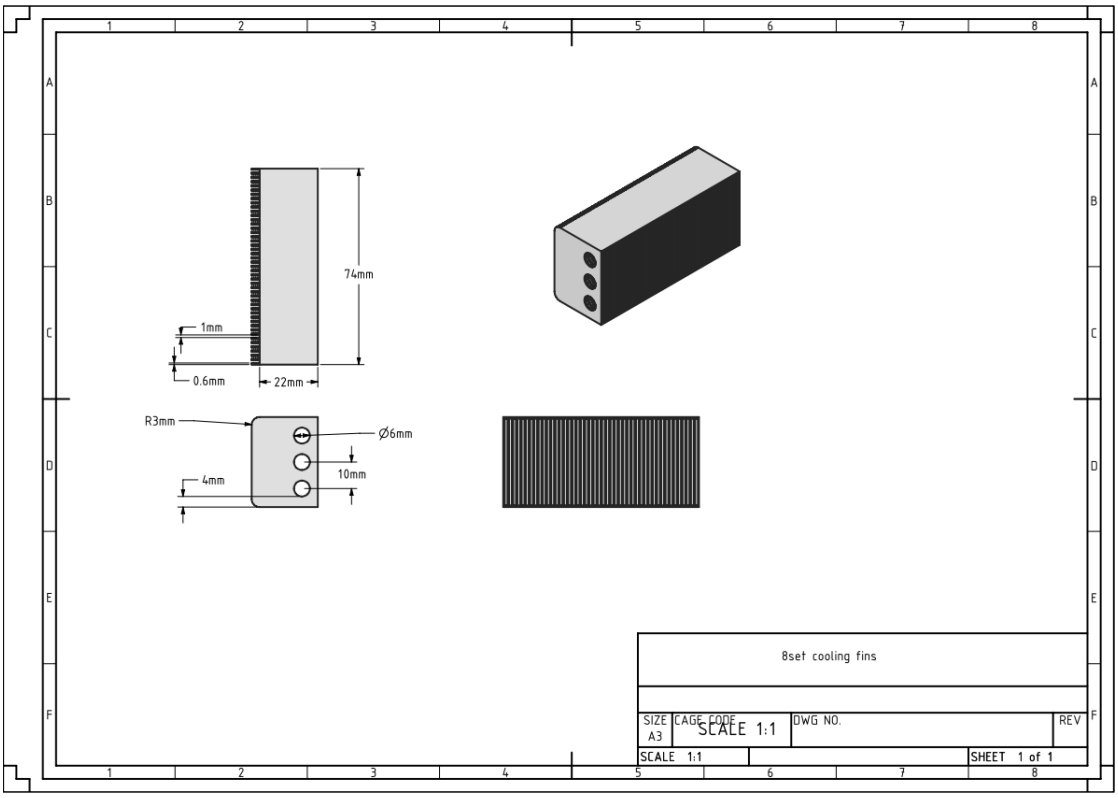

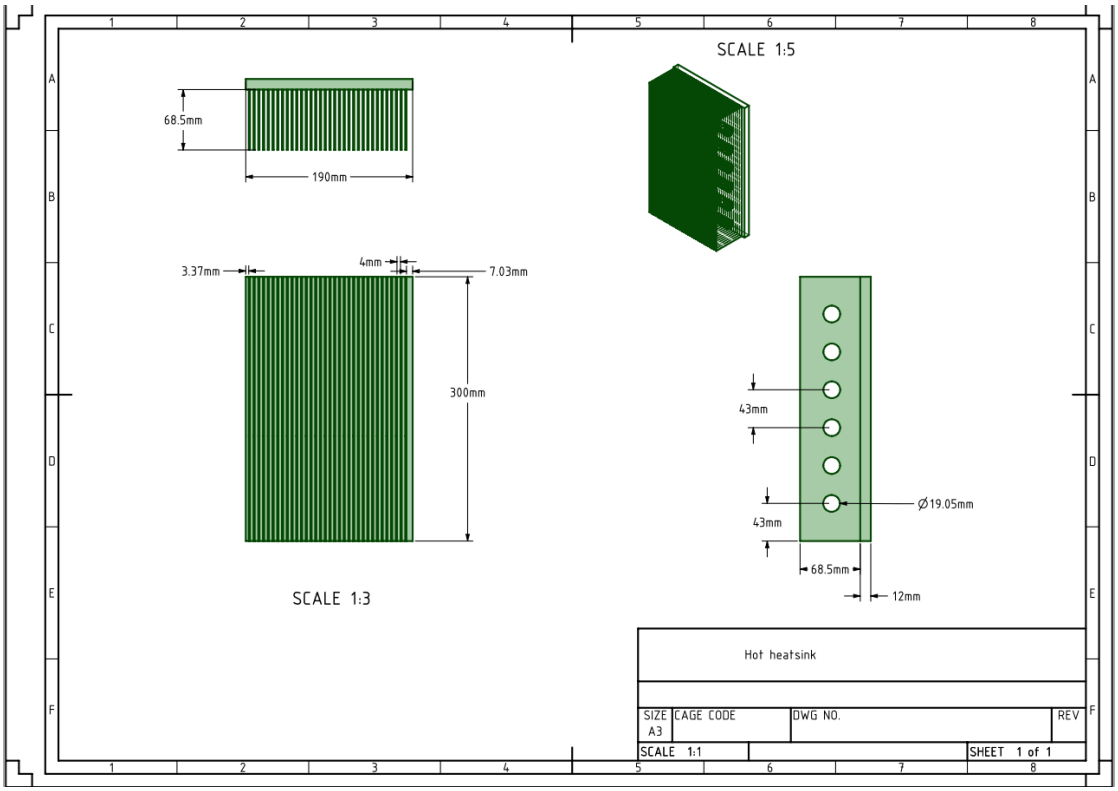

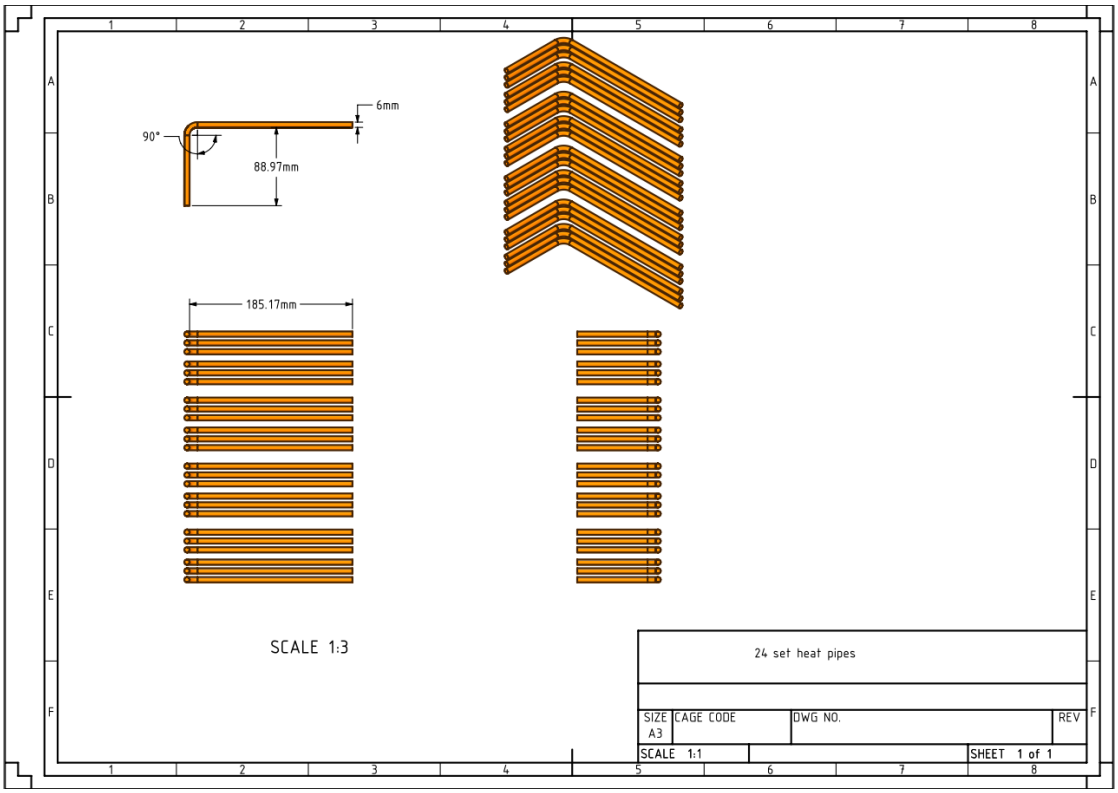
6mm
90°
88.97mm
185.17mm
SCALE 1:3
24 set heat pipes
SIZE A3
CAGE CODE
DWG NO.
REV
SCALE 1:1
SHEET 1 of 1

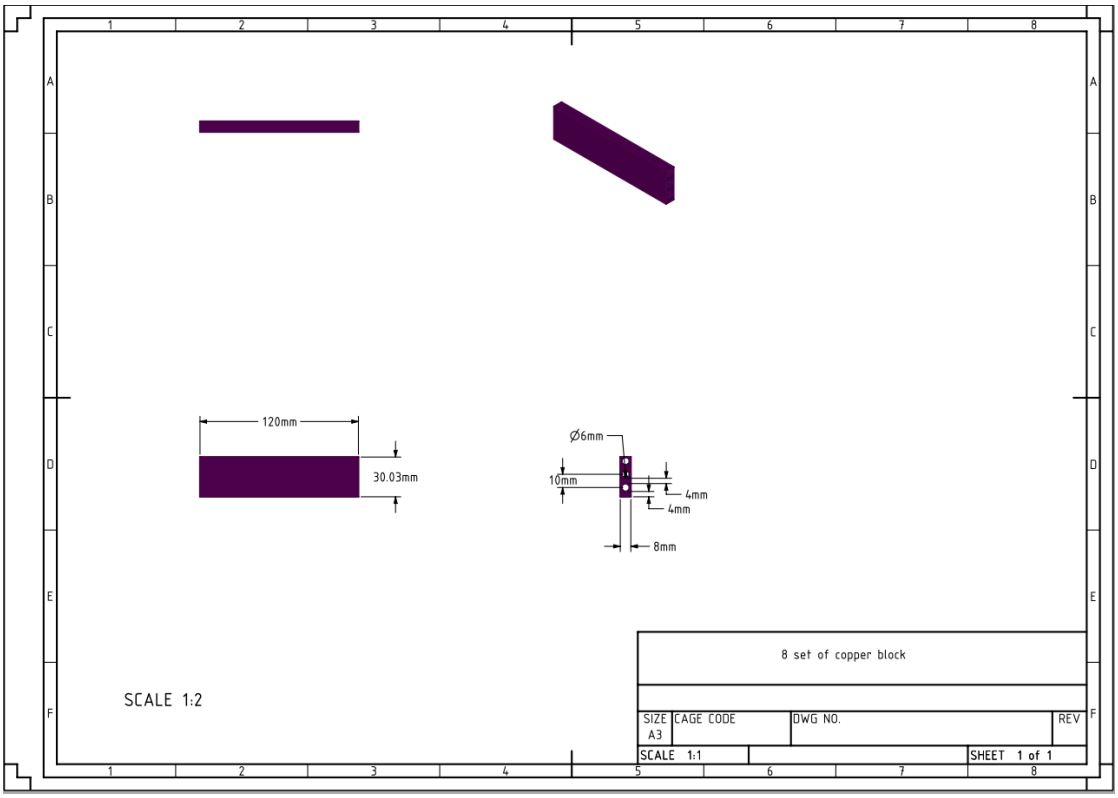
120mm
30.03mm
Ø6mm
10mm
4mm
4mm
8mm
SCALE 1:2
8 set of copper block
SIZE A3
CAGE CODE
DWG NO.
REV
SCALE 1:1
SHEET 1 of 1

APPENDIX D

IHR Components Drawing

2

Components



Li-Ion Battery



Diode



DC/DC Converter 24V – 48V



DC/DC Converter 24V – 12V

3 Fittings



Gauge Regulator



Pressure Gauge 400 bar

APPENDIX E

FC Circuit Diagram

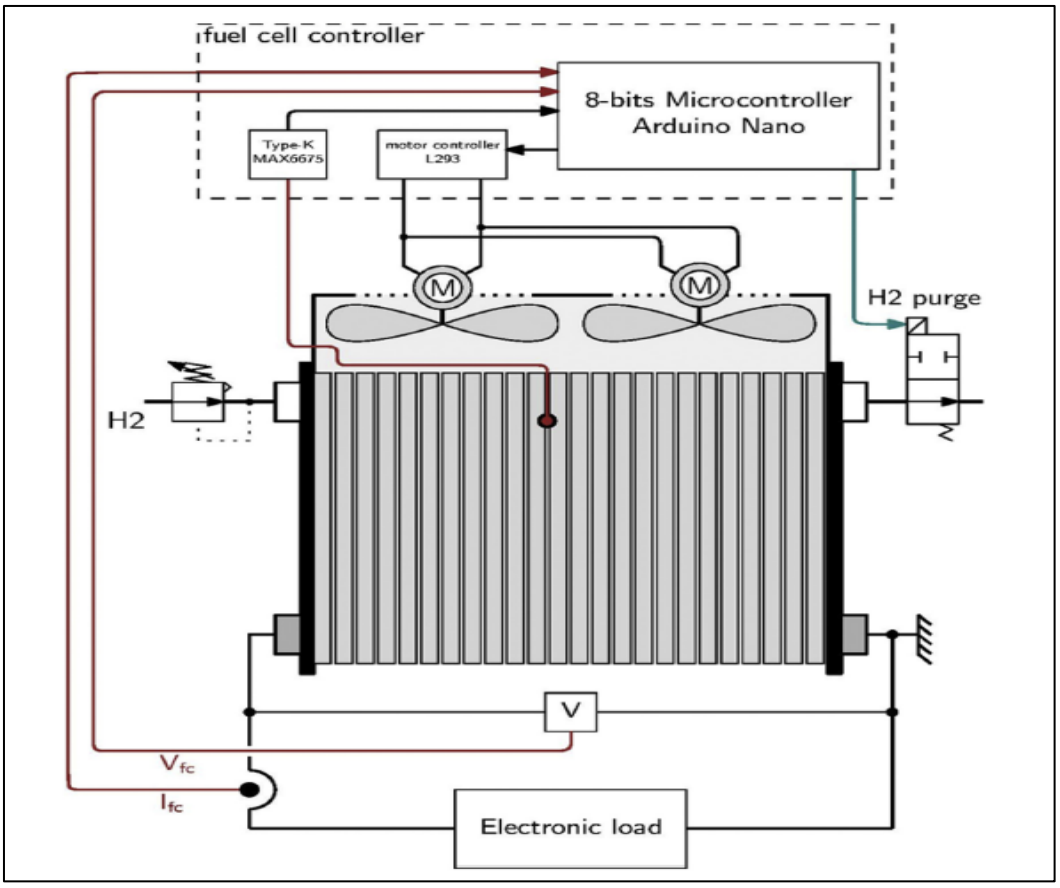



APPENDIX F

Buggy Raw Data

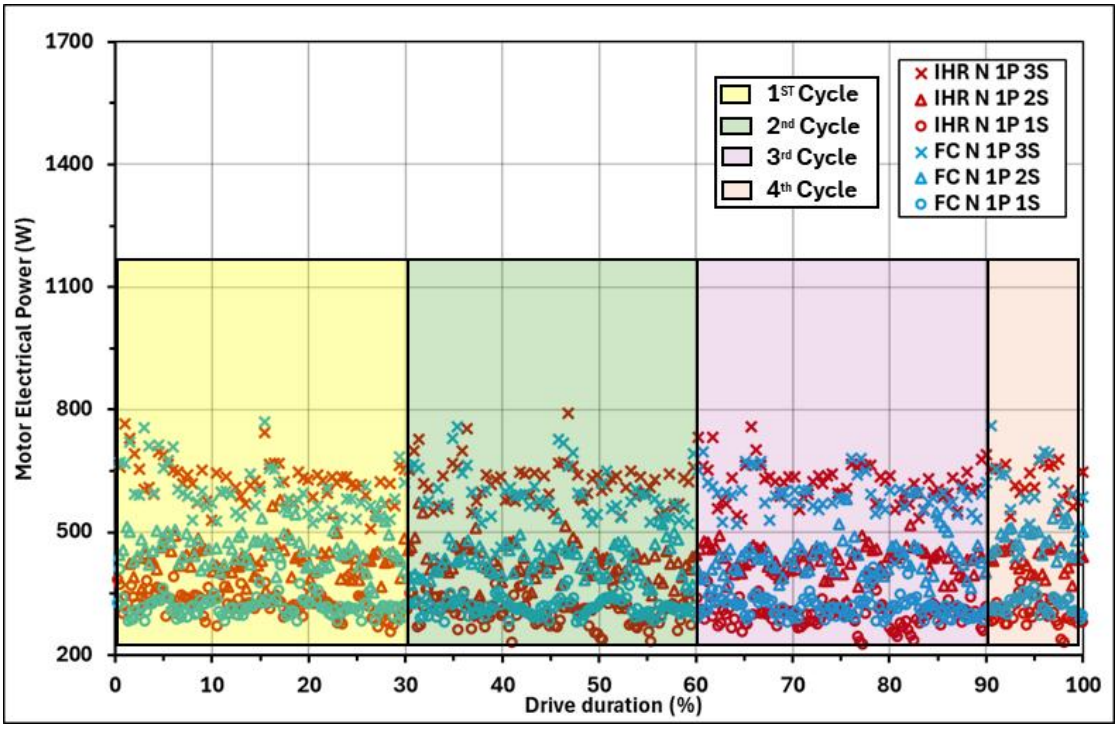

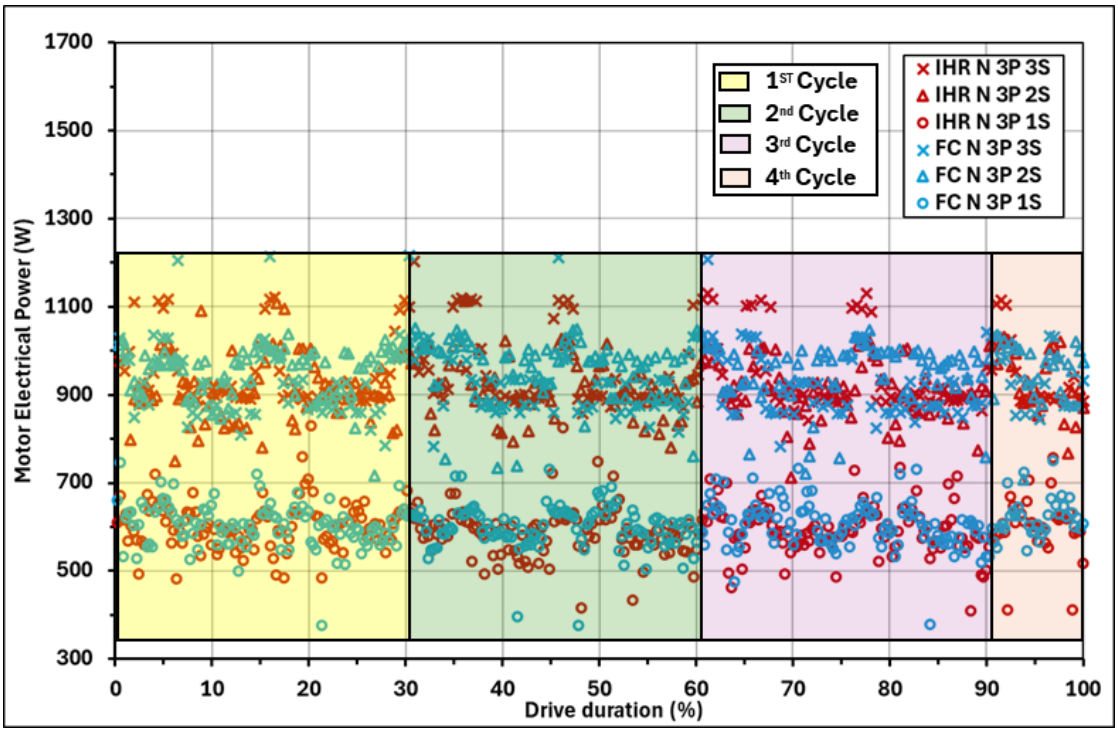
1ST Cycle
2nd Cycle
3rd Cycle
4th Cycle
IHR N 3P 3S
IHR N 3P 2S
IHR N 3P 1S
FC N 3P 3S
FC N 3P 2S
FC N 3P 1S
Motor Electrical Power (W)
Drive duration (%)

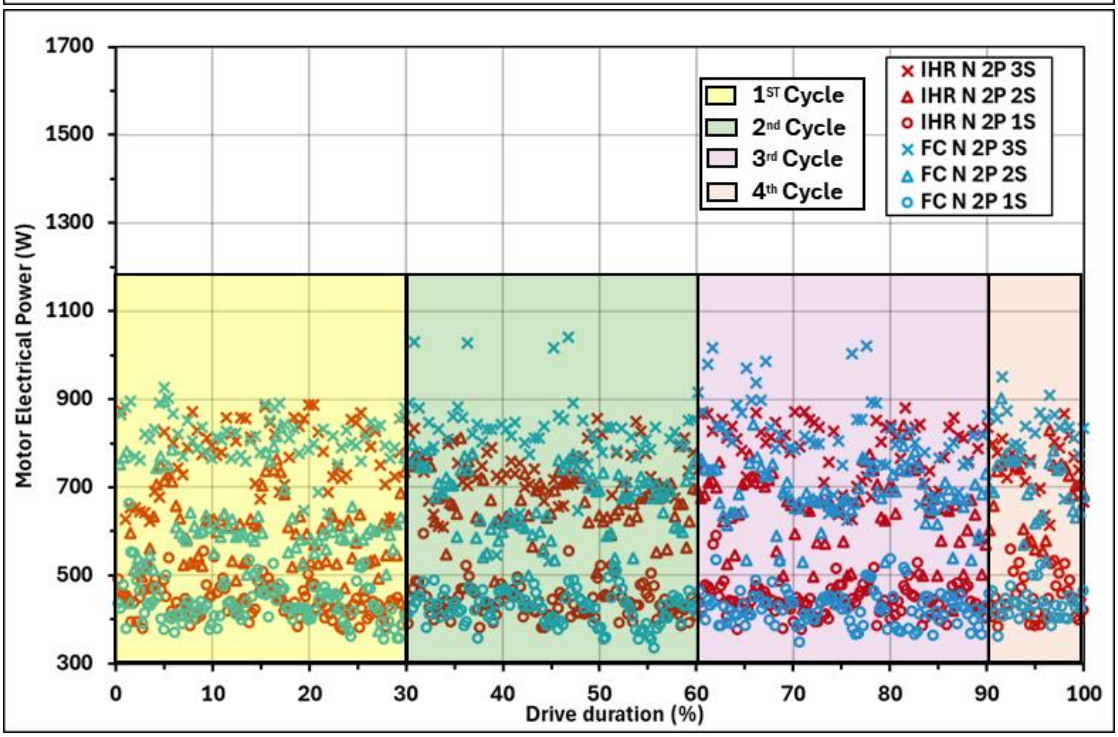
1ST Cycle
2nd Cycle
3rd Cycle
4th Cycle
IHR N 2P 3S
IHR N 2P 2S
IHR N 2P 1S
FC N 2P 3S
FC N 2P 2S
FC N 2P 1S
Motor Electrical Power (W)
Drive duration (%)

APPENDIX X

FC Raw Data

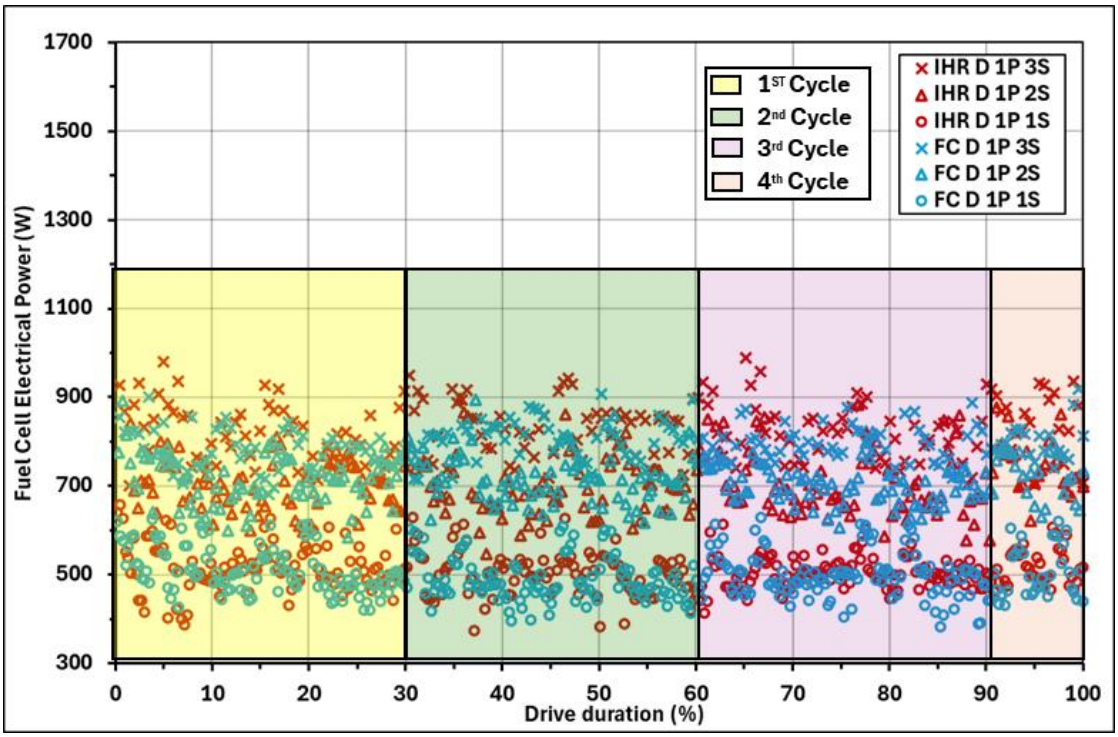

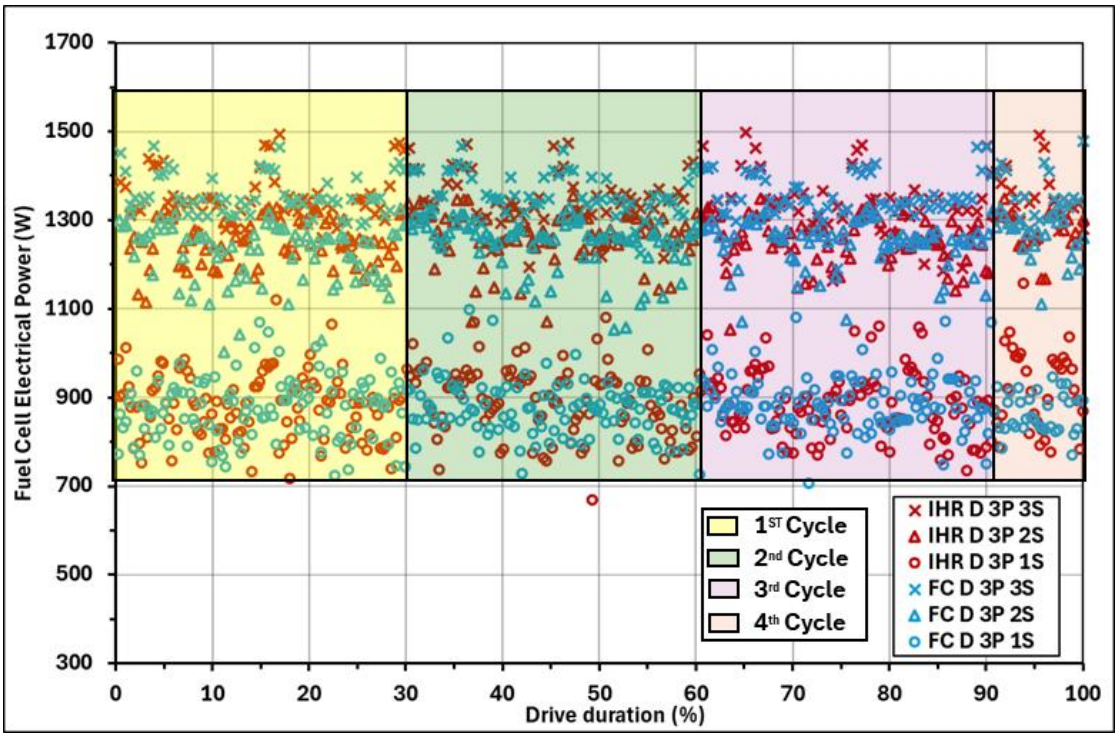
Fuel Cell Electrical Power (W)
1700
1500
1300
1100
900
700
500
300
0
10
20
30
40
50
60
70
80
90
100
Drive duration (%)
1ST Cycle
2nd Cycle
3rd Cycle
4th Cycle
IHR D 3P 3S
IHR D 3P 2S
IHR D 3P 1S
FC D 3P 3S
FC D 3P 2S
FC D 3P 1S

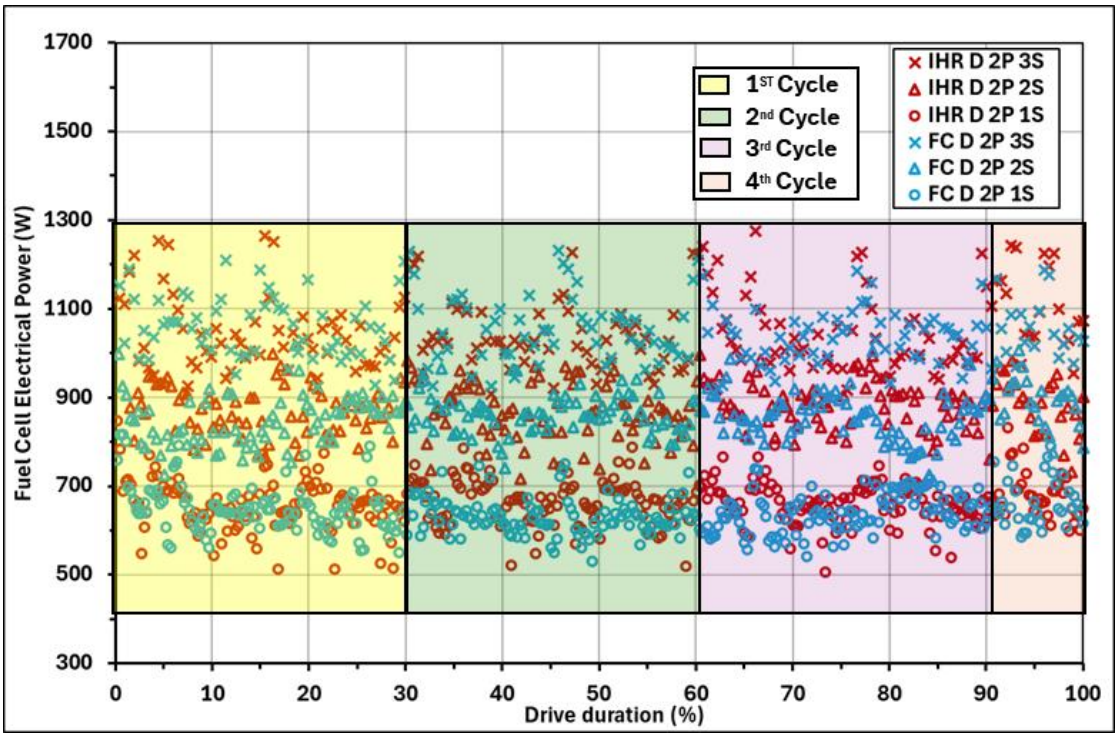
Fuel Cell Electrical Power (W)
1700
1500
1300
1100
900
700
500
300
0
10
20
30
40
50
60
70
80
90
100
Drive duration (%)
1ST Cycle
2nd Cycle
3rd Cycle
4th Cycle
IHR D 2P 3S
IHR D 2P 2S
IHR D 2P 1S
FC D 2P 3S
FC D 2P 2S
FC D 2P 1S

AUTHOR'S PROFILE



Muhammad Hadrami bin Hamdan, born in Ampang, Kuala Lumpur on July 26, 1994, received his Diploma and Bachelor of Engineering with Honors in Mechanical Engineering from Universiti Teknologi MARA in 2015 and 2019, respectively. Since enrolling in a Doctor of Philosophy program in 2021, the author has dedicated his academic pursuits to the optimization of advanced energy conversion technologies and the development of sustainable vehicular powertrains. His primary research interests encompass the complex thermal management of polymer electrolyte membrane fuel cells, the design of passive waste heat recovery architectures, and the integration of solid state thermoelectric generation. Recognizing the strict thermodynamic limitations inherent to lightweight mobility, he attempts to bridge the critical gap between idealized mathematical models and the volatile realities of physical operation. With specific expertise spanning thermodynamics and energy conversion, the author has actively contributed to numerous research publications, academic conferences, and engineering competitions. Drawing upon extensive experience in mathematical modelling and physical experimental testing, his future aspirations include expanding industry collaborations and advancing green technologies to further the global transition toward renewable energy.

LIST OF PUBLICATIONS

1. **Hamdan**, M.H., Mohamed, W.A.N.W., Aminudin, M.A., Kamarudin, S.K., Zakaria, I.A. and Singh, B. (**2025**), An Integrated Heat Recovery System Design for a Fuel Cell Buggy With Hydrogen Preheating and Thermoelectric

Generator. FuelCells,25:e202400037. https://doi.org/10.1002/fuce.202400037

2. **Hamdan, M. H**., Zamri, N. F., Fairuz, M., Huda, N., Hanim, M., Jamilah, H., Fatmi, M., Najmi, A., & Mohamed, W. (**2024**). Performance of thermoelectric generator system to generate electrical output from a low-grade waste heat temperature under linear and swirling waste heat streams. *ESTEEM Acedemic Journal*, *20*, 100–116. https://doi.org/10.24191/esteem.v20iSeptember.18
3. Mohamed, W., **Hamdan, M. H.**, Zamri, N. F., Zakaria, I. A., & Mohamad, M. F. (**2021**). Integrated Heat Regenerator (IHR) Designs with Hydrogen Preheater and Thermoelectric Generator for Power Enhancement of a 2 kW Fuel Cell Vehicle. *International Journal of Integrated Engineering*, *0*, 1–4.
4. **Hamdan**, Muhammad & Som, Nur & Rashid, Amirul & Jimmy, Gilbert. (**2021**). Performance analysis on series and parallel circuit configurations of a four-cell thermoelectric generator module design. Journal of Applied Engineering Design and Simulation. 1. 10.24191/jaeds.v1i1.18.
5. Mohamed, W. A. N. W., Zamri, N. F., **Hamdan, M. H**., Shah, H. J. M. F., & Hanim, N. H. M. (**2023**). Performance of Single Cell and Double Stacked Thermoelectric Generator Modules for Low Temperature Waste Heat Recovery. *IOP Conference Series: Earth and Environmental Science*, *1261*(1). https://doi.org/10.1088/1755-1315/1261/1/012007
6. Zamri, N. F., **Hamdan, M. H**., Anuar, S. N. A., Mohamed, W. A. N. W., & Remeli, M. F. (**2022**). Performance of A Plate-Finned Thermoelectric Generator (TEG) Module for Industrial Waste Heat Recovery. *Journal of Mechanical Engineering*, *19*(3), 257–272. https://doi.org/10.24191/jmeche.v19i3.19817
7. Zamri, N. F., Rahin, A. N., & **Hamdan, M. H**. (**2023**). Representative Value of Thermal Conductivity for Wickless Heat Pipe in a Thermoelectric Generator System via Computational Numerical Analysis. *Journal of Applied Engineering Design & Simulation*, *3*(1), 40–50. https://doi.org/10.24191/jaeds.v3i1.61